POLITECNICO
MILANO 1863

DIPARTIMENTO DI
INGEGNERIA CIVILE E AMBIENTALE

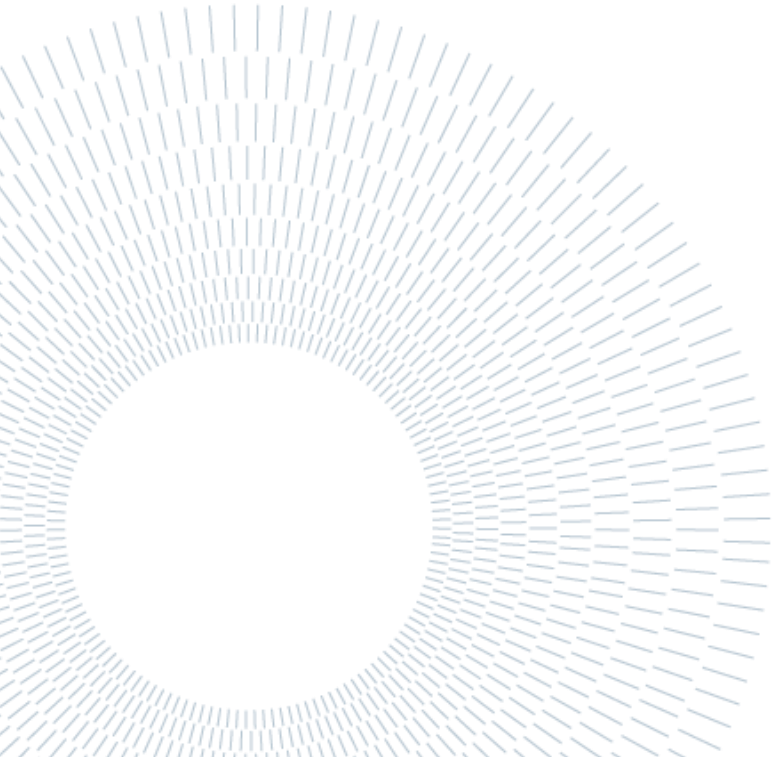
AGGRADATION WAVE DYNAMICS UNDER SEDIMENT OVERLOADING IN UNSTEADY SUPERCRITICAL FLOW CONDITIONS

TESI DI LAUREA MAGISTRALE IN
INGEGNERIA CIVILE PER LA MITIGAZIONE DEL RISCHIO
CIVIL ENGINEERING FOR RISK MITIGATION

Author: Mahdi Mokhtarzadeh

Student ID: 257699
Advisor: Prof. Alessio Radice
Co-advisor: Dr. Hasan Eslami
Academic Year: 2025-26

To my mother, whose love, sacrifices, and unwavering support made more possible than she knows.



Abstract (English)

Sediment transport in river systems is a fundamental geomorphological process that takes place across a wide range of spatial and temporal scales, with significant consequences for fluvial dynamics and natural hazard assessment. Beyond its direct influence on flood behavior, this process is closely linked to environmental health, cultural heritage preservation, and a variety of economic activities. A better understanding of sediment transport therefore contributes not only to improved knowledge of river behavior, but also to the development of more reliable early warning systems that can help reduce the impacts of extreme flow events.

Mountainous environments are particularly relevant in this context, where steep channel gradients and intense rainfall create conditions prone to erosion and landslides, leading to large amounts of sediment being delivered to river channels. When sediment supply exceeds the transport capacity of the channel during high-flow periods, rapid riverbed aggradation occurs, reducing channel conveyance and increasing flood risk. In this setting, estimating the propagation celerity of aggradation waves is essential for predicting when sediment will reach critical downstream locations and for supporting flood risk management decisions. From an engineering perspective, the morphological changes caused by sediment overloading can directly lead to hydraulic hazards, which makes celerity a parameter of clear practical importance.

The main objective of this thesis is to investigate the celerity of sediment aggradation wave propagation under supercritical, unsteady flow conditions through ten experiments. The experimental results were found to correspond reasonably well with steady flow conditions reported in earlier studies, and the load ratio was identified as the most influential parameter in the celerity analysis.

Key-words: sediment transport capacity, aggradation, celerity, dimensionless celerity, supercritical flow, critical flow rate, dimensionless time, unsteady flow, propagation celerity, Froude number, loading ratio

Abstract (Italian)

Il trasporto di sedimenti nei sistemi fluviali è un processo geomorfologico fondamentale che si svolge su un'ampia gamma di scale spaziali e temporali, con conseguenze significative per la dinamica fluviale e la valutazione dei rischi naturali. Al di là della sua influenza diretta sul comportamento delle piene, questo processo è strettamente legato alla salute ambientale, alla conservazione del patrimonio culturale e a una varietà di attività economiche. Una migliore comprensione dei meccanismi di trasporto dei sedimenti contribuisce quindi non solo a una maggiore conoscenza del comportamento dei corsi d'acqua, ma anche allo sviluppo di sistemi di allerta precoce più affidabili, in grado di ridurre gli impatti degli eventi di piena estremi.

Gli ambienti montani sono particolarmente rilevanti in questo contesto, dove le forti pendenze dei canali e le precipitazioni intense creano condizioni favorevoli all'erosione e alle frane, determinando un apporto elevato di sedimenti ai canali fluviali. Quando, durante i periodi di alta portata, l'apporto di sedimenti supera la capacità di trasporto del canale, si verifica una rapida aggradazione del fondo alveo, con conseguente riduzione della capacità di deflusso e aumento del rischio di esondazione. In questo contesto, stimare la celerità di propagazione delle onde di aggradazione è essenziale per prevedere i tempi di arrivo dei sedimenti nelle zone critiche a valle e per supportare le decisioni di gestione del rischio idraulico. Dal punto di vista ingegneristico, le modificazioni morfologiche causate dal sovraccarico di sedimenti possono tradursi direttamente in pericoli idraulici, rendendo la celerità un parametro di chiara importanza pratica.

Alla luce di quanto sopra, l'obiettivo principale di questa tesi è studiare la celerità di propagazione dell'onda di aggradazione dei sedimenti in condizioni di moto supercritico e non stazionario attraverso dieci esperimenti. I risultati sperimentali hanno mostrato una corrispondenza ragionevole con le condizioni di moto stazionario riportate in studi precedenti, e il rapporto di carico è stato identificato come il parametro più influente nell'analisi della celerità.

Parole chiave: capacità di trasporto dei sedimenti, aggradazione, celerità, celerità adimensionale, moto supercritico, portata critica, tempo adimensionale, moto non stazionario, celerità di propagazione, numero di Froude, rapporto di carico

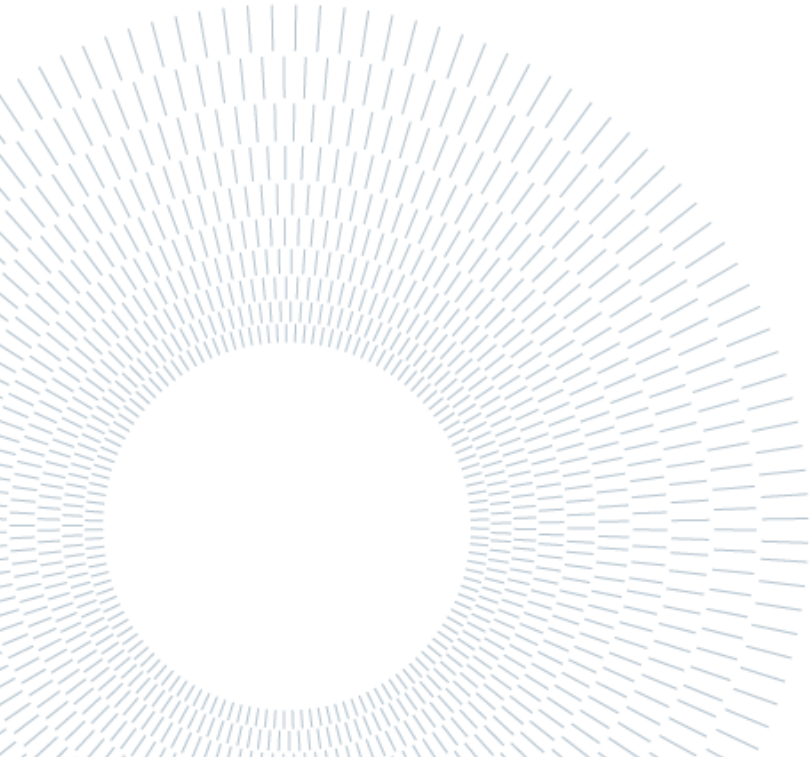
Abstract (Persian)

انتقال رسوب در سیستم‌های رودخانه‌ای یک فرآیند ژئومورفولوژیکی اساسی است که در طیف گسترده‌ای از مقیاس‌های زمانی و مکانی اتفاق می‌افتد و پیامدهای قابل توجهی برای دینامیک رودخانه‌ای و ارزیابی مخاطرات طبیعی دارد. فراتر از تأثیر مستقیم آن بر رفتار سیلاب، این فرآیند با سلامت محیط زیست، حفاظت از میراث فرهنگی و طیف متنوعی از فعالیت‌های اقتصادی در ارتباط نزدیک است. درک بهتر مکانیزم‌های انتقال رسوب بنابراین نه تنها به بهبود شناخت رفتار رودخانه کمک می‌کند، بلکه به توسعه سیستم‌های هشدار اولیه قابل اعتمادتری نیز منجر می‌شود که می‌توانند در کاهش اثرات رویدادهای جریانی شدید مؤثر باشند.

محیط‌های کوهستانی در این زمینه از اهمیت ویژه‌ای برخوردارند، جایی که شیب‌های تند کانال و بارندگی شدید شرایطی مستعد فرسایش و زمین‌لغزش ایجاد می‌کنند و منجر به ورود مقادیر زیادی رسوب به کانال‌های رودخانه‌ای می‌شوند. هنگامی که در دوره‌های پرآبی، عرضه رسوب از ظرفیت انتقال کانال فراتر می‌رود، تجمع سریع رسوب در بستر رودخانه رخ می‌دهد که ظرفیت هدایت کانال را کاهش داده و خطر سیل را افزایش می‌دهد. در این شرایط، تخمین سرعت انتشار امواج تجمع رسوب برای پیش‌بینی زمان رسیدن رسوب به مناطق حساس پایین‌دست و حمایت از تصمیم‌گیری‌های مدیریت ریسک سیلاب ضروری است. از منظر مهندسی، تغییرات مورفولوژیکی ناشی از اضافه‌بار رسوبی می‌تواند مستقیماً به مخاطرات هیدرولیکی منجر شود، که این امر سرعت انتشار را به یک پارامتر با اهمیت عملی آشکار تبدیل می‌کند.

با توجه به این پیش‌زمینه، هدف اصلی این پایان‌نامه بررسی سرعت انتشار موج تجمع رسوب تحت شرایط جریان فوق‌بحرانی و ناپایا از طریق ده آزمایش است. نتایج آزمایشگاهی با شرایط جریان پایای گزارش‌شده در مطالعات پیشین تطابق قابل قبولی نشان داد و نسبت بار به عنوان تأثیرگذارترین پارامتر در تحلیل سرعت انتشار شناسایی شد.

واژگان کلیدی: ظرفیت انتقال رسوب، بالاآمدگی بستر، سرعت انتشار موج، سرعت انتشار موج بی‌بُعد، جریان فوق‌بحرانی، دبی بحرانی، زمان بی‌بُعد، جریان غیرماندگار، سرعت پیشروی موج، عدد فرود، نسبت بار رسوب



Contents

Abstract (English) ..... **i**

Abstract (Italian) ..... **ii**

Abstract (Persian) ..... **iii**

Contents ..... **v**

1 **Chapter 1: Introduction** **7**

1.1. Motivation and structure of the work 7

1.2. Generalities on Sediment Transport 8

1.2.1. Geometrical and Physical Properties of Sediment 9

1.2.2. Sediment Transport Mechanisms 11

1.2.3. Threshold of Motion 12

1.2.4. Bed-Load Transport Rate Estimation 15

1.3. Aggradation, Prior campaigns, objectives 16

1.3.1. Review of Previous Studies 17

1.3.2. Research Gap and Objectives of This Thesis 20

2 **Chapter 2: Experimental setup** **21**

2.1 Laboratory Facility and Experimental Setup 21

2.1.1. Experimental Channel 22

2.1.2. Water Supply and Flow Control System 24

2.1.3. Sediment Material 27

2.1.4. Sediment Feeding System 31

2.2. Experimental Procedure 36

2.2.1. Pre-experimental Phase 36

2.2.2. Experimental Phase 37

2.2.3. Post-experimental Phase 38

2.3. Data Acquisition and Monitoring Systems 39

2.3.1. Imaging System 39

2.3.2. Water Discharge Monitoring 41

2.3.3. Sediment Feed Monitoring 43

2.3.4. Bed and Water Surface Elevation Detection 47

.2.4 Initial Sediment Transport Capacity and Loading Ratio 53

2.4.1. Sediment Capacity (SC) Experiments 53

2.4.2. Continuity Method in Unsteady Experiments 56
3 Chapter 3: Results and Analysis 62
3.1. Aggradation Experiments 62
3.1.1. Experimental Conditions 62
3.1.2. Mass Conservation Analysis 67
3.2. Experimental Results 69
3.2.1. Bed elevation, Water Surface elevation and Slope Evolution 69
3.2.2. Initial sediment transport capacity 81
3.3. Aggradation Wave Celerity 89
3.3.1. Celerity Definition and Dimensionless form 90
3.3.2. Spatial and Temporal Evolution of Celerity 93
.3.3.3 Bulk Celerity Analysis and dependency on Control Parameters 96
.3.3.4 Steady–Unsteady Comparison and Experimental Limitations 105
3.4. Dimensionless Bed Slope Evolution and Steady-Flow Comparison . 106
4 Chapter 4: Summary and Conclusion 111
Bibliography 114
Appendix 117
List of Figures 147
List of Tables 151
Acknowledgments 153

1 Chapter 1: Introduction

1.1. Motivation and structure of the work

The phenomenon of river sediment transport has been widely studied by researchers and engineers due to its critical role in triggering a series of processes that lead to significant consequences during floods. Designing hydraulic structures such as dams, analyzing bridge pier scour — which is a major cause of bridge failure during floods — assessing flood risk, river management, and developing emergency plans are just some of the practical applications of sediment transport assessment. Studying sediment transport helps us better understand river behavior and supports the improvement of early warning systems, thereby reducing the negative impacts of hazardous events. From a hydrological perspective, heavy or prolonged rainfall combined with sediment accumulation are two important drivers of flooding. Aggradation is defined as a rise in bed elevation resulting from sediment inflow exceeding the channel's initial transport capacity. Sediment aggradation alters the riverbed over time and space and can significantly affect river behavior. Furthermore, morphological changes can set off a chain of processes within the river and its surrounding environment, making the detection and analysis of riverbed and water surface evolution a primary research motivation. Radice et al. (2013) highlighted that sediment transport plays a key role in flood hazards and their timing, noting that peak bed aggradation may trigger river outflow before peak discharge is reached — a finding that underlines the importance of not underestimating sediment aggradation when assessing flood and debris flow risks. This thesis will be indeed focused on the aggradation process due to sediment overloading.

Experimental analysis has traditionally represented one of the primary approaches for investigating sediment transport processes under controlled hydraulic and morphological conditions. To obtain reliable results, experiments must account for the influential factors present in natural conditions. Although mountain streams are typically supercritical, many previous experimental studies investigating aggradation processes have mainly focused on subcritical flow conditions (García, 2008; Viparelli et al., 2010; Chavarrías et al., 2019). Furthermore, unsteady flow, which varies over time, better represents the complex and dynamic nature of real conditions compared to steady flow; the supercritical, unsteady flow scenario is therefore considered a more realistic and meaningful model. In hazard assessments, the temporal scales of processes and events must also be taken into account when planning emergency

mitigation strategies. These time scales are governed not only by water velocity, but also by the rate at which sediments propagate along the riverbed — referred to as celerity — which can be directly applied in early warning systems.

In recent years, a series of experimental theses were carried out at the Laboratory of Mountain Hydraulics of Politecnico di Milano (Unigarro Villota, 2017; Zanchi, 2018; Zucchi, 2018; Heydari, 2020; Eslami et al., 2021; Tavakoli et al., 2022; Hiteh et al., 2023; El Achkar and Hassan, 2024; Eslami, 2025; Bahadori, 2026), investigating sediment aggradation under both subcritical and supercritical flow conditions. These studies aimed to characterize both the magnitude of aggradation and its propagation celerity along the channel, with key findings published by Radice and Zanchi (2018), Zanchi et al. (2019), Zanchi and Radice (2021), and Eslami et al. (2022, 2025a, 2025b).

The present study shares the core objectives of the prior ones — namely, riverbed and water surface detection and the determination of propagation celerity, correlating the latter with the Froude number and the sediment load ratio. The key distinction of this work lies in the use of unsteady flow and feeding conditions, whereas all prior studies were conducted under steady flow and sediment feeding rates.

Chapter overview:

Chapter 1: introduces the motivation and goals of this research and outlines the fundamental aspects of sediment transport, as well as the need for a new experimental campaign.

Chapter 2: describes the laboratory setup and data collection methods, presents an overview of the experimental procedures, and explains the approach used to determine the initial sediment transport capacity.

Chapter 3: presents an analysis of the morphological experimental results. This includes the evolution of channel bed slope over the course of the experiments, the spatial and temporal evolution of celerity, and the determination of bulk celerity values for different stages along a hydrograph.

Chapter 4: provides a summary and conclusion of the experimental results, and recommendations for future research.

1.2. Generalities on Sediment Transport

Sediment transport refers to the displacement of solid particles under the combined influence of fluid motion and gravitational forces. These processes operate in a variety of natural environments, including rivers, oceans, and lakes. In river networks, sediment is typically conveyed from high-elevation headwaters to lower regions such as plains and coastal zones (Schumm, 1977). An understanding of how a river system

collects, transports, and deposits sediment is central to addressing both applied and theoretical questions in fluvial engineering (Reid, 2016).

1.2.1. Geometrical and Physical Properties of Sediment

Sediment particles are classified based on their morphological features and material composition, which together govern their entrainment, transport, and deposition behavior.

Size

Particle size is the most fundamental property of sediment, directly influencing its mobility and transport behavior. Two methods are widely used for size determination: the nominal diameter, defined as the diameter of a sphere having the same volume as the particle; and the sieve diameter, defined as the minimum side length of a square sieve opening through which the particle can pass (Pye, 1994). For a particle retained between two sieve openings $D_1$and D_2, the representative size is taken as either the algebraic mean $\frac{D_1+D_2}{2}$or the geometric mean $\sqrt{D_1 D_2}$.

Shape and Roundness

Particle shape refers to the overall geometry of a sediment grain, commonly described by attributes such as sphericity, elongation, and flatness. One widely used classification is the Zingg scheme, which characterizes grain shape based on the ratios of the major (a), intermediate (b), and minor (c) axes, as illustrated in *Figure 1.1*. The Corey shape factor SFprovides a quantitative measure of particle geometry (Vanoni, 2006):

$$SF = \frac{c}{\sqrt{ab}} \qquad (1.1)$$

A perfectly spherical particle yields $SF = 1$. Roundness describes the sharpness of particle edges and reflects the degree of abrasion during transport. Following the index introduced by Wadell (1932):

$$\text{Roundness} = \frac{\sum_{i=1}^{n} \left(\frac{r_i}{R}\right)}{n} \qquad (1.2)$$

where r_i is the radius of curvature of each particle corner, R is the radius of the largest inscribed sphere, and $n$is the number of measured corners. *Figure 1.2* and *Figure 1.3* illustrate the geometry of particle roundness and a visual reference chart for roundness classes.

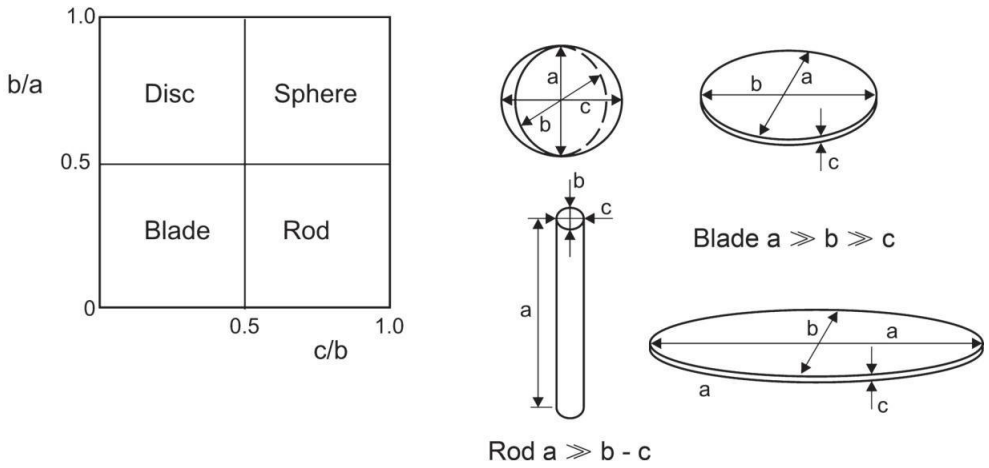


Figure 1.1: Zingg diagram for grain shape classification

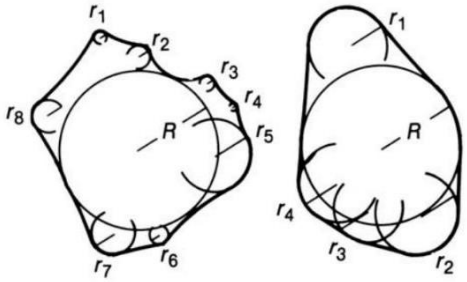


Figure 1.2 Grain radii (Friedman et al., 1992)

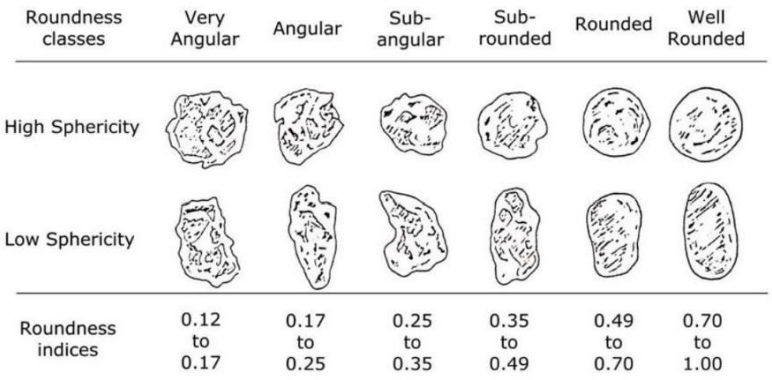


Figure 1.3: Grain roundness classes (Powers, 1953)

Density

Particle density ρ_s is defined as the mass of sediment solids per unit volume, and is related to the specific weight γ_s as follows (García, 2008):

$$\rho_s = \frac{m_s}{V_s} = \frac{\gamma_s}{g} \qquad (1.3)$$

where m_s is the mass of the solid, V_s is the solid volume, and g is gravitational acceleration.

Porosity

Porosity λ_p quantifies the fraction of a sediment deposit that consists of void space:

$$\lambda_p = \frac{V_v}{V_T} = \frac{V_v}{V_v + V_s} \qquad (1.4)$$

where V_v is the volume of voids and V_T is the total volume. When a known mass of sediment is deposited, the resulting deposit volume must account for the void fraction, as it significantly affects bed elevation calculations (García, 2008).

1.2.2. Sediment Transport Mechanisms

Transported material in rivers is broadly divided into two main modes. Bedload consists of particles that move along the channel bed through rolling, sliding, and saltating, maintaining contact with the floor. Bedload comprises heavier, coarser material such as gravel and sand, and transport rates increase with flow velocity above the threshold of motion (Julien, 2010). Suspended load, on the other hand, consists of finer particles lifted into the water column by turbulent upward currents. Turbulence causes exchanges of mass and momentum between fluid layers, keeping particles in suspension when turbulent diffusion balances the settling tendency (Dey, 2014). There is an active interchange between the two modes depending on flow conditions, as illustrated in *Figure 1.4*. In the present study, which focuses on coarse PVC sediment under supercritical flow, bedload is the dominant transport mode.

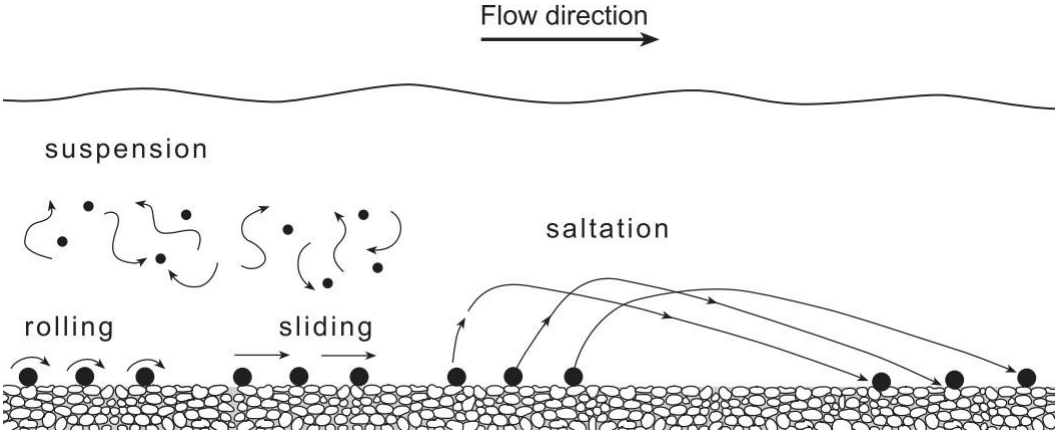


Figure 1.4: Forms of sediment transport (Fryirs & Brierley, 2019)

1.2.3. Threshold of Motion

The analysis of sediment particle motion is governed by a variety of interrelated factors, including hydraulic conditions, sediment properties, and the forces acting on individual grains. The onset of motion can be described using either velocity-based or shear stress-based criteria.

Threshold Velocity Concept

The threshold velocity is the flow velocity just sufficient to initiate particle motion. It can be expressed as a near-bed velocity u_{cr} or a depth-averaged velocity U_{cr}, as illustrated in *Figure 1.5*. While depth-averaged velocity is practical, near-bed velocity is physically more meaningful as it directly reflects the forces on individual grains (García, 2008). Goncharov (1964) defined the threshold as the lowest average velocity at which particles detach from the bed:

$$U_{cr} = 1.07(\Delta g d)^{0.5} \log\left(8.8\frac{h}{d_{95}}\right) \qquad (1.5)$$

where h is the flow depth, $d$is the median sediment diameter, $\Delta = s - 1$ is the submerged relative density, $s = \frac{\rho_s}{\rho}$ is the relative sediment density, and subscript 95 refers to the 95th percentile grain size. Neill (1968) developed a design curve for coarse gravels:

$$U_{cr} = 1.41(\Delta g d)^{0.5}\left(\frac{h}{d}\right)^{1/6} \qquad (1.6)$$

The threshold velocities as a function of median particle size for quartz sediments are shown in *Figure 1.6*. Despite these contributions, the threshold velocity concept has not been universally adopted due to ambiguities in defining near-bed velocity. This has led researchers toward the more widely accepted framework of threshold bed shear stress (García, 2008).

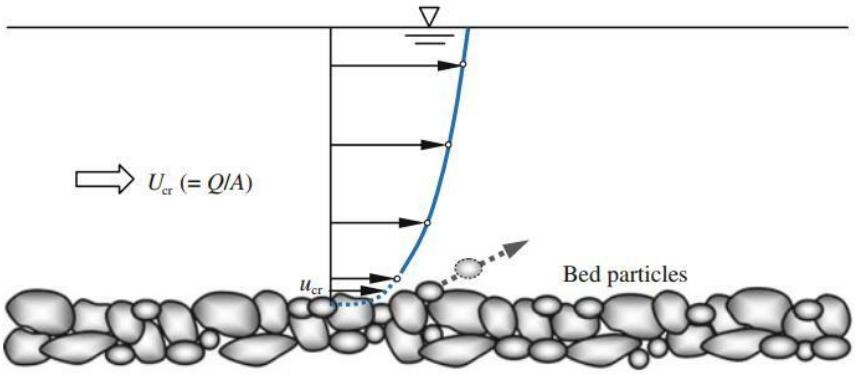


Figure 1.5: Definition sketch of threshold velocity concept

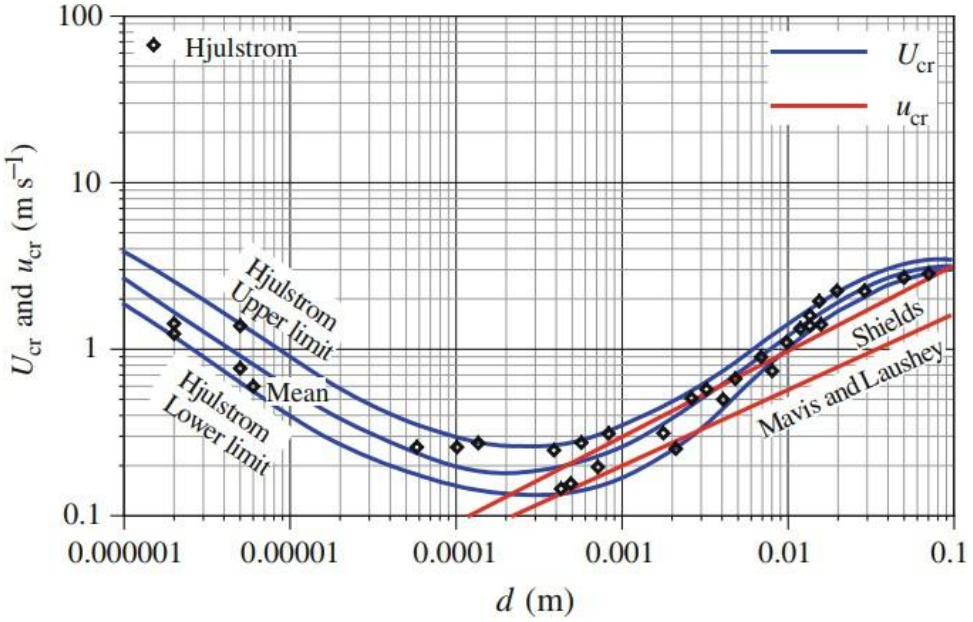


Figure 1.6: Threshold velocities vs. median particle size for quartz sediments (Vanoni, 1977)

Threshold Bed Shear Stress Concept

Shields (1936) was the first to formalize the threshold condition in a semi-theoretical framework, expressing it as the dimensionless Shields parameter Θ, defined as:

$$\Theta = \frac{\tau_0}{\Delta \rho g d} = \frac{u_*^2}{\Delta g d} \qquad (1.7)$$

where τ_0 is the bed shear stress, $\Delta = \frac{\rho_s - \rho}{\rho}$ is the submerged relative density, and u_* is the shear velocity. The forces acting on a particle at the threshold of motion are schematically shown in *Figure 1.7*. At the onset of motion, Θ reaches the critical value $\Theta_c = f(R_*)$, where $R_* = \frac{u_* k_s}{\nu}$ is the shear Reynolds number, as shown in the Shields diagram (*Figure 1.8*). Three flow regimes are identified:

- **Hydraulically smooth flow** ($R_* \leq 2$): $\Theta_c = \frac{0.1}{R_*}$
- **Hydraulically rough flow** ($R_* \geq 500$): $\Theta_c \approx 0.056$
- **Transitional flow** ($2 < R_* < 500$): minimum of $\Theta_c \approx 0.032$at $R_* \approx 12$(Dey, 2014)

White (1940) further contributed to this framework by analyzing particle equilibrium separately for rough and smooth flow regimes, as illustrated in *Figure 1.9* and *Figure 1.10*.

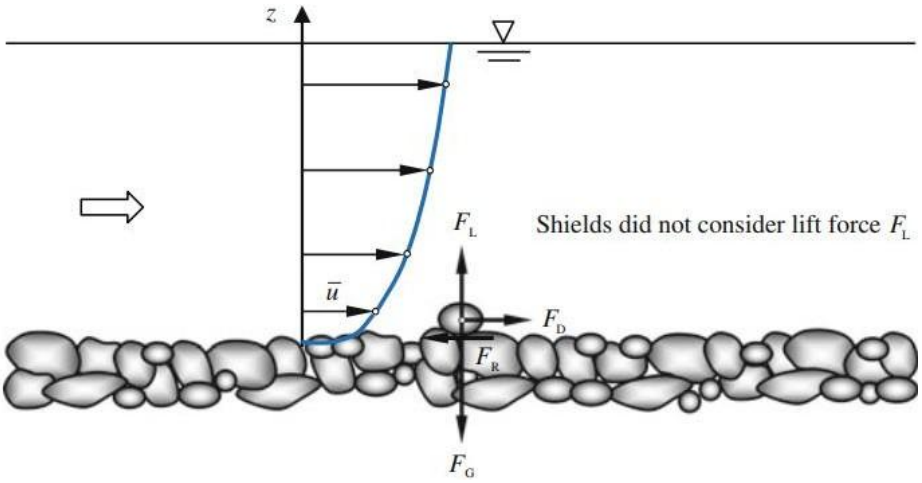


Figure 1.7: Forces acting on a sediment particle (Rowinski, 2014)

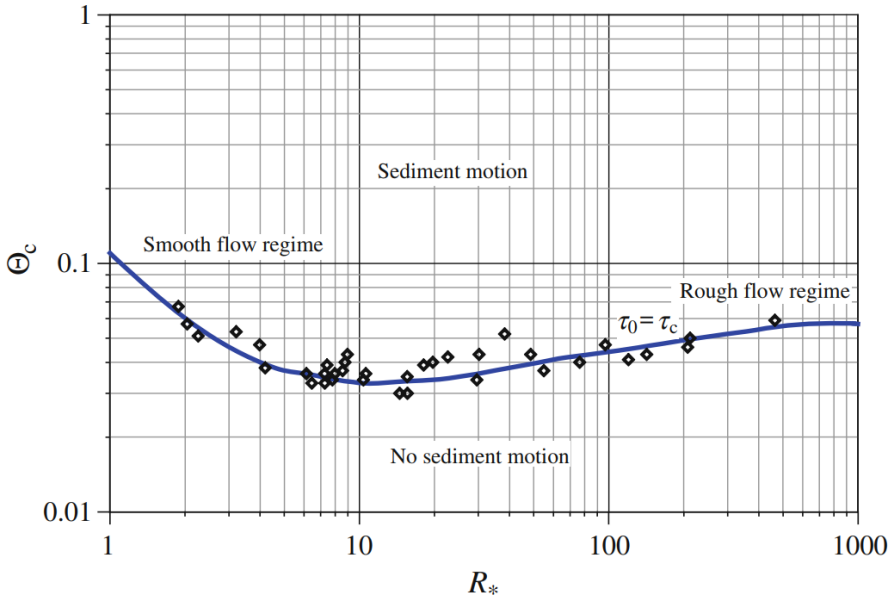


Figure 1.8: Shields diagram — Θ_c as a function of R_*(Shields, 1936)

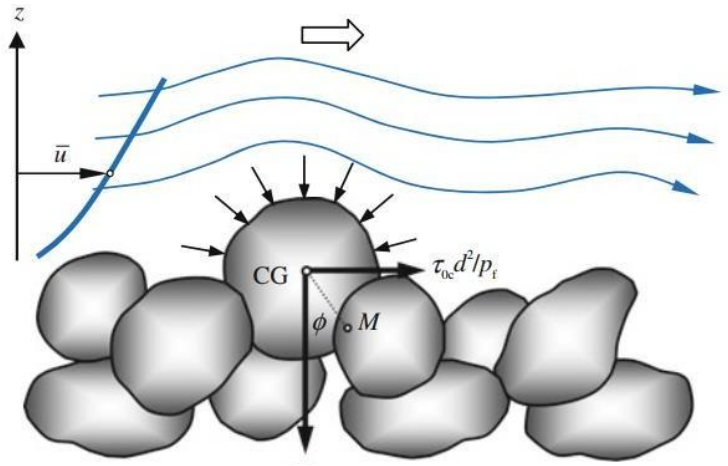


Figure 1.9: Particle equilibrium in transitional and rough flow (Rowinski, 2014)

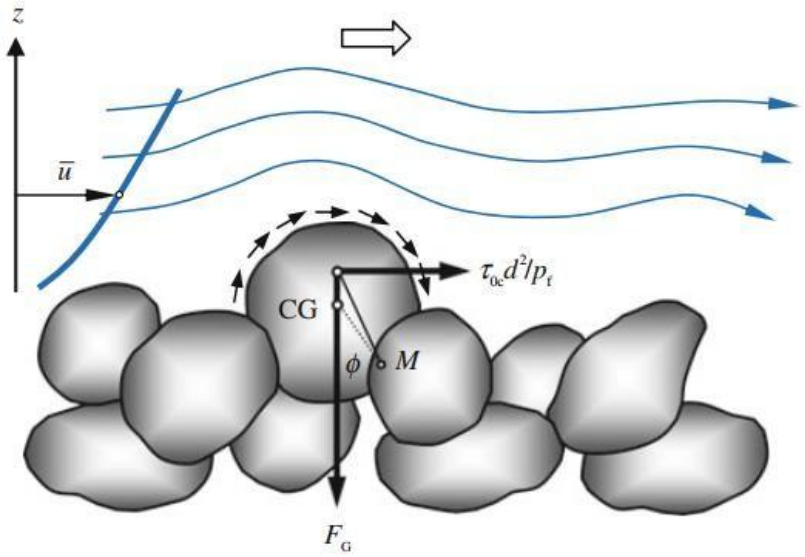


Figure 1.10: Particle equilibrium in smooth flow (Rowinski, 2014)

1.2.4. Bed-Load Transport Rate Estimation

Over the past decades, a wide range of equations have been developed to quantify bed-load transport rates in open-channel flows. Among these, the Meyer-Peter and Müller (1948) formula — commonly referred to as the MPM formula — is one of the most widely applied in fluvial engineering. It relates the dimensionless sediment transport rate Φto the excess Shields stress:

$$\Phi = 8(\theta - \theta_c)^{3/2} \qquad (1.8)$$

where θ is the Shields parameter and θ_c is the critical Shields parameter, commonly taken as $\theta_c = 0.047$. The Shields parameter is calculated as:

$$\theta = \frac{\tau_0}{\rho_w g d(s-1)} \qquad (1.9)$$

where ρ_w is the water density, g is gravitational acceleration, d is the sediment diameter, $s = \frac{\rho_s}{\rho_w}$ is the relative sediment density, and τ_0 is the bed shear stress:

$$\tau_0 = \rho_w g R_H S_f \qquad (1.10)$$

where R_H is the hydraulic radius and S_f is the friction slope, evaluated using the Manning formula:

$$S_f = \frac{n^2 u^2}{R_H^{4/3}} \qquad (1.11)$$

The dimensional sediment discharge per unit width q_s is then obtained from (Einstein, 1942):

$$q_s = \Phi\sqrt{g(s-1)d^3} \qquad (1.12)$$

Substituting the MPM formula yields:

$$q_s = 8(\theta - \theta_c)^{3/2}\sqrt{g(s-1)d^3} \qquad (1.13)$$

1.3. Aggradation, Prior campaigns, objectives

Aggradation is defined as a rise in bed elevation resulting from sediment deposition when the supplied load exceeds the local transport capacity of the channel. It represents one of the two primary morphological responses of a river system to an imbalance between sediment supply and transport capacity — the other being degradation, which occurs when supply falls below capacity (Sear et al., 1995; Church, 2006).

A key parameter used to quantify the degree of overloading is the **loading ratio** L_r, defined as the ratio of the sediment inflow discharge Q_{sin} to the initial sediment transport capacity Q_{s0} (El Achkar and Hassan, 2024):

$$L_r = \frac{Q_{sin}}{Q_{s0}} \qquad (1.28)$$

Aggradation occurs when $L_r > 1$, meaning that sediment supply exceeds transport capacity. Conversely, when $L_r < 1$, the channel is underloaded and degradation takes place. Equilibrium is reached when $L_r = 1$. Previous studies conducted at the Laboratory of Mountain Hydraulics of Politecnico di Milano have consistently shown that the loading ratio is one of the most influential parameters governing both the magnitude of bed aggradation and the celerity of the aggradation wave (Eslami et al., 2025a; El Achkar and Eslami , 2024).

The temporal evolution of aggradation is governed not only by the magnitude of sediment overloading but also by the rate at which the depositional process propagates downstream, commonly referred to as celerity. Under supercritical flow conditions, no distinct sediment front develops; instead, aggradation occurs in the form of a dispersive depositional wedge (Eslami et al., 2025b). Understanding celerity is therefore essential for predicting the timing of sediment propagation toward critical downstream locations and for improving flood risk management strategies.

1.3.1. Review of Previous Studies

The experimental investigation of sediment aggradation and its associated time scales has been the subject of a growing body of research over the past decades. Early pioneering contributions focused predominantly on subcritical flow conditions. Soni (1981) studied stream aggradation resulting from increased sediment load, integrating experimental findings with an analytical diffusion model. Yen et al. (1992) extended this framework to non-uniform sediment under sequential overloading and underloading conditions, demonstrating that complete bed recovery is only feasible with uniform sediment. Alves and Cardoso (1999) conducted six aggradation experiments in subcritical flow, examining the role of dune formation and Manning coefficient evolution on the celerity of the observed sediment front. These early works laid the conceptual foundation for subsequent experimental campaigns, particularly in terms of relating aggradation wave celerity to flow and sediment parameters.

At the Laboratory of Mountain Hydraulics of Politecnico di Milano, a systematic series of experimental campaigns has progressively extended the understanding of sediment aggradation to supercritical flow conditions. The first investigations in this setting were conducted by Unigarro Villota (2017), Zanchi (2018) and Zucchi (2018), who examined aggradation under subcritical flow conditions, characterizing both the height and celerity of the aggradation front. A key finding of these studies was a strong dependence of the dimensionless front celerity on the square of the Froude number, with limited sensitivity to the loading ratio — a result that would later be revisited under supercritical conditions.

The transition to supercritical flow was initiated by Heydari (2020), who conducted three aggradation experiments at an initial bed slope of 1.2%, obtaining bulk celerity values on the order of a few centimeters per second. Building on this foundation, Eslami et al. (2021) conducted eight aggradation experiments under supercritical conditions, combining experimental and numerical approaches. Their study introduced a novel method for determining celerity locally in the time-space domain — rather than seeking a single representative value per experiment — and employed the BASEMENT numerical solver for model calibration. A key outcome was the quantification of the Manning coefficient and bedload factor as functions of the Froude number. Simultaneously, Eslami et al. (2022) published results on how the definition and measurement of bed elevation affect key quantities in sediment overloading under supercritical flow, providing important methodological insights for subsequent campaigns.

Tavakoli et al. (2022) extended the experimental database with six additional supercritical experiments, introducing the computation of eigenvalues of the governing PDE system based on De Vries' approach and comparing them to locally

determined celerity values. Their analysis showed that the Manning coefficient, bedload factor, final bed slope, celerity, and eigenvalues all depend on both the Froude number and the loading ratio.

Hiteh et al. (2023) further expanded the experimental campaign for near-critical and supercritical conditions, conducting seven aggradation experiments. Their work provided a detailed analysis of local celerity, dimensionless eigenvalues, and bulk celerity values, comparing results across different flow regimes. An important finding was that the dimensionless celerity increases with the loading ratio across all tested conditions, confirming the dominant role of $L_r$in governing aggradation wave dynamics.

El Achkar and Hassan (2024) conducted thirteen aggradation experiments under supercritical flow conditions, providing the most extensive experimental dataset within the Politecnico di Milano campaign to date. Their work examined the dependence of dimensionless celerity on both loading ratio and Froude number through a comprehensive bulk analysis, demonstrating that the loading ratio exerts a substantially stronger influence on celerity than the Froude number. Additionally, they developed a dimensionless framework for the temporal evolution of bed slope and derived a predictive equation valid across all experiments.

Building on the full body of experimental evidence, Eslami et al. (2025a) developed a predictor for the bulk celerity of aggradation wave propagation under supercritical flow, expressed as a function of the loading ratio. Their results confirmed that the aggradation wave celerity amounts to only a few percent of the initial flow velocity — a finding with direct practical implications for flood early warning systems. Eslami et al. (2025b) further investigated the celerity of small perturbations through an eigenvalue-based approach, showing that the eigenvalues of the governing equations alone cannot reliably predict the timing of sediment arrival at downstream locations. The steady-flow aggradation campaign comprises 26 experiments conducted under supercritical flow conditions at bed slopes of 1.37% and 2.20%, covering a range of water discharges and loading ratios. The main parameters of all experiments are summarized in *Table 1.1*.

Table 1.1 Parameters of AE, steady campaign

Run	***T (s)***	***S_0 (%)***	***Q (m^3/s)***	***Q/Qc***	***H (m)***	***U (m/s)***	***Fr***	***Qsin (m^3/s)***	***Qs0 (m^3/s)***	***Lr***
AE1	1019	1.37%	0.003	3.6	0.019	0.518	1.190	1.14×10^{-4}	6.25×10^{-5}	1.83
AE2	812	1.37%	0.003	3.6	0.019	0.518	1.190	1.28×10^{-4}	6.25×10^{-5}	2.05
AE3	774	1.37%	0.004	4.8	0.023	0.576	1.209	1.25×10^{-4}	8.05×10^{-5}	1.56

Run	*T (s)*	*S_0 (%)*	*Q (m^3/s)*	*Q/Qc*	*H (m)*	*U (m/s)*	*Fr*	*Qsin (m^3/s)*	*Qs0 (m^3/s)*	*Lr*
AE4	686	1.37%	0.004	4.8	0.023	0.576	1.209	1.68×10^{-4}	8.05×10^{-5}	2.09
AE5	559	1.37%	0.004	4.8	0.023	0.576	1.209	2.27×10^{-4}	8.05×10^{-5}	2.81
AE6	638	1.37%	0.005	6.0	0.027	0.625	1.221	1.55×10^{-4}	9.59×10^{-5}	1.61
AE7	452	1.37%	0.005	6.0	0.027	0.625	1.221	1.99×10^{-4}	9.59×10^{-5}	2.07
AE8	482	1.37%	0.005	6.0	0.027	0.625	1.221	2.48×10^{-4}	9.59×10^{-5}	2.58
AE9	442	1.37%	0.005	6.0	0.027	0.625	1.221	3.03×10^{-4}	9.59×10^{-5}	3.16
AE10	594	1.37%	0.006	7.2	0.030	0.667	1.230	1.70×10^{-4}	1.20×10^{-4}	1.42
AE11	462	1.37%	0.006	7.2	0.030	0.667	1.230	2.62×10^{-4}	1.20×10^{-4}	2.19
AE12	384	1.37%	0.006	7.2	0.030	0.667	1.230	3.30×10^{-4}	1.20×10^{-4}	2.76
AE13	363	1.37%	0.006	7.2	0.030	0.667	1.230	3.94×10^{-4}	1.20×10^{-4}	3.29
AE14	567	1.37%	0.007	8.4	0.033	0.705	1.236	1.90×10^{-4}	1.33×10^{-4}	1.43
AE15	368	1.37%	0.007	8.4	0.033	0.705	1.236	2.77×10^{-4}	1.33×10^{-4}	2.09
AE16	316	1.37%	0.007	8.4	0.033	0.705	1.236	4.28×10^{-4}	1.33×10^{-4}	3.22
AE17	388	1.37%	0.008	9.6	0.036	0.738	1.240	2.57×10^{-4}	1.60×10^{-4}	1.61
AE18	371	1.37%	0.008	9.6	0.036	0.738	1.240	2.64×10^{-4}	1.60×10^{-4}	1.65
AE19	344	1.37%	0.008	9.6	0.036	0.738	1.240	3.46×10^{-4}	1.60×10^{-4}	2.16
AE20	276	1.37%	0.008	9.6	0.036	0.738	1.240	4.42×10^{-4}	1.60×10^{-4}	2.76
AE21	319	1.37%	0.009	10.8	0.039	0.769	1.244	2.92×10^{-4}	1.87×10^{-4}	1.56
AE22	275	1.37%	0.009	10.8	0.039	0.769	1.244	4.16×10^{-4}	1.87×10^{-4}	2.23
AE23	496	2.20%	0.004	7.3	0.020	0.669	1.513	2.52×10^{-4}	1.43×10^{-4}	1.76
AE24	422	2.20%	0.005	9.1	0.023	0.726	1.531	2.80×10^{-4}	1.83×10^{-4}	1.53
AE25	375	2.20%	0.006	10.9	0.026	0.776	1.544	3.27×10^{-4}	2.13×10^{-4}	1.53
AE26	324	2.20%	0.007	12.7	0.028	0.821	1.554	3.80×10^{-4}	2.51×10^{-4}	1.52

1.3.2. Research Gap and Objectives of This Thesis

A common feature of all the experimental campaigns reviewed above is that they were conducted under **steady flow and sediment feeding conditions** — that is, both water discharge and sediment supply were held constant throughout each experiment. While this simplification has enabled a systematic characterization of aggradation dynamics and celerity under supercritical flow, it does not reflect the inherently unsteady nature of real flood events in mountain catchments, where discharge and sediment supply vary continuously over time.

The present thesis addresses this gap directly. After a first study of Bahadori (2026), aimed at characterizing the ability to control experiments by repeatability analysis, this work, by conducting experiments under **supercritical, unsteady flow conditions**, extends the experimental database of the Politecnico di Milano campaign and investigates how temporal variations in flow and sediment supply affect the propagation celerity of aggradation waves. In the experiments, flow rate, sediment feeding rate, and load ratio are varied stepwise, mimicking an unsteady process.

The main objectives of this thesis are:

1. To characterize the spatial and temporal evolution of bed and water surface elevations under supercritical, unsteady flow and sediment feeding conditions.
2. To determine the local and bulk celerity of aggradation wave propagation for each experimental phase of the hydrograph.
3. To assess the dependence of dimensionless celerity on the loading ratio and Froude number under unsteady conditions.
4. To analyze the temporal evolution of the channel bed slope throughout the experiments and assess its relationship with the imposed flow and sediment feeding conditions.
5. To evaluate whether the findings of prior steady-state studies remain applicable — at least approximately — when flow conditions are unsteady.

2 Chapter 2: Experimental setup

2.1 Laboratory Facility and Experimental Setup

All experiments in this study were conducted at the Mountain Hydraulics Laboratory of Politecnico di Milano, located at the Lecco campus in Italy. The experimental system is designed to replicate the hydraulic and sediment transport conditions typical of steep mountain streams, and consists of several interconnected components described in the following sections. Figure 2.1 and 2.2 provide , respectively, a schematic representation and a photograph of experimental setup.

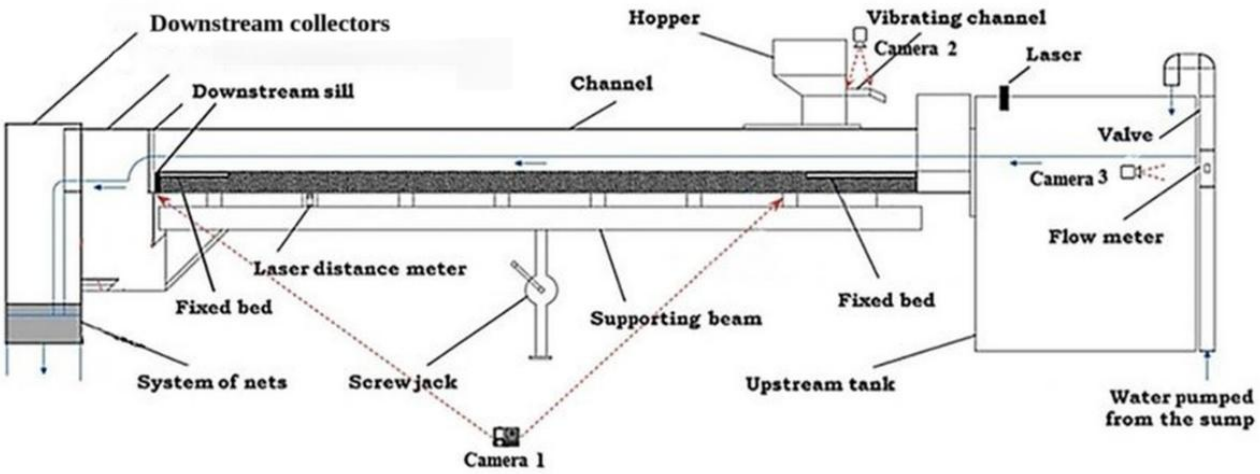


Figure 2.1: Schematic representation of experimental setup and camera positions (Eslami,2025)



Figure 2.2: Experimental setup

2.1.1. Experimental Channel

The experimental channel is a rectangular flume constructed entirely from transparent Plexiglas, with a total length of 5.2 m, a width of 0.30 m, and a bank height of 0.45 m. The use of transparent material allows optical access to the flow field and the channel bed, enabling image-based data acquisition through cameras installed along the channel walls.

The channel slope is adjustable by means of a screw jack mechanism located beneath the flume. The vertical distance between the channel bottom and the laboratory floor is measured using a laser distance meter mounted on the channel frame and is subsequently converted into the corresponding bed slope through a calibration function developed by Fazzini and Mottini (2015). The slope is set to the target value before each experiment begins.

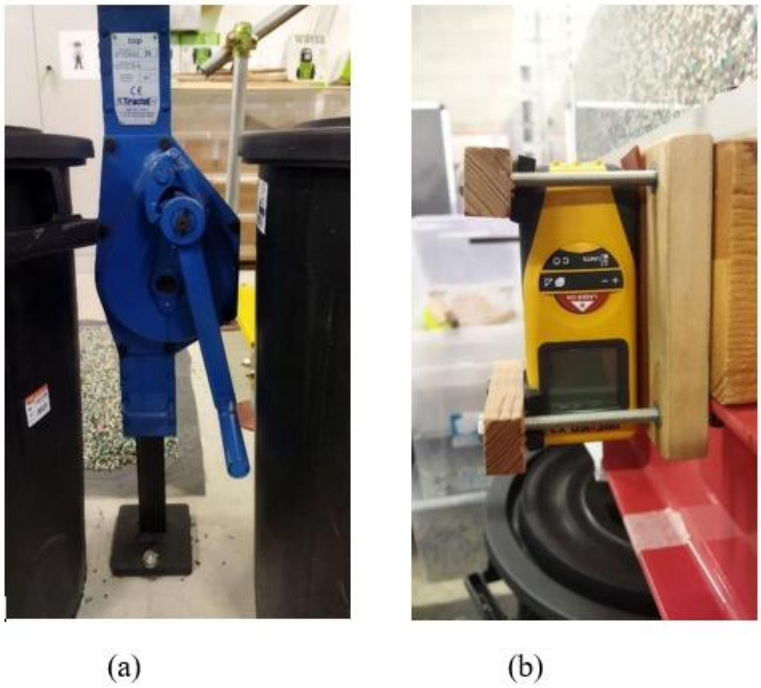


Figure 2.3: (a) Screw jack and (b) Laser distance meter

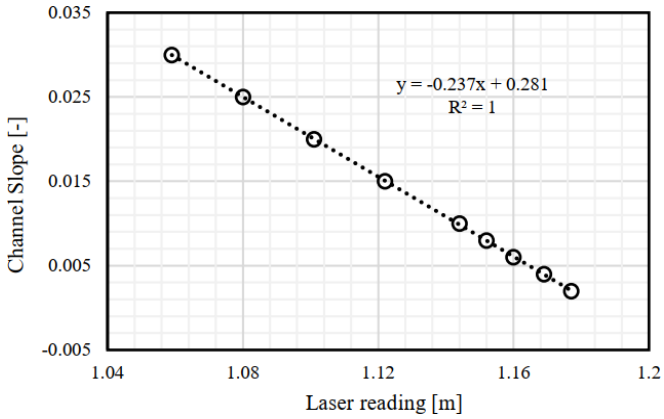


Figure 2.4 Relationship between laser distance reading and channel slope (Fazzini and Mottini, 2015)

The erodible bed of the channel consists of a 15 cm thick layer of polyvinyl chloride (PVC) particles, uniformly arranged along the flume floor. This artificial bed material simulates the mobile sediment layer of a natural stream while preventing scratching of the channel walls during the experiments. To avoid unwanted local scour near the inlet and outlet sections, the bed is fixed over a length of 75 cm at the upstream end and 60 cm at the downstream end. These fixed sections are made of plastic plates with the same sediment particles glued to their surfaces to maintain a roughness consistent with that of the mobile bed.

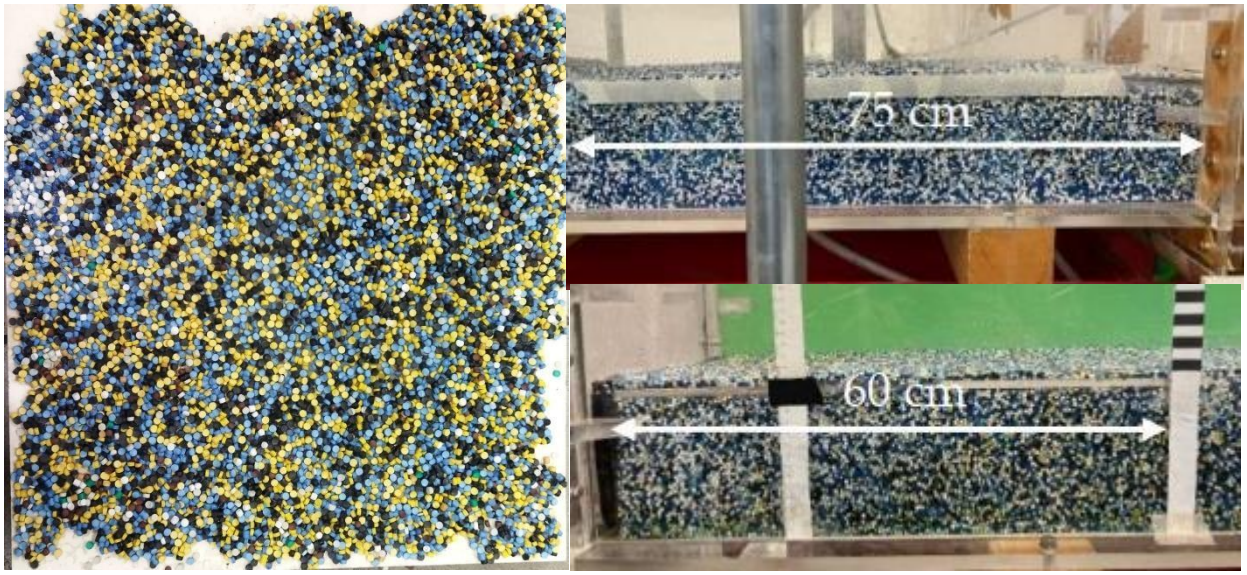
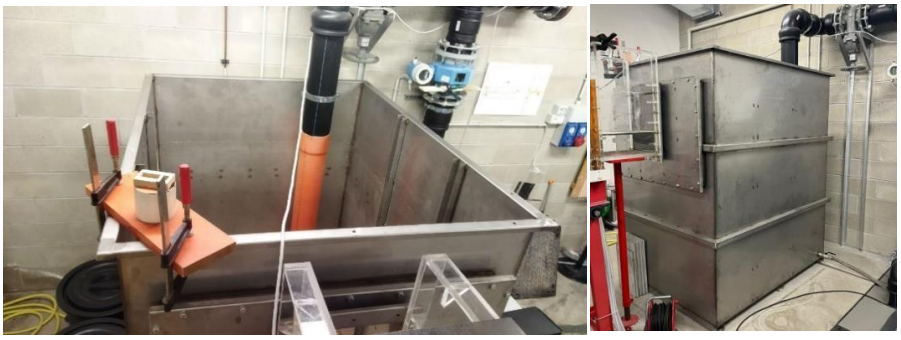


Figure 2.5: Fixed plastic plates at upstream and downstream ends (Gamal et, al.,2023)

2.1.2. Water Supply and Flow Control System

Water is pumped from an underground storage tank located beneath the laboratory floor into an upstream header tank connected to the inlet section of the experimental channel (*Figure 2.6*). As the tank gradually fills, water begins to flow into the channel once the water level reaches the channel bed elevation. The discharge is then adjusted to the target value using a guillotine valve installed near the upstream tank, and is continuously monitored by an electromagnetic flowmeter.



(a)



(b)

Figure 2.6: (a) Upstream water tank and (b) Flow meter

At the downstream end of the channel, two collectors are installed in series (*Figure 2.7*). During the steady campaign, the second collector was sufficient to prevent sediment particles from entering the underground storage tank, thereby allowing clean water to be recirculated. However, during the unsteady campaign, the substantially higher amount of transported sediment meant that a significant portion still passed through the second collector. Therefore, an additional sediment screen was installed in the underground channel to capture sediments before they reached the underground storage tank (*Figure 2.8*), increasing the effective sediment storage capacity and allowing longer experiments to be carried out without interruption.

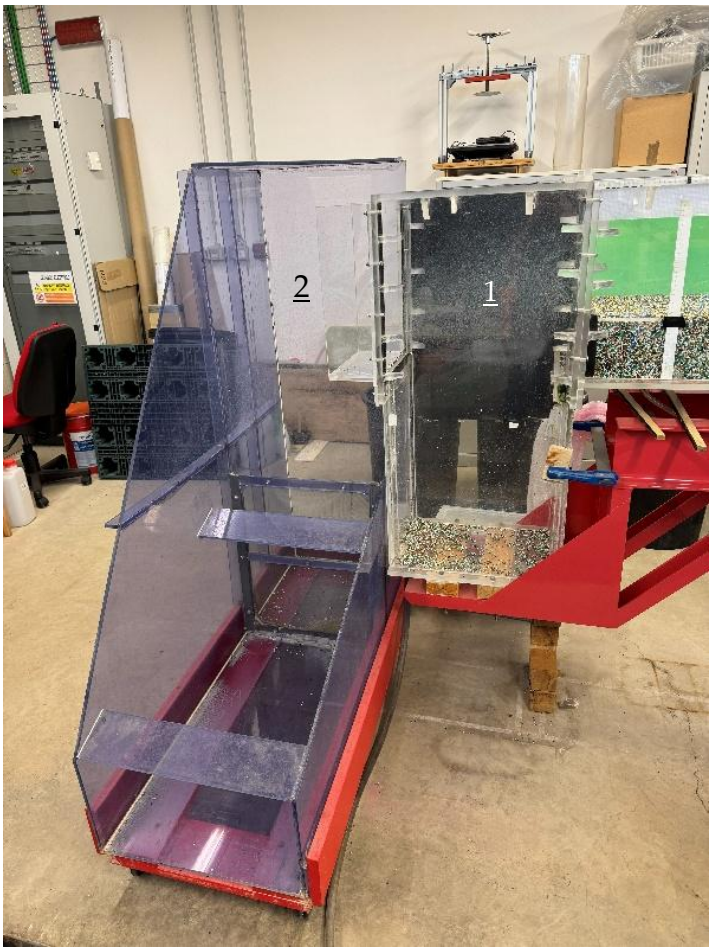


Figure 2.7: Two downstream collectors



Figure 2.8: Modified underground channel

Since the discharge entering the channel can differ from the flowmeter reading — particularly during the transient phases of the hydrograph — a laser distance sensor was installed on top of the upstream tank to continuously record the water surface elevation (*Figure 2.9*). The actual discharge flowing through the channel inlet was then computed by combining the laser sensor readings with the flowmeter data, applying the continuity principle to the upstream tank. This procedure is described in detail in section 2.3.2.



(a)



(b)

Figure 2.9: Inlet tank water level monitoring system: (a) computer setup; (b) laser sensor installation slot

2.1.3. Sediment Material

The sediment used in this study consists of polyvinyl chloride (PVC) particles of cylindrical shape, available in multiple colors, as shown in *Figure 2.10*. PVC was chosen as the bed material because its relatively low density compared to natural sediment allows the simulation of bedload transport conditions at reduced flow velocities, making it well suited for laboratory experiments in steep-channel settings. Two types of PVC sediment were used across the experimental campaign, referred to here as **old sediment** and **new sediment**, whose properties are described in the following sections.



(a)



(b)

Figure 2.10: PVC sediment particles — (a) new and (b) old material

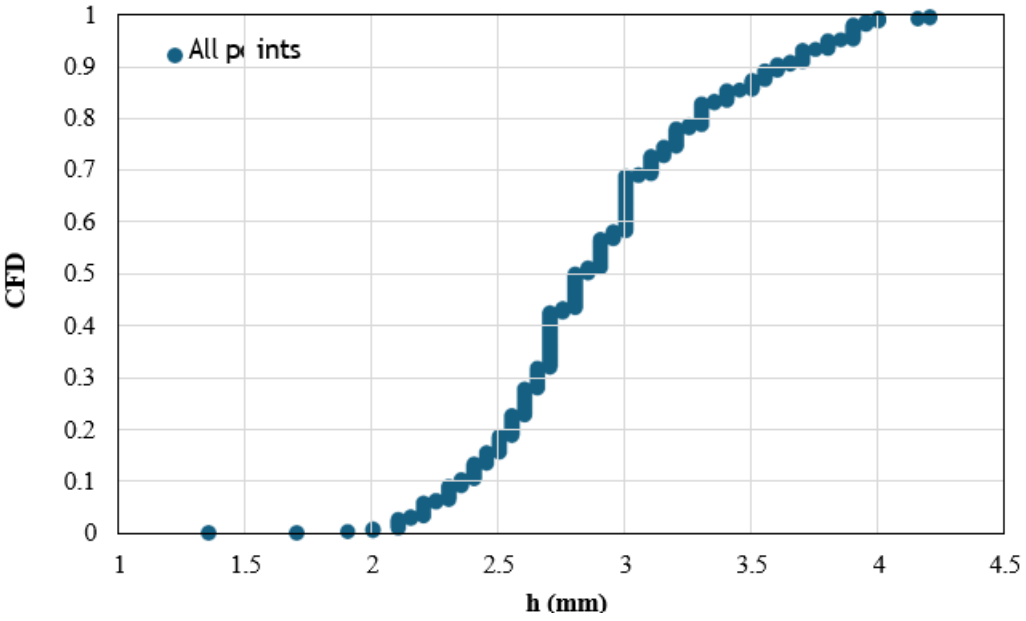
Old sediment Properties

The old sediment was used in experiments conducted prior to this campaign and its physical characteristics were originally determined by Unigarro Villota (2017). It consists of PVC cylindrical particles with an equivalent mean diameter $d_{50} = 3.8$ mm, a uniformity coefficient of 1.04, a material density of $\rho_s = 1443$ kg/m³, and a porosity of $p_0 = 0.45$. These values have been consistently adopted across all previous experimental campaigns conducted at the Mountain Hydraulics Laboratory of Politecnico di Milano.

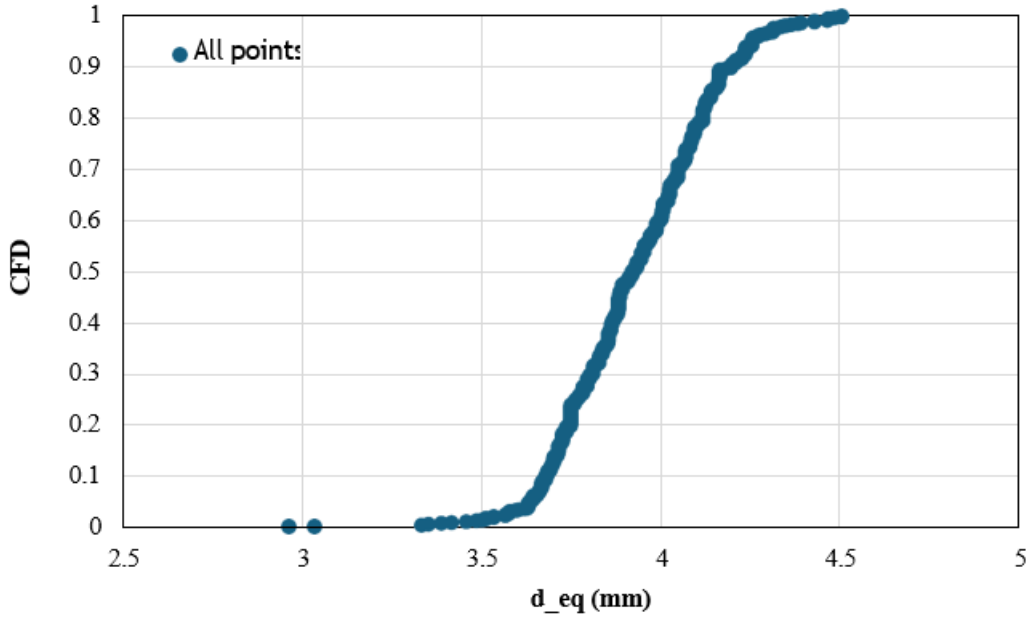
New Sediment Properties

New sediment was purchased to extend the experimental campaign and enable longer runs to be performed, as the available quantity of old material was insufficient for the full unsteady experimental program. The new material consists of PVC particles available in six different colors and is physically similar to the old sediment.

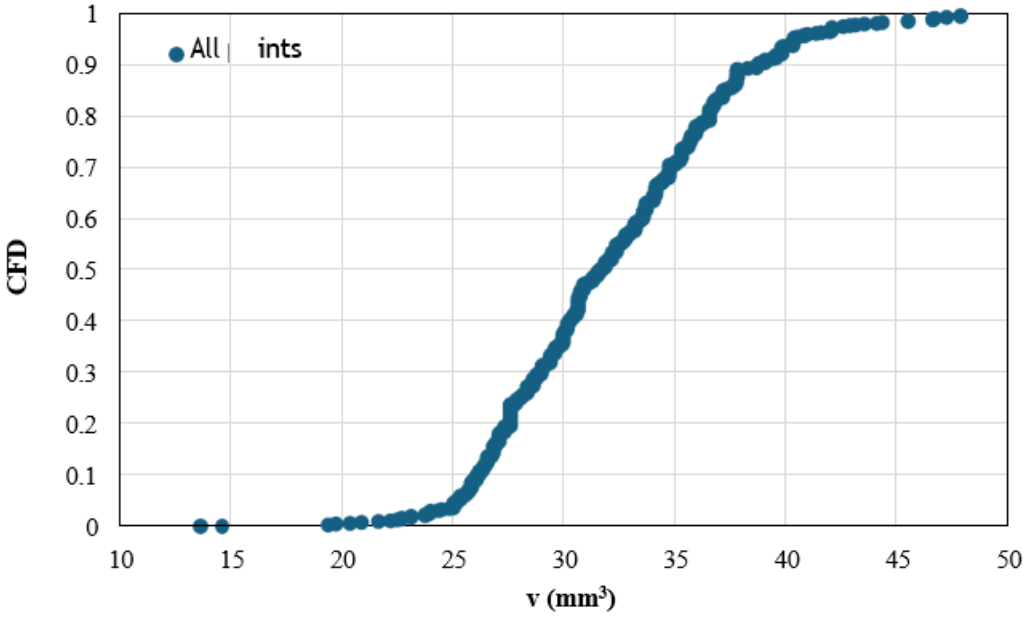
To determine the grain size distribution of the new sediment, 100 samples were collected from each color — 600 samples in total — and analyzed individually. The height and diameter of each cylindrical particle were measured directly, and based on these measurements, the particle volume and equivalent diameter — defined as the diameter of a sphere having the same volume — were calculated. The results are presented in the form of Cumulative Frequency Distribution (CFD) plots in *Figure 2.11*.



(a)



(b)



(c)

Figure 2.11: CFD plots of new material — (a) height, (b) equivalent mean diameter, (c) volume

Density and Porosity Measurements

The physical properties of the new sediment were determined experimentally through a series of laboratory measurements. For each color, three trials were conducted and the reported values represent the average of eighteen trials in total.

Porosity p_0 is defined as the ratio of void volume to total volume of the sediment deposit:

$$p_0 = \frac{V_{pore}}{V_{total}} \qquad (2.1)$$

The pore volume is estimated from the volume of water required to fill the void space between particles in a cylindrical container of known dimensions:

$$V_{pore} = V_W = \frac{W_W - W_{full}}{\rho_w} \qquad (2.2)$$

$$V_{total} = V_0 = \frac{\pi D^2}{4} H \qquad (2.3)$$

Combining these expressions yields the working formula for porosity:

$$p_0 = \frac{V_W}{V_0} = \frac{4(W_W - W_{full})}{\rho_w \pi D^2 H} \qquad (2.4)$$

where W_W is the mass of the container filled with particles and water, W_{full} is the mass of the container filled with particles only, $\rho_w = 1000$ kg/m³ is the water density, D is the container diameter, and H is the container height.

Particle density ρ_p is defined as the mass of solid particles per unit volume of solid:

$$\rho_p = \frac{W_p}{V_p} \qquad (2.5)$$

where the particle mass is:

$$W_p = W_{full} - W_{empty} \qquad (2.6)$$

and the solid volume is obtained by subtracting the pore volume from the total container volume:

$$V_p = V_0 - V_W = V_0(1 - p_0) = \frac{\pi D^2}{4} H(1 - p_0) \qquad (2.7)$$

where W_{empty} is the mass of the empty container. Substituting into Equation (2.5) gives the final expression for particle density:

$$\rho_p = \frac{4(W_{full} - W_{empty})}{\pi D^2 H(1 - p_0)} \qquad (2.8)$$

The new sediment has an equivalent mean diameter of $d_{50} = 3.92$ mm, a uniformity coefficient of 1.06, a material density of $\rho_s = 1505$ kg/m³, and a porosity of $p_0 = 0.394$. The properties of both sediment types are summarized in *Table 2.1*.

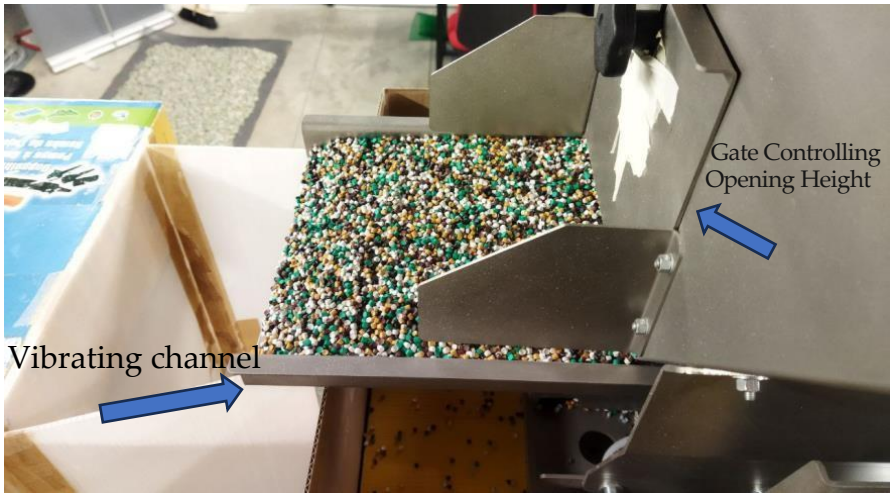
Table 2.1 Material characteristics comparison

Material	Density (ρ_s)	Porosity (p_0)	Equivalent mean diameter (d_{eq_50})	Uniformity Coefficient
New	1505.35 Kg/m^3	0.394	3.92 mm	1.06
Old	1443 Kg/m^3	0.45	3.8 mm	1.04

2.1.4. Sediment Feeding System

A sediment feeding system is installed 30 cm downstream of the channel inlet to supply the flume with sediment identical to the bed material during each experiment. The system consists of three main components: a hopper, an adjustable gate, and a vibrating channel, as shown in *Figure 2.12*. Sediment is loaded into the hopper and released through the gate — whose opening height can be manually adjusted — into the vibrating channel below, which delivers the material into the flume at a controlled rate.

The sediment feeding rate is governed by two parameters: the gate opening height and the vibration intensity of the channel. Increasing either parameter results in a higher sediment inflow discharge Q_{sin}. During steady-flow experiments, both parameters are kept constant throughout the run. However, in the unsteady campaign conducted in this study, the feeding rate must vary in time to follow the imposed hydrograph in order to guarantee aggradation during the experiments — making the accurate calibration of the feeding system a critical requirement, as described in Section 2.1.4.1.



(a)



(b)



(c)

Figure 2.12: (a) adjustable gate and vibrating channel; (b) vibration intensity indicator; (c) location of the hopper within the experimental channel

2.1.4.1. Hopper Calibration

The objective of the calibration procedure is to derive reliable **transfer functions** that relate the mean sediment particle velocity u_{mean} — measured from video recordings — to the sediment inflow discharge Q_{sin}. These transfer functions are established through a dedicated preliminary calibration campaign conducted prior to the main experimental program.

For each gate opening height — namely 1.65, 2, 2.5, 3, 3.5, and 4 cm — a series of runs are performed at different vibration levels ranging from 7.5 to 10 in increments of 0.5, resulting in six vibration settings per opening height. For each combination, ten short-duration tests (lasting approximately 20 to 90 seconds each) are conducted, giving a total of 360 calibration trials. During each run, a GoPro 7 camera mounted above the vibrating channel (*Figure 2.19*) records the motion of the sediment particles, while the sediment exiting the channel is collected in a bucket placed beneath the feeder. The accumulated sediment mass W_s is measured at the end of each run, and the average sediment inflow discharge is computed as:

$$Q_{sin} = \frac{W_s/\rho_s}{t} \qquad (2.9)$$

where ρ_s is the sediment density and t is the duration of the run. The mean value of the ten repetitions is taken as the representative discharge for each combination of opening height and vibration level. The resulting feeding rates across all opening heights and vibration levels are shown in *Figure 2.13* .

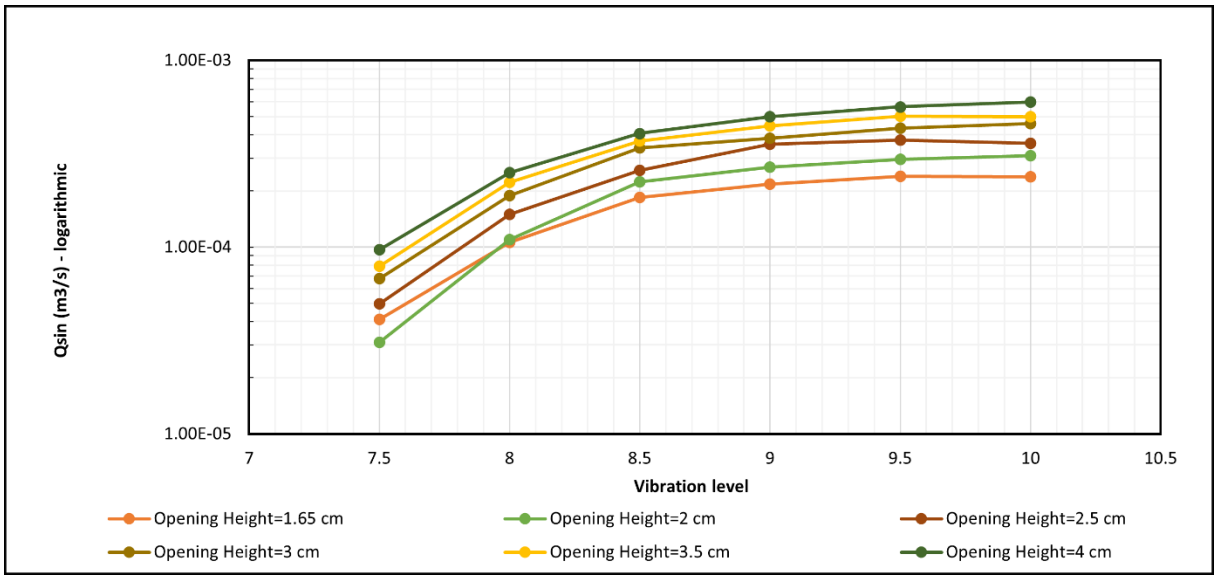


Figure 2.13: Sediment feeding rates across vibration levels and opening heights

In parallel, the temporal evolution of sediment particle velocity is extracted from the recorded videos using a PIV algorithm (described in Section 2.3.3.1). The time-averaged particle velocity u_{mean} for each run is calculated from this velocity signal, yielding a corresponding pair of (u_{mean}, Q_{sin}) values for each trial. These data pairs are then used to establish the transfer relationship between particle velocity and sediment inflow discharge.

The collected data are fitted using a second-degree polynomial of the form:

$$Q_{sin} = a(u_{mean})^2 + b(u_{mean}) \qquad (2.10)$$

where the constant term is set to zero to satisfy the physical condition that sediment discharge must be zero when particle velocity is zero. This quadratic formulation provides a better fit over the full velocity range compared to a linear model. A distinct transfer function is derived for each gate opening height considered in the study, as illustrated in *Figure 2.14*.

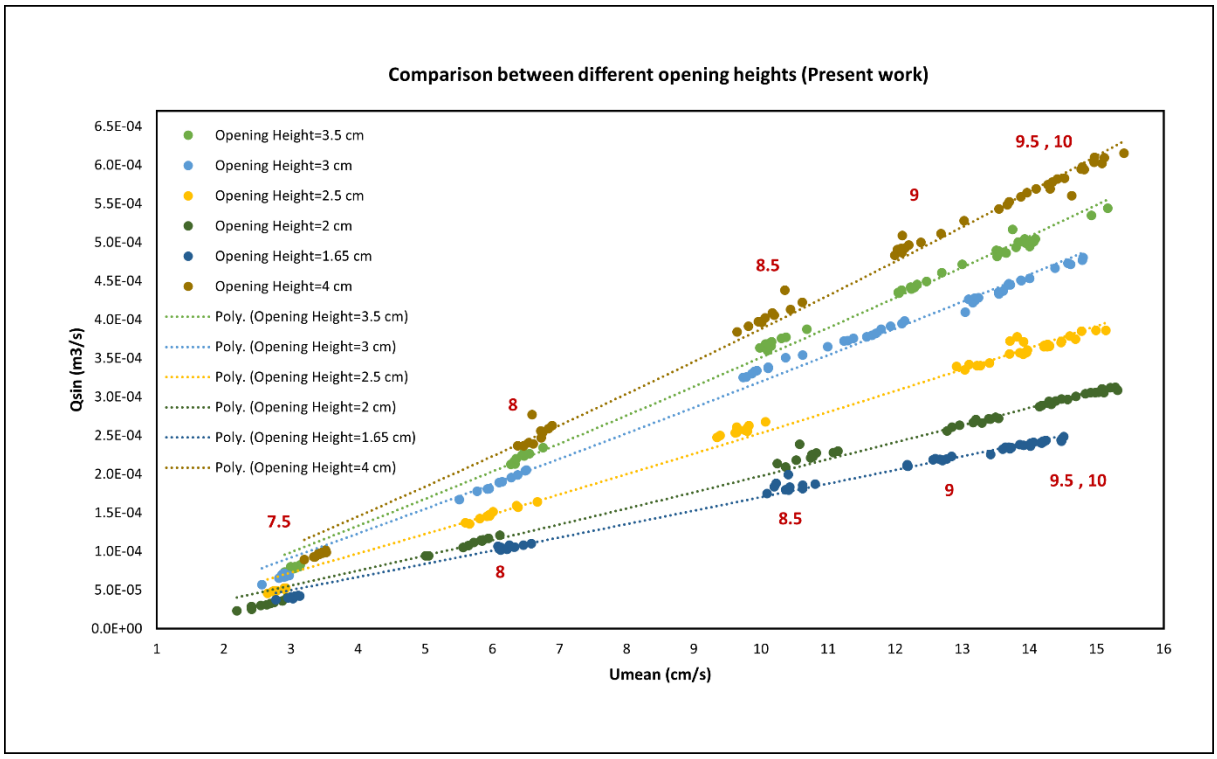


Figure 2.14: Transfer functions for all opening heights — current work (red numbers: vibration levels)

It is worth noting that for the new sediment material, a new set of transfer functions was derived and compared against those obtained in previous campaigns, as shown in *Figure 2.15*. The comparison confirms that the new material produces slightly different feeding rates for the same mechanical settings, justifying the need for a dedicated calibration.

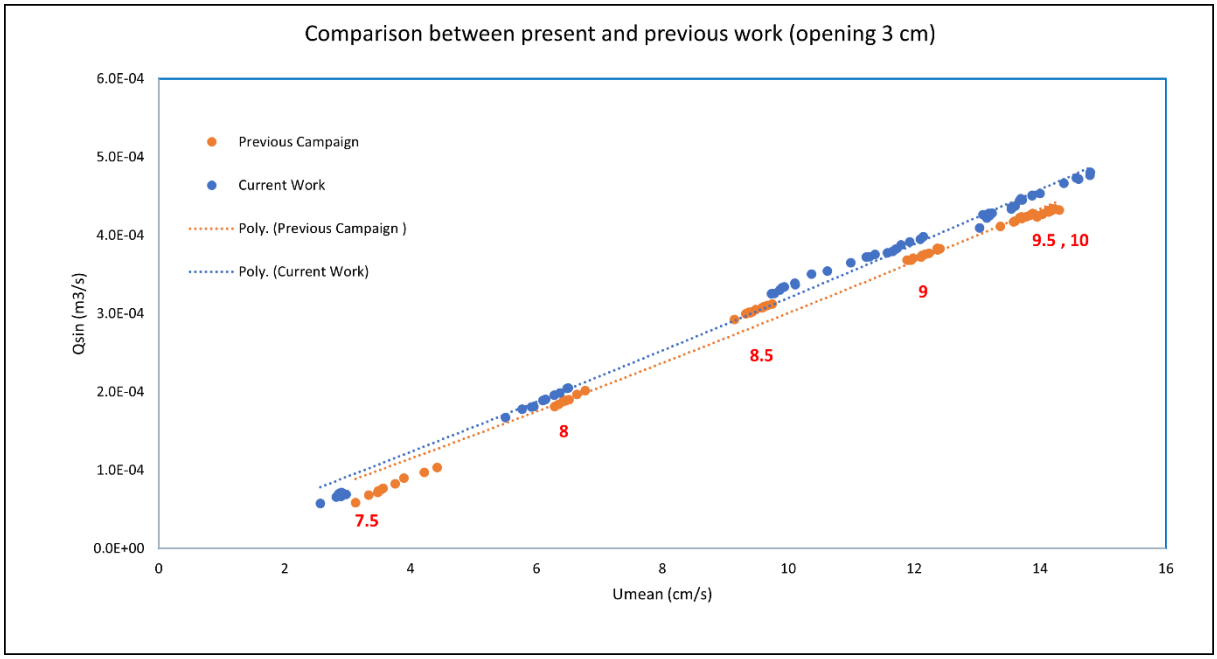
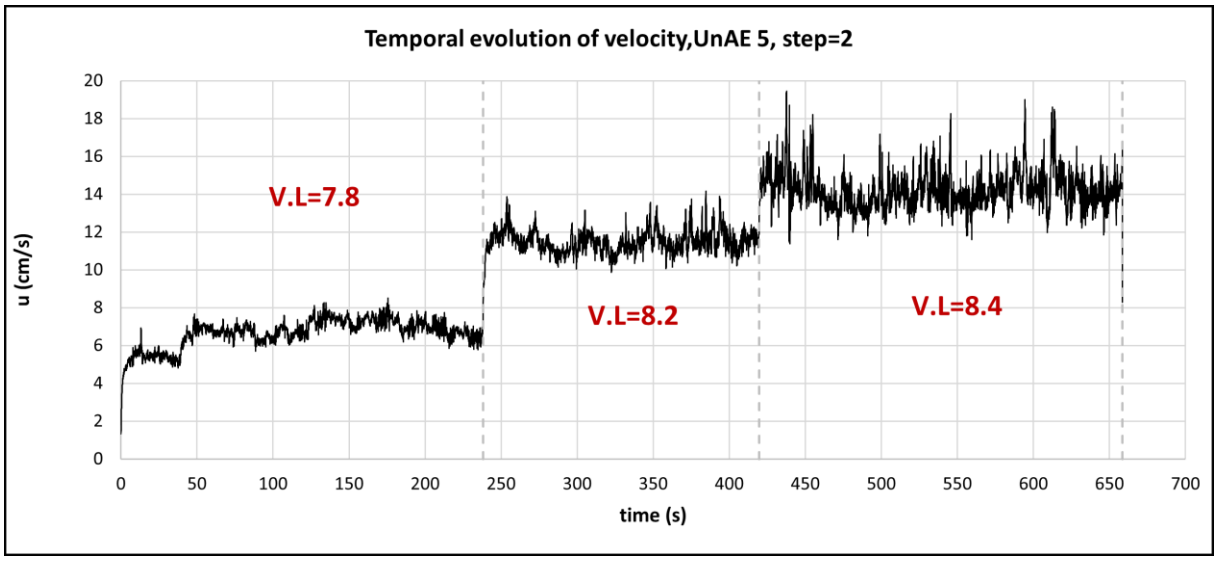
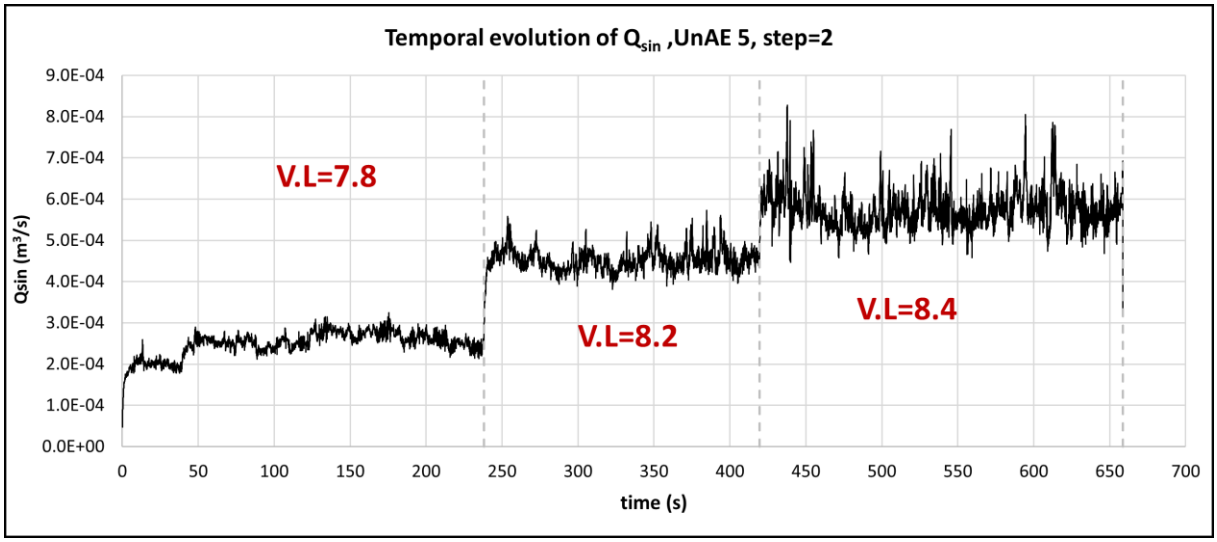


Figure 2.15: Comparison of transfer functions between current and previous campaign in different vibration levels for opening height = 3 cm

Once established, these transfer functions are used during the aggradation experiments to convert the temporal evolution of particle velocity — obtained by applying the PIV algorithm to video footage continuously recorded by the camera positioned above the vibrating channel — into the temporal evolution of sediment inflow discharge $Q_{sin}(t)$. This approach is particularly important for the unsteady campaign, where the feeding rate must vary in time to follow the imposed hydrograph. An example of the temporal evolution of u_{mean} and the corresponding $Q_{sin}(t)$ for experiment UnAE05 is shown in *Figure 2.16*.



(a)



(b)

Figure 2.16: Temporal evolution of (a) U_{mean} and (b) Q_{sin} for experiment UnAE05

To ensure consistency in sediment feeding throughout each experiment, the sediment level in the hopper was maintained as constant as possible by manual refilling, since variations in sediment level can significantly affect the feeding rate.

2.2. Experimental Procedure

Each experiment was carried out following a structured three-stage procedure consisting of a preparation phase, the experiment itself, and a post-experiment phase. This protocol was consistently applied across all runs to ensure reproducibility and to maintain comparable conditions between experiments.

2.2.1. Pre-experimental Phase

Prior to each experiment, a series of preparatory steps were carried out to ensure that the channel and all monitoring systems were in the correct configuration.

The channel slope was first adjusted to the target value of $S_0 = 1.37\%$ using the screw jack mechanism, and the correct inclination was verified using the laser distance meter and the calibration function of Fazzini and Mottini (2015) (*Figure 2.4*). The water level in the underground storage tank was then checked to confirm a sufficient supply for the duration of the experiment and to ensure proper operation of the pumping system.

The sediment bed inside the channel was carefully leveled and maintained at a uniform thickness of 15 cm above the channel floor. To prevent unintended sediment motion during the initial introduction of water — particularly due to surface tension effects — atomized water was gently sprayed over the bed surface prior to starting the pump.

The hopper was filled with the sediment material and the gate opening height and vibration intensity were set according to the target sediment inflow discharge $Q_{s,in}$ required for each experimental phase. The opening height was selected to achieve the required feeding rate for each phase, while the vibration intensity was varied between phases depending on the estimated $Q_{s,in}$ for each case. It should be noted that these estimations were not derived from the transfer functions directly; instead, the selection of both gate opening height and vibration intensity was based on the calibration diagram shown in *Figure 2.13*, which relates the feeding rate to the vibration level for each opening height.

External light interference was minimized by covering the laboratory windows with black curtains. Finally, all cameras were positioned and verified to be operational, and their activation times were recorded to allow subsequent synchronization of the video data.

2.2.2. Experimental Phase

The experiment was initiated by activating the water pumping system to fill the upstream tank. At the beginning, the flow rate was kept relatively high to accelerate the filling process. It was then gradually reduced to a small discharge, below 0.5 L/s, as water entered the channel, in order to avoid disturbing the mobile sediment bed. Once the bed was fully saturated, the discharge was increased over approximately one minute until the target value for the first phase was reached. This value was selected to exceed the threshold required for sediment motion. At this stage, limited rolling of sediment grains may have occurred, but no significant net sediment transport was observed.

The laser distance sensor and all cameras were activated at predetermined times, and their activation times were recorded. The sediment feeding system was then switched on, and this moment was taken as the official start time of the experiment. From this point onward, the water discharge and sediment inflow were monitored throughout the run.

Phase transitions are a key feature of the unsteady experimental campaign and distinguish these experiments from the previous steady-flow runs. At each

predetermined transition time, the water discharge was manually adjusted to the target value of the next phase by operating the guillotine valve. At the same time, the vibration level of the hopper was manually changed to obtain the desired sediment inflow discharge, ($Q_{s,in}$). Although these adjustments were performed manually, they were carried out as quickly as possible so that the transition could be approximated as a step change in the subsequent analysis. The exact timing of each transition was recorded and used to define the boundaries between phases during data processing. Throughout each phase, the hopper was manually refilled when necessary to keep the sediment level as constant as possible, since variations in the hopper fill level can affect the feeding rate, as discussed in Section 2.1.4.1.

At the end of the experiment, the sediment feeder, pump, and cameras were turned off, and the finishing time was recorded to determine the total experiment duration. Flowmeter readings were recorded throughout the experiment using a camera positioned in front of it (*Figure 2.20*), providing a continuous record of the imposed discharge for verification purposes.

2.2.3. Post-experimental Phase

Upon completion of each experiment, the video footage from all cameras was downloaded and archived for subsequent data processing. The sediment accumulated in the downstream collectors and within the channel was carefully collected and spread onto nets to dry (*Figure 2.17*). Once fully dried, the sediment was weighed to determine the total mass of material transported out of the channel and deposited along the channel during the experiment. This measurement was used to verify the overall sediment mass balance and to assess the precision and reliability of measured $Q_{s,in}$ during each run, as described in detail in Chapter 3. The channel was then cleaned and restored to its initial flat-bed configuration in preparation for the next experiment.

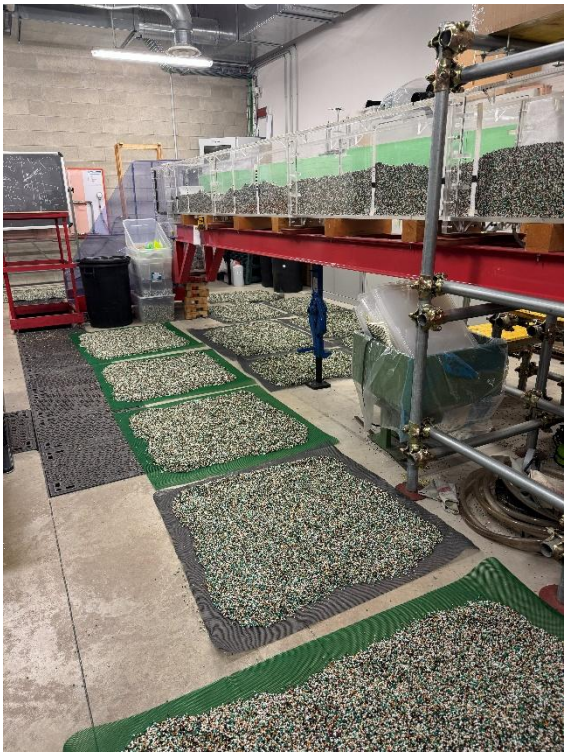


Figure 2.17: Sediments spread for drying

2.3. Data Acquisition and Monitoring Systems

2.3.1. Imaging System

Due to the rapid nature of the aggradation process — particularly under supercritical flow conditions — it is practically impossible to measure key parameters manually with sufficient spatial and temporal resolution. Three GoPro cameras were therefore employed in all experiments, with their technical specifications listed in *Table 2.2*. Camera 1 captured a side view of the channel to record the spatial and temporal evolution of the bed and water surface. Camera 2 was positioned above the vibrating channel to monitor sediment particle motion for the PIV analysis. Camera 3 recorded the flowmeter display to provide a continuous log of the imposed water discharge throughout the experiment.

Table 2.2: Technical specifications of cameras

Camera name	Imaging area	Camera type	Frame rate (*fps*)	Resolution
Camera 1	Flume	GoPro Hero 9	30	5K
Camera 2	Vibrating channel	GoPro Hero 7	30	3840×2160, 2K
Camera 3	Flowmeter	GoPro Hero 7	30	3840×2160, 2K

Camera 1 was positioned along the side of the channel to capture the spatial and temporal evolution of the bed and water surface profiles along the flume length, as shown in *Figure 2.18*.



Figure 2.18: Camera 1 positioned along the channel side

Camera 2 was mounted above the sediment feeding system, oriented perpendicular to the vibrating channel surface, to monitor particle motion and provide the video input for the PIV algorithm described in Section 2.3.3.1 (*Figure 2.19*).



Figure 2.19: Camera 2 positioned above the vibrating channel

Camera 3 was directed at the flowmeter display to provide a continuous visual record of the imposed water discharge throughout the experiment (*Figure 2.20*).



Figure 2.20: Camera 3 recording the flowmeter

All cameras recorded at a frame rate of 30 fps. The video footage was subsequently processed using dedicated image analysis techniques to extract the measurements required for the analysis, as described in the following sections.

2.3.2. Water Discharge Monitoring

Each experiment was conducted at a predetermined nominal water discharge Q, selected to ensure supercritical flow conditions throughout the run. During the experiment, the flowmeter readings were continuously monitored and efforts were

made to maintain them as close as possible to the target values related to each phase. However, the actual discharge entering the flume can differ from the flowmeter reading under two conditions.

First, at the start of each phase — and particularly at the beginning of the experiment — a portion of the incoming water was used to fill the upstream tank before it overflows into the channel. During this period, the discharge entering the flume was lower than indicated by the flowmeter. Furthermore, during phase transitions in the unsteady campaign, the discharge requires a finite time to stabilize following each step change, introducing a transient period during which the flume discharge and flowmeter readings diverge.

Second, the feeding system was activated earlier to prevent excessive bed scour caused by water entering the flume, rather than waiting for the water discharge to stabilize at the desired value. As a result, the sediment introduced at the channel inlet partially obstructed the water flow, creating a backwater effect and further reducing the initial flow rate in the channel compared to the flowmeter readings.

To account for these discrepancies, the water surface elevation in the upstream tank was recorded at 5-second intervals throughout each experiment using the laser distance sensor described in Section 2.1.2. These measurements were used to compute the rate of change of the water volume stored in the tank:

$$Q_{tank} = \frac{A_{tank}\Delta Z_{tank}}{\Delta t} \qquad (2.11)$$

where $A_{tank} = 1.8$ m² is the horizontal cross-sectional area of the tank, ΔZ_{tank} is the change in water level over the time interval, and $\Delta t = 5$s.

Applying the continuity principle, the actual discharge entering the flume (Q_{flume}) was then obtained as:

$$Q_{flume} = Q_{flowmeter} - Q_{tank} \qquad (2.12)$$

where $Q_{flowmeter}$ is the flowmeter reading at the corresponding time step, extracted from the Camera 3 footage. A comparison between the flowmeter readings and the computed flume discharge for a representative experiment is shown in *Figure 2.21*, illustrating the transient behavior at the start of each phase.

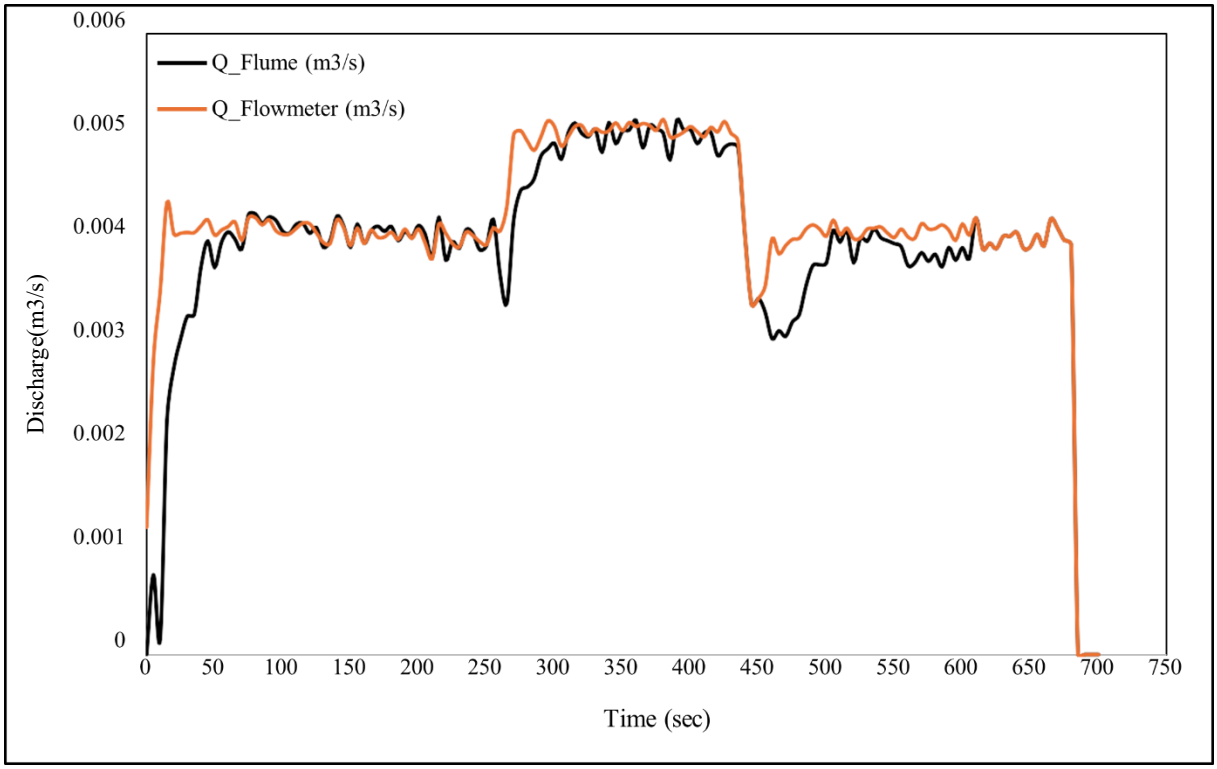


Figure 2.21: Comparison between flume and flowmeter discharge — UnAE03

2.3.3. Sediment Feed Monitoring

The temporal evolution of the sediment inflow discharge $Q_{s,in}$ during each experiment was not measured directly but was derived from the particle velocity recorded by Camera 2, using the transfer functions established during the calibration procedure described in Section 2.1.4.1. The particle velocity was extracted from the video footage using a Particle Image Velocimetry (PIV) algorithm, as detailed in the following section.

2.3.3.1. PIV Algorithm

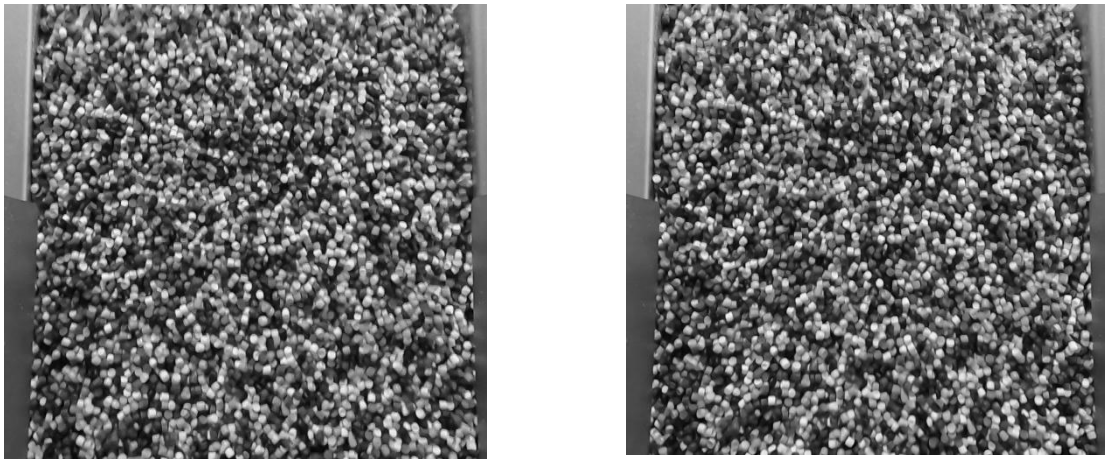
The PIV algorithm, originally developed by Radice (2006) and later modified by Zanchi (2018), was used to estimate the velocity of sediment particles moving along the vibrating channel over short consecutive time intervals. A GoPro Hero 7 camera was positioned above the hopper opening to record the motion of the particles on the

vibrating channel surface (*Figure 2.19*). The recorded footage was then used as the input for the algorithm.

After extracting individual frames from the video, the images were converted from RGB to grayscale, reducing the data from three color channels to a single intensity channel.

Step 1 — Frame selection:

Two frames F_1 and F_2 were selected from the video sequence (*Figure 2.22*). The first frame F_1 corresponds to time t_1, while the second frame F_2 corresponds to time t_2, with $t_2 > t_1$. The selection of the frames was controlled by two parameters: **Jump** and **Step**. Jump defines the spacing between the first frames of two successive iterations, whereas Step defines the spacing between the two frames used within the same iteration (*Figure 2.23*). In this study, Jump was set to 1 to avoid data loss, while Step was set to 2, following the sensitivity analyses performed in previous studies (Unigarro Villota, 2017; Zanchi, 2018).



(a) (b)

Figure 2.22: (a) first selected frame F1; (b) second selected frame F2

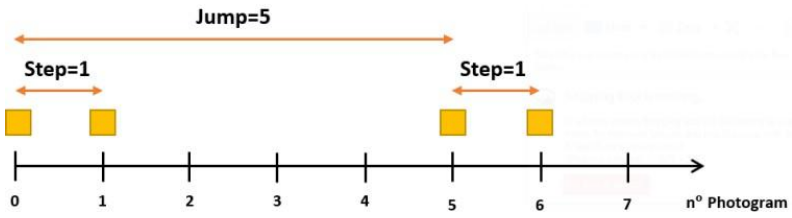


Figure 2.23: graphical explanation of Jump and Step parameters

Step 2 — Working area definition:

A working area was selected in the first frame F_1 (*Figure 2.24*), and the pixel intensities within this area were stored in a matrix A_1. This region was chosen to represent the sediment motion on the vibrating channel while avoiding image areas that were not relevant to the particle displacement analysis.

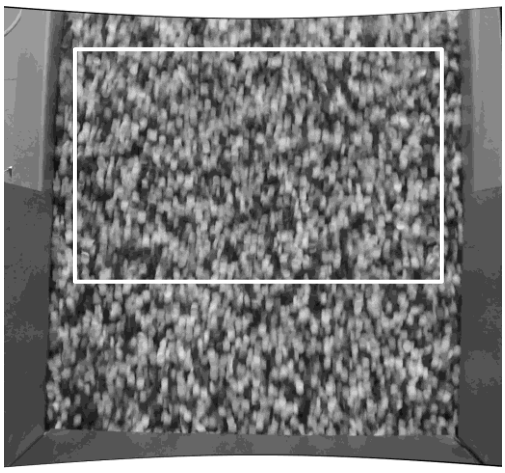


Figure 2.24: working area defined within F1

Step 3 — Search window displacement:

In the second frame F_2, a search window with the same size as the working area selected in F_1 was moved pixel by pixel within a predefined search region. At each position, the pixel intensities were stored in a matrix A_2, and the mismatch parameter S was computed as:

$$S = \frac{N_x N_y}{\sum_{i=1}^{N_x} \sum_{j=1}^{N_y} | A_1(i,j) - A_2(i,j) |} \qquad (2.13)$$

where N_x and N_y are the dimensions of the working area in the x and y directions respectively (*Figure 2.25*). The position corresponding to the minimum value of S was considered the best match between the two frames. The corresponding displacement d_x was therefore taken as the most probable particle displacement in the main direction of motion. To reduce computational cost and avoid unrealistic matches, maximum velocity limits were imposed in both directions. In this study, V_{max} was set to 0.5 cm/s since particle motion on the vibrating channel is predominantly in the x-direction — the primary direction of sediment fall — while displacements in the y-direction are negligible. A small value of V_{max} is therefore sufficient to constrain the search window without excluding any physically meaningful motion. U_{max}, on the

other hand, ranged between 18 and 24 cm/s depending on the experiment, reflecting the higher particle velocities expected in the primary direction of motion.

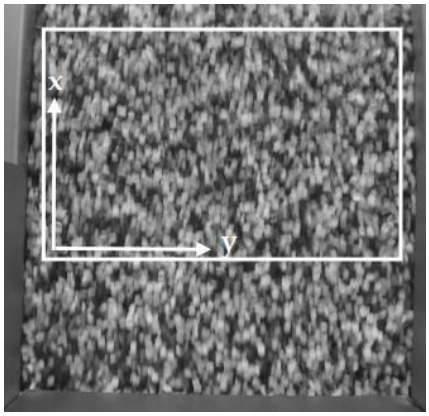


Figure 2.25: Working area and cartesian direction

Step 4 — Conversion from pixels to physical units:

The displacement d_x, initially obtained in pixels, was converted into physical units using a pixel-to-centimetre conversion factor. This factor was determined from the known physical width of the vibrating channel, equal to 22 cm, as shown in *Figure 2.26*.

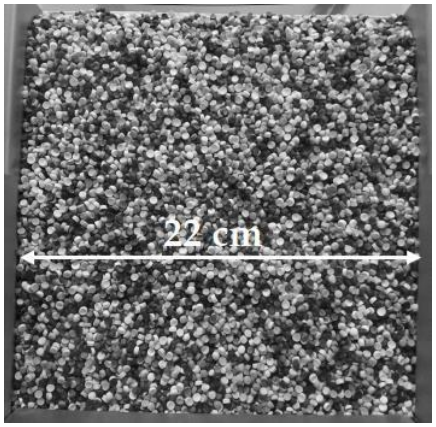


Figure 2.26: Width of vibrating channel — 22 cm

Step 5 — Velocity calculation:

The particle velocity in the x-direction was calculated as:

$$u = \frac{d_x \times fps}{conv \times Step} \qquad (2.14)$$

where fps is the camera frame rate, $conv$ is the pixel-to-centimeter conversion factor expressed in pixel/cm, and $Step$ is the frame interval used in the PIV calculation.

Step 6 — Temporal evolution of particle velocity and sediment inflow discharge:

The same procedure was repeated over the full sequence of frames, providing the temporal evolution of the mean particle velocity $u_{mean}(t)$ during the experiment. This velocity signal was then converted into the temporal evolution of the sediment inflow

discharge $Q_{sin}(t)$ using the transfer function obtained from the hopper calibration (Section 2.1.4.1).

2.3.4. Bed and Water Surface Elevation Detection

2.3.4.1. Definition of the Reference Bed

A critical challenge in measuring sediment aggradation is the definition and determination of bed elevation, particularly in experiments with steep slopes designed to reproduce mountain-stream conditions. Under such conditions, the high sediment transport capacity of the channel can lead to the formation of a relatively thick bedload layer, making it difficult to define a unique reference bed elevation. Studies based on sediment concentration and velocity profiles have shown that the moving sediment layer can be divided into an upper collisional sublayer and a lower dense sublayer located above the stationary deposit (e.g., Capart and Fraccarollo, 2011; Berzi et al., 2019). In the dense sublayer, grain velocity is significantly lower than in the collisional layer, while sediment concentration is close to that of the stationary bed, making the identification of the interface between the moving layer and the fixed bed particularly challenging.

The method used to measure bed elevation depends fundamentally on how the bed itself is defined. Eslami et al. (2022) investigated the sensitivity of key hydro-morphological parameters to two extreme definitions of bed elevation: one located at the upper edge of the bedload layer and the other at the lower edge, where no particle motion occurs. Their results showed that this choice can significantly affect the estimation of parameters such as the initial sediment transport capacity, the time scales of the aggradation process, water depth, and Froude number, and can also influence the calibration of numerical models.

In the present study, the bed is defined as the region below the bedload layer, corresponding to the highest elevation at which no sediment motion is detected. The bedload layer is therefore considered part of the moving mixture, while the bed surface is identified as the interface between this moving layer and the stationary sediment deposit. Accordingly, the motion-based method originally developed by Eslami et al. (2022) and later refined by Tavakoli et al. (2022) is adopted to determine both the bed and water surface elevations. This approach is consistent with the methodology used in all previous experimental campaigns carried out at the Mountain Hydraulics Laboratory of Politecnico di Milano (Eslami et al., 2021; Tavakoli et al., 2022; Hiteh et al., 2023; El Achkar and Hassan, 2024).

2.3.4.2. Motion-Based Detection Method

Camera 1 (GoPro Hero 9) monitors the channel from one side, providing an approximately perpendicular view of the monitored reach of the flume during each

experiment. Before applying the motion-based algorithm, the recorded videos were trimmed to match the duration of each experiment and spatially cropped to the monitored channel length using MATLAB routines developed during previous experimental campaigns are then used to extract grayscale frames from the videos at a rate of 30 frames per second. Since the GoPro Hero 9 includes automatic lens distortion correction, no additional manual radial correction is applied to these frames. A representative grayscale frame extracted during experiment UnAE05 is shown in *Figure 2.27*.

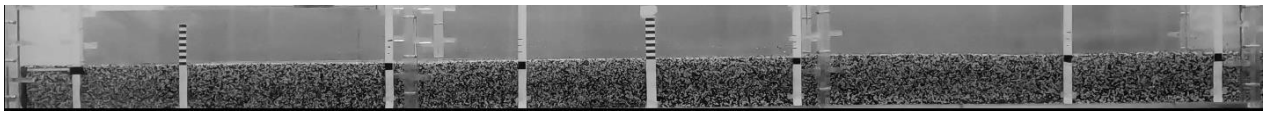


Figure 2.27: Cropped grayscale frame of the channel during UnAE05

The motion-based algorithm is applied to the processed frames through the following steps.

Step 1 — Frame Selection:

Two subsequent frames F_1 and F_2 are selected from the video sequence, each representing the state of the channel at a given instant. Frame selection is controlled by two parameters: Jump and Step. For the bed and water surface detection algorithm, Jump is set to 30 — corresponding to a temporal interval of one second at 30 fps — while Step is set to 1. The pixel intensities of F_1 are stored in matrix A_1, and those of F_2 are stored in matrix A_2.

Step 2 — Gaussian Filtering:

A Gaussian filter is applied to both frames to reduce image noise and prevent spurious pixel differences from being incorrectly interpreted as particle motion. The filter intensity is selected individually for each experiment according to the image quality and ambient lighting conditions.

Step 3 — Binary Image Generation:

The absolute pixel-wise difference between matrices A_1 and A_2 is computed and compared with a predefined threshold. Pixels for which the difference exceeds the threshold are classified as motion regions and assigned an intensity value of zero, appearing black in the binary image. All other pixels are assigned an intensity value of one, appearing white. The result is a binary image in which black regions represent areas of detected motion — including both the bedload layer and the overlying water — while white regions correspond to stationary areas, as shown in *Figure 2.28*. The threshold value is determined through trial and error and typically ranges between 0.04 and 0.06.

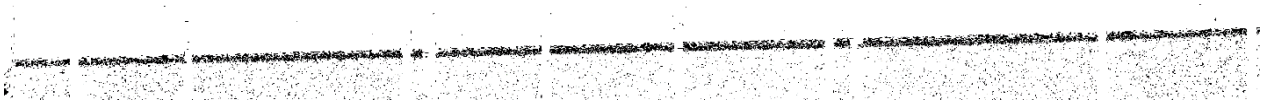


Figure 2.28: Binary image showing detected motion in black

Step 4 — Detection of Bed and Water Surface Boundaries:

The black layer in the binary image represents the motion layer. Its lower boundary corresponds to the interface between the stationary bed and the moving bedload layer, while its upper boundary corresponds to the water surface. To detect these boundaries, a moving window of size 5×20 pixel² is applied. The window scans the binary image column by column, moving from top to bottom before shifting one pixel to the right, as illustrated in *Figure 2.29*.



Figure 2.29: Schematic of moving window in initial position

At each position, the mean pixel intensity inside the moving window is computed, producing an intensity profile for each vertical column, as shown in *Figure 2.30* and *Figure 2.31*. The signal remains nearly flat within the white regions, drops sharply at the upper boundary of the black motion layer — corresponding to the water surface — and rises sharply again at the lower boundary — corresponding to the stationary bed.

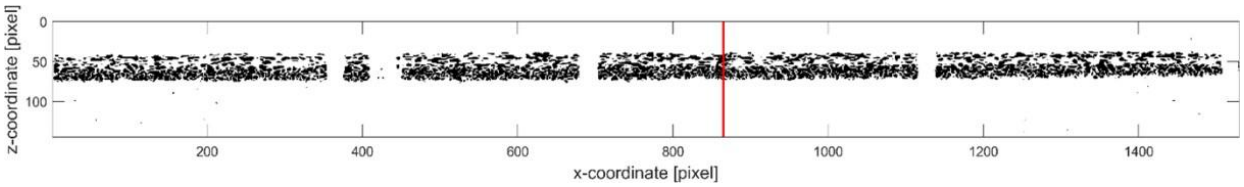


Figure 2.30: Selected vertical column used to extract the intensity profile.

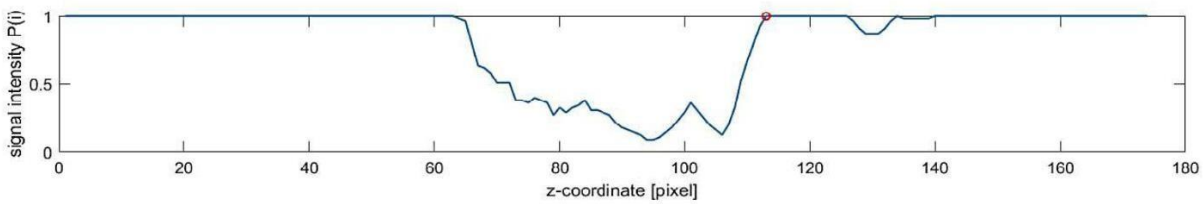


Figure 2.31: Intensity profile used to identify the water surface and stationary bed boundaries.

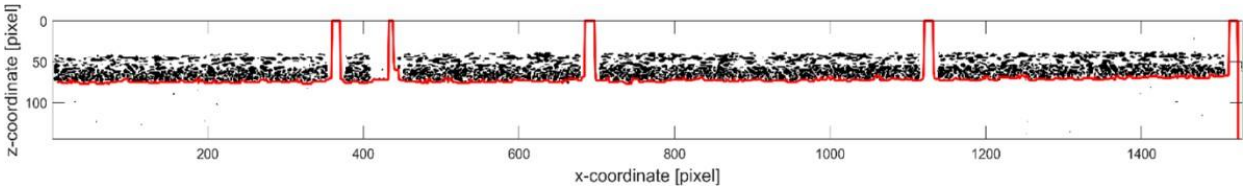


Figure 2.32: Bed elevation profile (Eslami et al.,2022)

The MATLAB function **findchangepts** is used to identify the locations of these abrupt changes in the intensity profile. Since the detected locations initially correspond to the center of the moving window rather than the true boundaries, a correction equal to half of the vertical window size is applied to shift the detected positions to the actual locations of the water surface and bed elevation. By repeating this procedure across all columns, complete spatial profiles of both the bed elevation and the water surface elevation are obtained for each time step.

Step 5 — Error Identification and Correction:

As with most image-based measurement techniques, the motion-based method is subject to different sources of error, as illustrated in *Figure 2.34*:

- **(a) Residual noise** — despite Gaussian filtering, residual noise may occasionally be misclassified as motion. Improved lighting conditions and higher-quality cameras can help reduce this source of error.
- **(b) Detection gaps** — in some portions of the image, the bed or water surface may not be correctly identified, requiring interpolation or local correction to fill the missing values.
- **(c) External motion** — movements unrelated to the sediment or water — such as reflections or people moving behind the channel — may be incorrectly detected as part of the motion layer. To minimize this effect, green paper is placed along one side of the channel, while black curtains are used to block external light from entering through the laboratory windows (*Figure 2.35*).

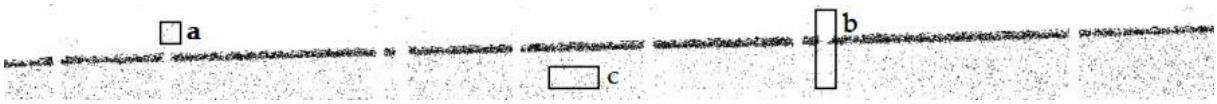


Figure 2.34: Three types of errors in the detection process — (a) residual noise; (b) detection gap; (c) external motion (Achkar et al.,2024)



(a) (b)

Figure 2.35: (a) Black Curtain Covering Windows (b) Green Paper Covering Noises Behind Channel

After the initial detection, remaining errors are corrected using the MATLAB function **filloutliers**, which identifies data points deviating from the local mean by more than a specified number of standard deviations and replaces them with interpolated values. The threshold and neighborhood size are selected through trial and error for each experiment. The resulting corrected bed and water surface profiles provide smoother and more reliable representations of the detected interfaces, as shown in *Figure 2.36*.

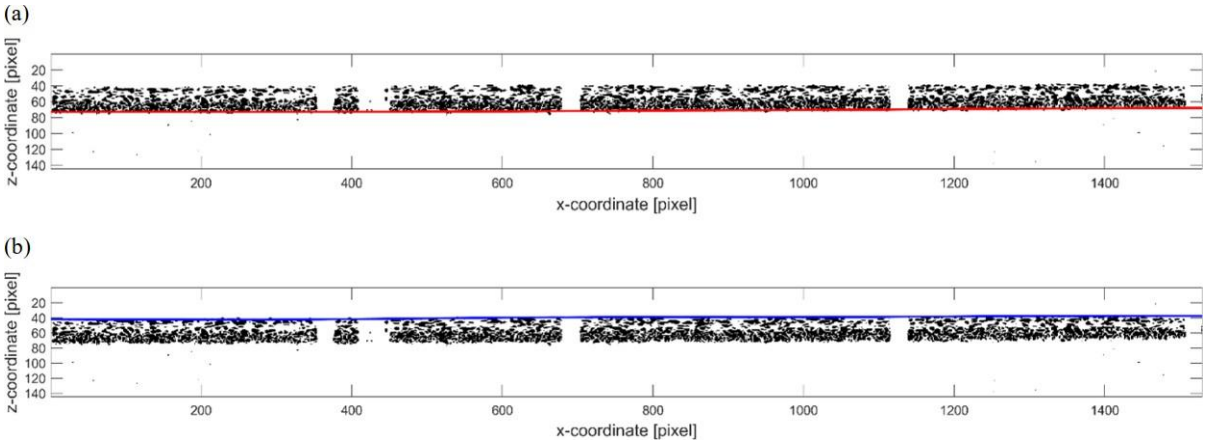


Figure 2.36: (a) Corrected bed and (b) Water surface profiles (Eslami et al.,2022)

Step 6 — Unit Conversion and Coordinate Referencing:

The bed and water surface profiles obtained from the motion-based algorithm require additional post-processing before they can be used in the morphodynamic analysis. First, remaining outliers and missing values are corrected using interpolation and local filtering, ensuring that isolated detection errors do not affect the interpretation of the bed and water surface evolution. The corrected profiles are then converted from pixel coordinates to physical coordinates using a conversion factor obtained from known reference dimensions visible in the images — such as the monitored channel length or reference markers attached to the channel wall.

The coordinate system is defined with the x-direction measured from the channel inlet and increasing downstream. The vertical coordinate z is referenced to the black tape markers placed 15 cm above the channel bottom, representing the initial bed elevation before the experiment begins, with z increasing upward. The bed profile detected at the beginning of each experiment is used to verify this reference. Subsequent bed profiles are expressed relative to the initial bed level, allowing the aggradation height $\Delta z(x,t)$to be evaluated along the channel and throughout the experiment:

$$\Delta z(x,t) = z_b(x,t) - z_{b,0}(x) \quad (2.15)$$

where $z_b(x,t)$ is the detected bed elevation at position x and time t, and $z_{b,0}(x)$ is the initial reference bed elevation. Following the Jump and Step parameters defined above, the procedure is applied to every selected pair of frames, generating bed and water surface profiles at **one-second intervals** throughout the experiment. An example of the final corrected and referenced bed and water surface profiles at different time steps is shown in *Figure 2.37*.

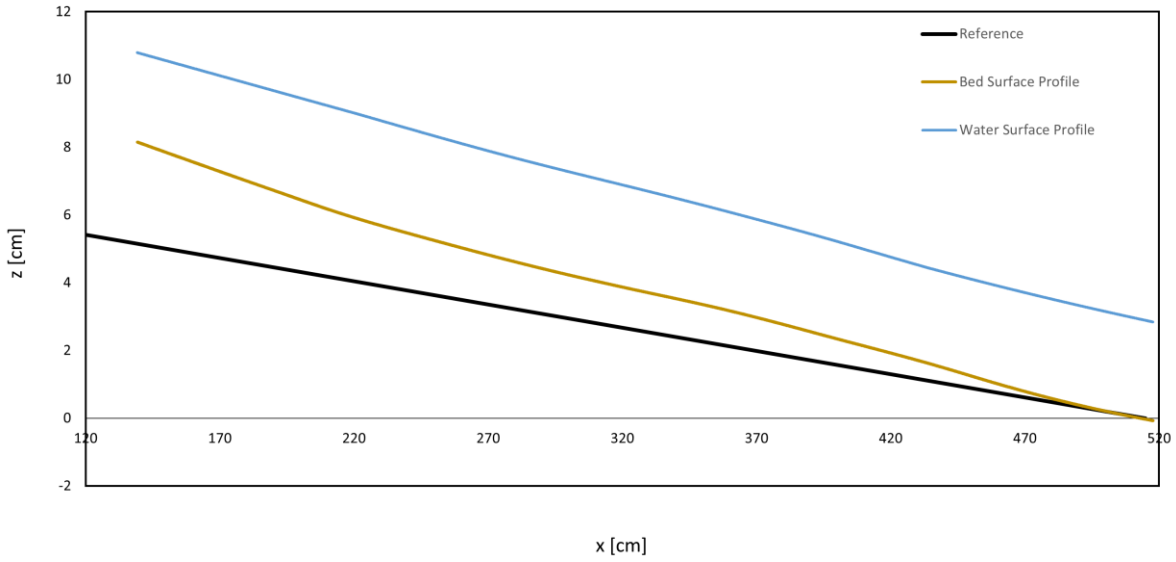


Figure 2.37: Bed and water surface profiles in the referenced coordinate system at t = 180 seconds during experiment UnAE06, with the reference initial bed defined by black tapes positioned 15 cm above the channel bottom.

2.4. Initial Sediment Transport Capacity and Loading Ratio

Sediment transport capacity within a channel reach is defined as the maximum sediment discharge that the flow can convey under given hydraulic, sediment, and morphological conditions. It is a key parameter for interpreting aggradation and degradation processes. Aggradation occurs when the incoming sediment supply exceeds the local transport capacity, whereas degradation occurs when the transport capacity exceeds the supplied sediment discharge. Morphological equilibrium is achieved when these two quantities are approximately balanced.

In the present study, the initial sediment transport capacity, Q_{s0}, is estimated using the Continuity Method, which is applied separately to each phase. In addition, Sediment Capacity (SC) experiments were conducted prior to the main experimental campaign to provide an independent assessment of the Continuity Method results during the first phase, where a direct comparison between the two approaches is possible. The following sections describe:

- Sediment Capacity Experiments (SC)
- Continuity Method

2.4.1. Sediment Capacity (SC) Experiments

The SC experiment is based on the concept of hydrodynamic equilibrium, in which the sediment inflow exactly matches the transport capacity of the channel so that no net aggradation or degradation occurs. Under these conditions, all sediment entering at the upstream end exits at the downstream end and the bed elevation remains stationary over time. Since channel geometry and sediment properties are kept constant throughout the experimental campaign, Q_{s0} is theoretically governed only by the water discharge and bed slope. A separate SC experiment was therefore conducted for each water discharge associated with the first phase of the unsteady experiments.

The experiment begins with predetermined settings for the hopper vibration level, gate opening height, and water discharge. Once the flow is established, the behavior of the channel bed is monitored and classified into one of three conditions:

- **Aggradation:** the sediment inflow exceeds the transport capacity — the vibration level is reduced in the next step to decrease the feeding rate.

- **Degradation:** the sediment inflow is below the transport capacity — the vibration level is increased to raise the feeding rate.
- **Equilibrium:** the sediment inflow matches the transport capacity — no adjustment is needed, though the experiment continues for a sufficient duration to confirm the stability of the bed.

None of these conditions manifest immediately — a certain amount of time must pass before the state of the channel can be reliably assessed. The process of adjusting the vibration level continues iteratively until a stable equilibrium condition is confirmed. The sediment inflow discharge Q_{sin} corresponding to the equilibrium vibration level is then determined using the PIV algorithm (Section 2.3.3.1) and taken as the initial sediment transport capacity Q_{s0} for that water discharge.

As an illustrative example, *Table 2.3* lists the results of experiment SC_{Q5}, carried out with a water discharge of $Q = 5$ l/s, showing the vibration levels tested and the corresponding mean sediment inflow discharges.

Table 2.3 SCQ5 Experimental results

Step 2		
Vibration Level	Time (s)	$Q_{sin,mean}$ (m^3/s)
8.05	375	1.56E-04
8	670	1.25E-04
7.9	270	9.57E-05

Figure 2.38 shows the temporal evolution of $Q_{s,in}$ obtained from the PIV method during this experiment, with the different vibration levels clearly distinguishable. *Figure 2.39* shows the corresponding temporal evolution of bed elevation at several cross-sections along the channel, confirming the progressive approach to equilibrium as the vibration level is adjusted. The results indicate that morphological equilibrium — where no changes occur in the bed compared to its initial state — is achieved at a vibration level of 8. The average $Q_{s,in}$ value at this vibration level is therefore taken as the initial sediment transport capacity of the channel, $Q_{s0,SC}$, for this experiment.

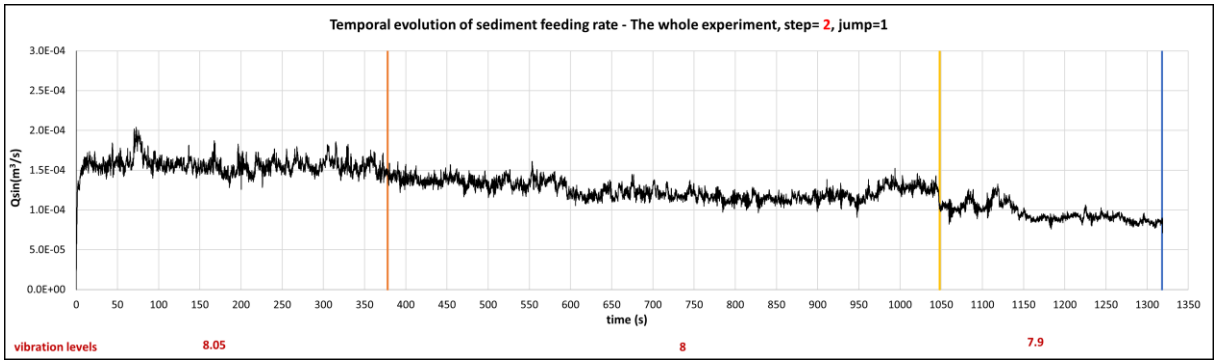
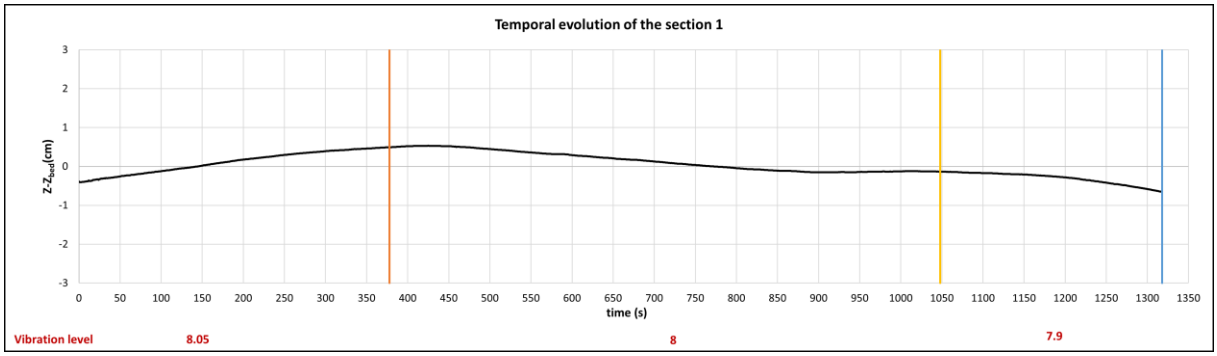
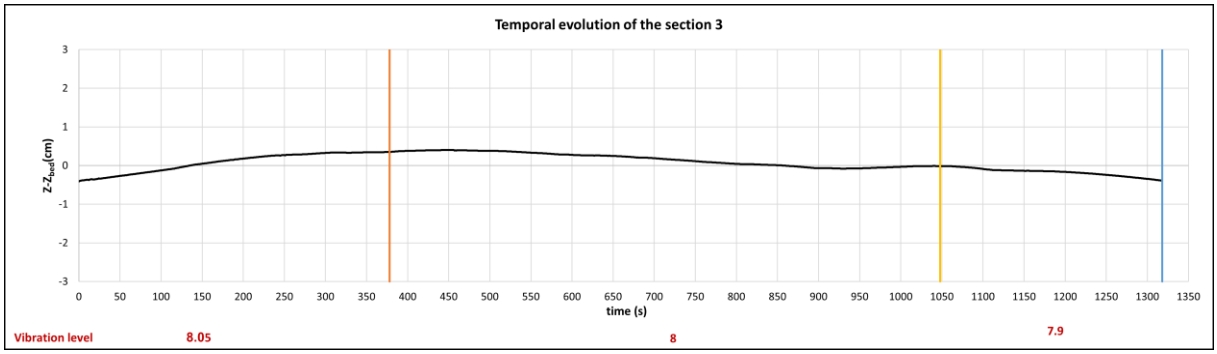
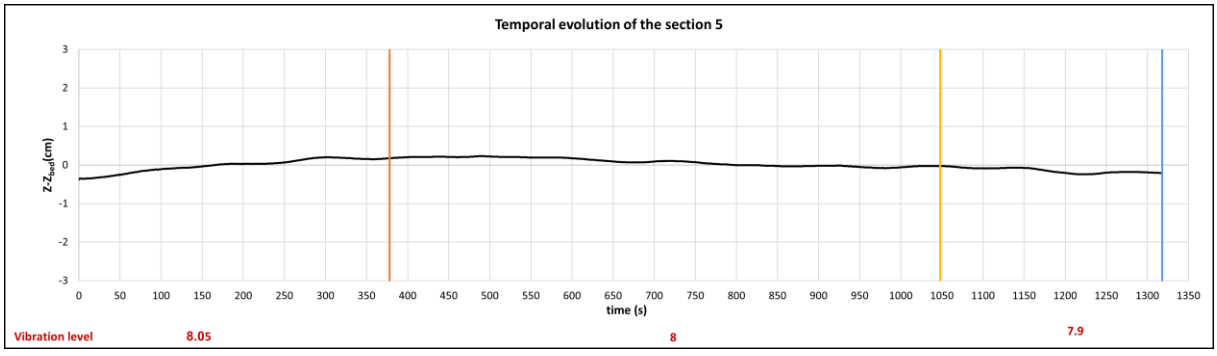


Figure 2.38: SC test temporal evolution of Q_{sin} from PIV







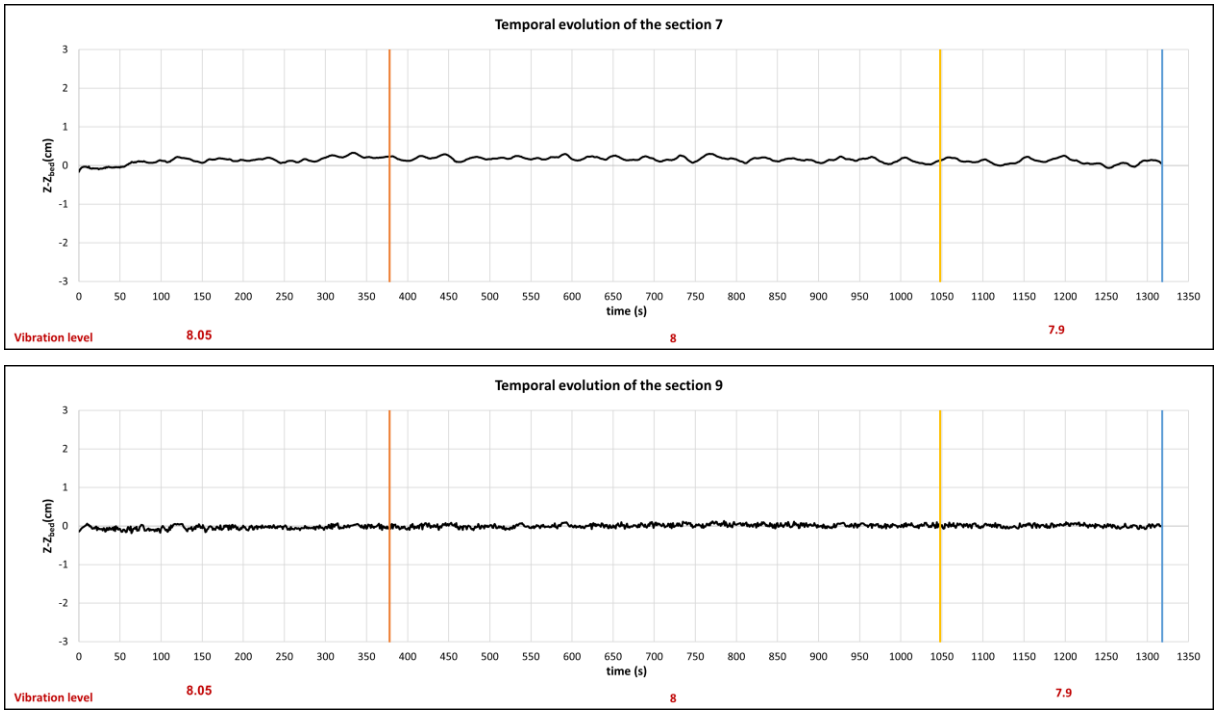


Figure 2.39: Temporal evolution of bed elevation at different x

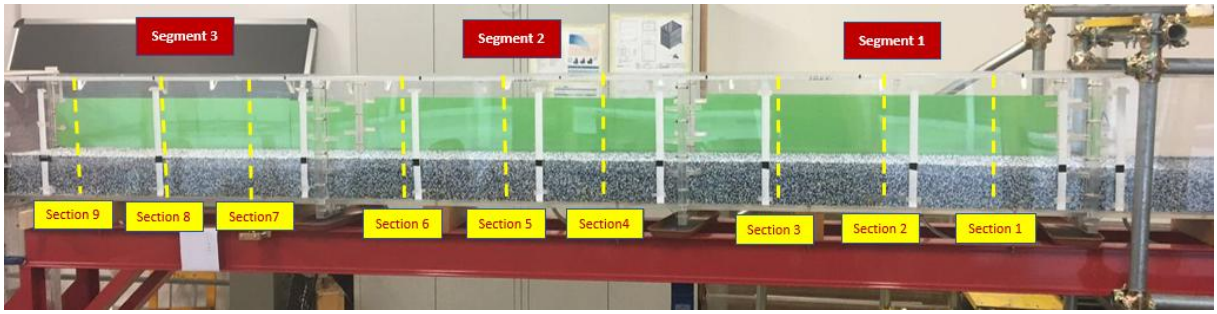


Figure 2.40: Channel sections location

2.4.2. Continuity Method in Unsteady Experiments

The Continuity Method is based on the principle of sediment mass conservation and represents an evolution of the approach originally developed by Zanchi and Radice (2021). During an aggradation experiment, part of the incoming sediment is deposited within the channel while the remainder exits through the outlet. The sediment transport capacity can therefore be estimated by subtracting the solid deposition rate from the sediment inflow discharge. Applying mass conservation:

$$Q_{s,in} = Q_{s0} + Q_{s,deposit}$$

which gives:

$$Q_{s0,continuity} = \bar{Q}_{s,in}(t_1, t_2) - m \cdot (1 - p_0) \qquad (2.16)$$

where $\bar{Q}_{s,in}(t_1, t_2)$ is the time-averaged sediment inflow discharge over the calculation window $[t_1, t_2]$, p_0 is the sediment porosity, and $m = \frac{dV_{measured_bed}}{dt}$ is the rate of increase of the total deposited volume including voids. Multiplication by $(1-p_0)$converts this volume rate into the corresponding solid sediment deposition rate.

The deposited volume $V_{measured_bed}$ at a given time $t$is computed from the detected bed profiles as:

$$V_{measured_bed}(t) = A_{bed}(t) \times B \qquad (2.17)$$

where $A_{bed}(t)$ is the side area of the depositional wedge at time $t$and $B = 0.30$m is the channel width.

Unmonitored upstream reach — CU and IU scenarios

A key challenge in computing $V_{measured_bed}$ arises from the unmonitored upstream portion of the channel. The sediment feeding point is located at $x = 30$cm from the channel inlet, whereas bed profiles are monitored starting from $x = 139.25$cm. The volume of sediment deposited between these two locations cannot be directly measured. To account for this uncertainty, two scenarios are considered for reconstructing the bed profile in the unmonitored upstream reach, as illustrated in *Figure 2.41*:

- **Constant Upstream (CU):** the bed aggradation height in the unmonitored reach is assumed to be constant and equal to the value detected at $x = 139.25$cm.
- **Inclined Upstream (IU):** the bed elevation in the unmonitored reach is reconstructed using a linear extrapolation based on the slope computed from the first monitored portion of the channel, between $x = 139.25$cm and $x = 248.5$cm.

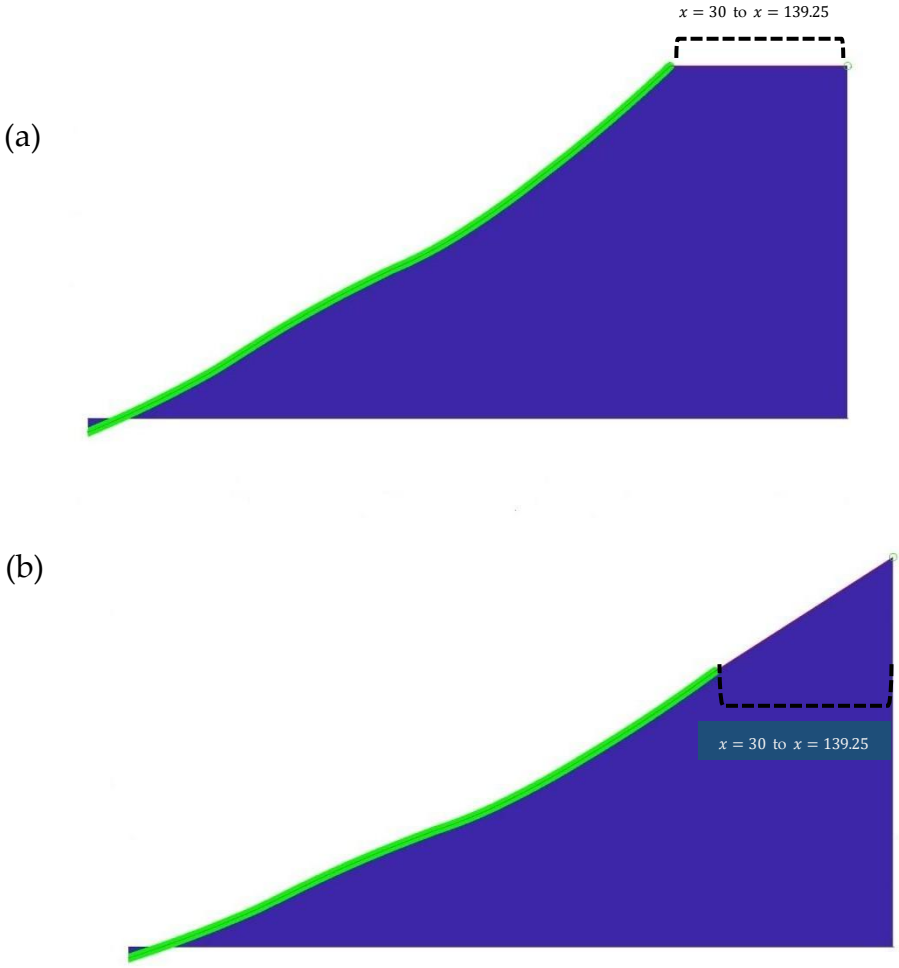


Figure 2.41 (a) CU (b) IU explanatory sketches in UnAE01

Using these two assumptions, $V_{measured_bed}$ is computed at regular time intervals. A comparison of the temporal evolution of $V_{measured_bed}$ for both scenarios for a representative experiment is shown in *Figure 2.42*.

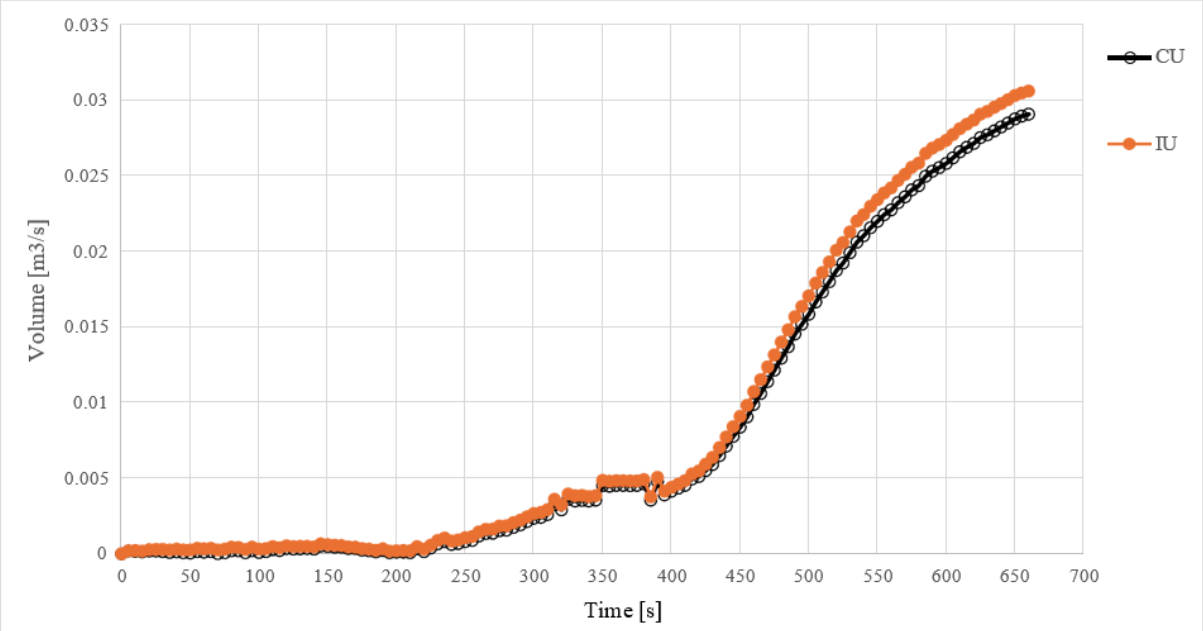


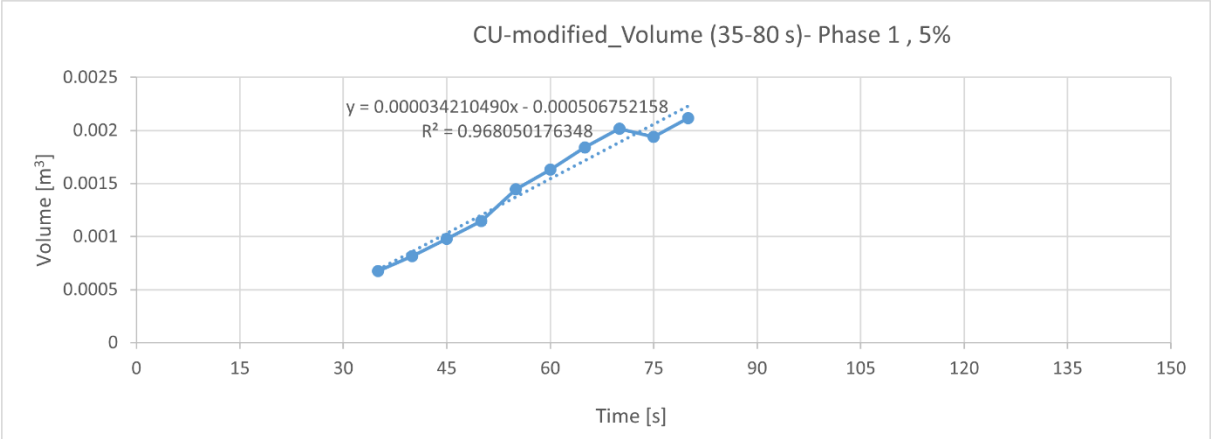
Figure 2.42: Comparison of V_(measured_bed) between CU and IU scenarios(UnAE03)

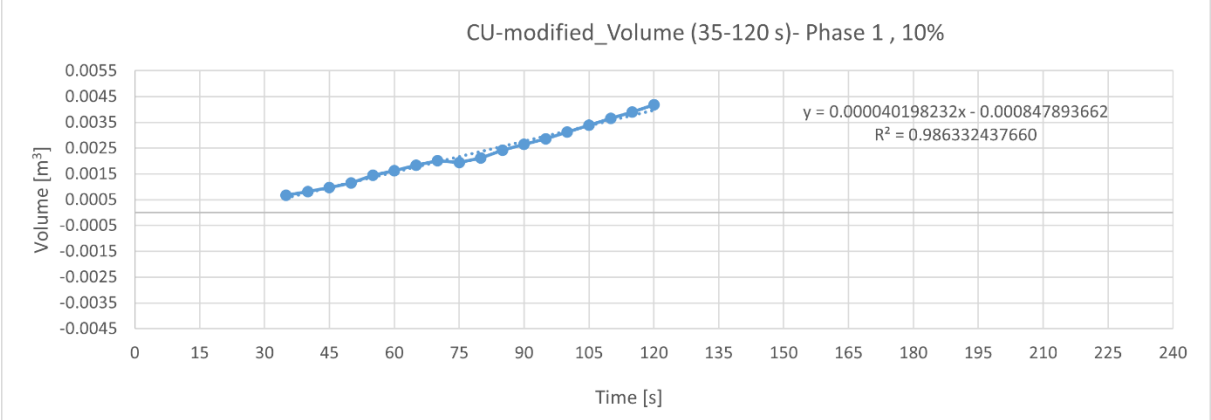
Definition of the calculation time window

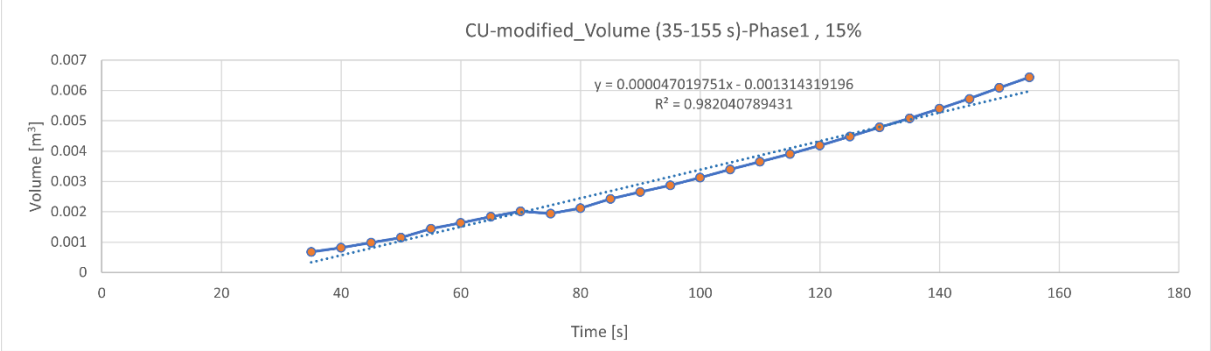
Since progressive aggradation modifies the bed slope and consequently affects the transport capacity, Q_{s0} must be estimated during the early stage of bed evolution, before substantial morphological changes occur. The time window $[t_1, t_2]$is therefore defined based on a bed slope evolution criterion. The final time t_2 is defined as the time at which the bed slope has increased by a prescribed percentage with respect to its value at t_1. Three thresholds are considered — **5%, 10%, and 15%** — to assess the sensitivity of the estimated Q_{s0} to the selected time window.

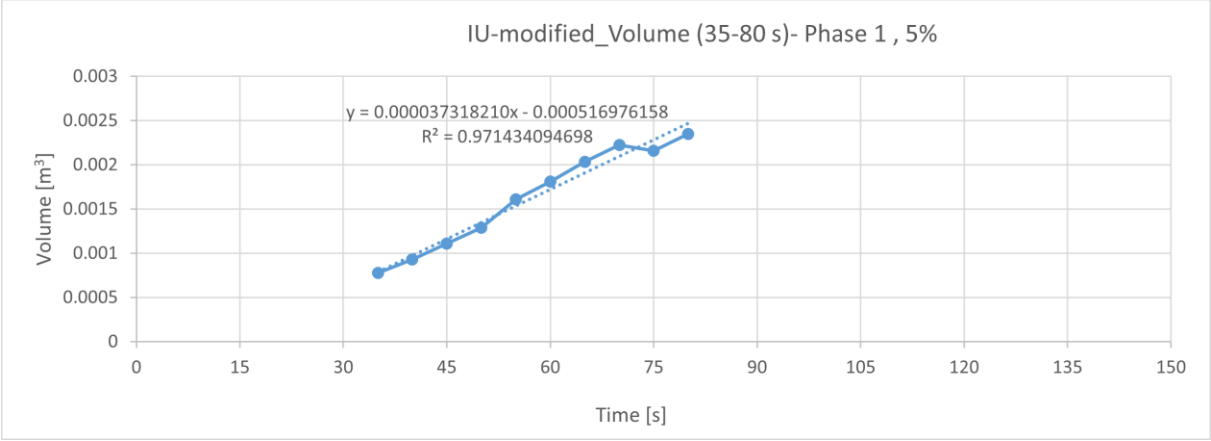
Regarding t_1, an important distinction is made between the first phase and subsequent phases. For Phase 2 onwards, t_1 corresponds to the moment of the discharge change. For the first phase, $t_1$is set to the moment at which the water discharge has fully stabilized at its target value — rather than $t = 0$— since the initial transient period does not represent a valid reference condition. As an example, for experiment UnAE08, the calculation for Phase 1 begins at $t_1 = 35$s (*Figure 2.43*).

It should be noted that, unlike the approach adopted in previous campaigns where $\bar{Q}_{s,in}$ was averaged over the entire phase, in the present study the sediment inflow discharge is averaged exclusively over the same time window $[t_1, t_2]$ defined by the slope evolution criterion. This ensures that both the deposition rate m and the sediment inflow $\bar{Q}_{s,in}$ are evaluated over a consistent time interval, yielding a more representative estimate of Q_{s0} for each phase.


CU-modified_Volume (35-80 s)- Phase 1 , 5%
y = 0.000034210490x - 0.000506752158
R² = 0.968050176348
Volume [m³]
Time [s]


CU-modified_Volume (35-120 s)- Phase 1 , 10%
y = 0.000040198232x - 0.000847893662
R² = 0.986332437660
Volume [m³]
Time [s]


CU-modified_Volume (35-155 s)-Phase1 , 15%
y = 0.000047019751x - 0.001314319196
R² = 0.982040789431
Volume [m³]
Time [s]


IU-modified_Volume (35-80 s)- Phase 1 , 5%
y = 0.000037318210x - 0.000516976158
R² = 0.971434094698
Volume [m³]
Time [s]

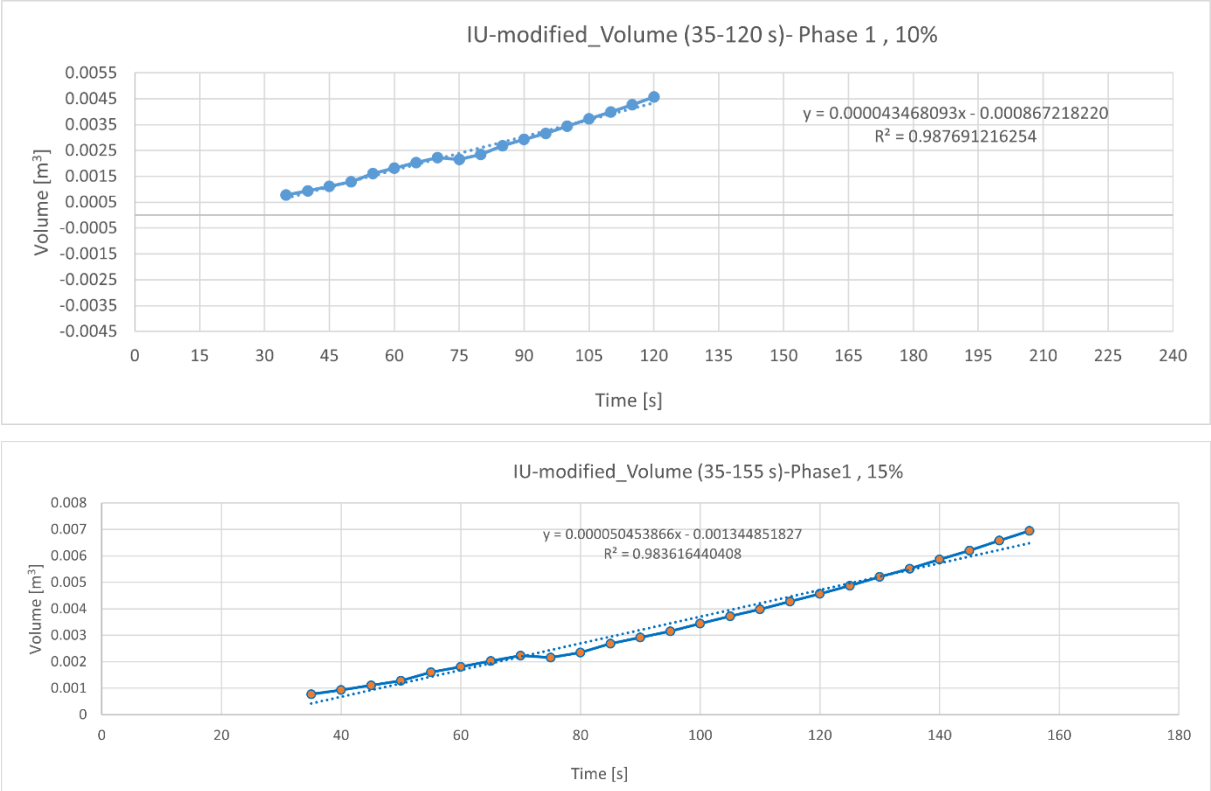


Figure 2.43: Temporal evolution of V_(measured_bed) for Phase 1 of UnAE08 —IU, CU scenarios — 5%, 10%, and 15% slope evolution thresholds

The detailed analysis of the resulting Q_{s0} and L_r values for all experimental phases, including their comparison with the steady-flow campaign, is presented in Chapter 3.

3 Chapter 3: Results and Analysis

3.1. Aggradation Experiments

This chapter presents the results of the unsteady aggradation campaign conducted at the Mountain Hydraulics Laboratory of Politecnico di Milano. The campaign consisted of ten experiments, denoted UnAE01 through UnAE10, designed to investigate the morphodynamic response of supercritical flows to variations in water discharge and sediment supply. The experimental conditions are first described in Section 3.1.1, followed by a mass conservation analysis in Section 3.1.2 used to assess the reliability of the measurements and the consistency of the sediment budget.

3.1.1. Experimental Conditions

The experimental campaign was characterized by different combinations of water discharge and sediment feeding rate as upstream boundary conditions. Depending on the specific objectives of each experiment, the hydrographs were composed of two, three, or five phases. Within each phase, water discharge and sediment feeding conditions were kept as constant as possible, while abrupt changes were imposed at the transition between consecutive phases. This approach allowed the investigation of the channel response to controlled variations in hydraulic and sediment supply conditions. While *Figure 3.1* provides a schematic overview of the hydrograph structure adopted in the campaign, *Figure 3.2* represents the designed hydrograph for each experiment and the average $Q_{s,in}$ obtained during each experimental phase for experiments UnAE05 and UnAE07, selected as representative examples of three-phase and five-phase hydrographs respectively.

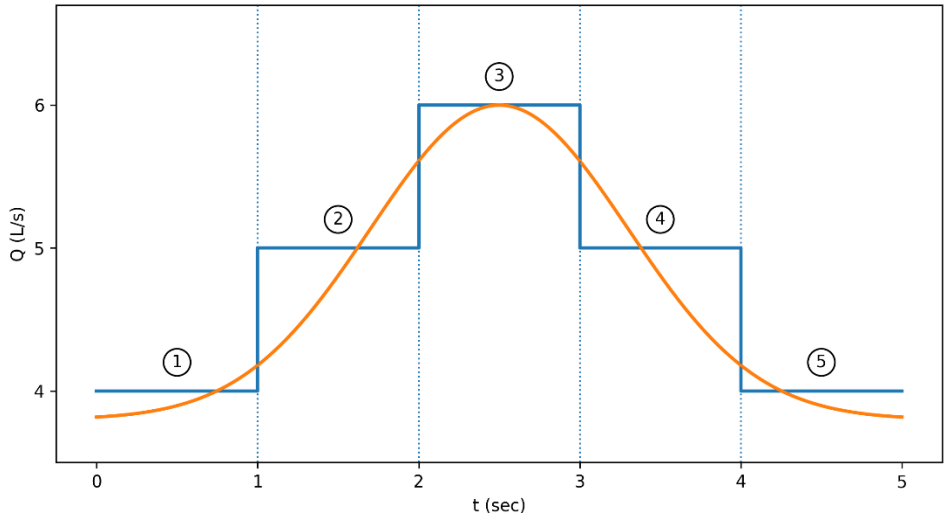
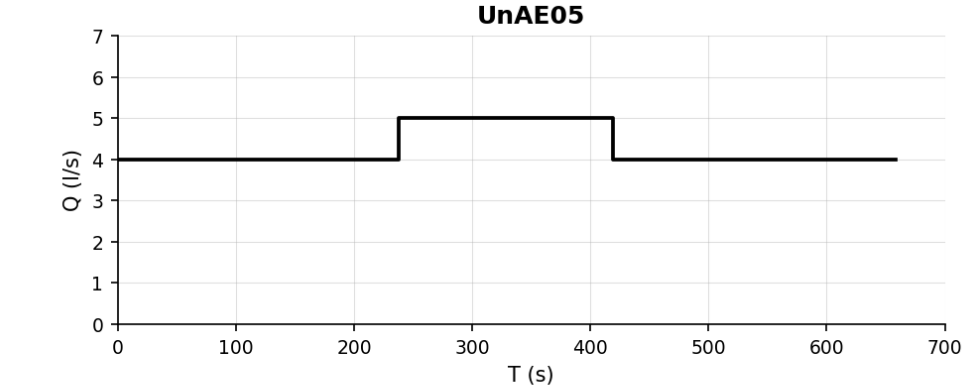
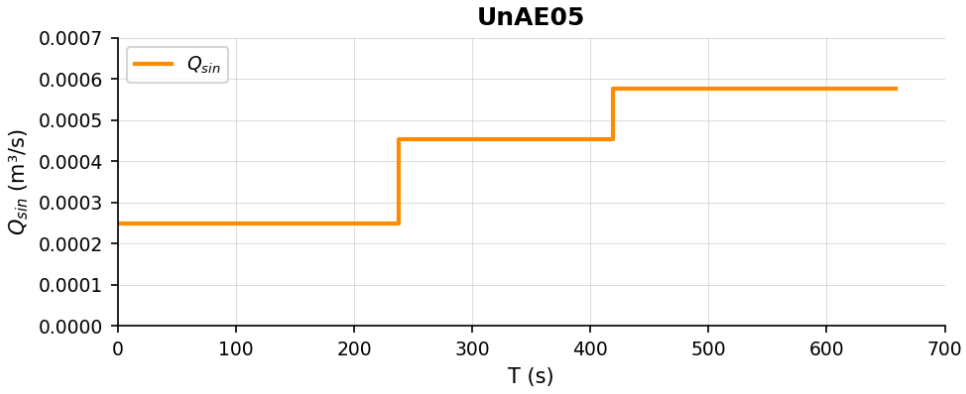


Figure 3.1: Schematic representation of a 5-step hydrograph used in experiments





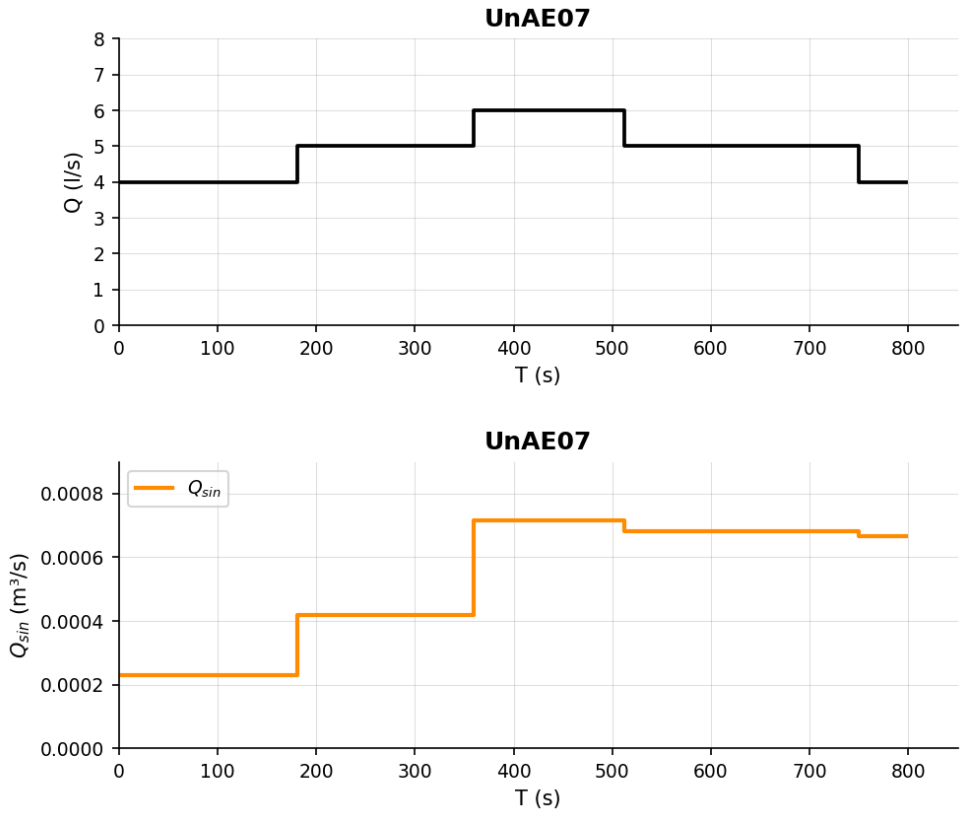


Figure 3.2: Temporal evolution of water discharge and $Q_{s,in}$ for UnAE05 & UnAE07

The adopted hydrographs and sediment graphs configurations were intended to reproduce the main characteristics of natural streams subjected to unsteady boundary conditions while maintaining experimental control. Since a fully continuous hydrograph is challenging to be implemented in the laboratory, the target discharge and sediment supply variations were approximated using a sequence of discrete phases.

In experiments UnAE01 through UnAE06 and UnAE10, a three-phase low–high–low discharge sequence was applied. Experiments UnAE07 and UnAE08 were conducted using a five-phase hydrograph to investigate the morphodynamic response under a longer and more complex unsteady boundary conditions, while experiment UnAE09 consisted of two phases. In all experiments, a sediment feeding rate $Q_{S,in}$ was set such that the resulting loading ratio L_r exceeded unity, with the aim of inducing aggradation throughout each phase. All channel configurations were kept constant across all experiments, including channel length, width, and nominal initial slope ($S_0 = 1.37\%$).

The parameters $Q_{s,in}$, Q_{water} and vibration levels were prescribed in advance, whereas load ratio was obtained from the experimental data.

To determine the Froude number, uniform flow conditions within the channel were assumed and the associated flow depth H was derived using the Gauckler–Strickler formulation:

$$Q = \frac{A}{n}\sqrt{S_0} \cdot R_H^{2/3} \qquad (3.1)$$

where $A = B \times H$ is the flow cross-sectional area, $S_0 = 1.37\%$ is the nominal channel slope at the beginning of each phase, $n = 0.015 \text{s}/m^{1/3}$ is the Manning roughness coefficient of the sediment particles, determined by Zanchi and Radice (2021) under clear water conditions, and R_H is the hydraulic radius. The depth-averaged velocity U and Froude number are then computed as:

$$U = \frac{Q}{B \times H} \qquad (3.2)$$

$$Fr = \frac{U}{\sqrt{g \times H}} \qquad (3.3)$$

The main parameters of all experimental phases are summarized in *Table 3.1*. Q_{s0} values used in the calculation of Lr were estimated according to the procedure described in Section 3.2.2.

Table 3.1: Unsteady experiments main parameters

Run	Phase	Phase duration (s)	$Q_{s,in}$(m³/s)	Q_{water}(l/s)	Opening Height (cm)	Vibration Levels (V.L)	S_0 (%)	H (m)	U (m/s)	Fr	Lr
UnAE01	Phase 1	0-238	1.30 E-04	4	2	7.8	1.37	0.0231	0.576	1.21	1.03
	Phase 2	238-418	2.11 E-04	5	2	8.4	1.65	0.0251	0.663	1.33	1.14
	Phase 3	418-660	2.62 E-04	4	2	8.9	1.98	0.0206	0.647	1.44	1.28
UnAE02	Phase 1	0-241	1.33 E-04	4	2	7.8	1.37	0.0231	0.576	1.21	1.25
	Phase 2	241-421	1.96 E-04	5	2	8.45	1.66	0.0251	0.664	1.39	1.25
	Phase 3	421-681	2.27 E-04	4	2	8.9	1.99	0.0206	0.648	1.44	1.24
UnAE03	Phase 1	0-240	1.06 E-04	4	2	7.8	1.37	0.0231	0.576	1.21	1.00

Run	Phase	Phase duration (s)	$Q_{s,in}$(m³/s)	Q_{water}(l/s)	Opening Height (cm)	Vibration Levels (V.L)	S_0 (%)	H (m)	U (m/s)	Fr	Lr
	Phase 2	240-420	1.85 E-04	5	2	8.3	1.35	0.0268	0.622	1.22	1.06
	Phase 3	420-663	2.11 E-04	4	2	8.5	1.51	0.0224	0.594	1.27	1.44
UnAE04	Phase 1	0-238	1.45 E-04	4	2	8.1	1.37	0.0231	0.576	1.21	1.09
	Phase 2	238-418	2.06 E-04	5	2	8.45	1.56	0.0256	0.651	1.30	1.13
	Phase 3	418-659	2.25 E-04	4	2	8.7	1.67	0.0217	0.613	1.33	1.28
UnAE05	Phase 1	0-238	2.49 E-04	4	4	7.8	1.37	0.0231	0.576	1.21	2.13
	Phase 2	238-420	4.52 E-04	5	4	8.2	2.37	0.0224	0.744	1.59	1.30
	Phase 3	420-658	5.76 E-04	4	4	8.4	3.28	0.0176	0.758	1.82	1.14
UnAE06	Phase 1	0-239	2.81 E-04	5	3.5	7.8	1.37	0.0267	0.625	1.22	2.19
	Phase 2	239-420	4.40 E-04	6	3.5	8.35	2.26	0.0255	0.783	1.56	1.38
	Phase 3	420-665	4.25 E-04	5	3.5	8.35	2.74	0.0214	0.778	1.70	1.07
UnAE07	Phase 1	0-180	2.28 E-04	4	4	7.8	1.37	0.0231	0.576	1.21	2.26
	Phase 2	180-359	4.19 E-04	5	4	8.05	2.20	0.0229	0.726	1.53	1.29
	Phase 3	359-512	7.17 E-04	6	4	10	3.24	0.0228	0.878	1.85	1.14
	Phase 4	512-750	6.82 E-04	5	4	10	4.06	0.0189	0.881	2.04	1.06
	Phase 5	750-797	6.66 E-04	4	4	10	4.13	0.0164	0.815	2.03	0.90
UnAE08	Phase 1	0-179	1.64 E-04	4	4	7.6	1.37	0.0231	0.576	1.21	1.14
	Phase 2	179-361	2.61 E-04	5	4	7.8	1.56	0.0256	0.651	1.30	1.28
	Phase 3	361-542	6.88 E-04	6	4	10	2.30	0.0254	0.788	1.58	1.31
	Phase 4	542-722	6.77 E-04	5	4	10	3.90	0.0192	0.870	2.00	1.15

Run	Phase	Phase duration (s)	$Q_{s,in}$(m³/s)	Q_{water}(l/s)	Opening Height (cm)	Vibration Levels (V.L)	S_0 (%)	H (m)	U (m/s)	Fr	Lr
	Phase 5	722-838	6.92 E-04	4	4	10	4.60	0.0158	0.843	2.13	1.11
UnAE09	Phase 1	0-187	1.40 E-04	4	4	7.6	1.37	0.0231	0.576	1.21	1.27
	Phase 2	187-364	1.43 E-04	5	4	7.8	1.55	0.0256	0.650	1.30	1.04
UnAE10	Phase 1	0-265	1.95 E-04	5	4	7.8	1.37	0.0267	0.625	1.22	1.29
	Phase 2	265-425	5.57 E-04	6	4	8.6	2.04	0.0257	0.777	1.54	1.56
	Phase 3	425-657	5.78 E-04	5	4	8.6	3.46	0.0199	0.838	1.90	1.44

3.1.2. Mass Conservation Analysis

A mass conservation analysis was conducted for each experiment to assess the consistency of the sediment budget and the reliability of the measurements. After each experiment, all sediment retained within the channel and recovered from the downstream collectors and sediment screen was dried and weighed to determine the total recovered sediment mass M_{total}. This value was then compared with the total sediment mass introduced into the channel, as computed from the $Q_{s,in}$ values obtained through the application of the PIV algorithm, during the experiment, M_{inflow}. Since the experiments consisted of multiple phases with different water discharge and sediment feeding conditions, the sediment inflow mass was calculated separately for each phase. For phase i, the inflow sediment mass was computed as:

$$M_{inflow,i} = Q_{s,in,i} \cdot T_i \cdot \rho_s \qquad (3.4)$$

where $Q_{s,in,i}$ is the mean sediment inflow discharge during phase i, T_i is the phase duration, and ρ_s is the sediment density. The total sediment mass introduced into the channel was then obtained by summing the contributions of all phases:

$$M_{inflow} = \sum_{i=1}^{m} M_{inflow,i} \qquad (3.5)$$

where m is the number of phases in the experiment. Under ideal conditions, M_{inflow} and M_{total} should be equal. The relative mass conservation error was therefore defined as:

$$\varepsilon = \left| \frac{M_{inflow} - M_{total}}{M_{inflow}} \right| \times 100\% \qquad (3.6)$$

The mass conservation results for all experiments are summarized in *Table 3.2*. The relatively small discrepancies observed confirm the overall consistency of the sediment measurements and experimental procedures. Possible sources of error included minor sediment losses during collection and handling, uncertainties in the PIV-based estimation of sediment inflow discharge.

Table 3.2: Mass conservation results of unsteady campaign

Experiment	**Experiment Duration T (sec)**	**M_{inflow} (kg)**	**M_{total} (kg)**	**Absolute Relative Error (%)**
UnAE01	660.40	194.55	202.45	4.06
UnAE02	681.96	187.87	199.85	6.38
UnAE03	663.46	167.14	176.60	5.66
UnAE04	659.96	189.65	206.10	8.67
UnAE05	658.56	420.15	407.7	2.96
UnAE06	665.53	378.01	355.4	5.98
UnAE07	797.6	631.9	632.35	0.07
UnAE08	838.8	608.04	570.3	6.21
UnAE09	364.53	119.98	105.2	12.32
UnAE10	657.1	425.43	416.9	2.01

3.2. Experimental Results

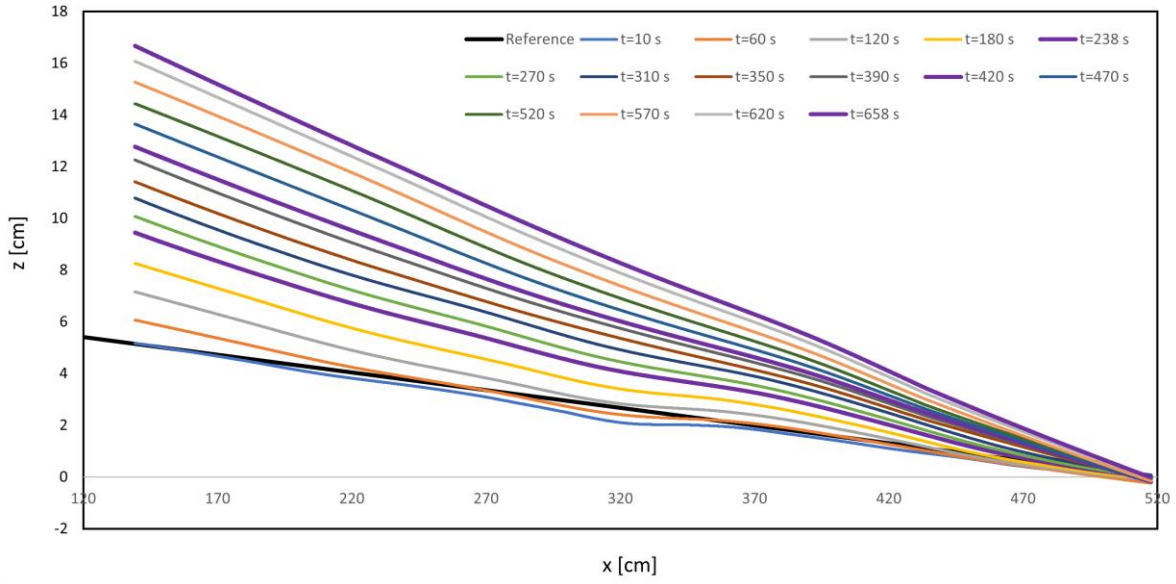
This section presents the raw experimental results obtained using the measurement techniques described in Chapter 2. The results are organized into two parts. Section 3.2.1 describes the spatial and temporal evolution of the bed and water surfaces elevations (along with the parameters derived from them, i.e., water depth, velocity, and Froude number), the corresponding color gradient maps, and the temporal evolution of the channel bed slope. Section 3.2.2 presents the initial sediment transport capacity estimates for all experimental phases.

3.2.1. Bed elevation, Water Surface elevation and Slope Evolution

Spatial and temporal evolution profiles of the bed and water surface elevations were obtained for all ten experiments using the methodology described in Chapter 2. The spatial profiles shows the distribution of bed and water surface elevations along the channel at selected times, while the temporal profiles depicts their evolution over time at fixed cross-sections located at distances of 170, 200, 235, 300, 365, and 430 cm from the channel inlet. The zero time in all graphs corresponded to the moment when the sediment feeding system was activated.

As representative examples, the results from experiments UnAE05 and UnAE07 are presented in this section (*Figure 3.3* to *Figure 3.6*). UnAE05 is selected as a representative three-phase experiment with relatively high loading ratios (L_r ranging from 1.14 to 2.13), while UnAE07 is chosen to illustrate the morphodynamic response under a more complex five-phase hydrograph (the corresponding control parameters are reported in *Table 3.1*). The results for the remaining experiments are provided in the Appendix.

(a)



(b)

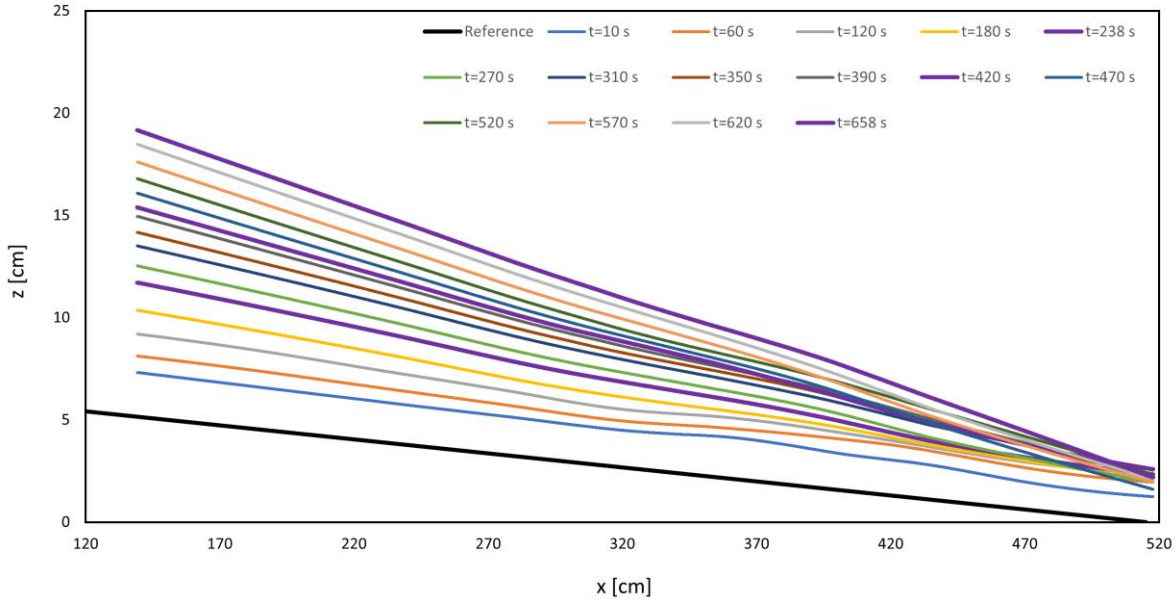
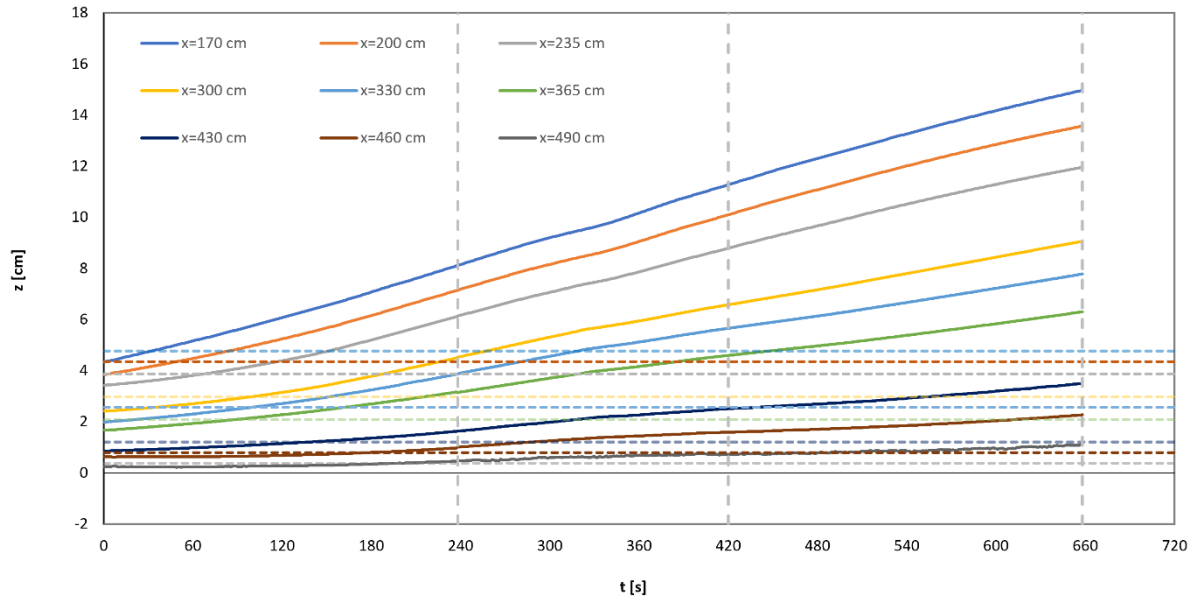


Figure 3.3: Spatial profiles of (a) bed elevation and (b) water elevation at selected times during experiment UnAE05. The black line indicates the initial bed profile. Bold lines correspond to the onset times of the second and third phases (t = 238 s and t = 420 s, respectively).

(a)



(b)

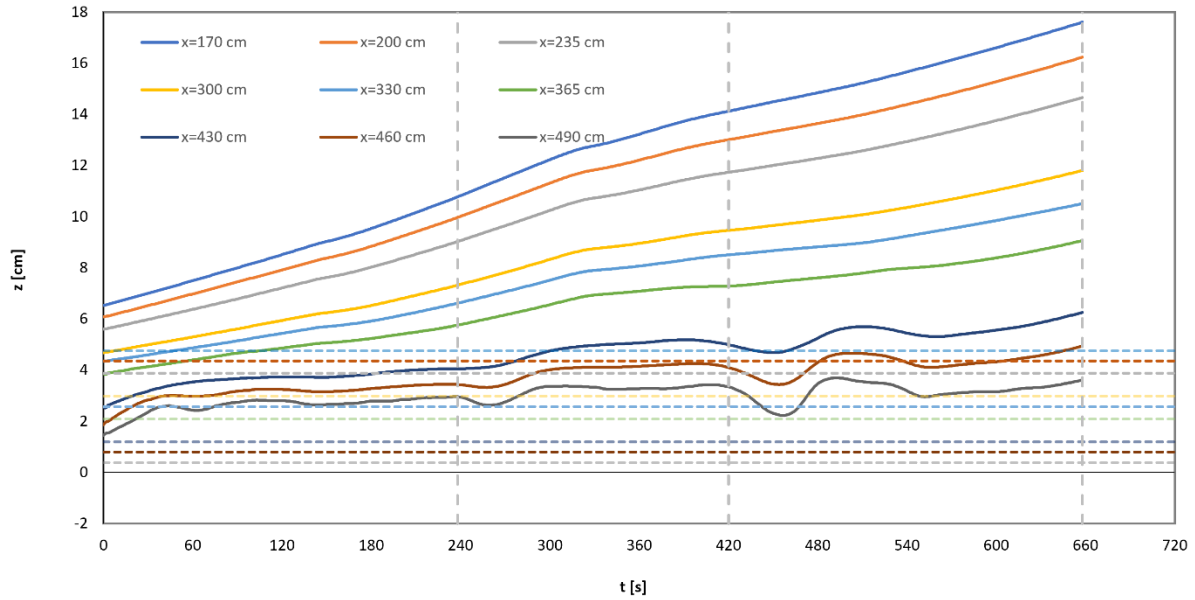
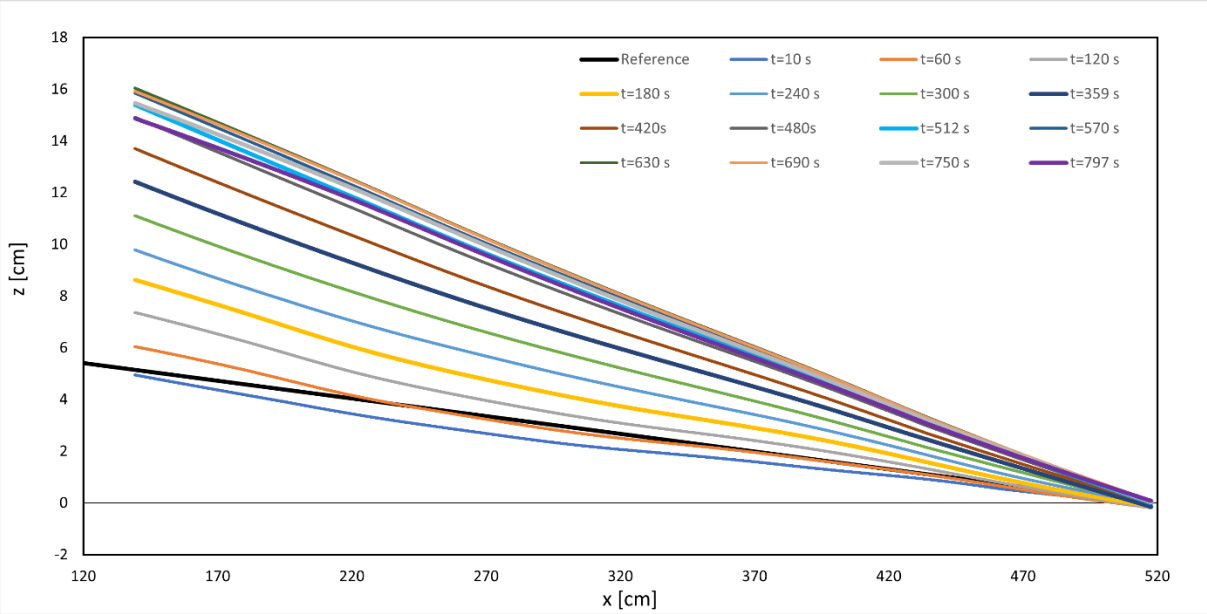


Figure 3.4: Temporal profiles of (a) bed elevation (b) water elevation at the selected locations along the channel during experiment UnAE05. The horizontal dash lines, matching the colors of the evolution curves, indicate the initial reference bed position at the corresponding locations.

(a)



(b)

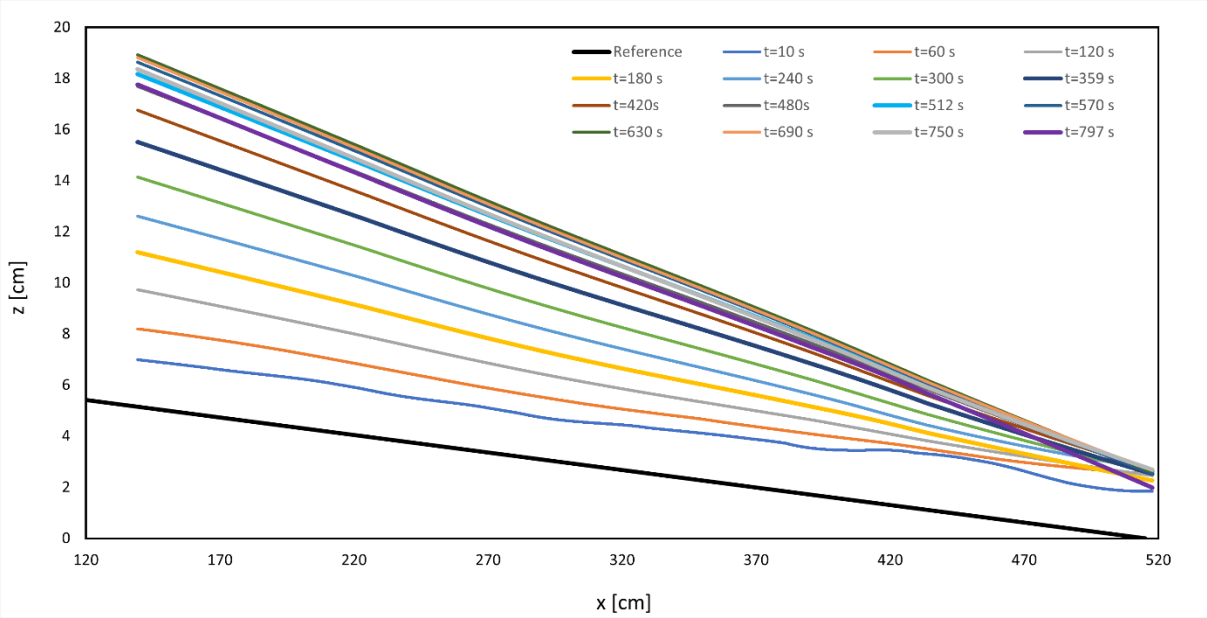
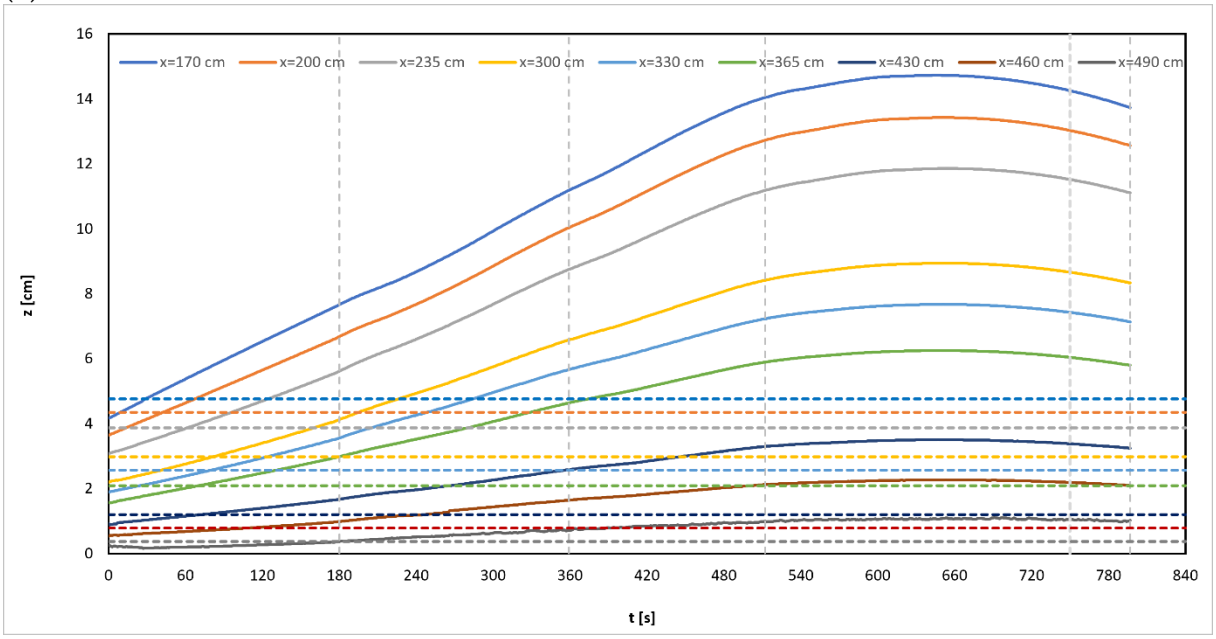


Figure 3.5: Spatial profiles of (a) bed elevation and (b) water elevation at selected times during experiment UnAE07. The black line indicates the reference bed profile. Bold lines correspond to the onset times of the second, third, fourth, and fifth phases (t = 180 s, 359 s, 512 s, and 750 s, respectively).

(a)



(b)

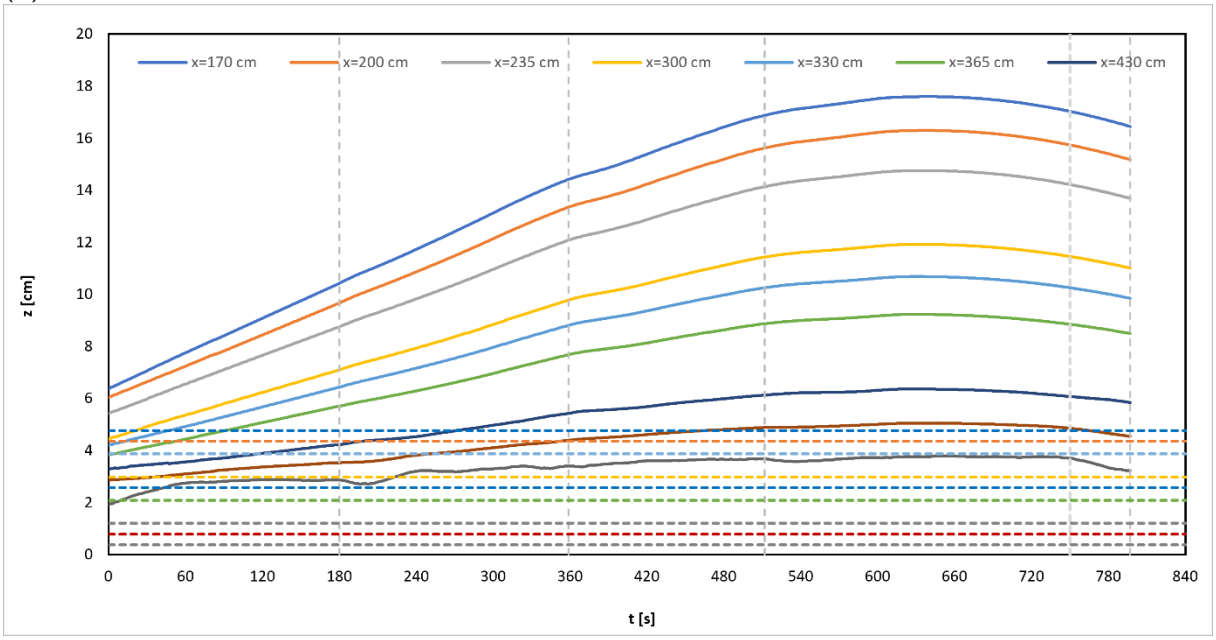


Figure 3.6: Temporal profiles of (a) bed elevation (b) water elevation at the selected locations along the channel during experiment UnAE07. The horizontal dash lines, matching the colors of the evolution curves, indicate the initial reference bed position at the corresponding locations.

The bed profiles showed that, in the early stages of each experiment, a slight scour was observed relative to the reference bed elevation. This initial degradation occurred before the activation of the sediment feeder, as water was introduced into the flume prior to the onset of sediment supply. Once sediment feeding commenced, the

imposed overloading conditions ($L_r > 1$) promoted progressive aggradation throughout the channel. Bed elevation increased continuously over time, with deposition occurring more rapidly in the upstream reach than in the downstream portion of the flume. Consequently, the bed slope increased progressively as the experiments evolved.

Unlike the steady-flow experiments, where the channel was allowed sufficient time to approach a morphological equilibrium condition, the unsteady experiments consisted of a sequence of prescribed phases characterized by abrupt changes in water discharge and sediment feeding rate. Each phase was terminated after a predefined duration, before equilibrium could be reached, and was immediately followed by new hydraulic and sediment supply conditions. As a result, every phase transition effectively reset the boundary conditions and initiated a new morphodynamic adjustment process on a bed that had already been modified by the preceding phase. The water surface profiles continuously adjusted to the evolving bed topography, reflecting the strong coupling between hydraulic and morphodynamic processes throughout the experiments.

Each phase was intentionally kept relatively short, this self-regulating adjustment process was interrupted before equilibrium conditions could be established. Consequently, the channel remained in a transient morphodynamic state throughout the entire experimental campaign.

A particularly noteworthy observation emerged from experiment UnAE07, where degradation occurred during the final phase despite the imposed sediment feeding conditions being expected to promote aggradation. This apparent discrepancy can be attributed to the substantial increase in bed slope generated during the preceding phases. As the channel bed progressively steepened, its sediment transport capacity increased accordingly. By the beginning of the final phase, the transport capacity had become sufficiently large to exceed the imposed sediment supply rate, resulting in a loading ratio of 0.90 — below unity — and consequently a net export of sediment from the channel and bed degradation. $L_r = Q_{sin}/Q_{s0}$, and $Q_{s0}$is a function of the bed slope at the end of the previous phase, which corresponds to the start of the new phase. Therefore, the role of bed slope is already accounted for within L_r.

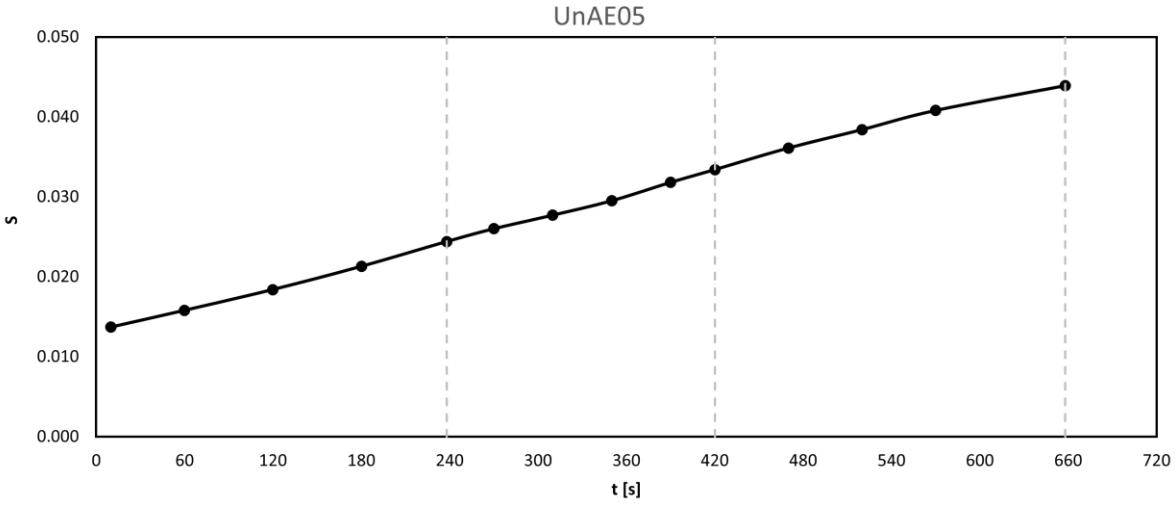
Bed Slope

The temporal evolution of the channel bed slope during experiments UnAE05 and UnAE07 is presented in *Figure 3.7*. At each time point, the bed slope was estimated from the detected bed profile by applying a linear regression over the monitored channel reach. The resulting time series provide insight into the progressive

morphological adjustment of the channel under unsteady boundary conditions. The vertical dashed lines indicate the phase transition times.

The slope generally increased throughout both experiments, reflecting the continuous morphological adjustment of the channel under sediment overloading conditions. In experiment UnAE07, however, a distinct change in trend was observed during the final phase, where the slope in the phase 4 was apparently stabilized and then in the phase 5 started to decrease slightly, indicating a shift from the aggradational behavior that characterized the earlier phases.

(a)



(b)

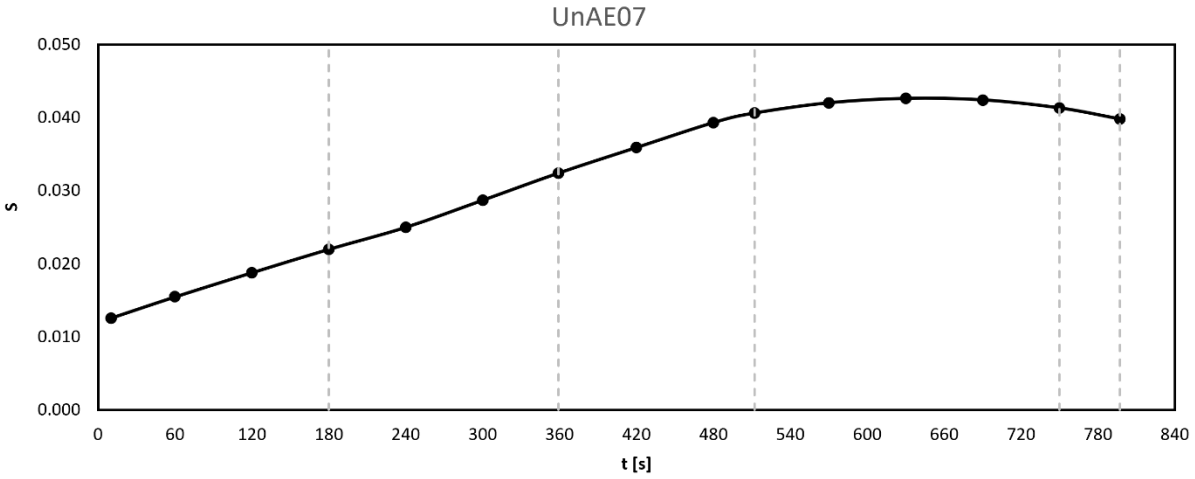


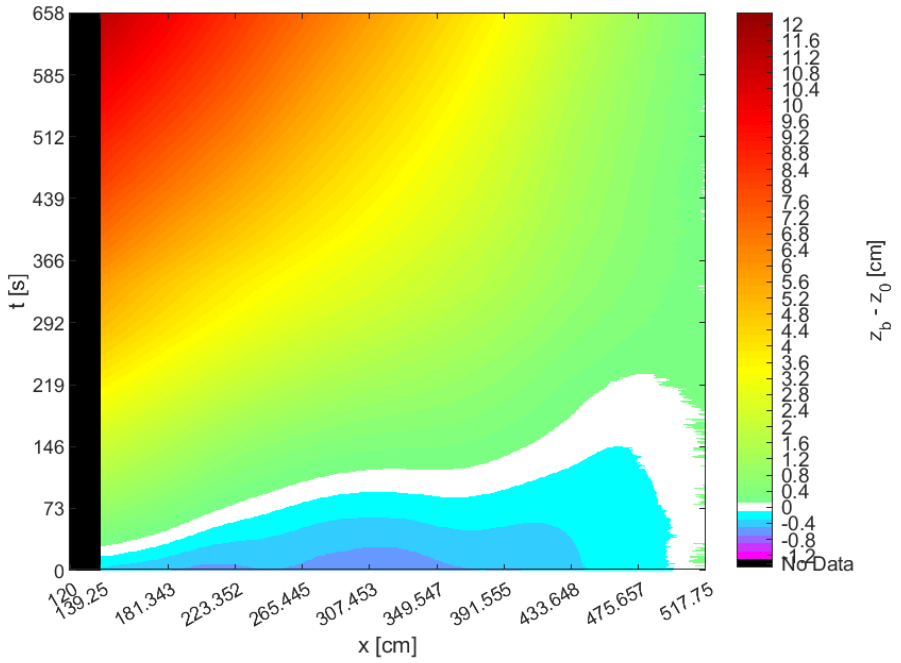
Figure 3.7: Temporal evolution of bed slope (a) UnAE05 & (b) UnAE07

Color Gradient Maps

To enable a simultaneous perception of the spatial and temporal evolution of bed and water surface elevations, a matrix was constructed for each experiment, incorporating

the acquired surface elevation data. Each element of the matrix represented the elevation of the bed or water surface at a specific time and location. The rows corresponded to different time steps — recorded at one-second intervals — while the columns represented spatial locations along the channel. These matrices were visualized as color gradient maps. The color gradient maps for experiments UnAE05 and UnAE07 are presented in *Figure 3.8* and *Figure 3.9* respectively.

(a)



(b)

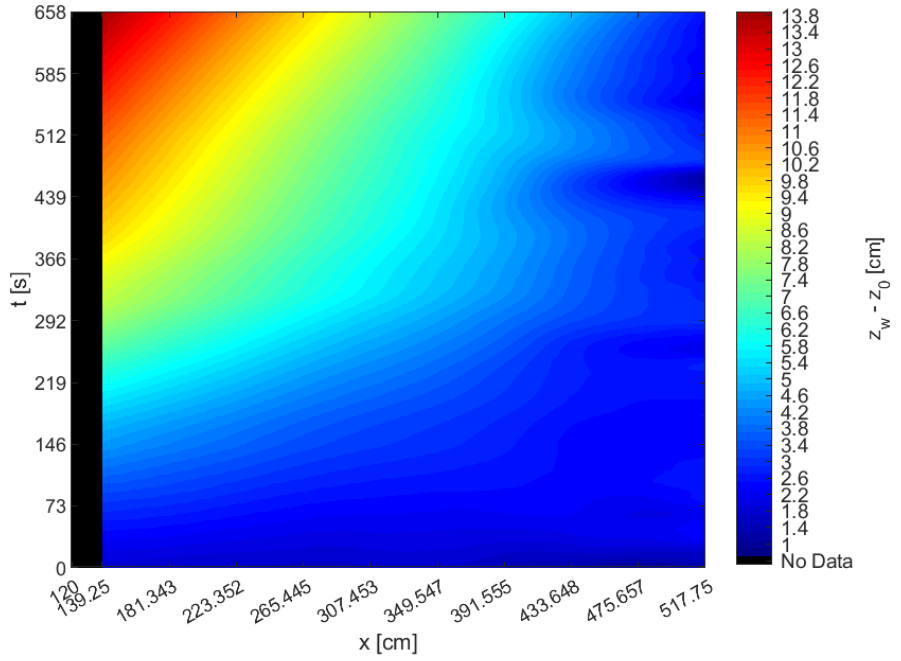
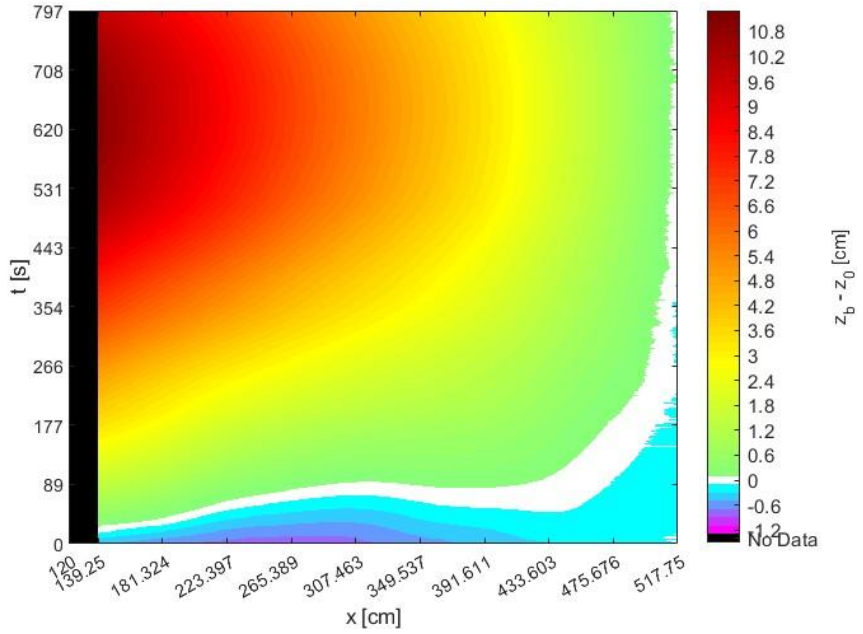


Figure 3.8: Color gradient maps of (a) bed elevation and (b) water elevation for experiment UnAE05

(a)



(b)

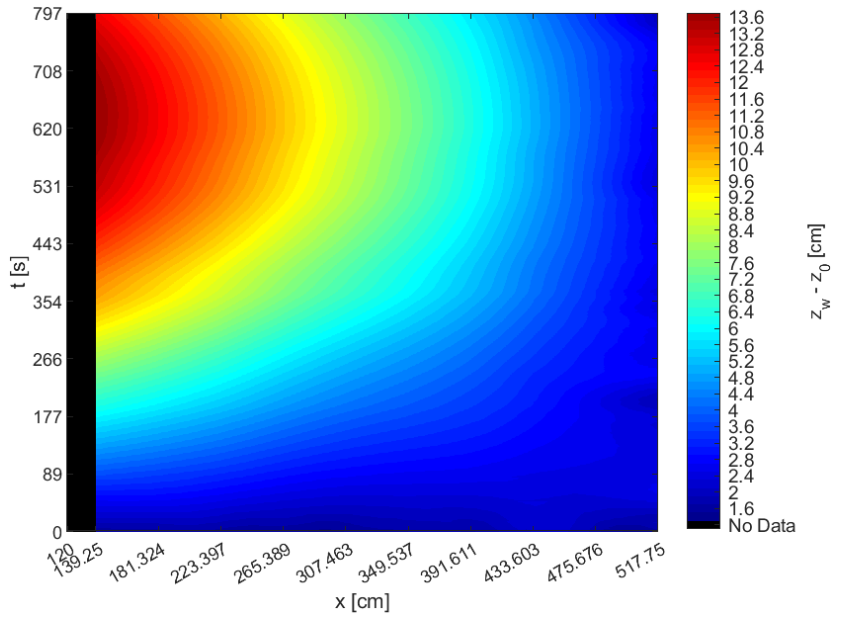


Figure 3.9: Color gradient maps of (a) bed elevation and (b) water elevation for experiment UnAE07

The experimental results demonstrated the significant influence of the loading ratio L_r on the hydro-morphological evolution of the channel. Phases with higher $L_r$values exhibited more pronounced sediment deposition and faster increases in bed slope compared to phases with lower L_r. This effect was particularly evident within experiment UnAE05, where Phase 1 — characterized by the highest loading ratio (L_r = 2.13) — produced the most rapid aggradation rate, while Phase 3, with the lowest

loading ratio (L_r=1.14) of the experiment, showed a comparatively slower rate of bed elevation increase.

In experiment UnAE07, the five-phase hydrograph provided a wider range of loading conditions, allowing a clearer observation of the role of L_r in controlling the morphodynamic response. The progressive increase in discharge across the first three phases was accompanied by a corresponding rise in sediment transport capacity, which — combined with the elevated feeding rates — produced increasingly steep bed slopes. As mentioned before, during the final phase, where L_r dropped below unity ($L_r = 0.90$), the channel transitioned from aggradation to degradation, further confirming that the loading ratio is the primary parameter governing the direction and magnitude of the morphological response.

Spatial and temporal evolution of water depth, water velocity, and Froude number

By subtracting the bed elevation from the water surface elevation, the water depth (H) was obtained at each spatial location and time point. The flow velocity (U) was then calculated using the actual flume discharge $Q_{flume}(t)$ as described in Chapter 2:

$$U = \frac{Q_{flume}}{BH} \qquad (3.7)$$

where B = 0.30 m was the channel width. Since the experiments were conducted under unsteady flow conditions, the time-varying $Q_{flume}(t)$ was used rather than a fixed nominal discharge value — a distinction that became especially relevant during phase transitions, when the discharge had not yet fully stabilized at its new target.

Once the spatial and temporal evolution of H and U were established, the Froude number was computed at each point in the space-time domain as:

$$Fr = \frac{U}{\sqrt{gH}} \qquad (3.8)$$

The resulting fields of water depth, water velocity, and Froude number were visualized as color gradient maps, providing a complementary view of the hydraulic evolution alongside the morphologic evolutions already presented in the section. The color gradient maps of the mentioned parameters for experiments UnAE05 and UnAE07 are shown in *Figure 3.10* and *Figure 3.11* respectively.

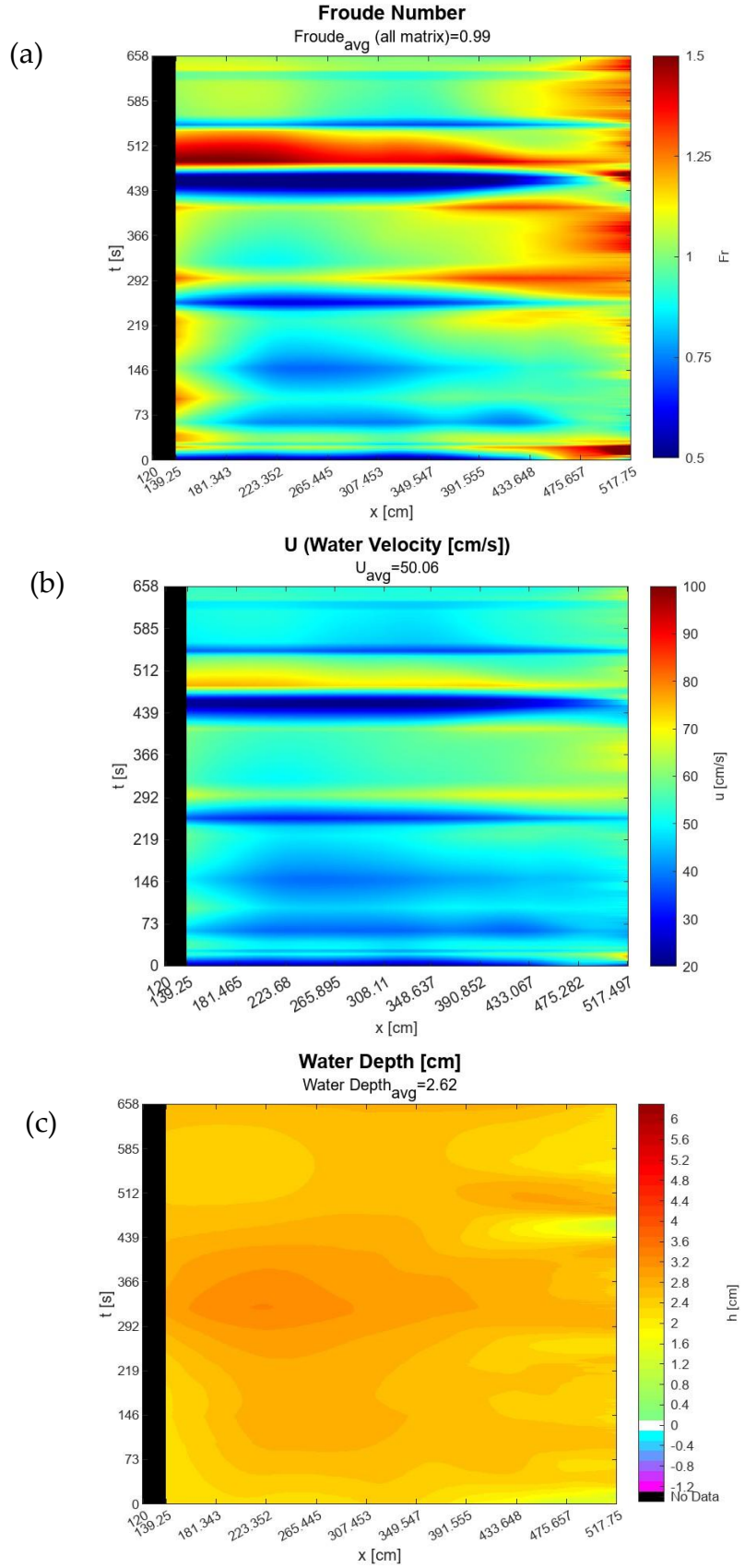


Figure 3.10: Color gradient maps of (a) Froude number, (b) water velocity and (c) water depth for experiment UnAE05

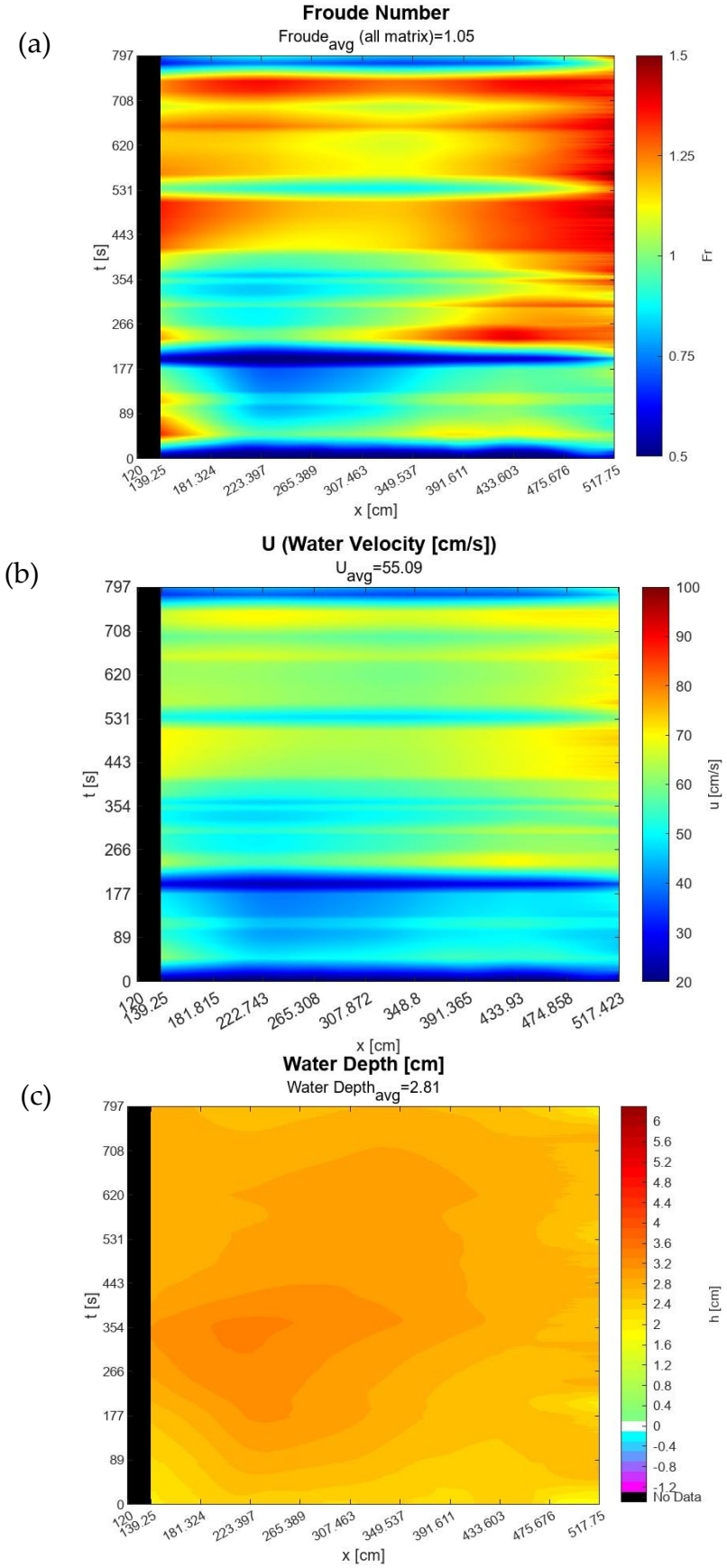


Figure 3.11: Color gradient maps of (a) Froude number, (b) water velocity and (c) water depth for experiment UnAE07

As expected, the water depth, velocity, and Froude number varied continuously in both space and time throughout each experiment, reflecting the unsteady nature of the hydro-morphlogical evolution of bed and water surface elevations. These parameters were strongly interconnected through the continuity equation and the Froude number relationship. Consequently, both hydraulic and morphological adjustments contributed to the observed spatial and temporal variability.

The loading ratio also influenced the hydraulic evolution during the experiments. Phases characterized by higher L_r values generally exhibited more rapid aggradation, promoting steeper bed profiles and affecting the evolution of water depth, flow velocity, and Froude number. In contrast, phases with lower L_r values were associated with a slower morphological adjustment and more gradual hydraulic changes.

As observed in the color-gradient maps, distinct shifts in velocity and Froude number occurred at the beginning of each phase. These shifts did not always follow the prescribed changes in water discharge. For example, despite the increase in discharge from Phase 1 to Phase 2 in Figure 3.11, both velocity and Froude number decreased. This behavior suggests that the observed variations were more closely related to the actual discharge entering the channel than to the prescribed hydrograph. During phase transitions, the increase in sediment feeding rate promoted deposition near the channel inlet, partially obstructing the inflow and reducing the effective discharge entering the channel. Consequently, lower velocity and Froude number values were observed despite the increase in the prescribed discharge. These abrupt adjustments were then followed by a more gradual evolution as the channel progressively adapted to the new hydraulic and sediment-supply conditions. For phases corresponding to the falling limb of the hydrograph, the observed reductions in velocity and Froude number may also be partly associated with the prescribed decrease in water discharge. However, this effect should be considered together with the influence of sediment deposition near the channel inlet.

In most experiments, the measured Froude number during the runs was lower than the initially set values of Fr reported in Table 3.1, and in some cases dropped below unity. This behavior is consistent with observations from the steady-flow campaign and reflects the influence of sediment transport on flow resistance as discussed by Eslami (2025). The presence of a moving bedload layer likely increased the effective roughness of the channel, reducing flow velocity and consequently lowering the Froude number relative to the initial clear-water conditions.

3.2.2. Initial sediment transport capacity

The initial sediment transport capacity Q_{s0} for each experimental phase was estimated using the continuity method described in Chapter 2. For each phase, six estimates were obtained by combining two scenarios for the unmonitored upstream reach — Constant

Upstream (CU) and Inclined Upstream (IU) — with three slope evolution thresholds of 5%, 10%, and 15%, referred to as CU1, CU2, CU3, IU1, IU2, and IU3 respectively.

Q_{s0} values in different scenarios for all experimental phases, along with their comparison across methods, are presented in *Table 3.3* and *Figure 3.12*.

Table 3.3: Initial sediment transport capacity of the channel determined using different methods.

Run	*Qi (m³/s)*	*S0 (%)*	Continuity method, CU (m³/s)			Continuity method, IU (m³/s)			Qs0,SC (m³/s)
			CU1 (5%)	CU2 (10%)	CU3 (15%)	IU1 (5%)	IU2 (10%)	IU3 (15%)	
UnAE1									
P1	0.004	1.37	1.29E-04	1.27E-04	—	1.29E-04	1.26E-04	—	1.09E-04
P2	0.005	1.65	1.93E-04	1.88E-04	1.86E-04	1.91E-04	1.86E-04	1.84E-04	—
P3	0.004	1.98	2.15E-04	2.09E-04	2.00E-04	2.11E-04	2.06E-04	1.97E-04	—
UnAE2									
P1	0.004	1.37	1.12E-04	1.11E-04	1.12E-04	1.12E-04	1.11E-04	1.11E-04	1.09E-04
P2	0.005	1.66	1.65E-04	1.58E-04	1.57E-04	1.63E-04	1.55E-04	1.54E-04	—
P3	0.004	1.99	1.92E-04	1.83E-04	1.80E-04	1.90E-04	1.81E-04	1.77E-04	—
UnAE3									
P1	0.004	1.37	1.07E-04	1.07E-04	1.07E-04	1.07E-04	1.07E-04	1.07E-04	1.09E-04
P2	0.005	1.35	1.76E-04	1.70E-04	—	1.75E-04	1.69E-04	—	—
P3	0.004	1.51	1.51E-04	1.40E-04	1.31E-04	1.44E-04	1.32E-04	1.25E-04	—
UnAE4									
P1	0.004	1.37	1.33E-04	1.31E-04	—	1.33E-04	1.31E-04	—	1.09E-04
P2	0.005	2.37	1.82E-04	—	—	1.82E-04	—	—	—
P3	0.004	3.28	1.78E-04	1.60E-04	1.46E-04	1.75E-04	1.55E-04	1.42E-04	—
UnAE5									

Run	*Qi (m³/s)*	*S0 (%)*	Continuity method, CU (m³/s)			Continuity method, IU (m³/s)			Qs0,SC (m³/s)
			CU1 (5%)	CU2 (10%)	CU3 (15%)	IU1 (5%)	IU2 (10%)	IU3 (15%)	
P1	0.004	1.37	1.20E-04	1.48E-04	1.49E-04	1.14E-04	1.43E-04	1.43E-04	1.09E-04
P2	0.005	2.37	3.51E-04	3.40E-04	3.41E-04	3.48E-04	3.38E-04	3.39E-04	—
P3	0.004	3.28	5.07E-04	4.86E-04	4.80E-04	5.04E-04	4.84E-04	4.78E-04	—
UnAE6									
P1	0.005	1.37	1.33E-04	1.36E-04	1.40E-04	1.23E-04	1.27E-04	1.31E-04	1.25E-04
P2	0.006	2.26	3.22E-04	3.28E-04	3.51E-04	3.16E-04	3.22E-04	3.47E-04	—
P3	0.005	2.74	3.99E-04	3.83E-04	3.88E-04	3.96E-04	3.81E-04	3.87E-04	—
UnAE7									
P1	0.004	1.37	1.04E-04	1.12E-04	1.14E-04	9.82E-05	1.07E-04	1.09E-04	1.09E-04
P2	0.005	2.20	3.25E-04	3.21E-04	3.08E-04	3.24E-04	3.20E-04	3.06E-04	—
P3	0.006	3.24	6.28E-04	6.21E-04	6.08E-04	6.25E-04	6.18E-04	6.05E-04	—
P4	0.005	4.06	6.46E-04	—	—	6.45E-04	—	—	—
P5	0.004	4.13	7.38E-04	—	—	7.40E-04	—	—	—
UnAE8									
P1	0.004	1.37	1.37E-04	1.31E-04	1.29E-04	1.35E-04	1.29E-04	1.27E-04	1.09E-04
P2	0.005	1.56	2.04E-04	2.12E-04	2.11E-04	2.01E-04	2.10E-04	2.08E-04	—
P3	0.006	2.30	5.30E-04	5.44E-04	5.37E-04	5.25E-04	5.39E-04	5.32E-04	—
P4	0.005	3.90	5.88E-04	6.08E-04	6.02E-04	5.88E-04	6.08E-04	6.01E-04	—
P5	0.004	4.60	6.23E-04	—	—	6.21E-04	—	—	—
UnAE9									
P1	0.004	1.37	1.10E-04	1.05E-04	—	1.11E-04	1.06E-04	—	1.09E-04
P2	0.005	1.55	1.38E-04	—	—	1.38E-04	—	—	—

Run	Qi (m³/s)	S0 (%)	Continuity method, CU (m³/s)			Continuity method, IU (m³/s)			Qs0,SC (m³/s)
			CU1 (5%)	CU2 (10%)	CU3 (15%)	IU1 (5%)	IU2 (10%)	IU3 (15%)	
UnAE10									
P1	0.005	1.37	1.53E-04	1.48E-04	1.43E-04	1.53E-04	1.48E-04	1.42E-04	1.25E-04
P2	0.006	2.21	3.66E-04	3.81E-04	3.74E-04	3.60E-04	3.75E-04	3.68E-04	—
P3	0.005	3.46	4.03E-04	4.08E-04	4.35E-04	3.99E-04	4.04E-04	4.32E-04	—

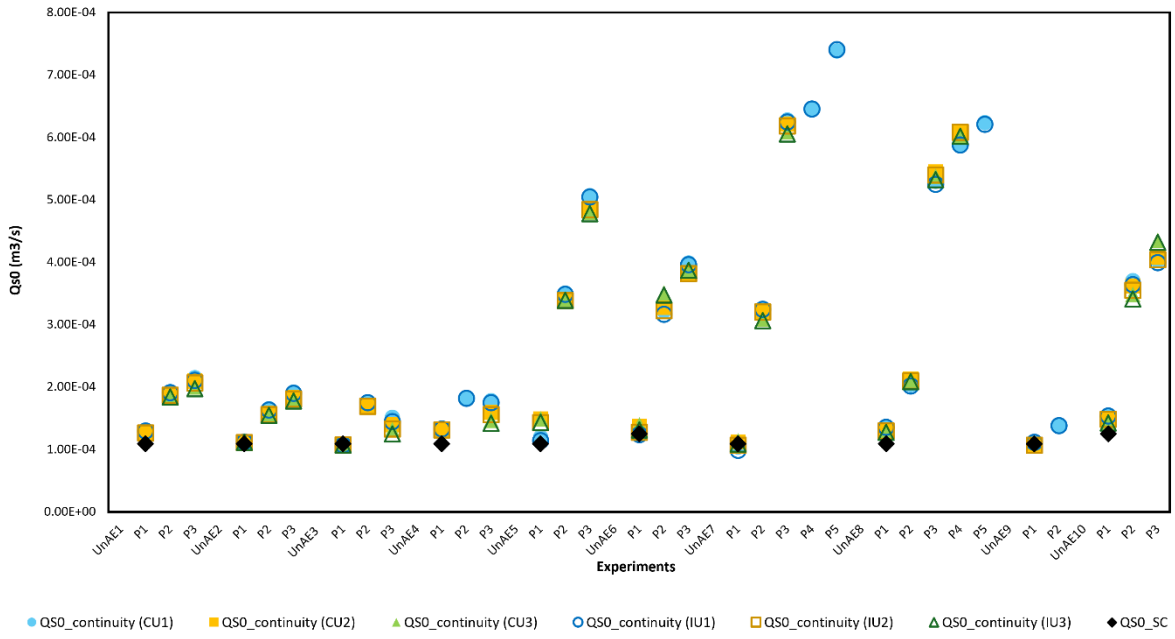


Figure 3.12: Comparison of the results from different methods used to estimate Q_{s0}.

To obtain a representative value for Q_{s0} in each phase of experiments, the results from various continuity methods were averaged. Two scenarios were considered for averaging purposes:

First, the CU1 and IU1 estimates corresponding to the same threshold level were averaged:

$$Q_{s0,continuity_average_IU1,CU1} = \frac{Q_{s0,CU1} + Q_{s0,IU1}}{2} \qquad (3.9)$$

A second averaging step was then applied to combine the estimates corresponding to the three threshold levels (5%, 10%, and 15%), yielding a single representative value of Q_{s0} for each experimental phase:

$$Q_{s0,average} = \frac{Q_{s0,IU1,CU1} + Q_{s0,IU2,CU2} + Q_{s0,IU3,CU3}}{3} \qquad (3.10)$$

As shown in *Table 3.4*, the two averaging approaches yielded comparable Q_{s0} estimates across most experimental phases. *Figure 3.13* presents a direct comparison between the two approaches for all experimental phases.

Table 3.4: Comparison between $Q_{s0,continuity_average}$ and $Q_{s0,continuity_average,CU1,IU1}$

Run	Q (m³/s)	Qs0,continuity_average (m³/s)	Qs0,continuity_average_CU1,IU1 (m³/s)
UnAE1			
P1	0.004	1.28E-04	**1.29E-04**
P2	0.005	1.88E-04	**1.92E-04**
P3	0.004	2.06E-04	**2.13E-04**
UnAE2			
P1	0.004	1.11E-04	**1.12E-04**
P2	0.005	1.59E-04	**1.64E-04**
P3	0.004	1.84E-04	**1.91E-04**
UnAE3			
P1	0.004	1.07E-04	**1.07E-04**
P2	0.005	1.72E-04	**1.75E-04**
P3	0.004	1.37E-04	**1.48E-04**
UnAE4			
P1	0.004	1.32E-04	**1.33E-04**
P2	0.005	1.82E-04	**1.82E-04**
P3	0.004	1.59E-04	**1.76E-04**
UnAE5			
P1	0.004	1.36E-04	**1.17E-04**
P2	0.005	3.43E-04	**3.49E-04**
P3	0.004	4.90E-04	**5.05E-04**

Run	Q (m^3/s)	$Qs0,continuity_average$ (m^3/s)	$Qs0,continuity_average_CU1,IU1$ (m^3/s)
UnAE6			
P1	0.005	1.32E-04	**1.28E-04**
P2	0.006	3.31E-04	**3.19E-04**
P3	0.005	3.89E-04	**3.97E-04**
UnAE7			
P1	0.004	1.07E-04	**1.01E-04**
P2	0.005	3.18E-04	**3.25E-04**
P3	0.006	6.18E-04	**6.26E-04**
P4	0.005	6.45E-04	**6.45E-04**
P5	0.004	7.39E-04	**7.39E-04**
UnAE8			
P1	0.004	1.32E-04	**1.36E-04**
P2	0.005	2.08E-04	**2.03E-04**
P3	0.006	5.35E-04	**5.27E-04**
P4	0.005	5.99E-04	**5.88E-04**
P5	0.004	6.22E-04	**6.22E-04**
UnAE9			
P1	0.004	1.08E-04	**1.10E-04**
P2	0.005	1.38E-04	**1.38E-04**
UnAE10			
P1	0.005	1.48E-04	**1.53E-04**
P2	0.006	3.57E-04	**3.67E-04**
P3	0.005	4.13E-04	**4.01E-04**

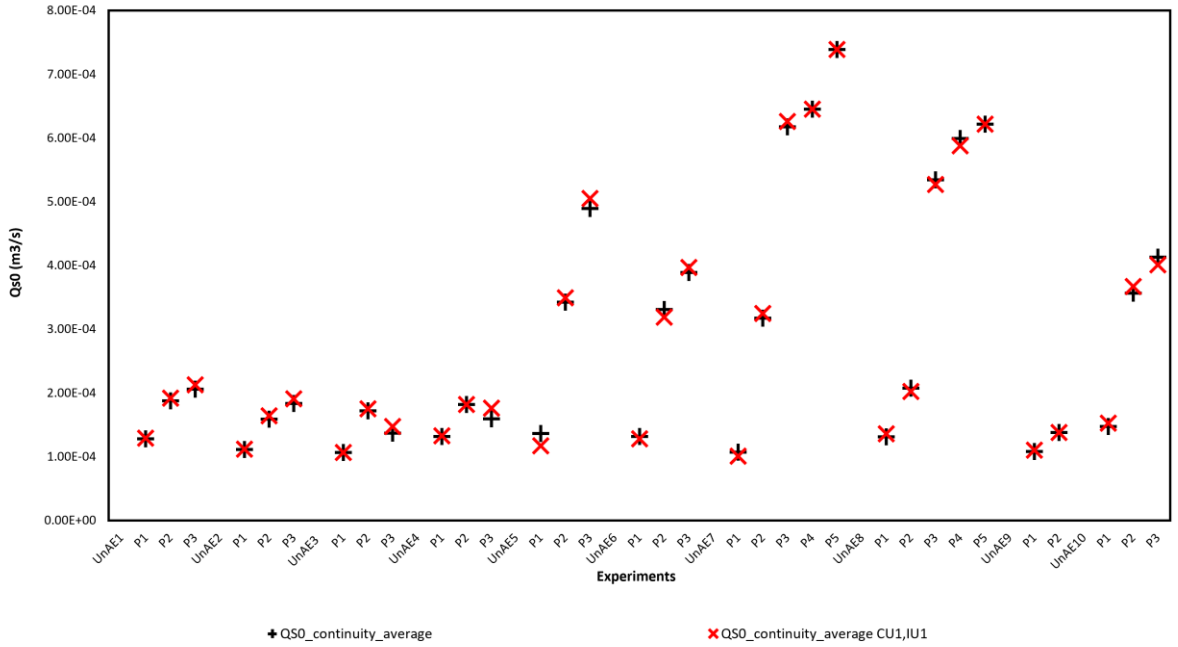


Figure 3.13: Comparison between $Q_{s0,continuity_average}$ *and* $Q_{s0,continuity_average,CU1,IU1}$

The final value adopted for Q_{s0} in each phase corresponds to the average of CU1 and IU1, as reported in Table 3.1. This choice was made because the present study seeks to estimate the initial sediment transport capacity of the channel, and the 5% threshold — corresponding to CU1 and IU1 — provides the closest approximation to this initial condition compared to the 10% and 15% thresholds, which reflect a more advanced stage of bed adjustment.

To validate the continuity method estimates, SC experiments were conducted independently for each water discharge value corresponding to the first phase of each experiment. The comparison between the SC results and the continuity method estimates for the first phase is shown in *Figure 3.14*, where most data points fall within the ±20% deviation band around the identity line, lending confidence to the estimates used throughout the remaining phases.

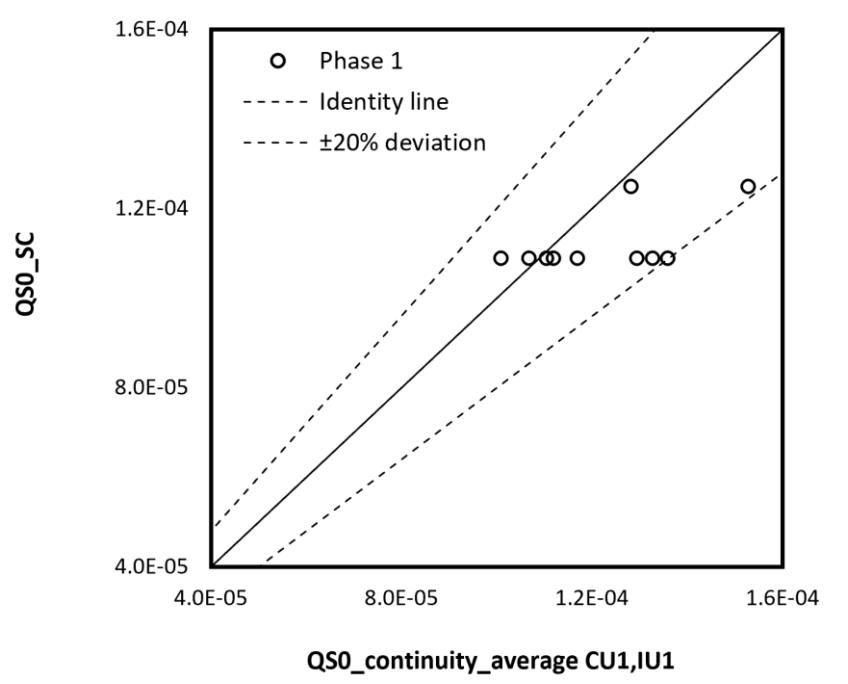


Figure 3.14: Comparison between SC test & continuity method.

A particularly notable observation can be made for experiment UnAE07, which featured one of the largest number of phases among all experiments in the unsteady campaign. As shown in *Table 3.3*, the Q_{s0} values estimated for phases P4 and P5, reaching 6.45×10^{-4} and 7.39×10^{-4} m³/s respectively, were the highest obtained during the entire experimental campaign. This progressive increase in transport capacity appears to be associated with the substantial bed aggradation accumulated during the preceding phases, which progressively modified the channel morphology and increased the bed slope. By phases P4 and P5, the estimated transport capacity approached or exceeded the maximum sediment supply that could be delivered by the feeder system. As a result, the sediment supply became insufficient to balance the transport capacity of the channel, which is consistent with the degradational tendency observed during these phases.

The estimated Q_{s0}values for all experimental phases were grouped according to the water discharge associated with each phase, resulting in three distinct categories: Q= 4 l/s, Q= 5 l/s, and Q= 6 l/s. This grouping allowed the relationship between water discharge and sediment transport capacity to be examined across the entire unsteady campaign.

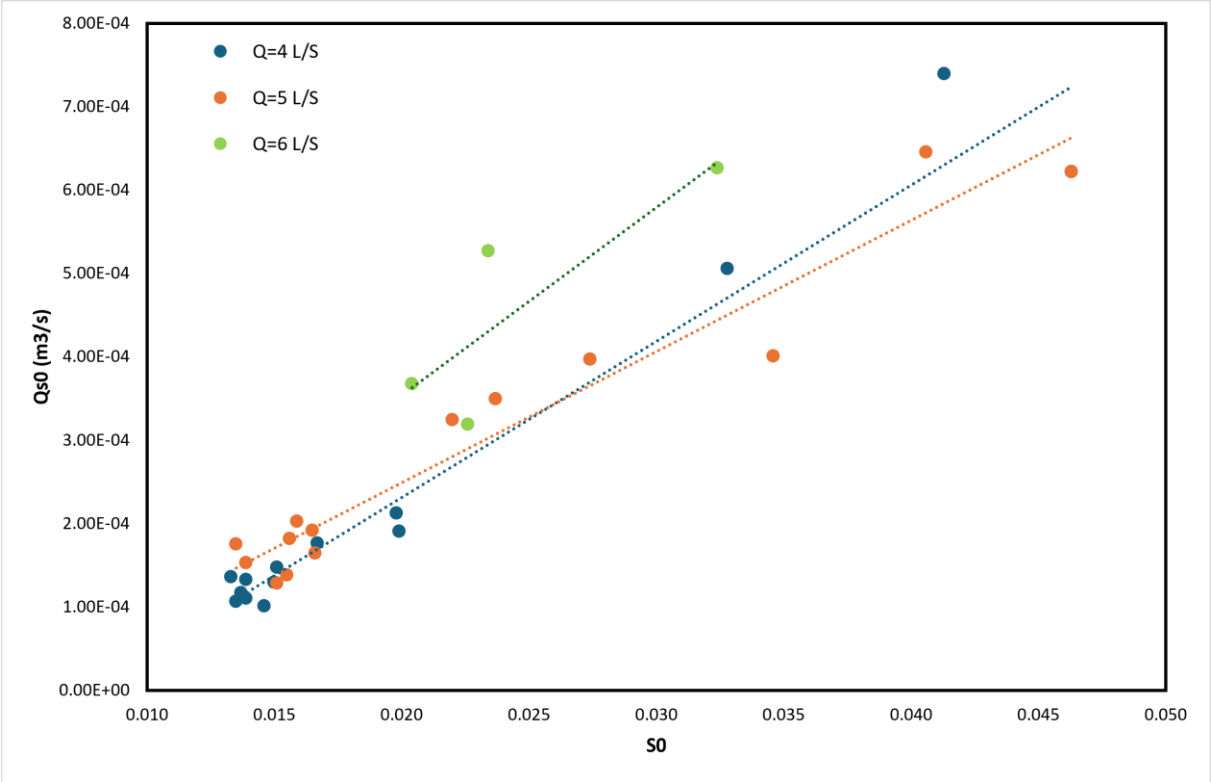


Figure 3.15: Q_{S0} as a function of bed slope S_0 (initial slope of each phase), grouped by water discharge

Figure 3.13 presents the estimated transport capacity discharge, Q_{S0}, as a function of the initial bed slope (S_0) for all phases of the experiments performed in the current campaign, grouped according to water discharge. A positive relationship between (Q_{S0}) and (S_0) is evident for all discharge classes, indicating that steeper bed slopes are associated with higher transport capacities. This behavior is consistent with the expected hydraulic response, as larger discharges increase the flow's ability to transport sediment. The results therefore indicate that the initial transport capacity of each phase is controlled by the combined effect of bed slope and water discharge, with both parameters contributing to the observed variability in Q_{S0}.

3.3. Aggradation Wave Celerity

The propagation of the aggradation wave is one of the central aspects of the present study. As the sediment supply exceeds the transport capacity of the flow, a depositional wave forms and advances downstream along the channel. Characterizing the celerity of this wave — that is, the speed at which it propagates — is essential for understanding the dynamics of the aggradation process and for assessing its potential hazard implications in real-world scenarios.

In the following sections, the concept of celerity is first defined and its dimensionless form introduced. The spatial and temporal evolution of celerity is then examined

across the experimental runs, followed by a bulk analysis relating the dimensionless celerity to key control parameters. Finally, the results are compared with those obtained from the steady-flow campaign.

3.3.1. Celerity Definition and Dimensionless form

When a channel is subjected to sediment overloading, morphological changes do not occur simultaneously throughout the entire reach. Instead, the effects of sediment deposition propagate progressively along the channel. The rate at which this propagation occurs is commonly described by the concept of celerity, which represents the speed at which a particular morphological state is transferred through the system relative to a stationary observer.

In the present study, celerity is associated with the propagation of bed elevation changes resulting from sediment aggradation. It therefore provides a quantitative measure of the rate at which bed elevation changes migrate through the channel.

Under subcritical flow conditions, sediment aggradation typically develops as a translating front that can be visually identified and tracked along the channel. In contrast, under supercritical and near-critical flow conditions, such as those imposed during the present experimental campaign, the aggradation front becomes increasingly dispersed and loses a clearly identifiable boundary. Consequently, direct tracking of a sediment front becomes difficult and alternative approaches are required for celerity estimation (*Figure 3.16*).

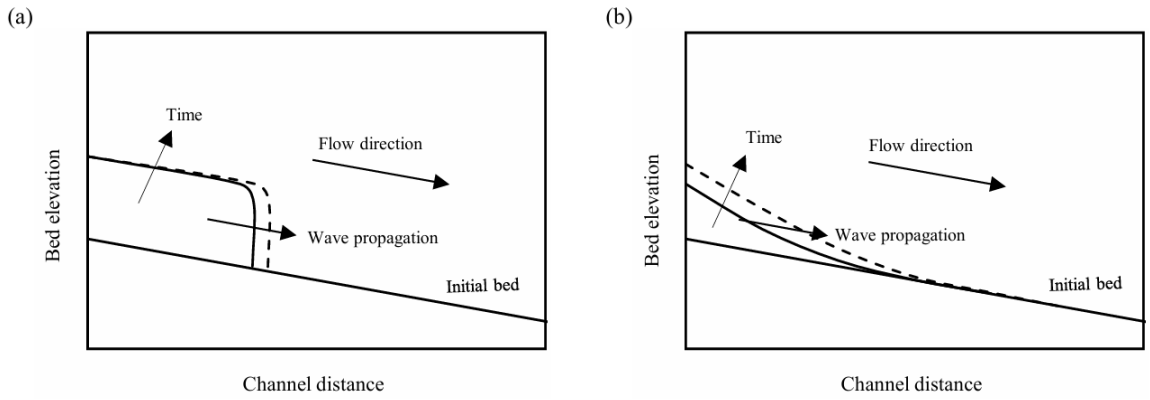


Figure 3.16: Different types of sediment front: (a) Translating; (b) Dispersive (Eslami, 2025)

To overcome this limitation, the present study adopts the kinematic approach previously applied by Tavakoli et al. (2022), Hiteh et al. (2023), Gamal et al. (2024), and Eslami (2025). The method is based on the propagation of a bed elevation contour within the space–time domain. Based on the definition given above, the celerity of propagation of $z_b(x,t)$can be determined by setting the total differential of bed elevation equal to zero over an infinitesimal time interval:

$$\frac{dz_b}{dt} = \frac{\partial z_b}{\partial t} + \frac{\partial z_b}{\partial x}\frac{dx}{dt} = 0 \qquad (3.11)$$

The celerity C is therefore defined as:

$$C = \frac{dx}{dt} = -\frac{\partial z_b / \partial t}{\partial z_b / \partial x} \qquad (3.12)$$

For application to the experimental data, Equation (3.12) was discretized using finite differences:

$$C = -\frac{\Delta z_b / \Delta t}{\Delta z_b / \Delta x} \qquad (3.13)$$

where $\frac{\Delta z_b}{\Delta t}$ represents the temporal rate of bed elevation change at a fixed location and $\frac{\Delta z_b}{\Delta x}$ represents the spatial bed elevation gradient at a fixed time.

The temporal gradient was computed as:

$$\frac{\Delta z_b}{\Delta t} = \frac{z_b(x_n, t_n + \Delta t) - z_b(x_n, t_n)}{\Delta t} \qquad (3.14)$$

while the spatial gradient was calculated as:

$$\frac{\Delta z_b}{\Delta x} = \frac{z_b(x_n + \Delta x, t_n) - z_b(x_n, t_n)}{\Delta x} \qquad (3.15)$$

where x_n and t_n represent the spatial and temporal coordinates, respectively.

The procedure is illustrated schematically in *Figure 3.17* and *Figure 3.18*, where the temporal and spatial bed elevation differences are extracted from the space–time matrix of detected bed elevations.

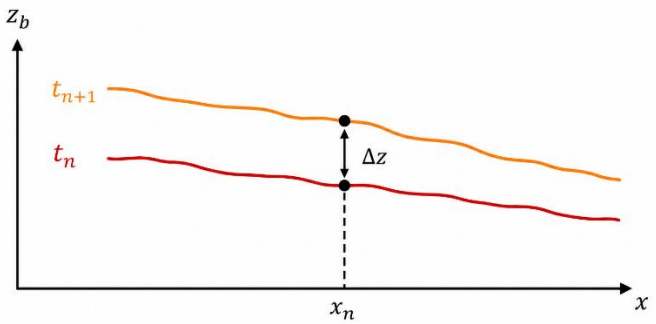


Figure 3.17: Elevation difference at constant location

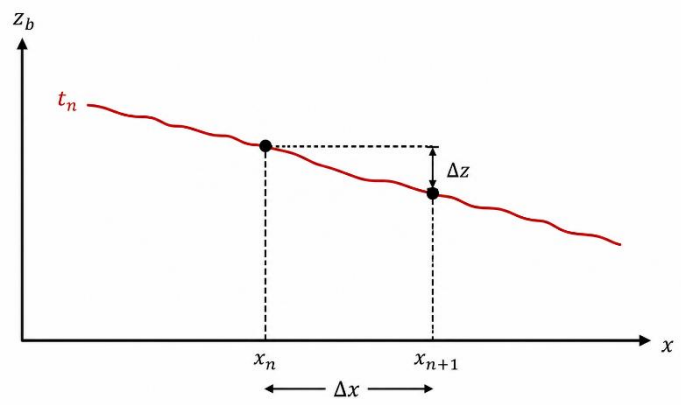


Figure 3.18: Elevation difference at constant time

The structure of the space–time matrix used for the calculations is shown in *Figure 3.19*. Because a forward finite-difference scheme was adopted, celerity values could not be computed for the final time row or the final spatial column.

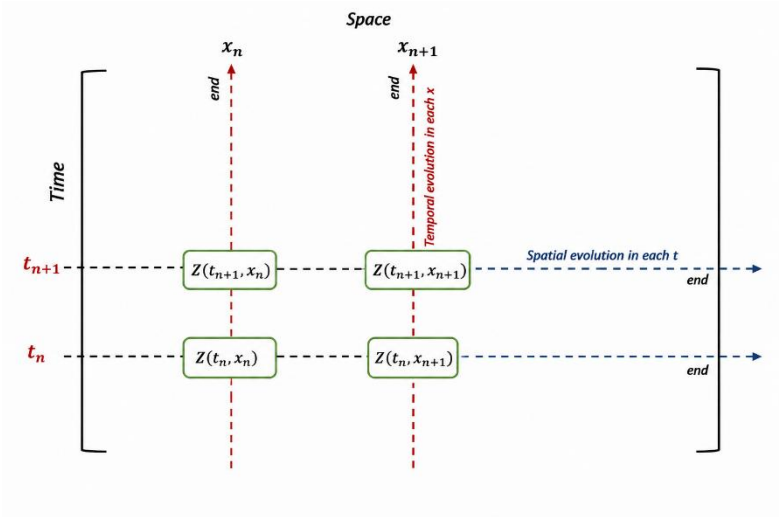


Figure 3.19: Schematic representation of the space–time bed elevation matrix

For all experiments, the temporal increment was fixed at $\Delta t = 1$s, corresponding to the temporal resolution of the bed-detection system. Following the methodology adopted by Tavakoli et. al., (2022), Hiteh et. al., (2023), Gamal et al. (2024) and Eslami (2025), the spatial increment was set to $\Delta x = 1.8$cm.

Preliminary analyses showed that smaller spatial increments produced unstable celerity estimates. When adjacent bed elevation values became nearly identical, the denominator $\frac{\Delta z_b}{\Delta x}$ approached zero, causing unrealistically large celerity values (*Figure 3.20*). In addition, local uncertainties associated with the bed-detection procedure became increasingly amplified at very small spatial scales. The selected value of $\Delta x = 1.8$cm therefore provided a compromise between spatial resolution and computational stability.

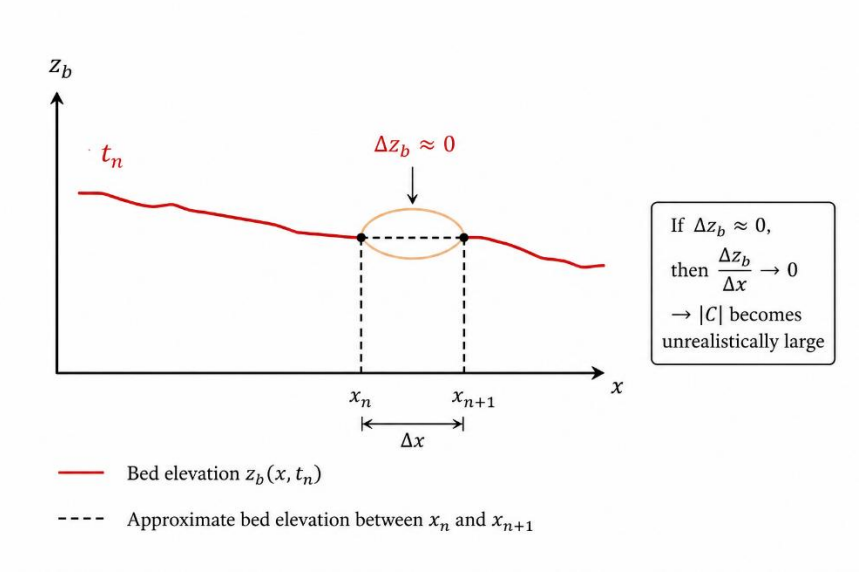


Figure 3.20: Influence of spatial increment on celerity estimation

To facilitate comparison between experiments conducted under different hydraulic conditions, a dimensionless celerity was also defined by normalizing the dimensional celerity with the local and instantaneous flow velocity:

$$C^* = \frac{C}{u} \qquad (3.16)$$

3.3.2. Spatial and Temporal Evolution of Celerity

The local and instantaneous celerity was computed throughout the space–time domain. The resulting fields of dimensional celerity (C) and dimensionless celerity (C^*) were visualised as colour gradient maps, following the same approach previously adopted for the analysis of bed elevation, water depth, and Froude number. Representative results for experiments UnAE05 and UnAE07 are presented in *Figure 3.21* and *Figure 3.22*, while the corresponding results for the remaining experiments are provided in the Appendix. As mentioned above, the local and instantaneous flow velocity was used as the normalization parameter to obtain the dimensionless celerity maps (Figures 3.10(b) and 3.11(b) for experiments UnAE05 and UnAE07, respectively). To refine the obtained maps, a smoothing process is applied: the space-time distribution of the celerity values is smoothed by replacing every 64 values (8×8 grid in space and time) with their average. *Figure 3.21* and *Figure 3.22* display the resulting smoothed maps of UnAE05 and UnAE07.

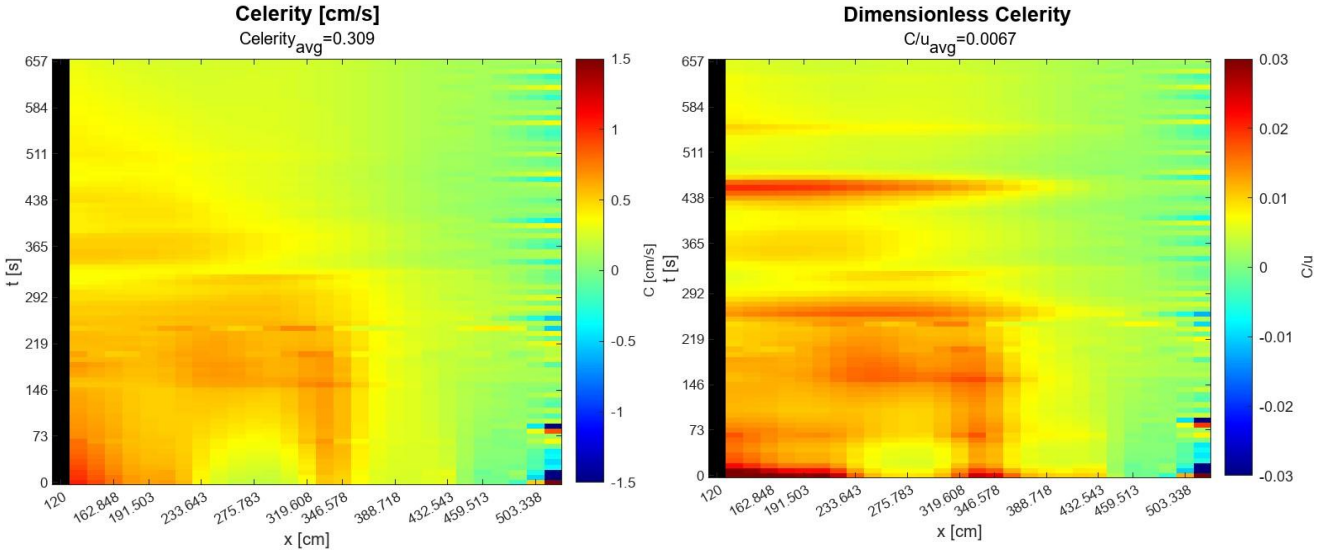


Figure 3.21: Color gradient maps of dimensional celerity C and dimensionless celerity C for experiment UnAE05*

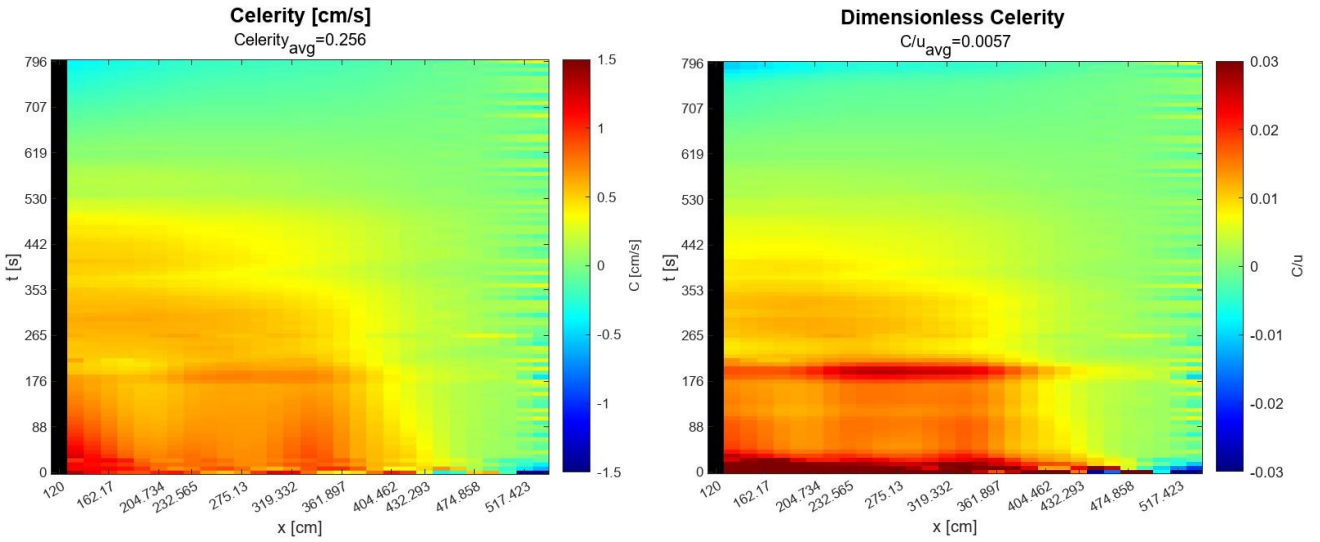


Figure 3.22: Color gradient maps of dimensional celerity C and dimensionless celerity C for experiment UnAE07*

Several common patterns can be identified from the celerity maps. During the initial stages of the experiments, the bedload layer was not yet fully developed, resulting in increased uncertainty in the bed-detection procedure. Since the detection method relies on the identification of a well-defined bedload layer, its incomplete formation at the beginning of the experiments may introduce errors in the detected bed position

(*Figure 3.23*) and, consequently, in the estimated celerity values. Therefore, celerity estimates obtained during the initial period should be interpreted with caution.

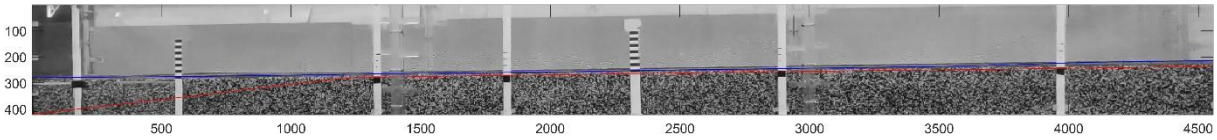


Figure 3.23: Example of bed and water surface detection uncertainty during the initial stage of UnAE05

In most phases of the experiments, celerity values were highest during the early stages of each phase and gradually decreased with time. This behavior is consistent with the rapid morphological adjustment that occurred immediately after the onset of sediment overloading. During the initial part of a phase, bed elevations changed relatively rapidly, producing larger values of $\frac{\Delta z_b}{\Delta t}$ and consequently higher celerity estimates. As the channel progressively adjusted to the imposed hydraulic and sediment supply conditions within each phase, the rate of bed elevation change generally decreased, and celerity values tended towards lower values. Equilibrium conditions were not reached because the hydraulic and sediment feeding conditions were intentionally modified before equilibrium could be established.

A clear spatial variation was also observed. In general, higher celerity values occurred in the upstream portion of the channel, whereas lower values were observed further downstream. This pattern is consistent with the bed evolution results presented previously, which showed that aggradation was generally more pronounced in the upstream reach and progressively decreased towards the downstream end of the flume. Consequently, larger temporal changes in bed elevation were typically observed upstream, resulting in higher celerity values.

Negative celerity values were occasionally detected, particularly near the downstream end of the channel. These values are likely associated with local uncertainties in the bed and water surface detection process, as well as with the sensitivity of Equation (3.13) to small values of $\frac{\Delta z_b}{\Delta x}$. When the spatial bed elevation gradient approached zero, relatively small measurement uncertainties could generate disproportionately large positive or negative celerity values.

A distinctive feature of the present unsteady campaign, not observed in the steady-flow experiments of Eslami (2025), is the response of celerity to the phase transitions. As shown in the color gradient maps, each transition in water and sediment discharge was associated with a distinct shift in celerity, reflecting the abrupt modification of the hydro-morphological conditions and the corresponding changes in the rate of morphological adjustment. These transitions were followed by a more gradual evolution of celerity within each phase as the channel progressively adapted to the new flow and sediment supply conditions.

The dimensionless celerity (C^*) exhibited spatial and temporal patterns similar to those observed for the dimensional celerity. However, the subsequent analyses were not performed directly on the dimensionless celerity maps. Instead, bulk celerity values were first extracted from the dimensional celerity maps and subsequently normalized using the corresponding bulk flow velocity. This procedure provided a consistent basis for comparing celerity behavior among the different experimental phases.

3.3.3. Bulk Celerity Analysis and dependency on Control Parameters

To examine the relationships among the key governing parameters — namely the Froude number, loading ratio, and dimensionless celerity — bulk analysis approach was adopted. Within this framework, each experimental phase is represented by a single characteristic value of these parameters, which are subsequently plotted together to investigate their mutual correlations and overall trends throughout the unsteady campaign.

A fundamental step in this analysis is the determination of a representative aggradation celerity for each phase. This requires a reliable procedure for extracting a single representative value from the spatially and temporally varying celerity fields presented in Section 3.3.2.

In the steady-flow campaign, Eslami (2025) adopted the analytical solution of a linear diffusion equation for channel aggradation proposed by Gill (1983) to define a representative averaging region within the celerity color gradient maps

Using this analytical framework, the characteristic time required for the analytical aggradation front to reach the downstream end of the channel, denoted t_e, could be estimated as follows (Gill 1983):

$$t_e = \left(\frac{L}{3.2\sqrt{K}}\right)^2 \qquad (3.18)$$

where L is the channel length and K is the linear diffusion coefficient.

In the steady-flow campaign, this time was used as the basis for selecting a representative averaging region on the celerity color gradient maps. Two distinct scenarios were considered, both based on triangular areas defined within the space–time domain (Gamal et al., 2023).

To assess the dependence of the estimated characteristic time (t_e) on the key governing parameters, the time variable was made dimensionless as follows in this study:

$$\tau = t_e \frac{U}{H} \qquad (3.19)$$

where U (cm/s) and H (cm) are the nominal flow velocity and water depth computed from Equations (3.2) and (3.1), respectively.

By examining the dependence of this dimensionless time on the key control parameters — including the Froude number Fr and the loading ratio L_r — the strongest correlation was found with $Fr/\sqrt{S_0}$. *Figure 3.24* presents the plot of τ against $Fr/\sqrt{S_0}$, where S_0 is the nominal channel slope, together with the best-fit curve obtained using a parabolic function.

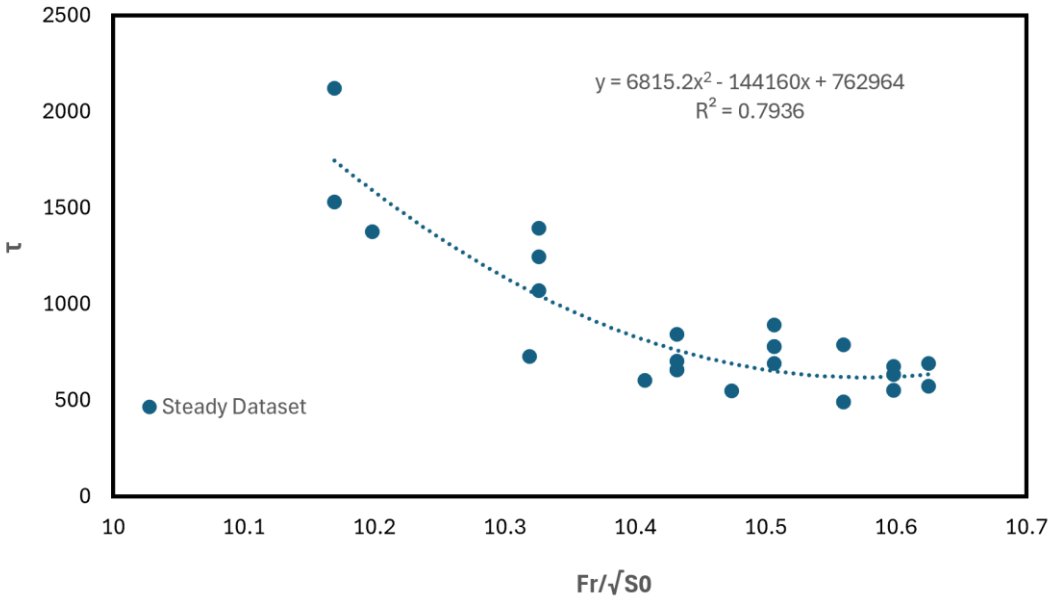


Figure 3.24: Dimensionless characteristic time τ as a function of $\frac{Fr}{\sqrt{S0}}$ for the steady-flow experimental dataset, together with the corresponding parabolic fit.

The strong dependence between τ and the Froude number confirms that Fr plays a significant role in estimating the arrival time of the analytical sediment front at the downstream end of the channel. The established equation for arrival time was subsequently used to define the representative averaging region on the celerity color gradient maps and to compute the dimensionless bulk celerity for each phase in the unsteady campaign.

The parabolic relationship between τ and $Fr/\sqrt{S_0}$, established from the steady-flow campaign, is expressed as:

$$\tau = 6815.2\left(\frac{Fr}{\sqrt{S_0}}\right)^2 - 144160\left(\frac{Fr}{\sqrt{S_0}}\right) + 762964 \qquad (3.20)$$

By applying Equation 3.20 to each phase of the unsteady campaign, the characteristic arrival time t_e was computed for all experimental phases. These values were then used to define the triangular averaging region within the celerity color gradient maps, from which the representative bulk celerity was extracted. The arrival times obtained for all phases of all experiments are summarized in *Table 3.5*.

Table 3.5: Characteristic arrival time t_e and corresponding averaging region parameters for all experimental phases

Run	Phase	Q (m^3/s)	Phase onset (s)	S_0	H (m)	U (m/s)	Fr	$Fr/\sqrt{Si}$	τ	te (s)
UnAE1	P1	0.004	0	0.0137	0.0231	0.576	1.209	10.326	1044.41	**42**
	P2	0.005	238	0.0165	0.0251	0.663	1.335	10.390	855.12	**32**
	P3	0.004	418	0.0198	0.0206	0.647	1.439	10.228	1443.89	**46**
UnAE2	P1	0.004	0	0.0137	0.0231	0.576	1.209	10.326	1044.41	**42**
	P2	0.005	241	0.0166	0.0251	0.664	1.338	10.388	858.74	**32**
	P3	0.004	421	0.0199	0.0206	0.648	1.443	10.227	1450.55	**46**
UnAE3	P1	0.004	0	0.0137	0.0231	0.576	1.209	10.326	1044.41	**42**
	P2	0.005	240	0.0135	0.0268	0.622	1.212	10.435	753.57	**32**
	P3	0.004	420	0.0151	0.0224	0.594	1.266	10.301	1133.97	**43**
UnAE4	P1	0.004	0	0.0137	0.0231	0.576	1.209	10.326	1044.41	**42**
	P2	0.005	238	0.0156	0.0256	0.651	1.299	10.403	823.14	**32**
	P3	0.004	418	0.0167	0.0217	0.613	1.328	10.275	1238.42	**44**
UnAE5	P1	0.004	0	0.0137	0.0231	0.576	1.209	10.326	1044.41	**42**
	P2	0.005	238	0.0237	0.0224	0.744	1.586	10.300	1138.37	**34**
	P3	0.004	420	0.0328	0.0176	0.758	1.826	10.081	2291.33	**53**
UnAE6	P1	0.005	0	0.0137	0.0267	0.625	1.221	10.432	759.84	**32**
	P2	0.006	239	0.0226	0.0255	0.783	1.564	10.402	826.44	**27**

Run	Phase	Q (m^3/s)	Phase onset (s)	S_0	H (m)	U (m/s)	Fr	$Fr/\sqrt{Si}$	τ	te (s)
	P3	0.005	420	0.0274	0.0214	0.778	1.699	10.262	1293.56	**36**
UnAE7	P1	0.004	0	0.0137	0.0231	0.576	1.209	10.326	1044.41	**42**
	P2	0.005	180	0.0220	0.0229	0.726	1.531	10.319	1068.50	**34**
	P3	0.006	359	0.0324	0.0228	0.878	1.856	10.314	1088.92	**28**
	P4	0.005	512	0.0406	0.0189	0.881	2.045	10.151	1853.41	**40**
	P5	0.004	750	0.0413	0.0164	0.815	2.034	10.009	2809.91	**56**
UnAE8	P1	0.004	0	0.0137	0.0231	0.576	1.209	10.326	1044.41	**42**
	P2	0.005	179	0.0156	0.0256	0.651	1.299	10.403	823.14	**32**
	P3	0.006	361	0.0230	0.0254	0.788	1.578	10.397	837.05	**27**
	P4	0.005	542	0.0390	0.0192	0.870	2.007	10.162	1786.17	**39**
	P5	0.004	722	0.0460	0.0158	0.843	2.139	9.975	3081.25	**58**
UnAE9	P1	0.004	0	0.0137	0.0231	0.576	1.209	10.326	1044.41	**42**
	P2	0.005	187	0.0155	0.0256	0.650	1.295	10.404	819.65	**32**
UnAE10	P1	0.005	0	0.0137	0.0267	0.625	1.221	10.432	759.84	**32**
	P2	0.006	265	0.0221	0.0257	0.777	1.547	10.407	814.36	**27**
	P3	0.005	425	0.0346	0.0199	0.838	1.897	10.197	1599.86	**38**

Using the characteristic arrival time t_e and the phase onset time, the temporal boundaries of the averaging regions on the celerity color gradient maps were defined for each phase. For UnAE05, the averaging intervals were set as $\Delta t_1 = (0 + 42)$s for the first phase, $\Delta t_2 = (238 + 34)$s for the second phase, and $\Delta t_3 = (420 + 53)$s for the third phase.

Once the representative averaging region was defined, a bulk celerity value was obtained for each phase by computing the mean of the local celerity values falling within the selected space–time area. It is worth mentioning that the aforementioned

negative celerity values and excessively large positive values were filtered out before the averaging process.

To establish the upper admissible threshold for celerity, an empirical relationship was first derived in the present study using the steady-flow experimental dataset. As shown in *Figure 3.24*, the relationship between C_{max}/U and L_r was first established using the steady-flow dataset and subsequently applied to the unsteady-flow experiments. The resulting expression relates the maximum dimensionless celerity to the loading ratio and satisfies the physical requirement that the propagation celerity vanishes as the loading ratio approaches unity:

$$\frac{C_{max}}{U} = 0.0441\ [\ln(L_r)]^{1.079} \qquad (3.21)$$

where C_{max} is the upper celerity threshold, U is the depth-averaged flow velocity at the onset of the experiment, and L_r is the loading ratio. The fitted relationship for steady campaign is shown in *Figure 3.25*.

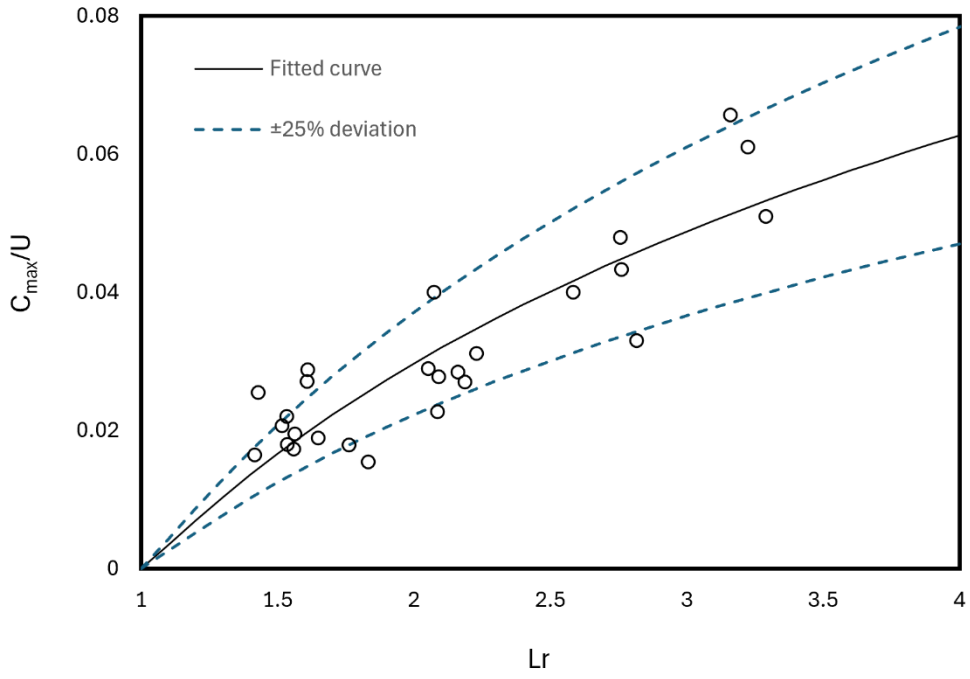


Figure 3.25: Relationship between Dimensionless Maximum Celerity and Loading Ratio (Steady Campaign)

In the present study, this expression was applied on a phase-by-phase basis to determine the corresponding upper filtering threshold for each experimental phase.

To compute the bulk celerity for each phase, a triangular region was first defined on the celerity color gradient maps. The spatial extent of this region corresponds to the

full channel length, while its temporal extent is determined by the characteristic arrival time t_e estimated for the phase from equation 3.20 accompanied with equation3.19. The representative bulk celerity was then obtained by averaging all valid celerity values contained within the selected region after applying the filtering criteria described above.

A schematic illustration of the triangular averaging regions defined for each phase in UnAE05 is presented in *Figure 3.26*.

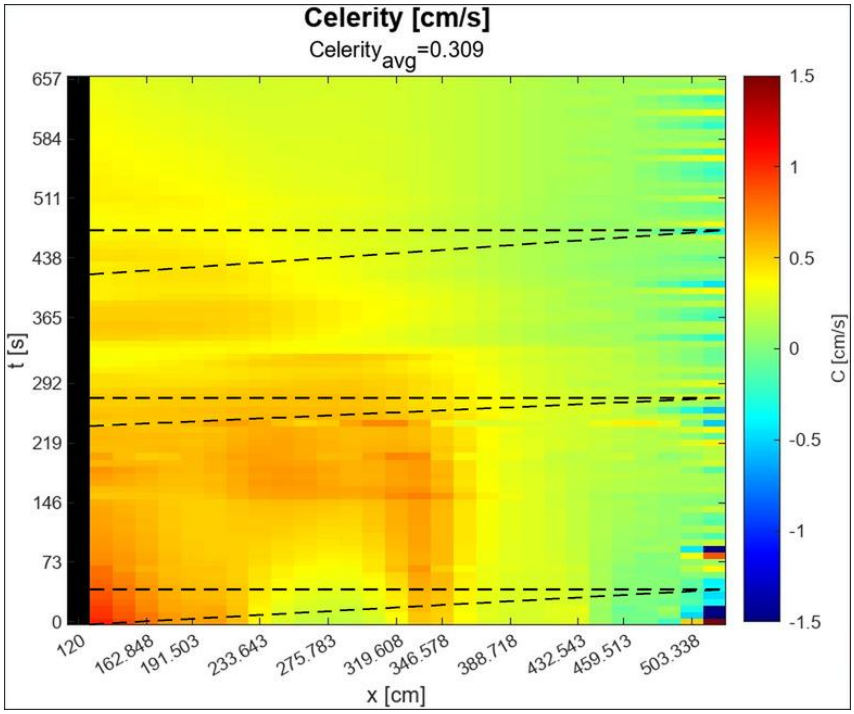


Figure 3.26: Schematic representation of the triangular averaging regions used for the bulk celerity calculation UnAE05

After obtaining a representative bulk celerity value for each experimental phase, the corresponding dimensionless bulk celerity was calculated by normalizing C_{ave} with the nominal flow velocity U associated with that phase. The velocity U was computed using the Strickler formulation described in Section 3.2, with the prescribed discharge Q, channel slope S_0 , and Manning roughness coefficient $n = 0.015$ as inputs.

The dimensionless bulk celerity values obtained from the unsteady experiments remained substantially smaller than unity throughout the experimental campaign, indicating that aggradation-wave propagation occurred at a considerably slower rate than the associated flow motion.

The extended dataset obtained in the present study provides an opportunity to assess whether the relationships previously identified from the steady-flow experiments remain applicable under unsteady conditions. In the steady-flow campaign, both the loading ratio L_r and the parameter $Fr/\sqrt{S_0}$ were evaluated as potential predictors of dimensionless bulk celerity. The results showed that C_{ave}/U exhibited a stronger

correlation with L_r than with $Fr/\sqrt{S_0}$. Consequently, L_r was selected as the independent variable for the present analysis.

Figure 3.27 and *Figure 3.28* present the relationship between $C_{ave}/U$and L_r, combining the results from the steady-flow and unsteady-flow campaigns. The fitted curve derived from the steady-flow dataset is given by:

$$\frac{C_{ave}}{U} = 0.0179[\ln(L_r)]^{0.7585} \qquad (3.22)$$

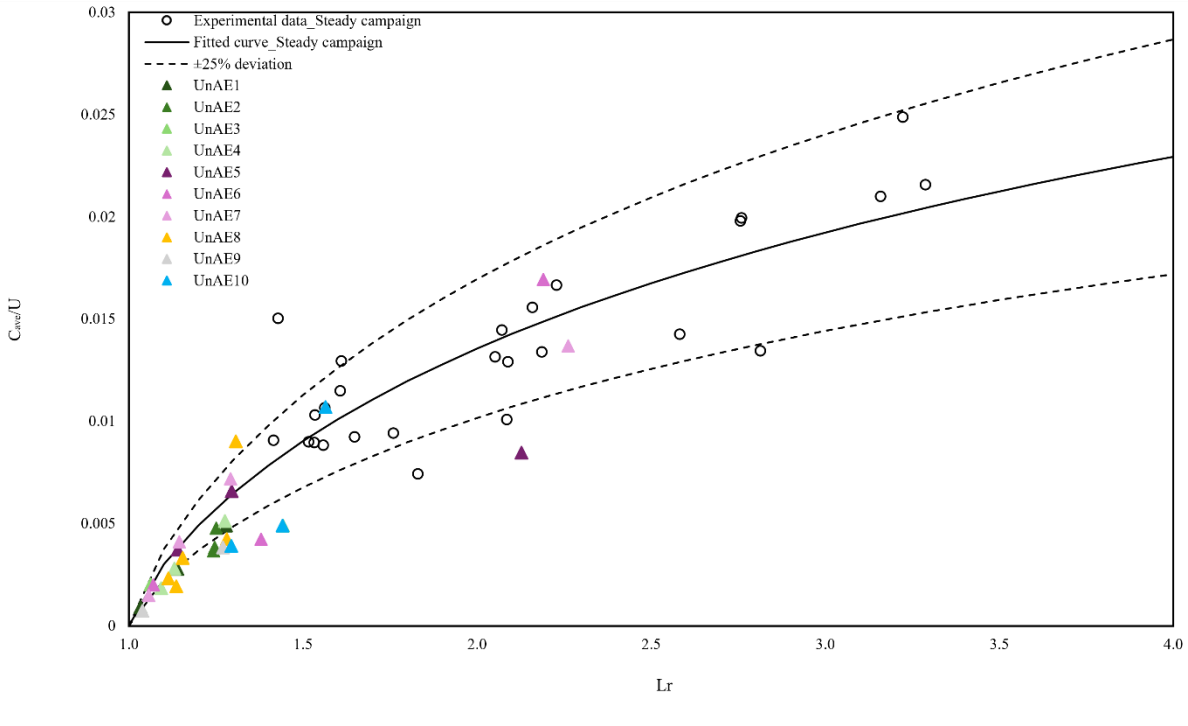


Figure 3.27: Dimensionless bulk celerity C_{ave}/U as a function of L_r, with unsteady campaign data grouped by experiment

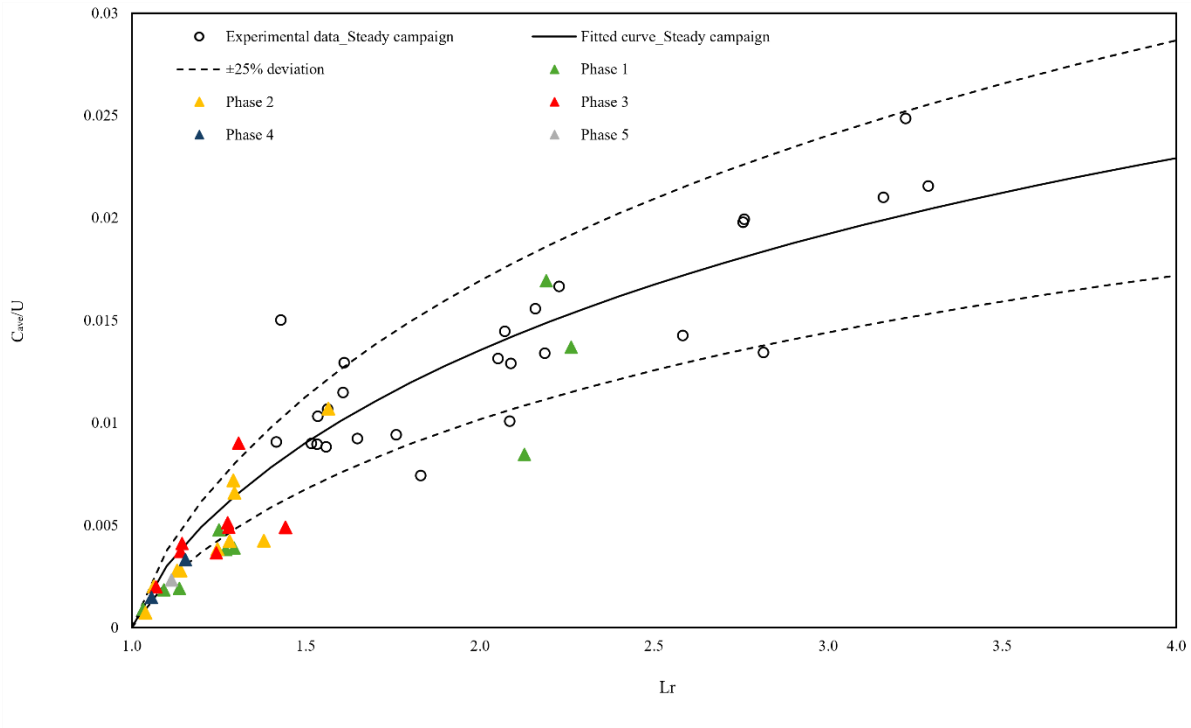


Figure 3.28: Dimensionless bulk celerity C_{ave}/U as a function of L_r, with unsteady campaign data grouped by phase number

In *Figure 3.27*, the unsteady data points are grouped by experiment, providing an overview of the overall distribution of results across the campaign. *Figure 3.28* presents the same data grouped by phase number, allowing the influence of phase sequence to be examined more clearly. Since each phase within an experiment is characterized by distinct hydraulic and morphological conditions, partly shaped by the cumulative aggradation produced during the preceding phases, grouping the data by phase number facilitates the comparison of results obtained under different phase conditions.

The results show that the unsteady data generally follow the same trend previously identified in the steady-flow campaign. Most of the data points fall within the ±25% deviation bounds of the reference curve, indicating a satisfactory agreement between the two datasets despite the different hydraulic, sediment supply, and morphological conditions under which they were obtained.

A clear positive correlation can be observed between dimensionless bulk celerity and loading ratio. As the loading ratio increases, larger values of dimensionless bulk celerity are generally obtained, indicating a faster propagation of the aggradation wave relative to the flow velocity. This behavior is physically consistent, since larger loading ratios correspond to stronger sediment overloading conditions and consequently more intense morphodynamic adjustment of the channel bed.

Although some scatter is present, particularly at intermediate loading ratios, the overall trend remains evident throughout the dataset. The agreement between the unsteady measurements and the reference relationship derived from the steady-flow campaign suggests that loading ratio remains one of the primary parameters governing aggradation-wave propagation, even under transient hydraulic conditions.

The consistency observed between the two datasets provides confidence that the dimensionless bulk celerity framework is not limited to steady-flow conditions and may be applicable over a broader range of hydraulic and sediment transport scenarios. To further investigate this relationship and to exploit the enlarged dataset available in the present study, the steady and unsteady data were subsequently combined and a new regression analysis was performed. The resulting fitted relationship is presented below.

$$\frac{C_{ave}}{U} = 0.01788[\ln(L_r)]^{0.8607} \qquad (3.23)$$

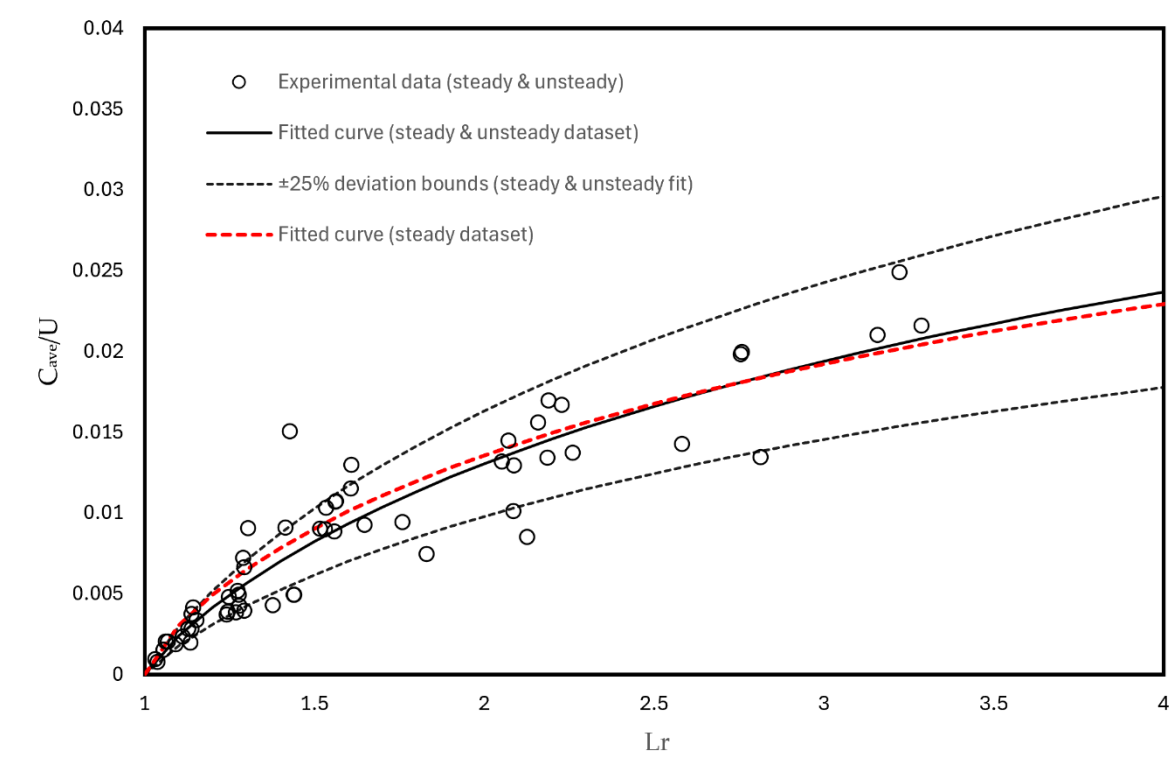


Figure 3.29: Average Dimensionless Bulk Celerity for the Combined Steady and Unsteady Campaigns

The enlarged dataset improves the robustness of the fitted relationship and extends its validity over a wider range of hydraulic and sediment transport conditions.

3.3.4. Steady–Unsteady Comparison and Experimental Limitations

Overall, the comparison between the steady and unsteady datasets indicates that the same general trends remain valid under both experimental conditions. In particular, the dimensionless relationships derived from the steady-flow campaign provided a satisfactory representation of the unsteady data, despite the additional complexity introduced by phase transitions and continuously evolving bed conditions. The majority of the unsteady data points follow the same overall tendency identified in the steady-flow experiments, supporting the applicability of the proposed dimensionless framework under transient hydraulic conditions.

An important consequence of this behavior is reflected in the loading-ratio evolution. In the steady-flow campaign, loading ratios greater than 3 were successfully achieved under several experimental conditions. In contrast, no comparable values were reached during the unsteady campaign. Even loading ratios exceeding approximately 2 were observed almost exclusively during the first phase of the experiments and became increasingly difficult to attain in the subsequent phases. Although the sediment feeding rates were initially selected on the basis of transport-capacity estimates in order to achieve high target loading ratios, the progressive increase in bed slope continuously increased the actual transport capacity of the channel. Consequently, the achieved loading ratios tended to decrease from phase to phase, even when the imposed sediment feeding conditions remained unchanged.

Additional experimental limitations further contributed to this behavior. Irregularities in the sediment feeder occasionally resulted in sediment supply rates that differed from the intended values. In some cases, larger-than-expected sediment inputs promoted additional aggradation and further increased the channel bed slope, accelerating the increase in transport capacity and making it even more difficult to maintain the desired loading-ratio conditions during the later phases.

Conversely, attempts to compensate for the increasing transport capacity by introducing larger sediment supply rates occasionally produced excessive sediment accumulation near the channel inlet. Under such conditions, sediment blockages could form and partially obstruct the flow entering the channel. A representative example is provided by experiment UnAE09, which was originally designed as a five-phase experiment. However, excessive sediment accumulation during the third phase led to the formation of a blockage near the inlet, forcing the experiment to be terminated prematurely. Consequently, only the first two phases were retained in the subsequent analyses.

These observations highlight one of the principal differences between the steady and unsteady campaigns. In the steady-flow experiments, higher initial loading-ratio

conditions could be imposed because each test began from a fixed initial channel configuration. In the unsteady experiments, however, achieving comparably high loading ratios in Phase 1 was deliberately avoided, as this would have produced a substantial increase in bed slope by the end of the phase. Consequently, maintaining aggradation during the subsequent phases would have required sediment feeding rates exceeding the operational limits of the hopper used in the experiments.

It should also be noted that the reported loading-ratio values in both the steady and unsteady campaigns correspond only to the initial conditions of each experiment or phase. Beyond this initial instant, L_r evolves continuously as the sediment transport capacity of the channel changes in response to the ongoing adjustment of bed morphology and slope during the run.

3.4. Dimensionless Bed Slope Evolution and Steady-Flow Comparison

The previous sections focused on the temporal evolution of bed profiles and aggradation celerity during the unsteady experimental campaign. However, an additional objective of this study is to investigate whether the bed-slope adjustment observed under unsteady flow conditions follows trends similar to those previously identified in steady-flow experiments.

To enable this comparison, the dimensionless bed-slope formulation developed from the complete steady-flow dataset of Eslami et al. (2024) was adopted. In that study, bed-slope evolution was described as a function of both loading ratio and dimensionless time, with the loading ratio identified as the primary control on equilibrium bed-slope increase.

The following analysis applies this formulation to the unsteady experiments to evaluate whether the relationships derived from the steady-flow campaign remain valid under transient hydraulic and sediment-feeding conditions.

To compare the temporal evolution of bed slope among experiments conducted under different loading conditions, Eslami et al. (2024) expressed the increase in mean bed slope using a dimensionless formulation. The evolution of bed slope was described as:

$$S - S_0 = A \cdot f(L_r) \cdot f(\tau) \qquad (3.24)$$

where S_0 is the initial bed slope, A is a fitting coefficient, L_r is the loading ratio, and τ is the dimensionless time.

The dimensionless time was defined as:

$$\tau = \frac{t \cdot U}{H} \qquad (3.25)$$

where t is the elapsed time, and U and H are the flow velocity and water depth corresponding to the initial flow condition.

The effect of the loading ratio was represented by:

$$f(L_r) = B \cdot \ln(L_r) \qquad (3.26)$$

while the temporal evolution was described by:

$$f(\tau) = 1 - e^{-C\tau^D} \qquad (3.27)$$

The calibrated values of the fitting parameters obtained from the complete steady-flow dataset are $A = 1.2870$, $C = 0.002159$, and $D = 0.7694$.

Using the calibrated dimensionless formulation, all available steady-flow experiments were expressed in terms of the dimensionless variables τ and $(S - S_0)/f(L_r)$. The resulting dimensionless representation is presented in *Figure 3.30*, where the experimental measurements are compared with the fitted relationship obtained from the original calibration.

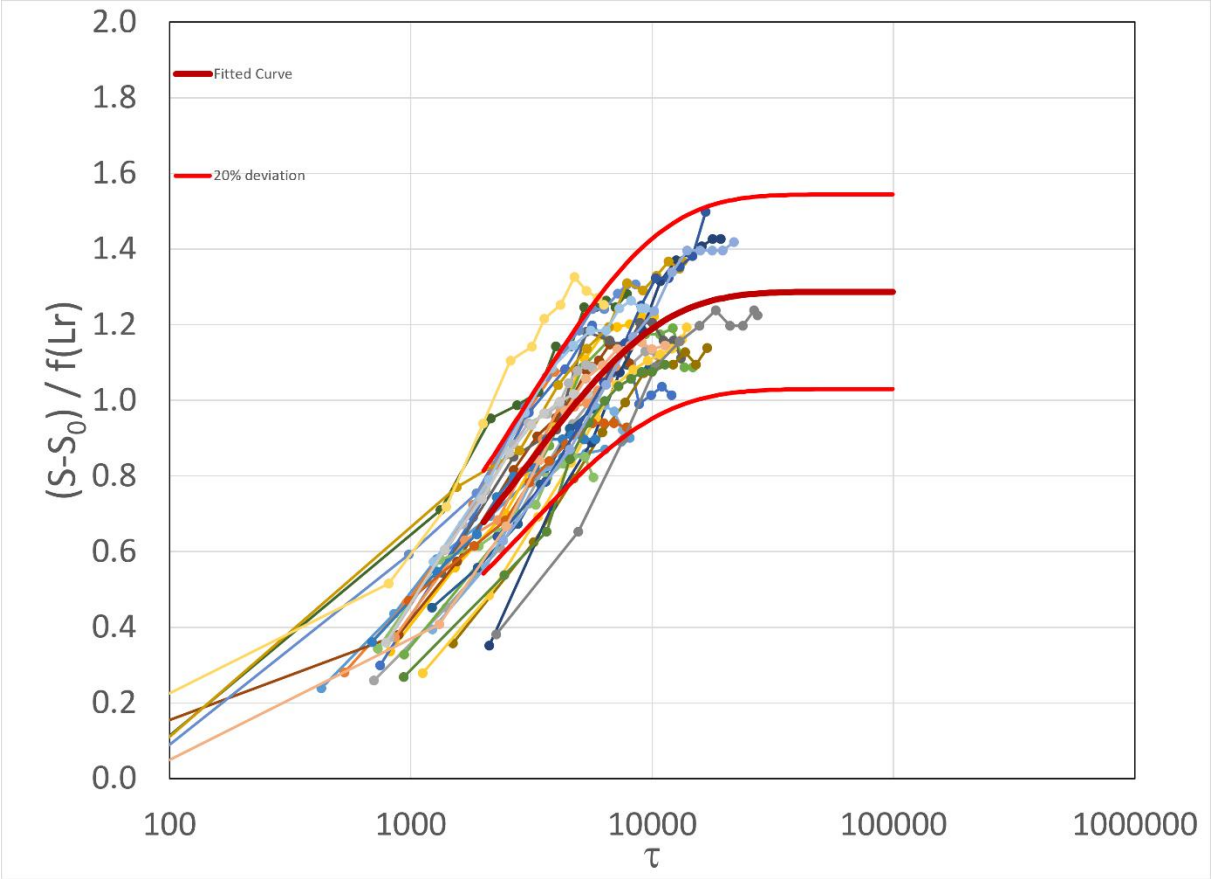


Figure 3.30: Dimensionless temporal evolution of bed slope for the complete steady-flow dataset, compared with the fitted curve f(τ)

It should be noted that the steady-flow dataset covers only loading ratios greater than 1.42, corresponding to the minimum loading-ratio condition investigated in the experimental campaign (AE10). Additional details regarding the loading-ratio range of the steady-flow experiments are provided in *Table 1.1*. This aspect should be considered when comparing the steady-flow trends with the unsteady dataset.

The same methodology was subsequently applied to the unsteady experiments. In the following analysis, the unsteady measurements were represented using the same dimensionless variables and normalization procedure described above.

Figure 3.31 presents the dimensionless temporal evolution of bed slope for the unsteady experimental campaign, obtained by applying the same normalization procedure and parameter values derived from the steady-flow dataset. The fitted curve shown in both figures corresponds to the relationship calibrated from the steady-flow experiments and serves as a reference for assessing the behavior of the unsteady data.

As mentioned above, the steady-flow formulation was originally calibrated using experiments with loading ratios greater than approximately 1.42. Consequently, unsteady phases characterized by loading ratios below this threshold fall outside the calibration range of the original model. To distinguish these cases, data points

corresponding to $L_r < 1.42$ are shown in grey, while phases with $L_r \geq 1.42$ are represented using colored symbols. This distinction allows the comparison to focus on the range of loading-ratio conditions for which the steady-flow relationship was originally developed, while still providing a visual indication of the behavior observed outside the calibration domain.

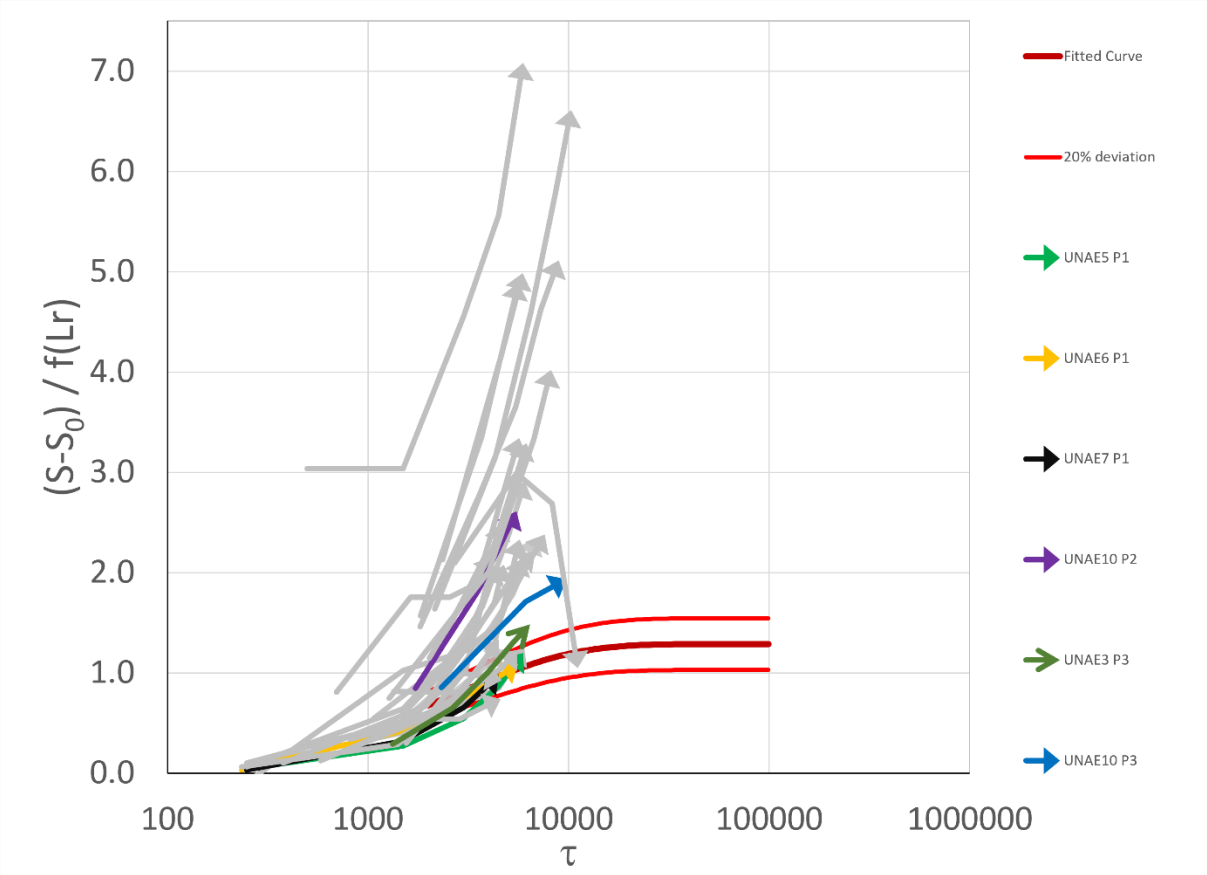


Figure 3.31: Dimensionless bed-slope evolution for all unsteady phases. Grey symbols represent phases with Lr < 1.42, while colored symbols indicate phases with Lr ≥ 1.42. The solid curve corresponds to the steady-flow fitted relationship.

Figure 3.32 compares the dimensionless bed-slope evolution observed in the unsteady experiments with the reference relationship derived from the steady-flow dataset for phases characterized by high loading-ratio conditions (Lr ≥ 1.42).

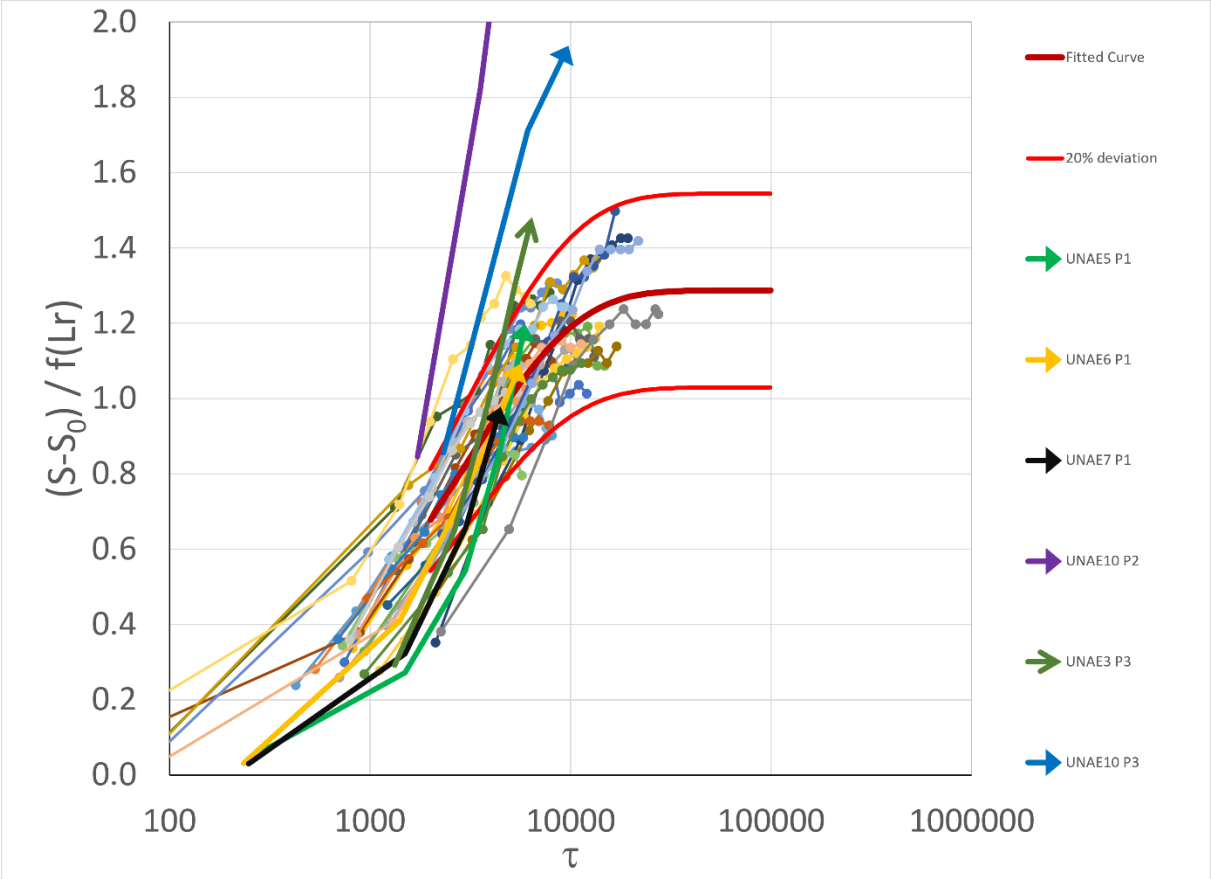


Figure 3.32: Comparison between the dimensionless bed-slope evolution observed in the steady-flow and unsteady datasets for phases with Lr ≥ 1.42.

Overall, the unsteady experimental data show a reasonable agreement with the relationship derived from the steady-flow campaign. Most of the unsteady data points (with Lr ≥ 1.42) follow the general trend established by the steady-flow dataset and remain within or close to the associated deviation bounds, indicating a generally consistent bed-slope response despite the transient hydraulic, sediment-supply, and morphological adjustments occurring during the experiments. The main exceptions are phases UnAE10p2 and UnAE10p3, which deviate from the fitted relationship. Nevertheless, the overall agreement between the two datasets suggests that the dimensionless bed-slope formulation derived from the steady-flow campaign remains applicable under unsteady conditions, provided that comparable loading-ratio conditions are considered.

4 Chapter 4: Summary and Conclusion

This study investigated sediment aggradation processes under unsteady supercritical flow conditions through a series of laboratory experiments designed to reproduce transient hydraulic and sediment-supply scenarios. The primary objective was to determine whether the morphodynamic behavior observed during individual phases of an unsteady hydrograph could be interpreted using relationships previously established from steady-flow experiments. Particular attention was given to the evolution of bed morphology, aggradation-wave celerity, and bed-slope adjustment, as well as to the applicability of dimensionless formulations developed under steady-flow conditions.

To investigate these processes under conditions more representative of natural rivers, the experimental campaign was designed using stepped hydrographs rather than conventional steady-flow tests. Each hydrograph consisted of successive phases with different combinations of water discharge and sediment supply, allowing the channel to evolve continuously while maintaining well-defined hydraulic conditions within each phase. This approach made it possible to compare the transient behavior observed during individual phases with equivalent steady-flow conditions.

Throughout the experiments, bed evolution, water-surface profiles, sediment feeding, and hydraulic conditions were monitored using complementary measurement techniques. Image-processing methods were employed to derive bed and water-surface profiles, while color-gradient maps were generated to quantify the spatial and temporal propagation of aggradation waves. These datasets formed the basis for estimating local, bulk, and dimensionless celerity values used throughout the analysis.

The experimental results showed that bed aggradation occurred in all investigated runs, producing progressive changes in bed elevation and channel slope throughout the experiments. The color-gradient maps proved effective in identifying the spatial and temporal propagation of aggradation waves and provided a quantitative basis for estimating local, bulk, and dimensionless celerity values.

Since the loading ratio was identified as the key parameter governing both celerity and bed-slope evolution, particular attention was devoted to its estimation. The initial sediment transport capacity (Q_{s0}) was first estimated from the hydraulic conditions at the beginning of each experimental phase. The loading ratio (L_r) was then calculated as the ratio between the imposed sediment supply and the corresponding transport capacity. This procedure provided a consistent basis for comparing experiments performed under different hydraulic conditions and constituted the foundation of the subsequent dimensionless analyses.

A key outcome of the study concerns the identification of the dominant controlling parameters. Among the investigated variables, the loading ratio L_r consistently emerged as the most influential parameter governing both celerity behavior and bed-slope evolution. Following the findings of the steady-flow campaign, loading ratio was adopted as the principal independent variable in the dimensionless analyses presented in this thesis. Based on the steady-flow results, it was assumed that the same dependence of bulk celerity on loading ratio also applies under unsteady boundary conditions, and this assumption was subsequently evaluated using the unsteady experimental dataset.

The comparison between the steady-flow and unsteady-flow datasets demonstrates that the relationships derived from the steady-flow campaign remain largely applicable under unsteady conditions. Most experimental phases follow the trends established from the steady-flow dataset and remain within the associated deviation bounds for both dimensionless bulk celerity and dimensionless bed-slope evolution. Consequently, the main research question of this thesis can be answered positively: the morphodynamic behavior observed during individual phases of an unsteady hydrograph can generally be described using the same dimensionless framework developed from steady-flow experiments. These findings indicate that, despite continuously evolving hydraulic and morphodynamic conditions, individual phases of the unsteady experiments can be interpreted as transient counterparts of steady-flow experiments characterized by comparable loading-ratio conditions, suggesting that the governing mechanisms controlling sediment aggradation remain consistent across both experimental approaches.

- **Main Findings**
- The principal findings of this study can be summarized as follows:
- Bed aggradation produced progressive changes in channel morphology and bed slope throughout the unsteady experiments.
- Color-gradient maps provided a clear visualization of sediment-wave propagation.
- Loading ratio was identified as the dominant parameter controlling both dimensionless bulk celerity and bed-slope evolution.
- Most unsteady experimental phases followed the same dimensionless relationships previously established from steady-flow experiments.
- Individual phases of an unsteady hydrograph can generally be interpreted as transient equivalents of steady-flow experiments characterized by similar loading-ratio conditions.
- The dimensionless framework developed from the steady-flow dataset remained applicable under unsteady conditions, with only limited deviations observed.

- **Limitations and Future Work**

The present study focused on laboratory-scale experiments performed under controlled conditions and using a limited range of hydraulic and sediment-supply scenarios. Although the results demonstrated encouraging agreement between steady and unsteady conditions, further investigation is required to assess the applicability of the proposed framework across a wider range of loading ratios, hydrograph shapes, and sediment characteristics.

Future research may extend the present framework to degradation processes, allowing the applicability of the proposed dimensionless relationships to be assessed under erosional conditions. In addition, extending the analysis to numerical modelling and field-scale applications would provide valuable insight into the transferability of the proposed relationships to natural river systems. Such investigations could contribute to improved prediction of aggradation processes and support more effective river-management and flood-risk-mitigation strategies.

Bibliography

El Achkar, G. M. H. (2024). *How and How Fast Does a Channel Respond to Sediment Overloading Under Supercritical Conditions?* Master's Thesis, Politecnico di Milano, Milan, Italy.

Eslami, H. (2025). *Aggradation Wave Dynamics Under Sediment Overloading in Supercritical Flows.* PhD Thesis, Politecnico di Milano, Milan, Italy.

Eslami, H., Iervolino, M., & Radice, A. (2025). Laboratory determination of aggradation wave celerity due to sediment overloading in supercritical flow. *Geomorphology, 486*, 109906.

Eslami, H., Yousefyani, H., Yavary Nia, M., & Radice, A. (2022). On how defining and measuring a channel bed elevation impacts key quantities in sediment overloading with supercritical flow. *Acta Geophysica, 70*(5), 2511–2528.

Fondriest Environmental, Inc. (2014). *Turbidity, Total Suspended Solids, and Water Clarity.* Fundamentals of Environmental Measurements.

Friedman, G. M., Sanders, J. E., & Kopaska-Merkel, D. C. (1992). *Principles of Sedimentary Deposits: Stratigraphy and Sedimentology.* Macmillan.

Fryirs, K. A., Wheaton, J. M., Bizzi, S., Williams, R., & Brierley, G. J. (2019). To plugin or not to plugin? Geomorphic analysis of rivers using the River Styles Framework in an era of big data acquisition and automation. *Wiley Interdisciplinary Reviews: Water, 6*(5), e1372. https://doi.org/10.1002/wat2.1372

García, M. (2008). *Sedimentation Engineering (Processes, Measurements, Modeling, and Practice).* American Society of Civil Engineers. ISBN 978-0-7844-0814-8.

Gomez, B. (1991). Bedload transport. *Earth-Science Reviews, 31*(2), 89–132.

Heydari, E. (2020). *Experimental Analysis of Channel Overloading in Supercritical Condition.* Master's Thesis, Politecnico di Milano, Milan, Italy.

Hiteh, M., Poursoleimanzade, E., & Yavary Nia, M. (2023). *Experimental Investigation of Overloaded Channel and Celerity of Sediment Aggradation Propagation in Nearcritical and Supercritical Conditions.* Master's Thesis, Politecnico di Milano, Milan, Italy.

Julien, P. Y. (2010). *Erosion and Sedimentation* (2nd ed.). Cambridge University Press.

Mavis, F. T., & Laushey, L. M. (1949). Formula for velocity at beginning of bed-load movement is reappraised. *Civil Engineering, 19*, 38–39.

Petit, F. (1987). The relationship between shear stress and the shaping of the bed of a pebble-loaded river (La Rulles-Ardennes). *Catena, 14*, 463–468.

Piotrowski, A. P., Napiorkowski, J. J., & Rowiński, P. M. (2014). Comparing large number of metaheuristics for artificial neural networks training to predict water temperature in a natural river. *Computers & Geosciences, 64*, 136–151.

Radice, A., Malavasi, S., & Ballio, F. (2006). Solid transport measurements through image processing. *Experiments in Fluids, 41*(5), 721–734.

Radice, A., Rosatti, G., Ballio, F., Franzetti, S., Mauri, M., Spagnolatti, M., & Garegnani, G. (2013). Management of flood hazard via hydro-morphological river modelling. The case of the Mallero in Italian Alps. *Journal of Flood Risk Management, 6*(3), 197–209.

Reid, L. M., Keppeler, E., & Hilton, S. (2016). *Post-landslide recovery patterns in a coast redwood forest.* In R. B. Standiford & Y. Valachovic (Eds.), Coast redwood science symposium—2016: Past successes and future direction (Gen. Tech. Rep. PSW-GTR-258, pp. 135–147). U.S. Department of Agriculture, Forest Service, Pacific Southwest Research Station.

Russell, C. E. (2025). Classification framework for assessing anthropogenic sedimentary facies. *The Sedimentary Record, 23*(1).

Shields, A. (1936). *Application of Similarity Principles and Turbulence Research to Bed-Load Movement* (Mitteilungen der Preussischen Versuchsanstalt für Wasserbau und Schiffbau, Heft 26). Berlin, Germany. [English translation: U.S. Army Corps of Engineers, 1966].

Simons, D. B., & Richardson, E. V. (1966). *Resistance to Flow in Alluvial Channels* (U.S. Geological Survey Professional Paper 422-J). U.S. Government Printing Office.

Tavakoli, K., Zadehali, E., & Zarrabi, R. (2022). *Experimental and Numerical Analysis of Channel Aggradation in Supercritical Condition.* Master's Thesis, Politecnico di Milano, Milan, Italy.

Unigarro Villota, S. (2017). *Laboratory Study of Channel Aggradation Due to Overloading.* Master's Thesis, Politecnico di Milano, Milan, Italy.

Vanoni, V. A. (Ed.). (2006). *Sedimentation Engineering* (2nd ed.). American Society of Civil Engineers.

Wadell, H. (1932). Volume, shape and roundness of rock particles. *The Journal of Geology, 40*(5), 443–451.

Yang, C. T. (2003). *Sediment Transport: Theory and Practice.* Krieger Publishing Company.

Bahadori, S. (2026). *Channel Aggradation Under Unsteady Supercritical Flow Conditions.* Master's Thesis, Politecnico di Milano, Milan, Italy.

Yavary Nia, M., Yousefyani, H., & Eslami, H. (2021). *Experimental and Numerical Analysis of Overloaded Channel in Supercritical Condition.* Master's Thesis, Politecnico di Milano, Milan, Italy.

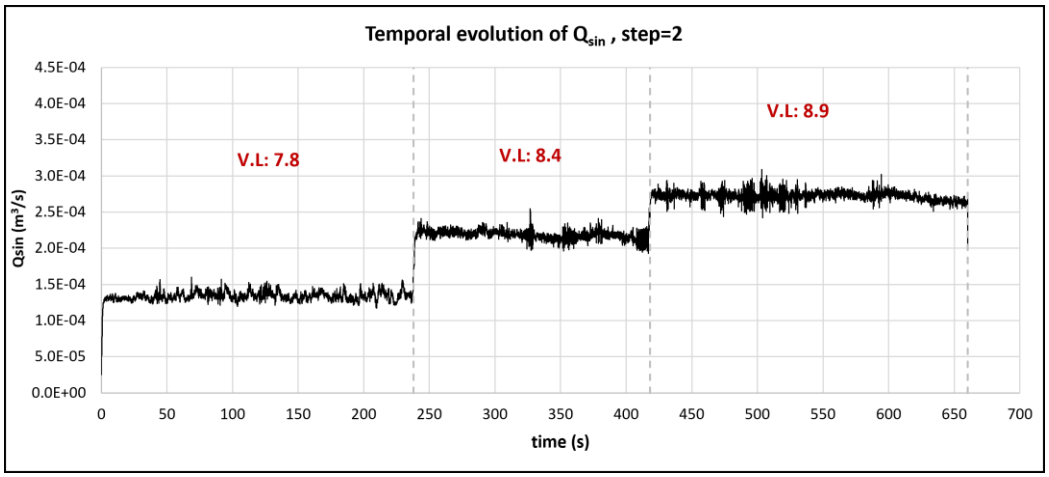
Zanchi, B. (2018). *Indagine sperimentale sul fenomeno di deposito in un canale a fondo mobile soggetto a sovralimentazione di materiale solido.* Master's Thesis, Politecnico di Milano, Milan, Italy.

Eslami, H., El Achkar, G., Hassan, A. G. M., & Radice, A. (2024). *Temporal Evolution of Bed Slope in Laboratory Channel Aggradation Under a Supercritical Flow.* In Proceedings of the XXXIX Convegno Nazionale di Idraulica e Costruzioni Idrauliche (IDRA24), Parma, Italy, 15–18 September 2024.

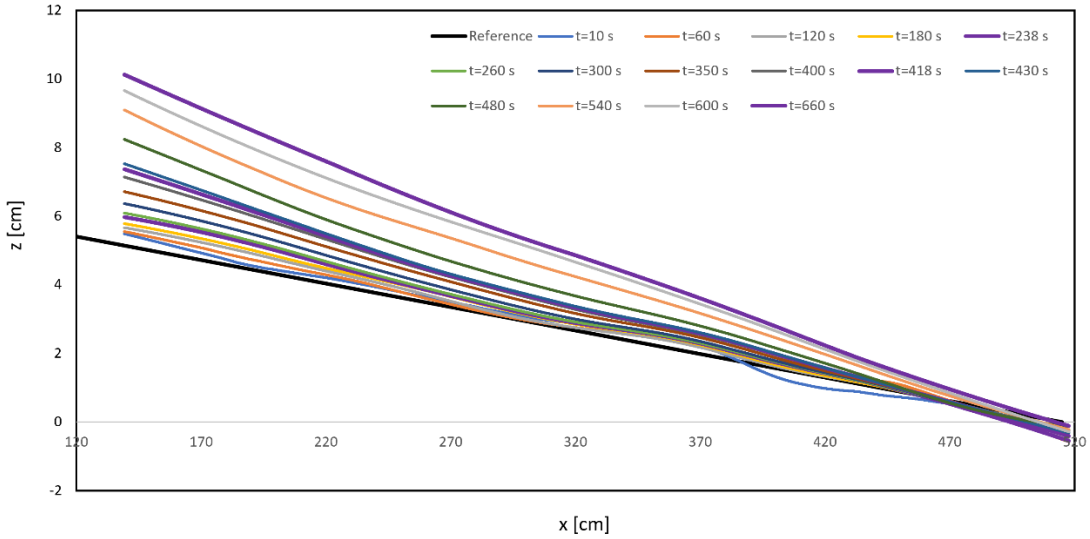
Appendix

Experiment UnAE01 Parameters

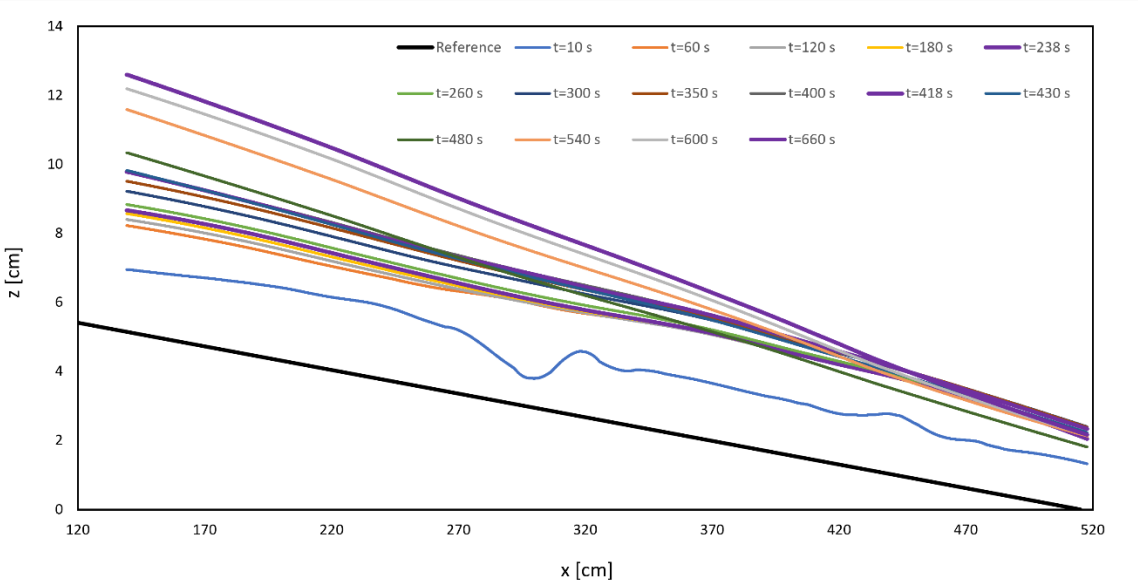
Phase	T (s)	S_0 (%)	Q (l/s)	h_0 (cm)	Fr	Vibration level	*Qsin (m³/s)*	*Qs0 (m³/s)*	Lr
P1	238	1.37	4	2.31	1.21	7.8	1.30E-04	1.23E-04	1.03
P2	182	1.65	5	2.51	1.33	8.4	2.11E-04	1.89E-04	1.14
P3	239	1.98	4	2.06	1.44	8.9	2.62E-04	2.00E-04	1.28



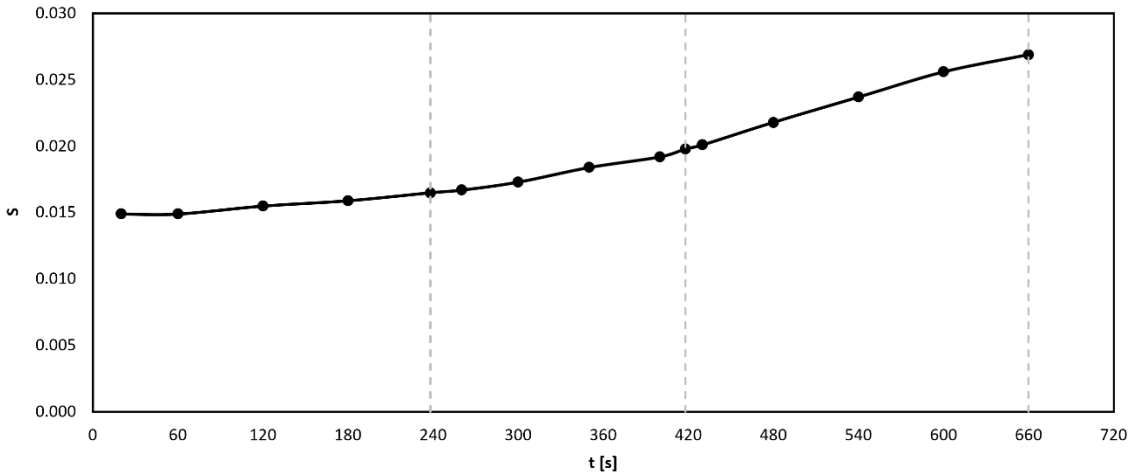
UnAE01 Temporal Evolution of Q_{sin}



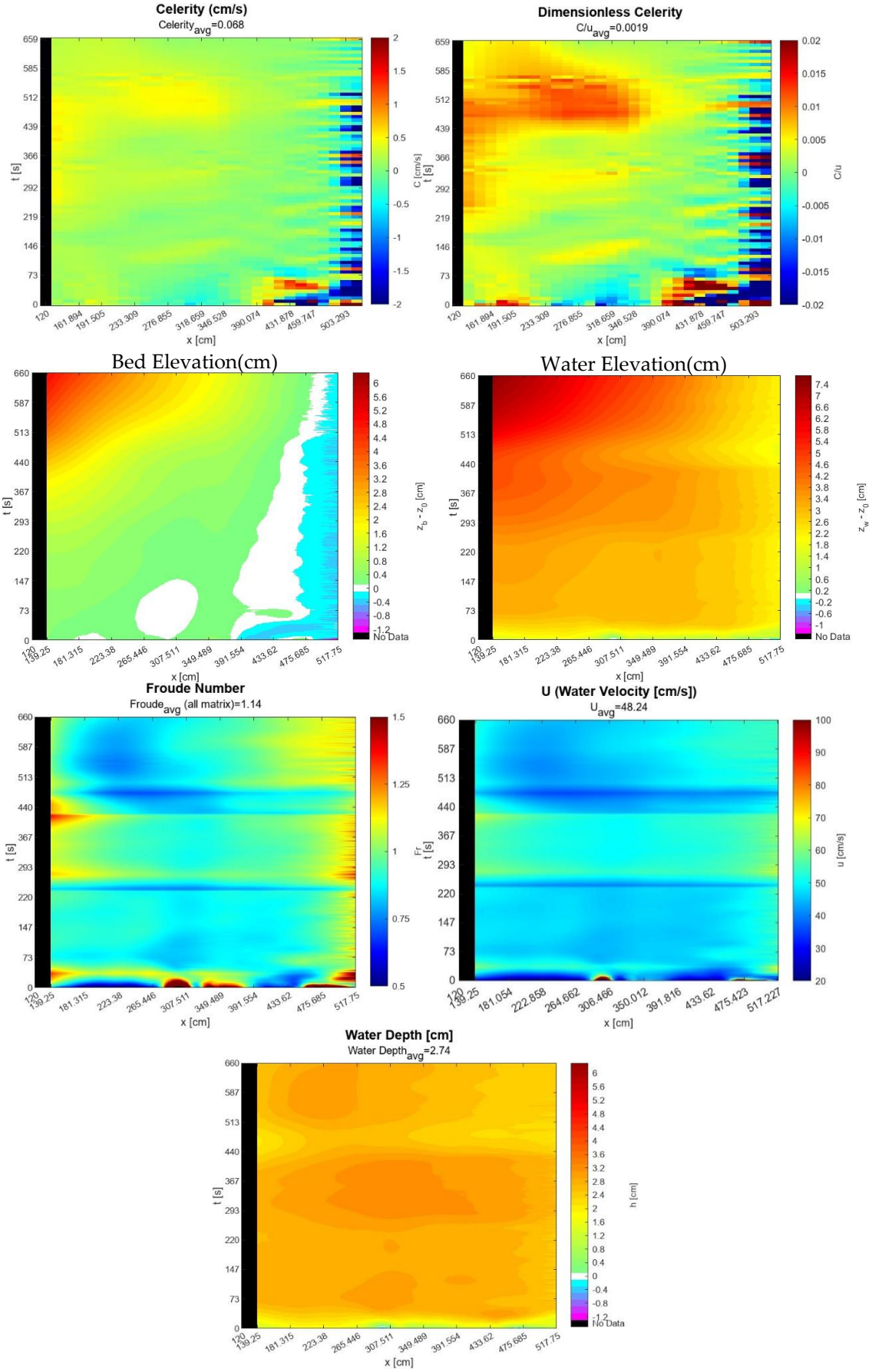
UnAE01 Spatial Bed Surface Profiles



UnAE01 Spatial Water Surface Profiles



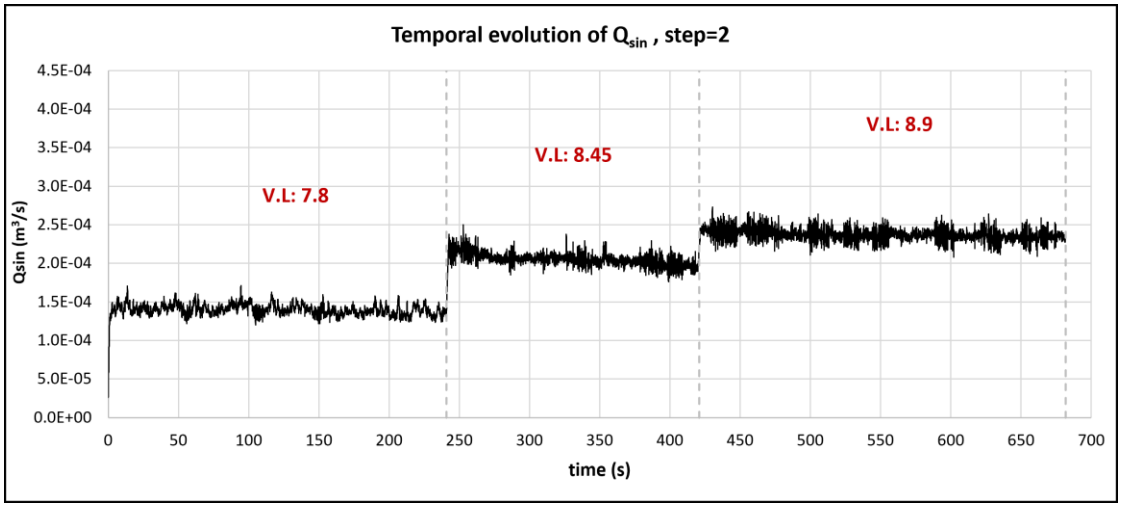
UnAE01 Temporal Evolution of Bed Slope



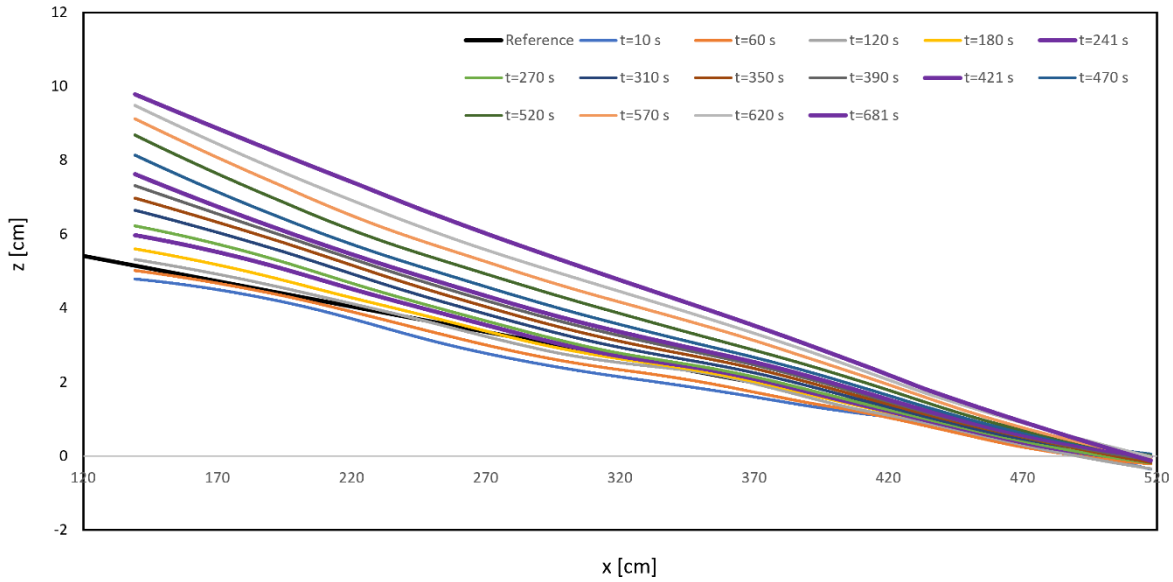
UnAE01 Color Gradient Maps

Experiment UnAE02 Parameters

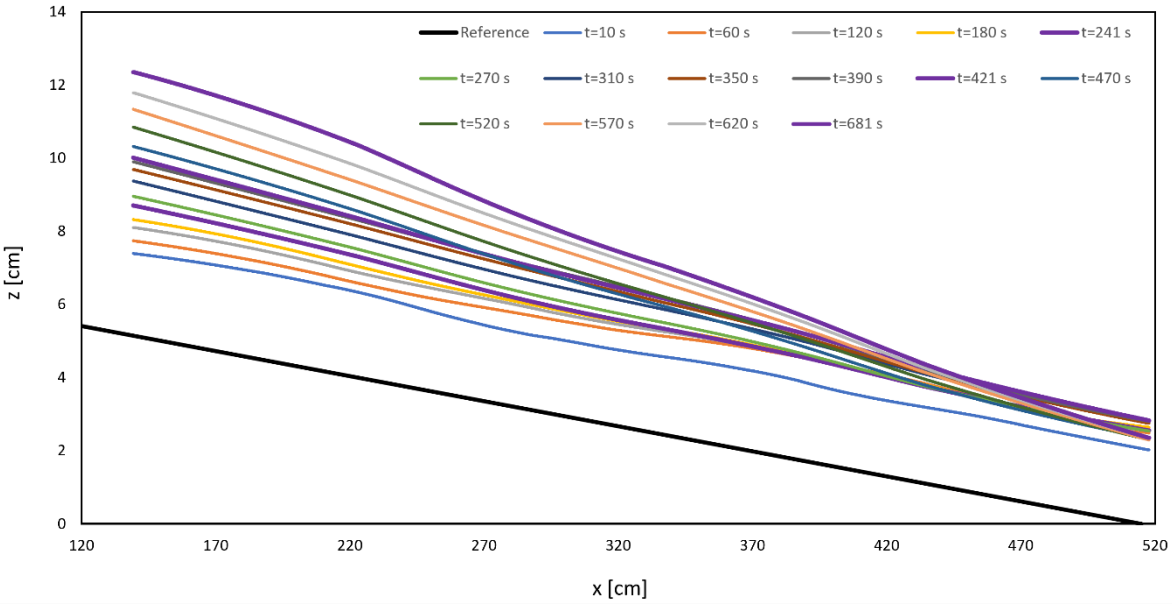
Phase	T (s)	S_0 (%)	Q (l/s)	h_0 (cm)	Fr	Vibration level	*Qsin (m^3/s)*	*Qs0 (m^3/s)*	Lr
P1	241	1.37	4	2.31	1.21	7.8	1.33E-04	1.05E-04	1.25
P2	180	1.66	5	2.51	1.39	8.45	1.96E-04	1.53E-04	1.25
P3	239	1.99	4	2.06	1.44	8.9	2.27E-04	1.77E-04	1.24



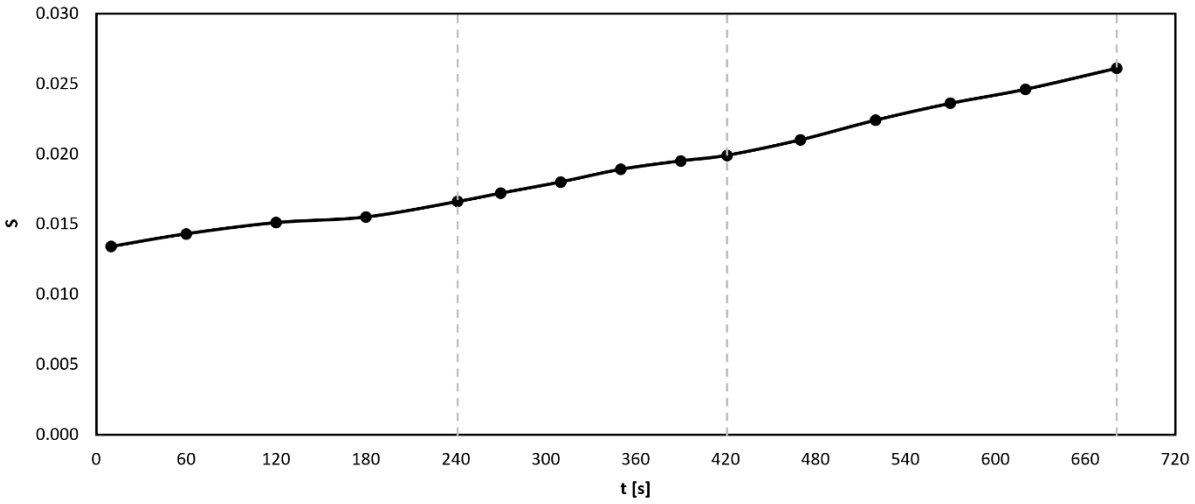
UnAE02 Temporal Evolution of Q_{sin}



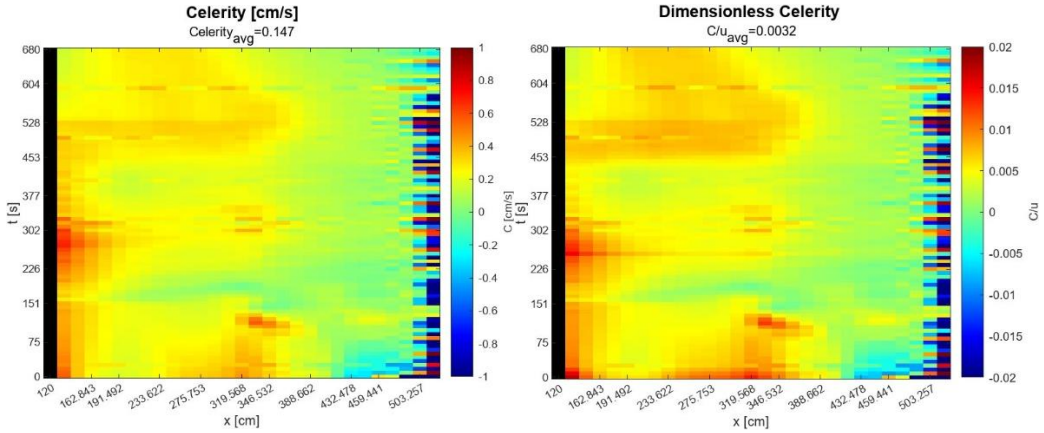
UnAE02 Spatial Bed Surface Profiles



UnAE02 Spatial Water Surface Profiles

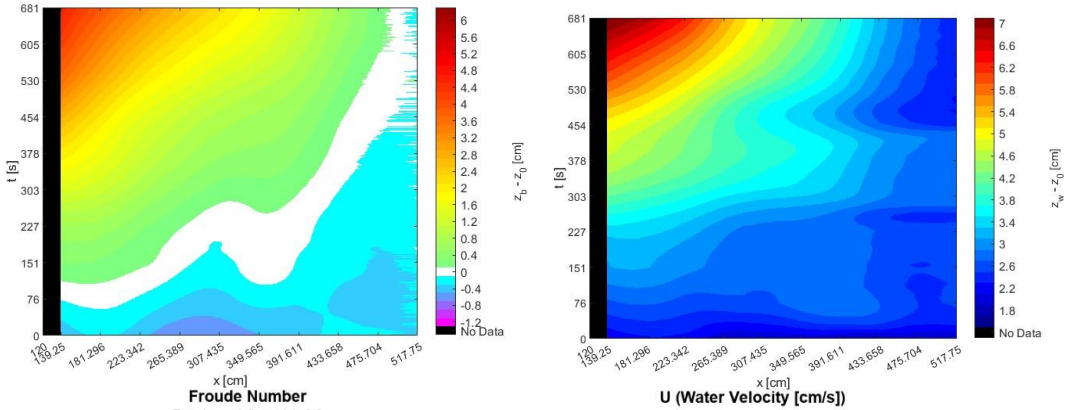


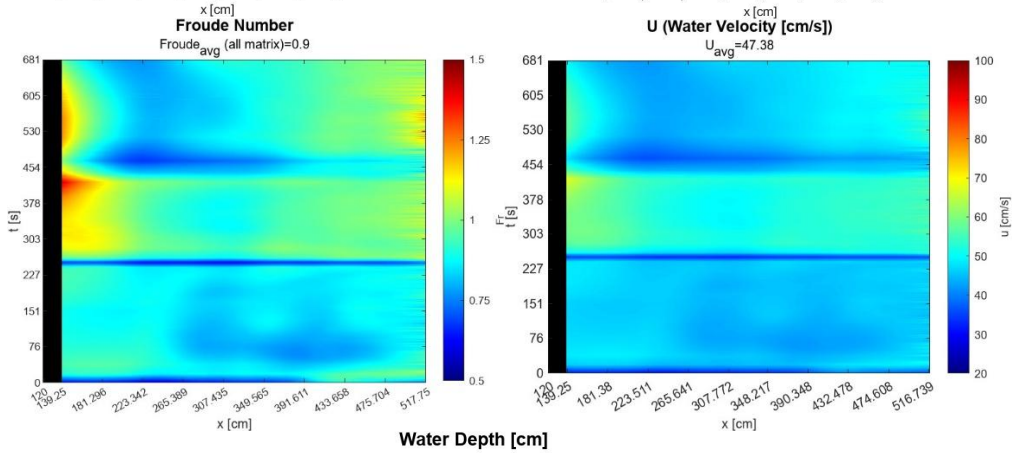
UnAE02 Temporal Evolution of Bed Slope

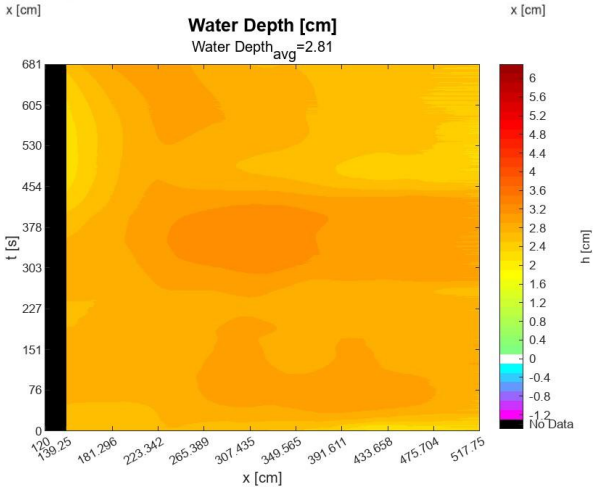


Bed Elevation (cm)

Water Elevation (cm)



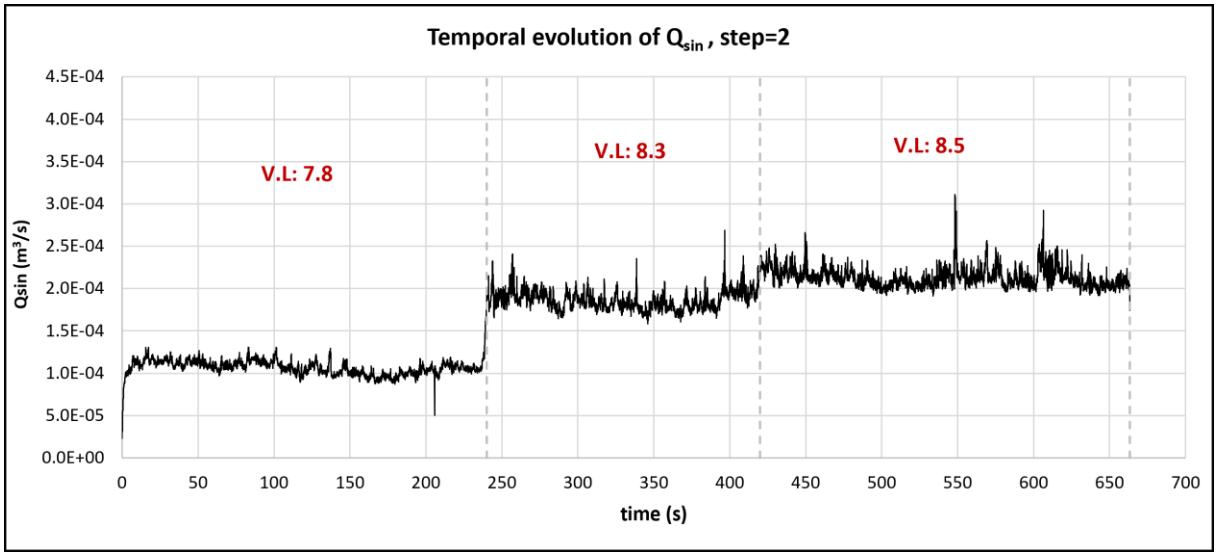




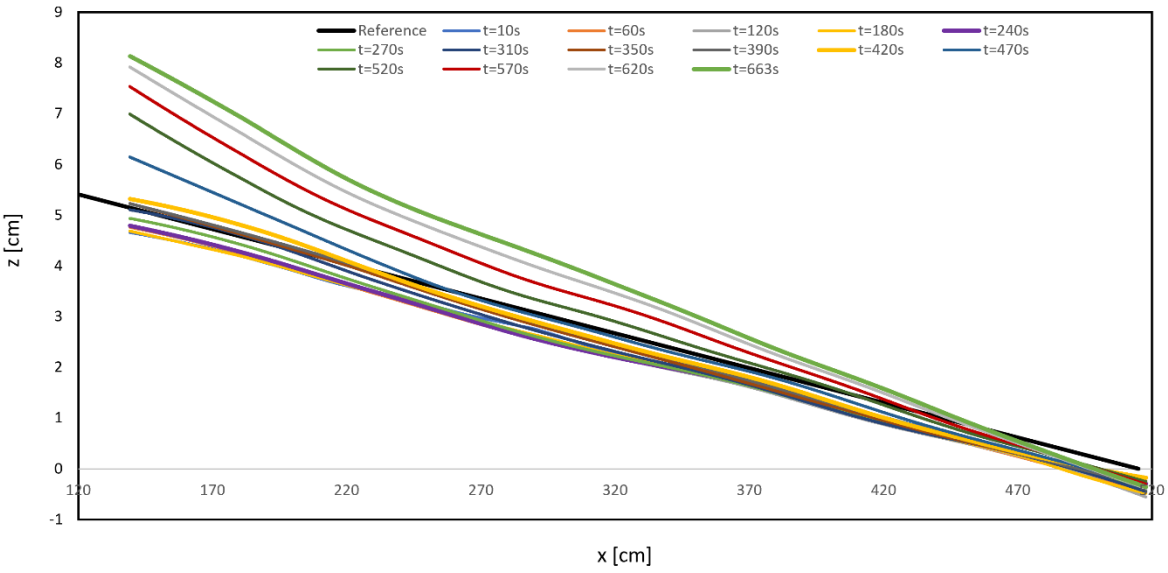
UnAE02 Color Gradient Maps

Experiment UnAE03

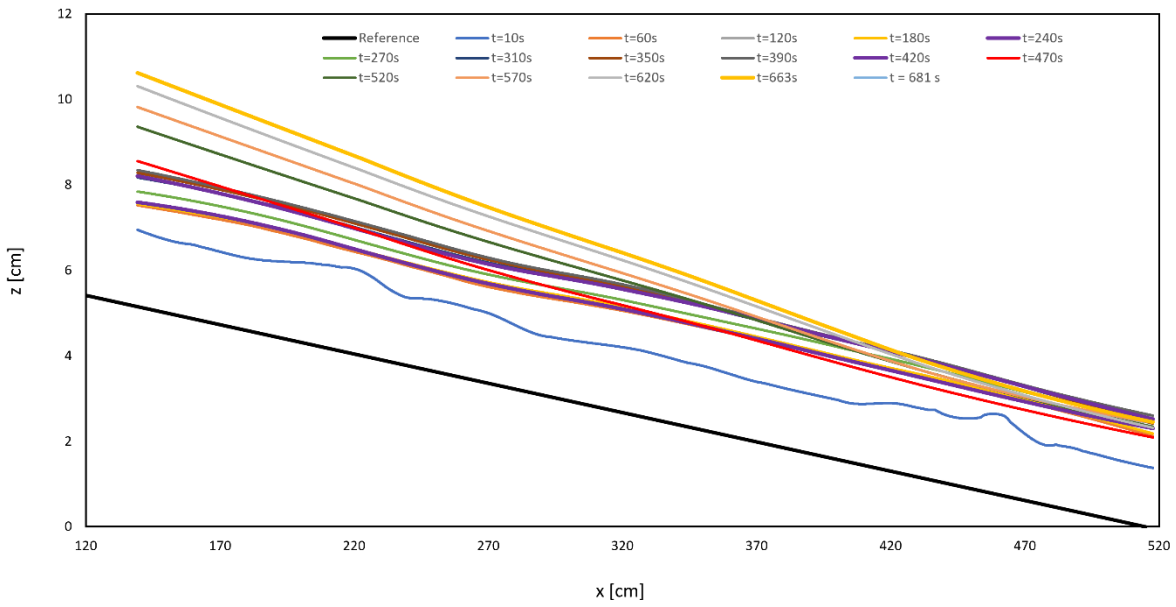
Phase	T (s)	S_0 (%)	Q (l/s)	h_0 (cm)	Fr	Vibration level	*Qsin (m³/s)*	*Qs0 (m³/s)*	Lr
P1	240	1.37	4	2.31	1.21	7.8	1.06E-04	1.06E-04	1.00
P2	180	1.35	5	2.68	1.22	8.3	1.85E-04	1.74E-04	1.06
P3	239	1.51	4	2.24	1.27	8.5	2.11E-04	1.42E-04	1.44



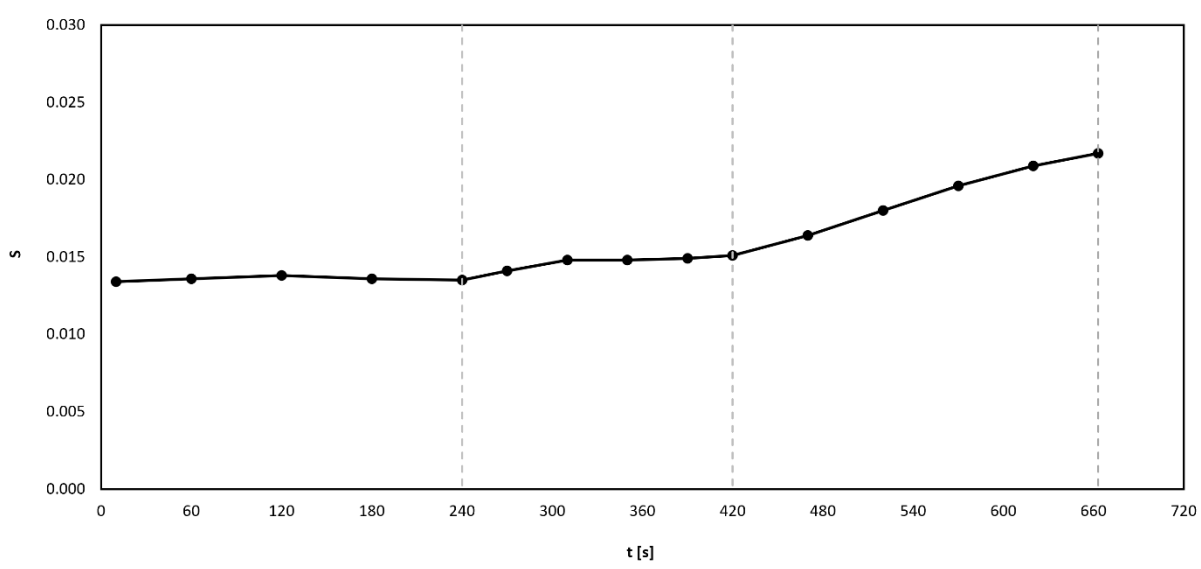
UnAE03 Temporal Evolution of Q_{sin}



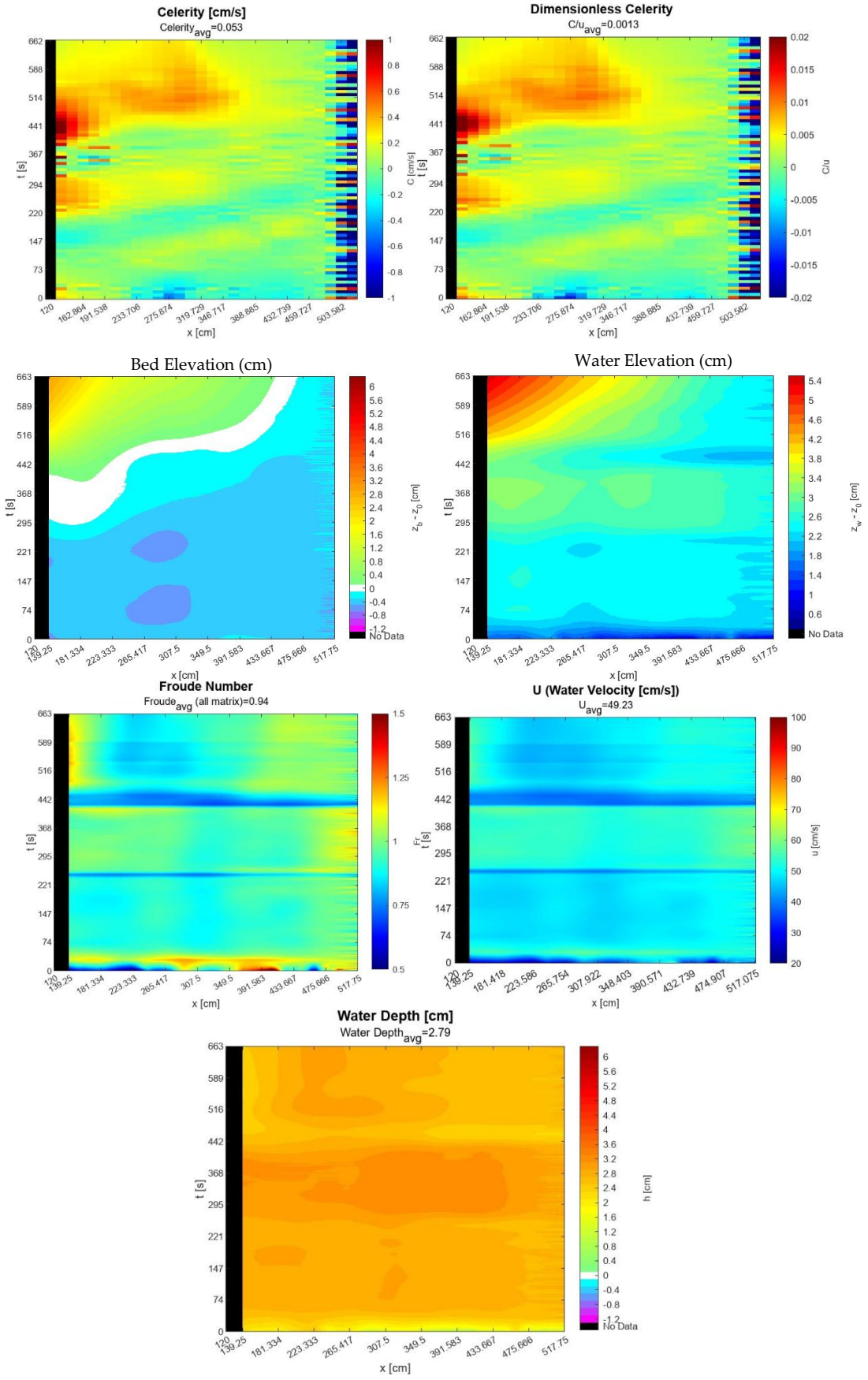
UnAE03 Spatial Bed Surface Profiles



UnAE03 Spatial Water Surface Profiles



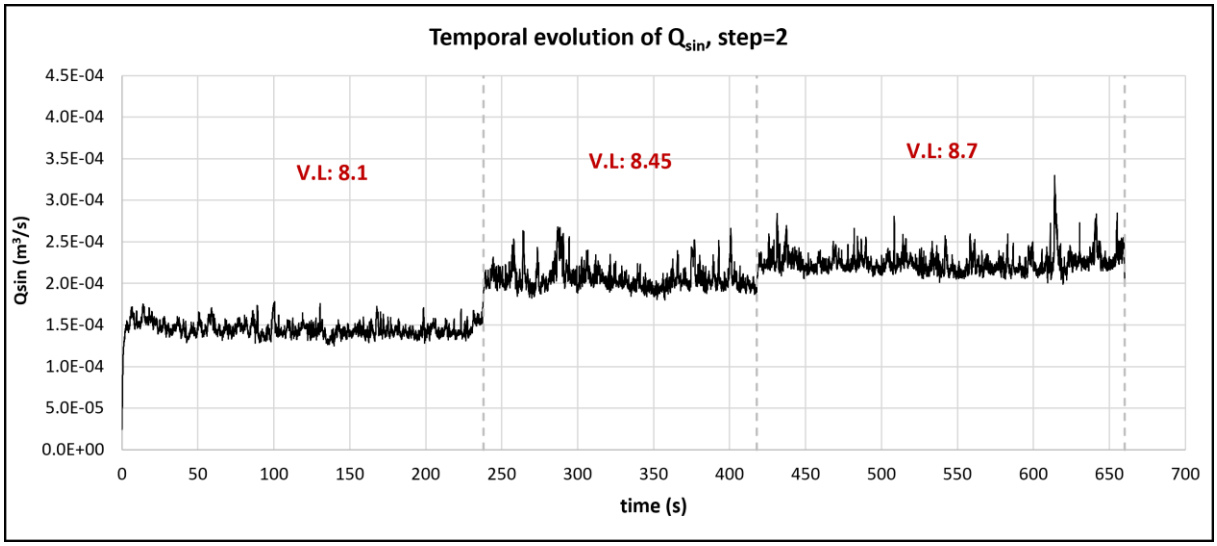
UnAE03 Temporal Evolution of Bed Slope



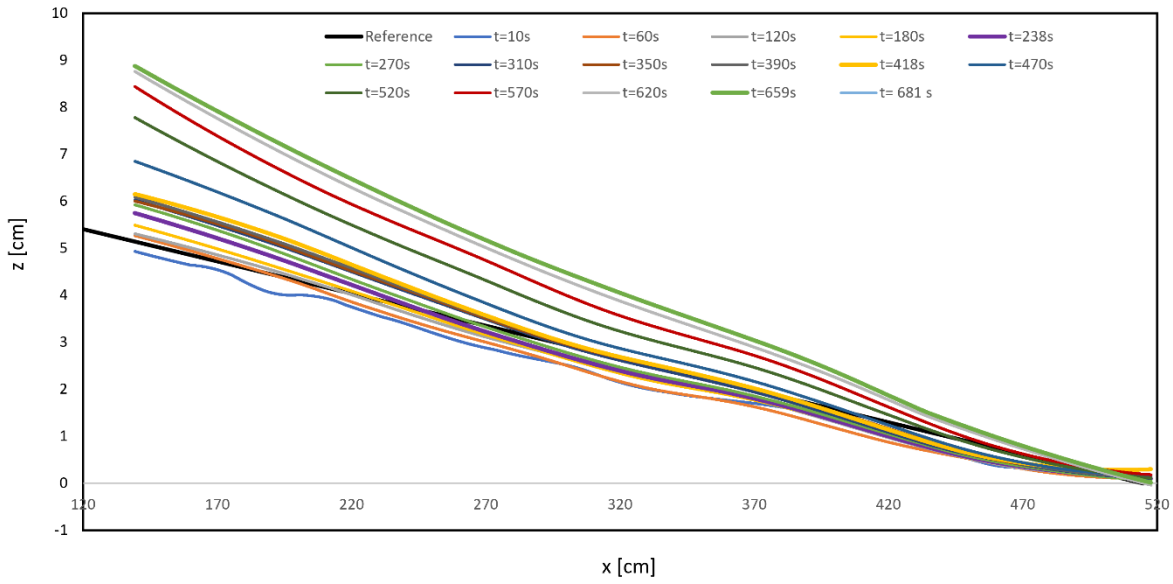
UnAE03 Color Gradient Maps

Experiment UnAE04 Parameters

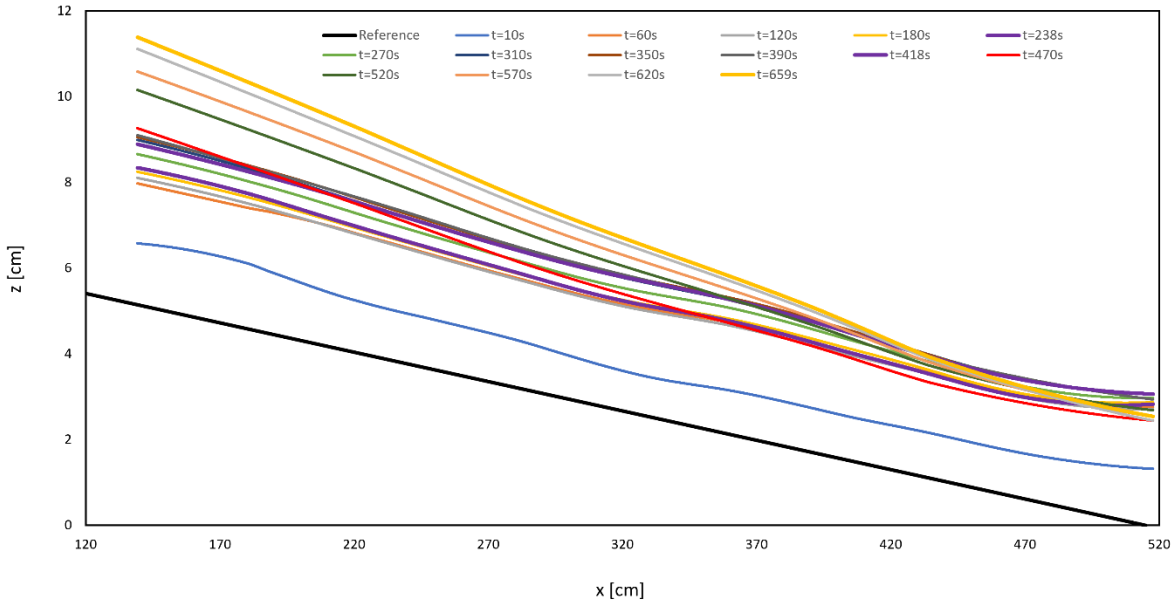
Phase	T (s)	S_0 (%)	Q (l/s)	h_0 (cm)	Fr	Vibration level	*Qsin* (m^3/s)	*Qs0* (m^3/s)	Lr
P1	238	1.37	4	2.31	1.21	8.1	1.45E-04	1.32E-04	1.09
P2	180	1.56	5	2.56	1.30	8.45	2.06E-04	1.88E-04	1.13
P3	238	1.67	4	2.17	1.33	8.7	2.25E-04	1.71E-04	1.28



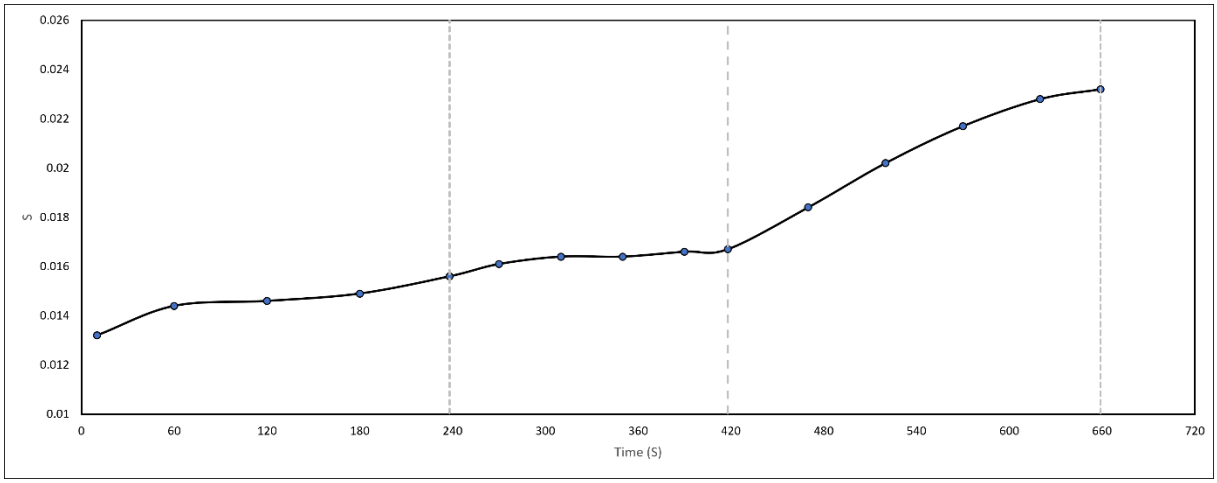
UnAE04 Temporal Evolution of Q_{sin}



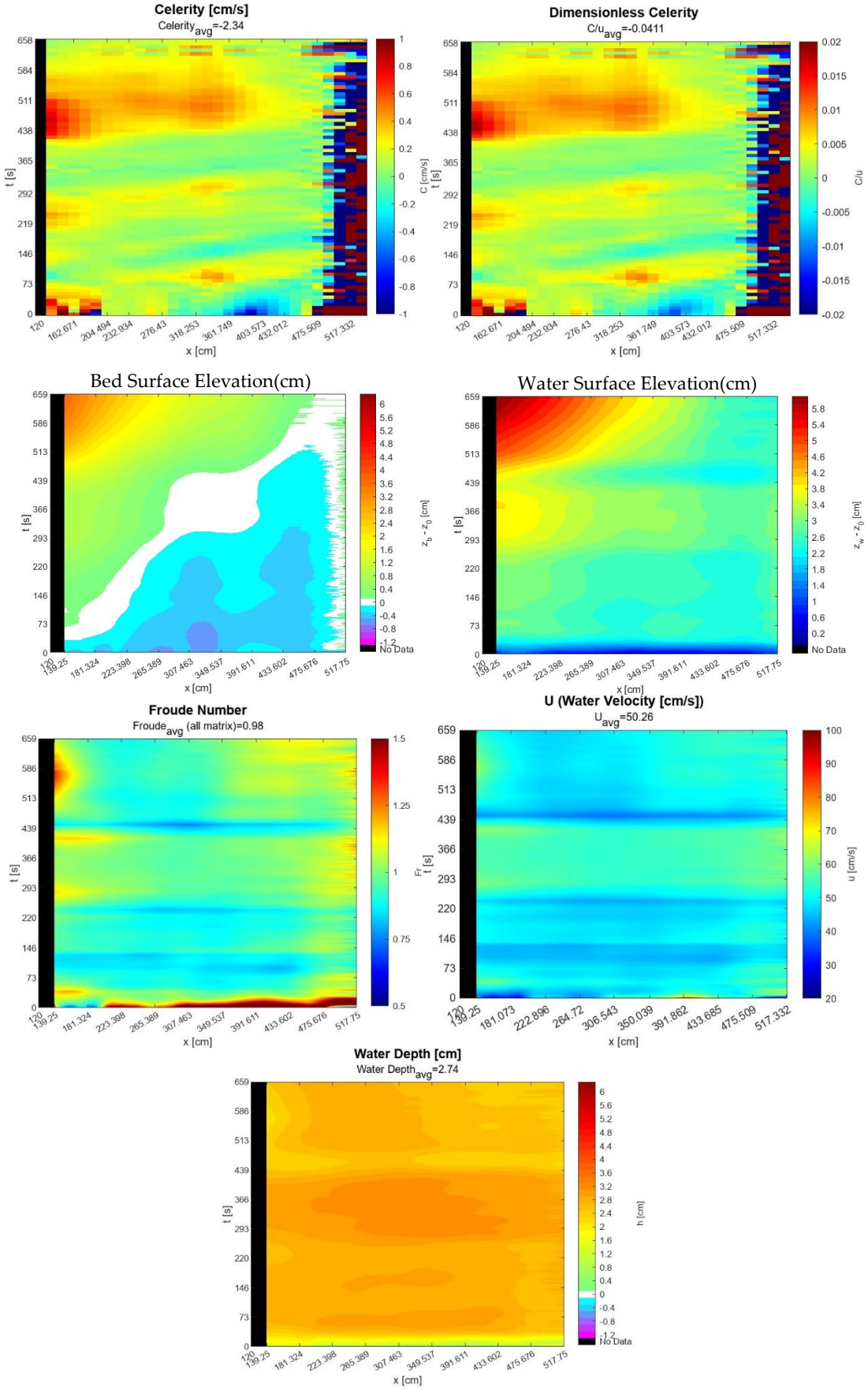
UnAE04 Spatial Bed Surface Profiles



UnAE04 Spatial Water Surface Profiles



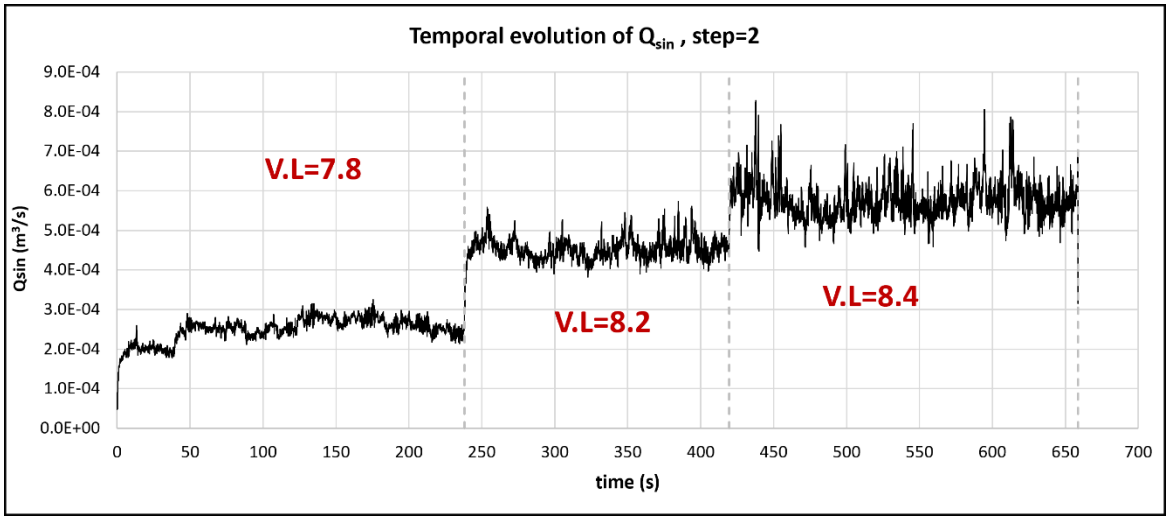
UnAE04 Temporal Evolution of Bed Slope



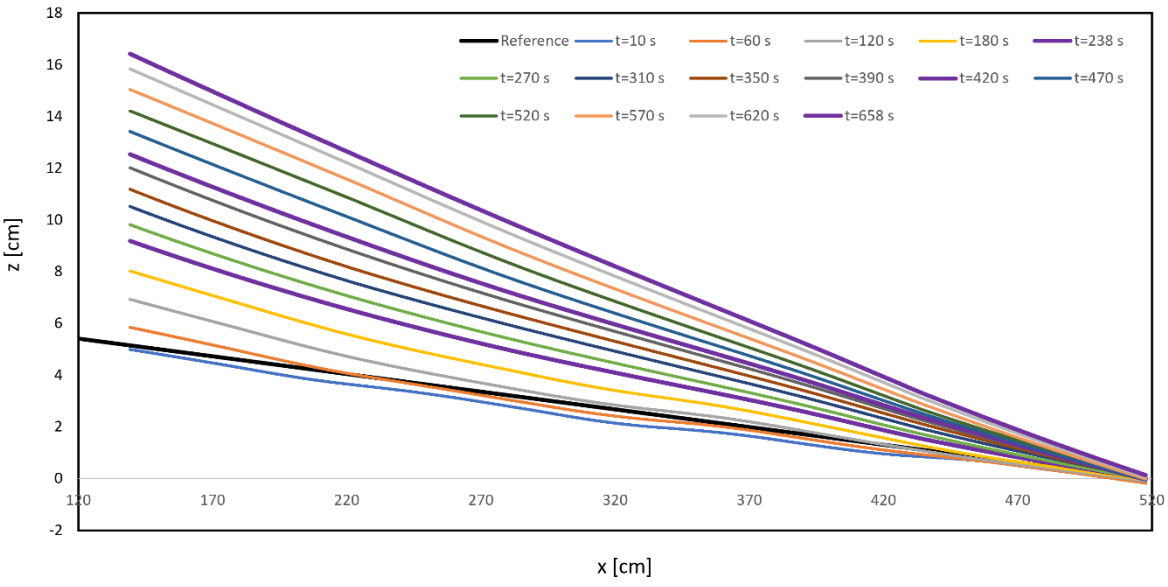
UnAE04 Color Gradient Maps

Experiment UnAE05 Parameters

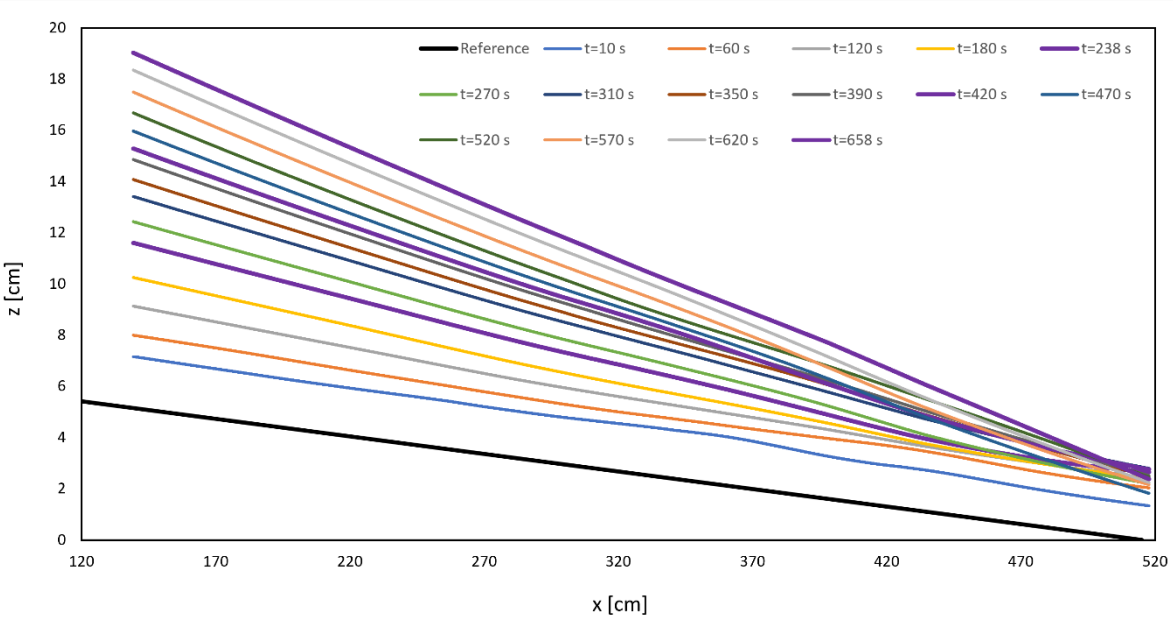
Phase	T (s)	S_0 (%)	Q (l/s)	h_0 (cm)	Fr	Vibration level	*Qsin* (m^3/s)	*Qs0* (m^3/s)	Lr
P1	238	1.37	4	2.31	1.21	7.8	2.49E-04	1.17E-04	2.13
P2	182	2.37	5	2.24	1.59	8.2	4.52E-04	3.49E-04	1.30
P3	239	3.28	4	1.76	1.82	8.4	5.76E-04	5.05E-04	1.14



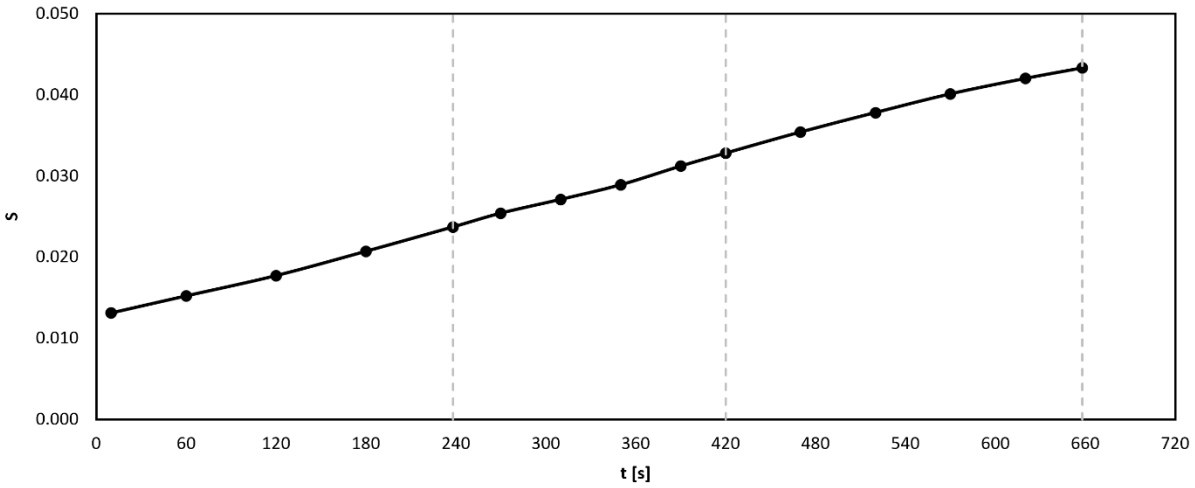
UnAE05 Temporal Evolution of Q_{sin}



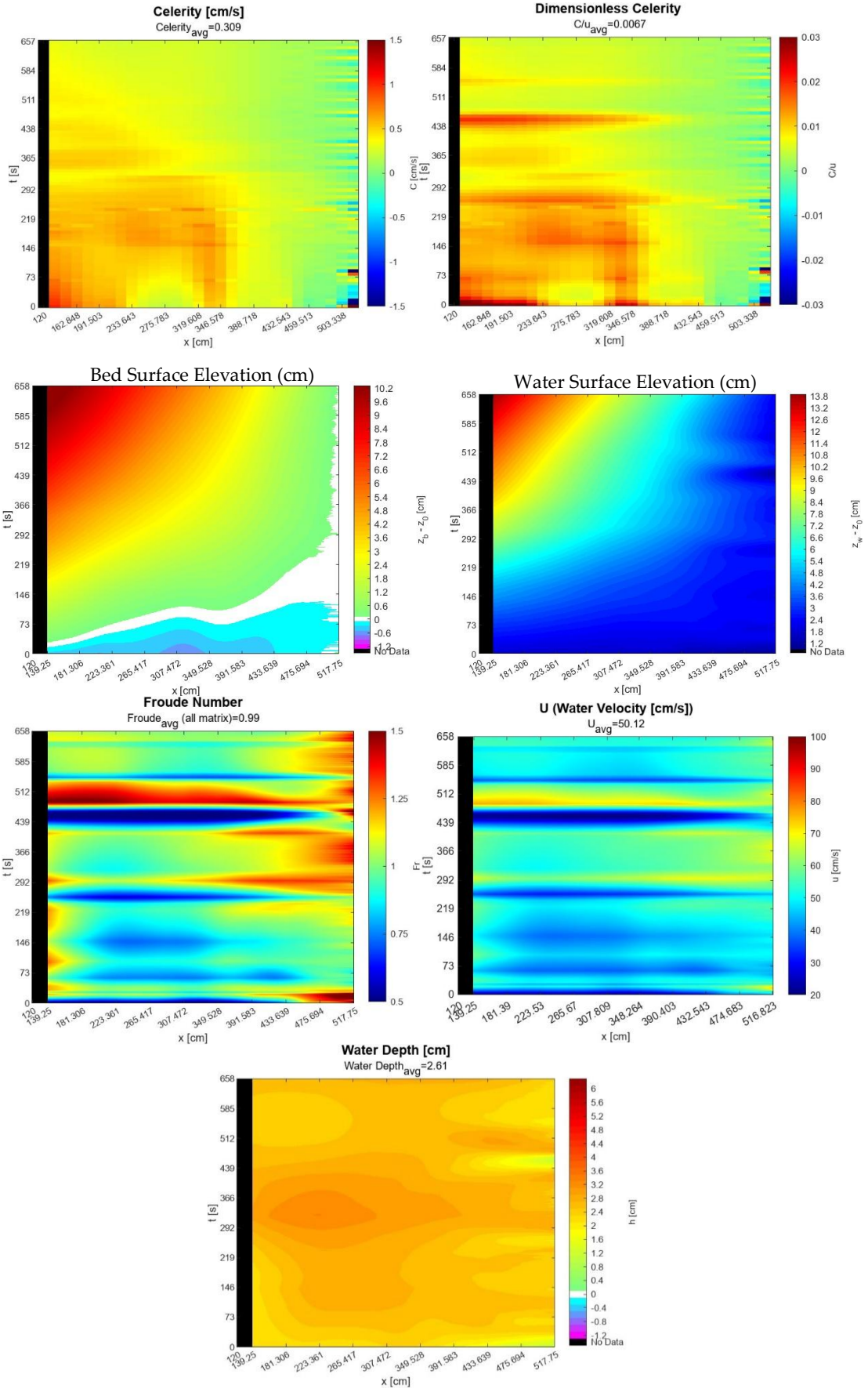
UnAE05 Spatial Bed Surface Elevation Profiles



UnAE05 Spatial Water Surface Elevation Profiles



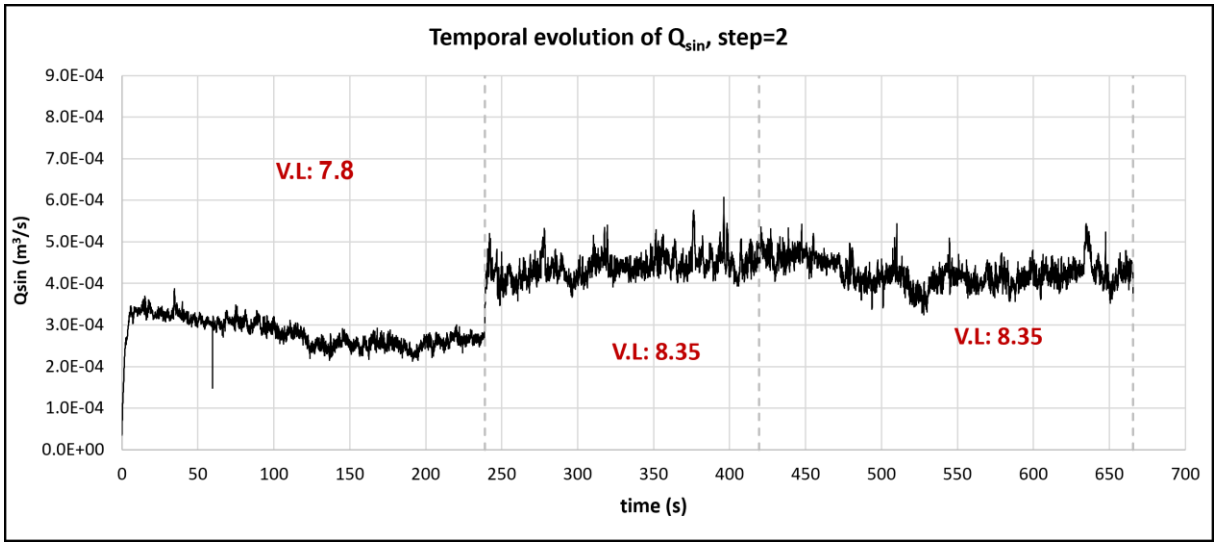
UnAE05 Temporal Evolution of Bed Slope



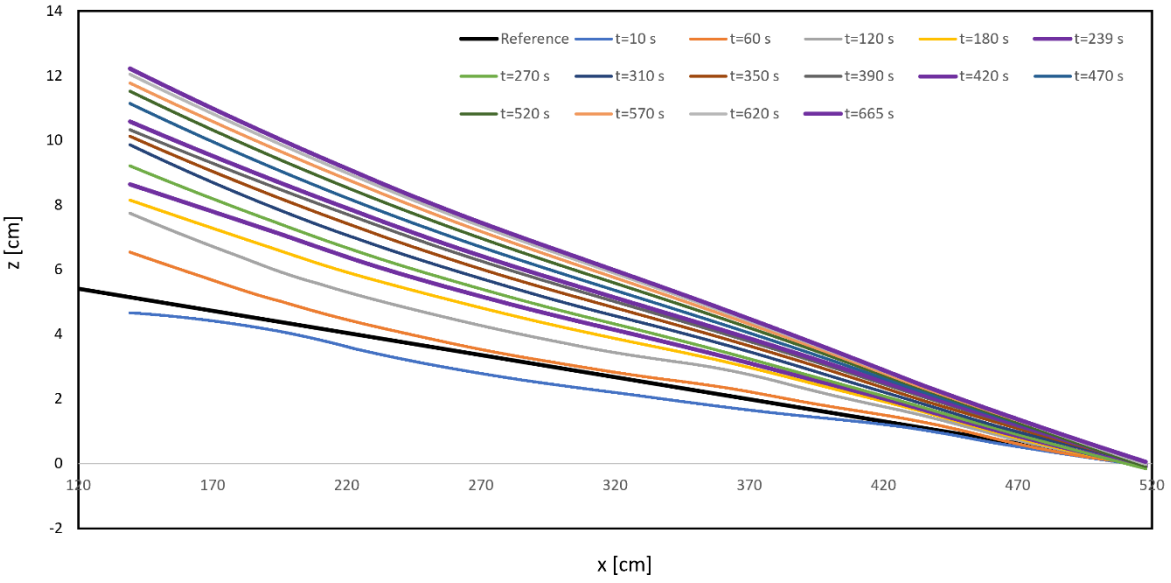
UnAE05 Color Gradient Maps

Experiment UnAE06 Parameters

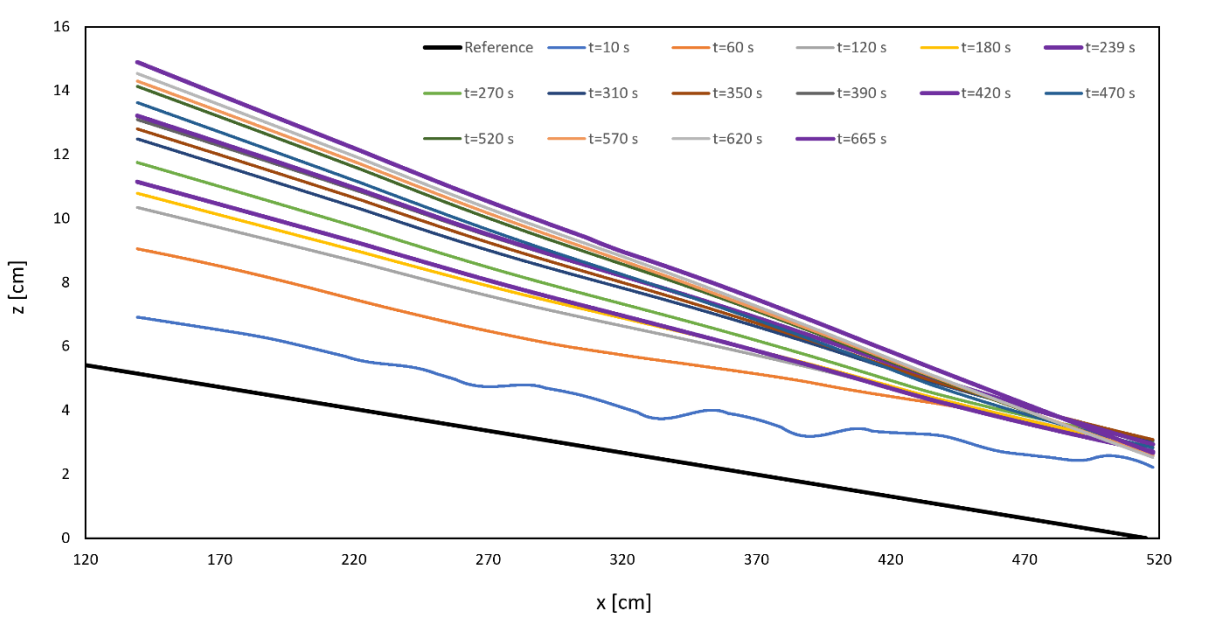
Phase	T (s)	S_0 (%)	Q (l/s)	h_0 (cm)	Fr	Vibration level	*Qsin (m^3/s)*	*Qs0 (m^3/s)*	Lr
P1	239	1.37	5	2.67	1.22	7.8	2.81E-04	1.28E-04	2.19
P2	181	2.26	6	2.55	1.56	8.35	4.40E-04	3.19E-04	1.38
P3	239	2.74	5	2.14	1.70	8.35	4.25E-04	3.97E-04	1.07



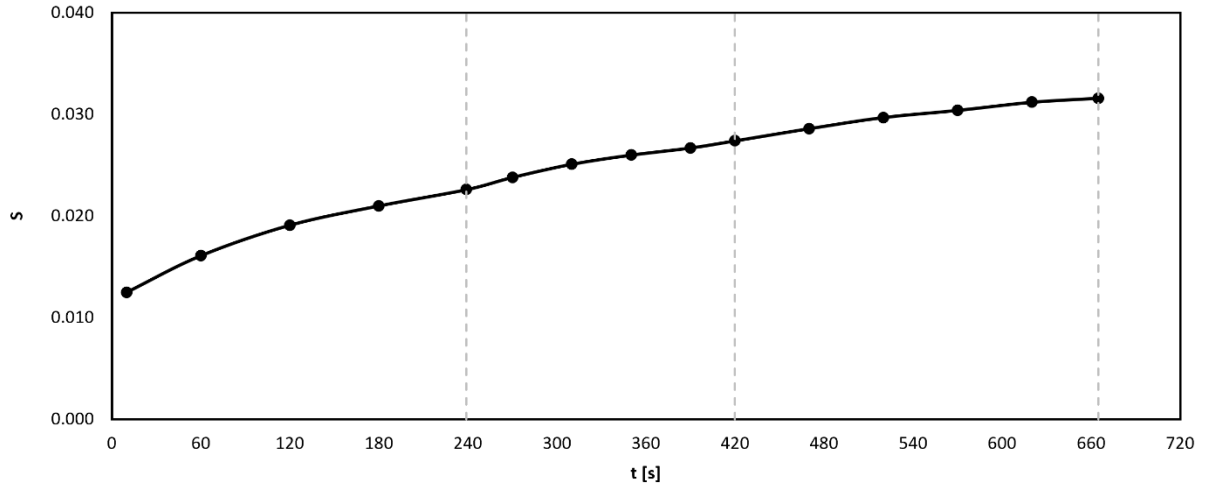
UnAE06 Temporal Evolution of Q_{sin}



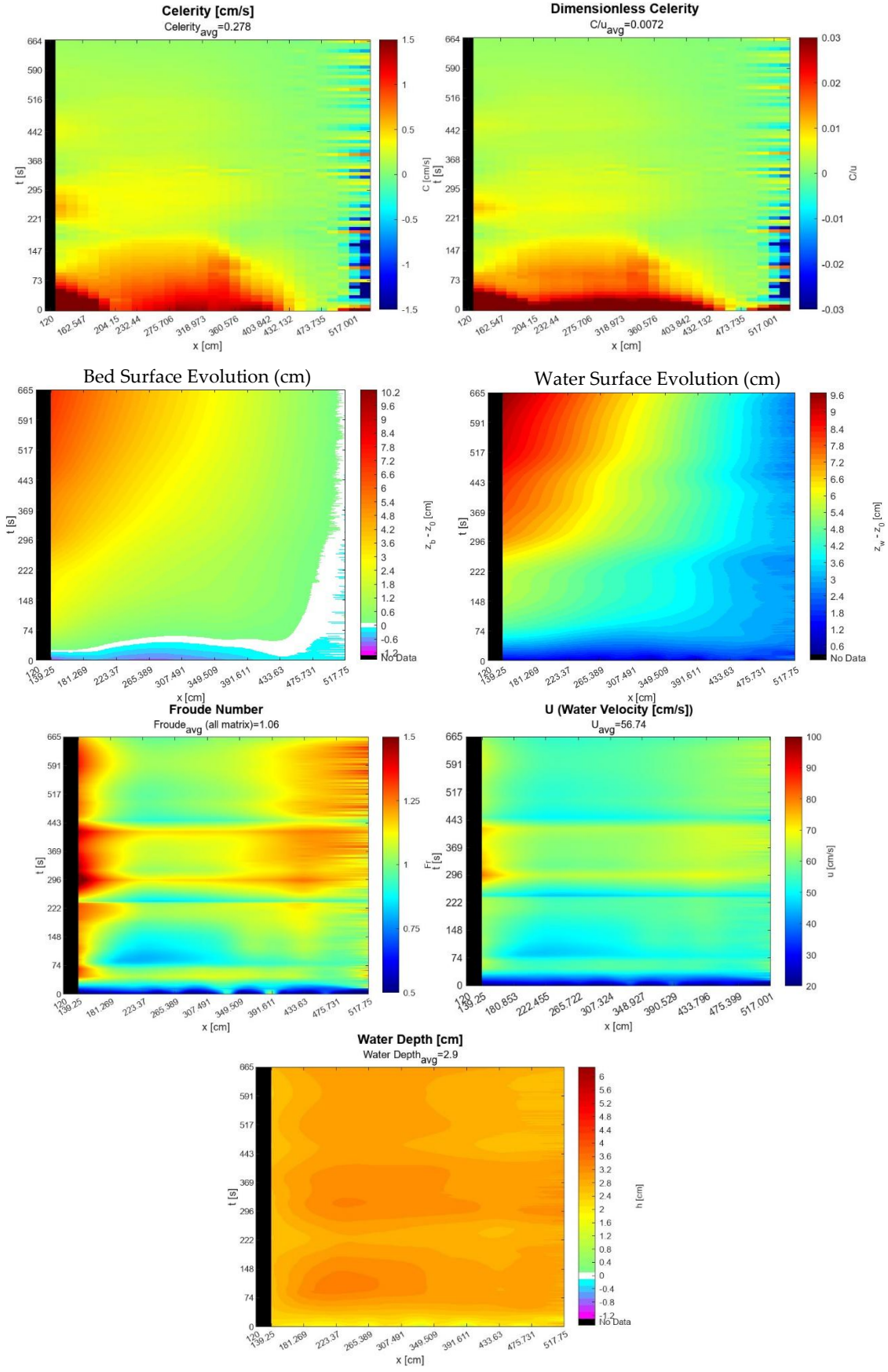
UnAE06 Spatial Bed Surface Elevation Profiles



UnAE06 Spatial Water Surface Elevation Profiles



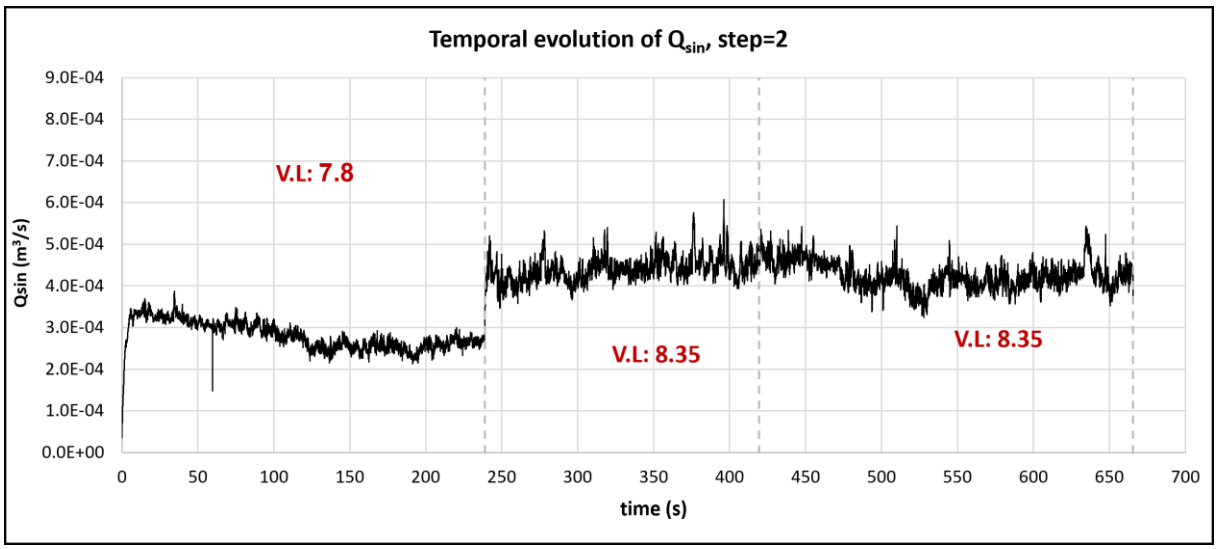
UnAE06 Temporal Evolution of Bed Slope



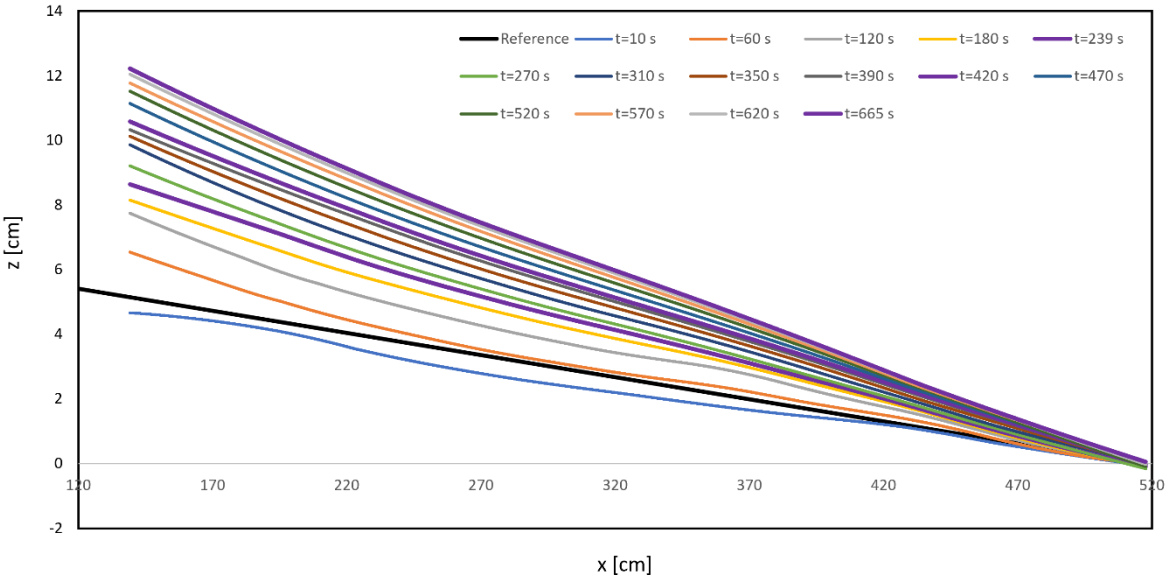
UnAE06 Color Gradient Maps

Experiment UnAE07 Parameters

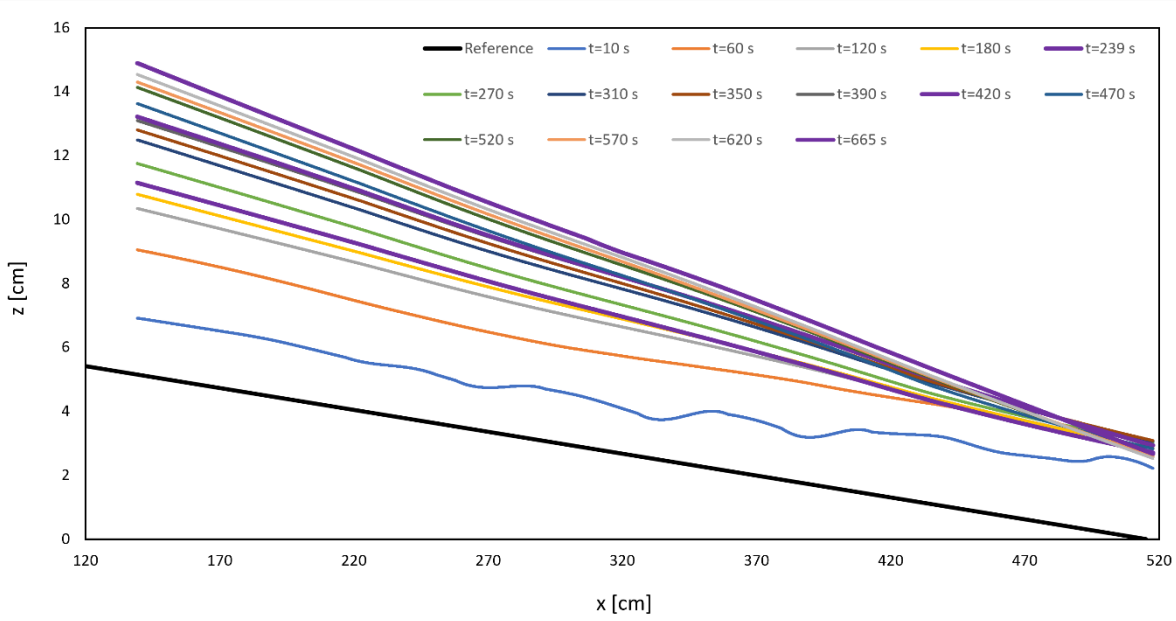
Phase	T (s)	S_0 (%)	Q (l/s)	h_0 (cm)	Fr	Vibration level	*Qsin (m³/s)*	*Qs0 (m³/s)*	Lr
P1	180	1.37	4	2.31	1.21	7.8	2.28E-04	1.01E-04	2.26
P2	179	2.20	5	2.29	1.53	8.05	4.19E-04	3.25E-04	1.29
P3	153	3.24	6	2.28	1.85	10	7.17E-04	6.26E-04	1.14
P4	238	4.06	5	1.89	2.04	10	6.82E-04	6.45E-04	1.06
P5	48	4.13	4	1.64	2.03	10	6.66E-04	7.39E-04	0.90



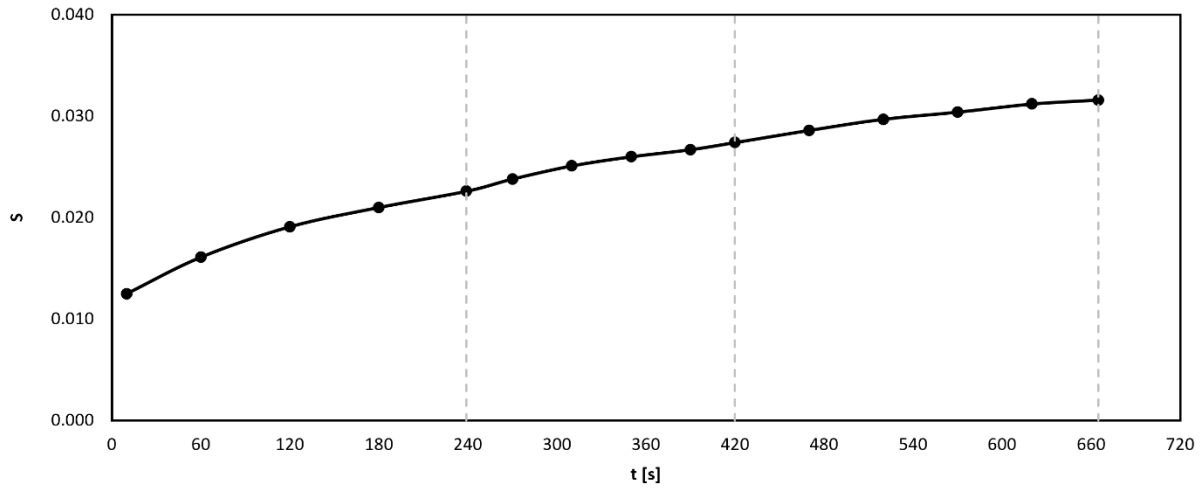
UnAE07 Temporal Evolution of Q_{sin}



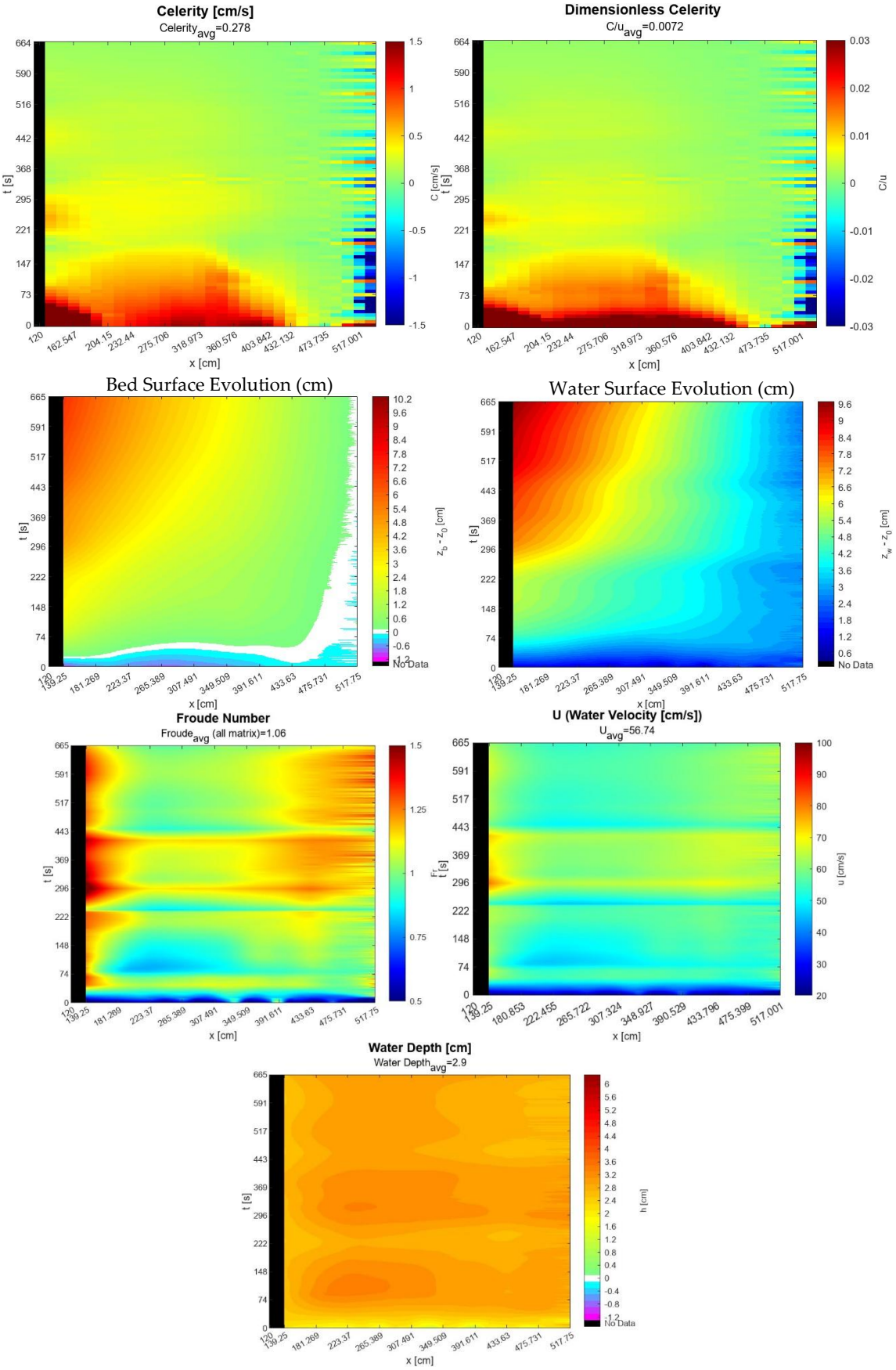
UnAE07 Spatial Water Surface Elevation Profiles



UnAE07 Spatial Water Surface Elevation Profiles



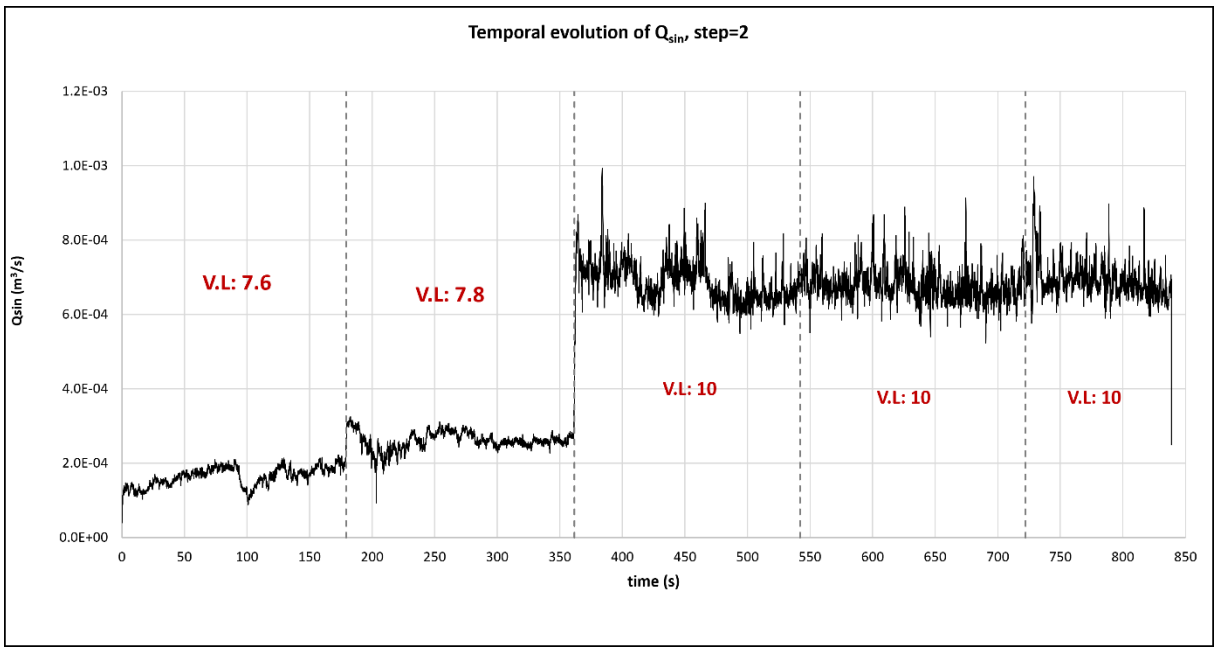
UnAE07 Temporal Evolution of Bed Slope



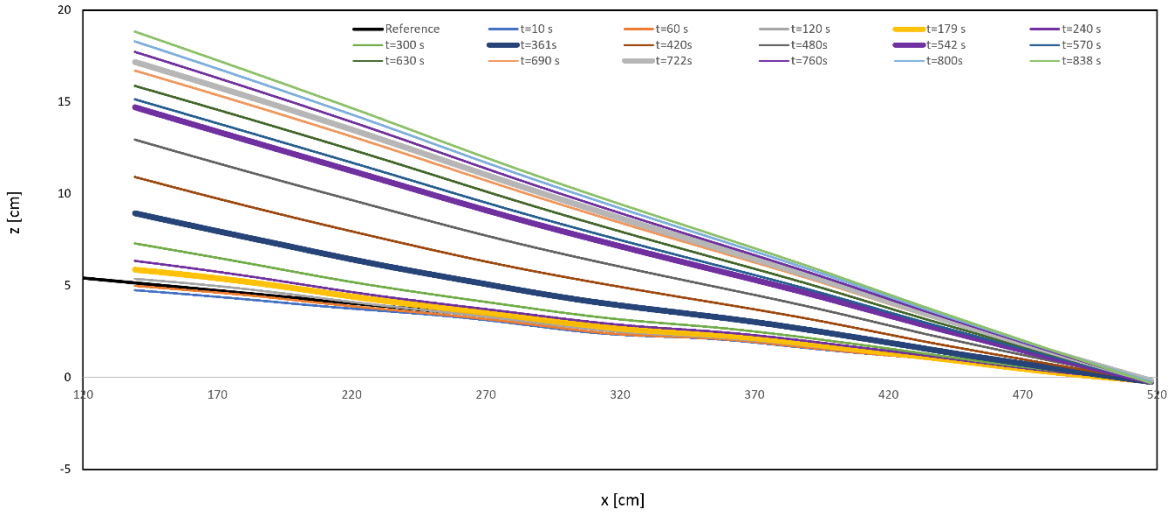
UnAE07 Color Gradient Maps

Experiment UnAE08 Parameters

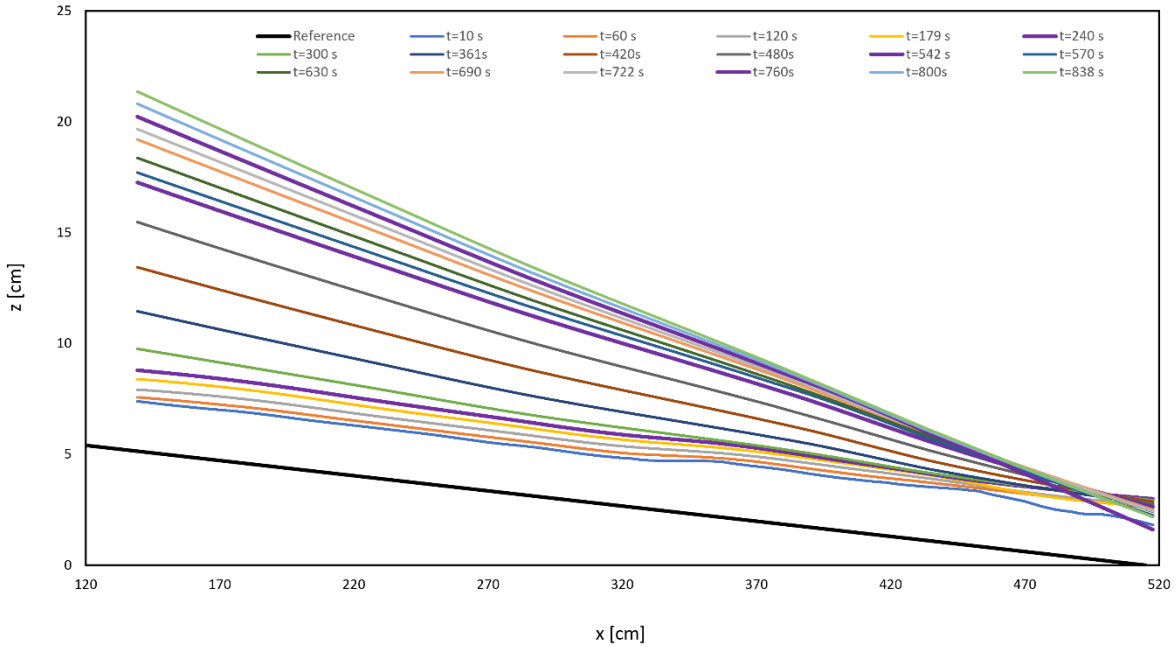
Phase	T (s)	S_0 (%)	Q (l/s)	h_0 (cm)	Fr	Vibration level	*Qsin (m^3/s)*	*Qs0 (m^3/s)*	Lr
P1	179	1.37	4	2.31	1.21	7.6	1.64E-04	1.32E-04	1.14
P2	182	1.56	5	2.56	1.30	7.8	2.61E-04	2.08E-04	1.28
P3	181	2.30	6	2.54	1.58	10	6.88E-04	5.35E-04	1.31
P4	180	3.90	5	1.92	2.00	10	6.77E-04	5.99E-04	1.15
P5	76	4.60	4	1.58	2.13	10	6.92E-04	6.22E-04	1.11



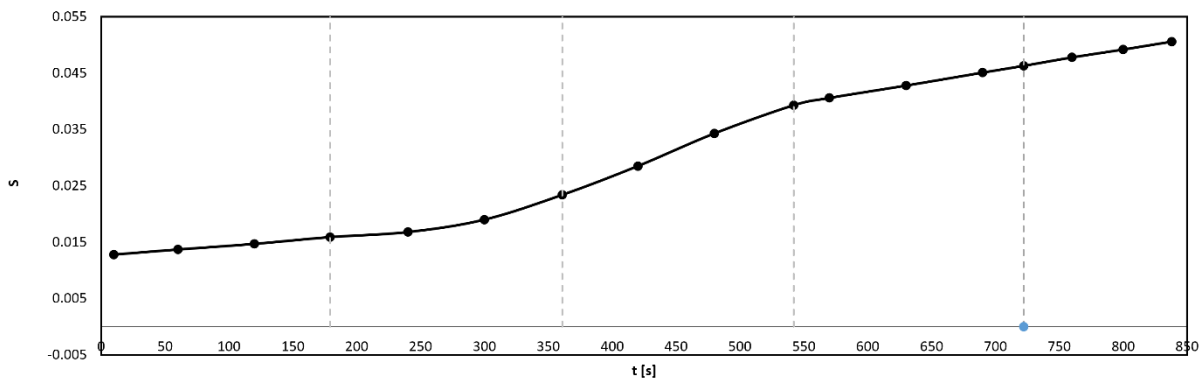
UnAE08 Temporal Evolution of Q_{sin}



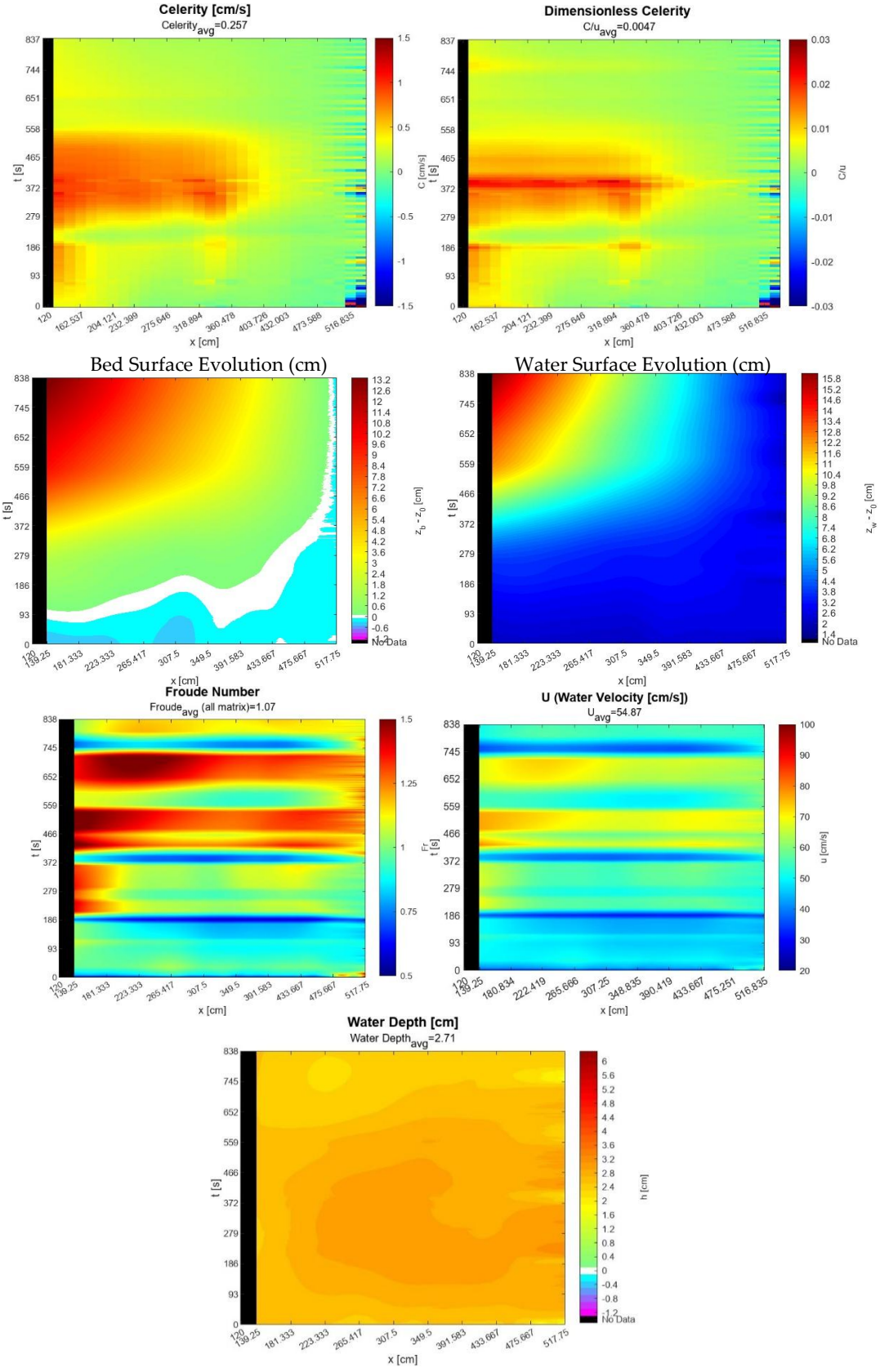
UnAE8 Spatial Bed Surface Elevation Profiles



UnAE8 Spatial Water Surface Elevation Profiles



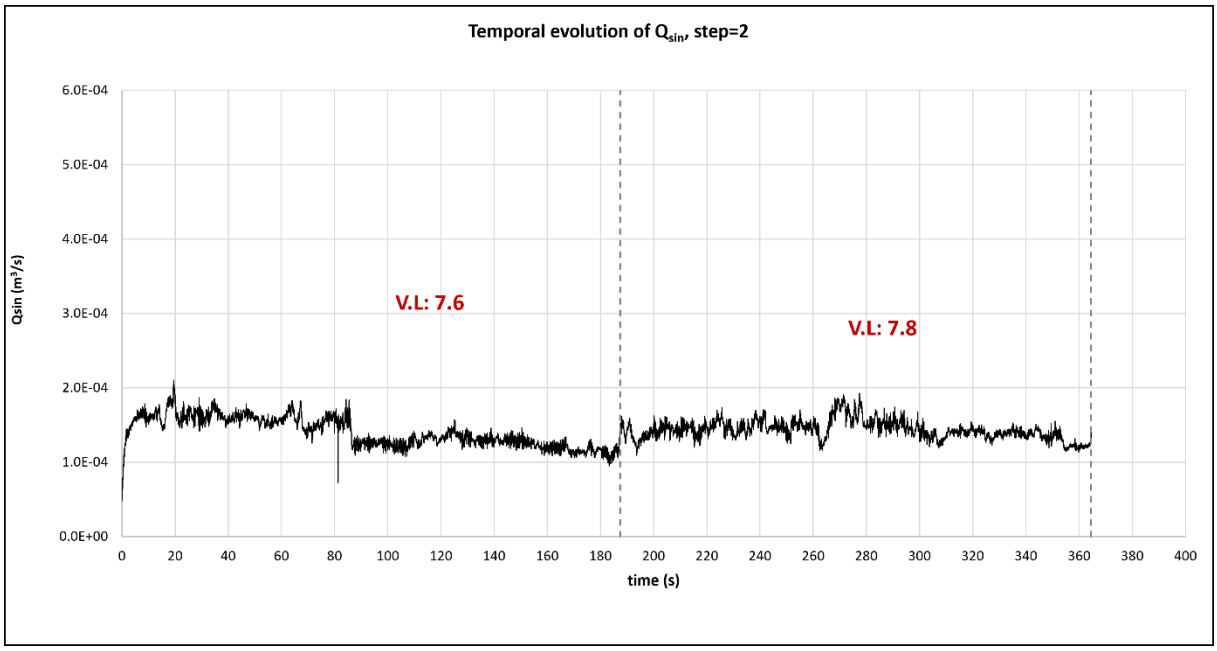
UnAE08 Temporal Evolution of Bed Slope



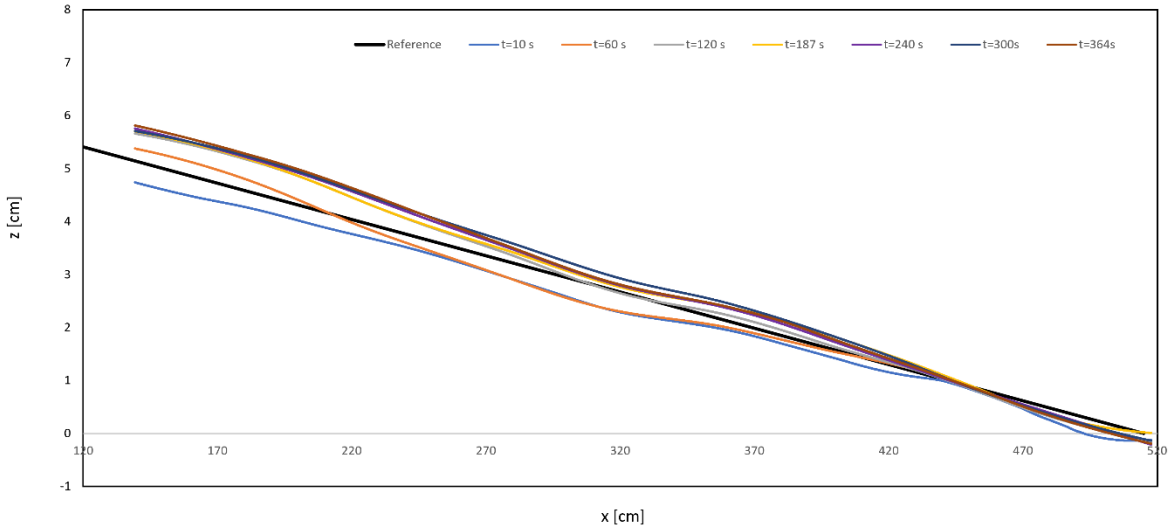
UnAE08 Color Gradient Maps

Experiment UnAE09 Parameters

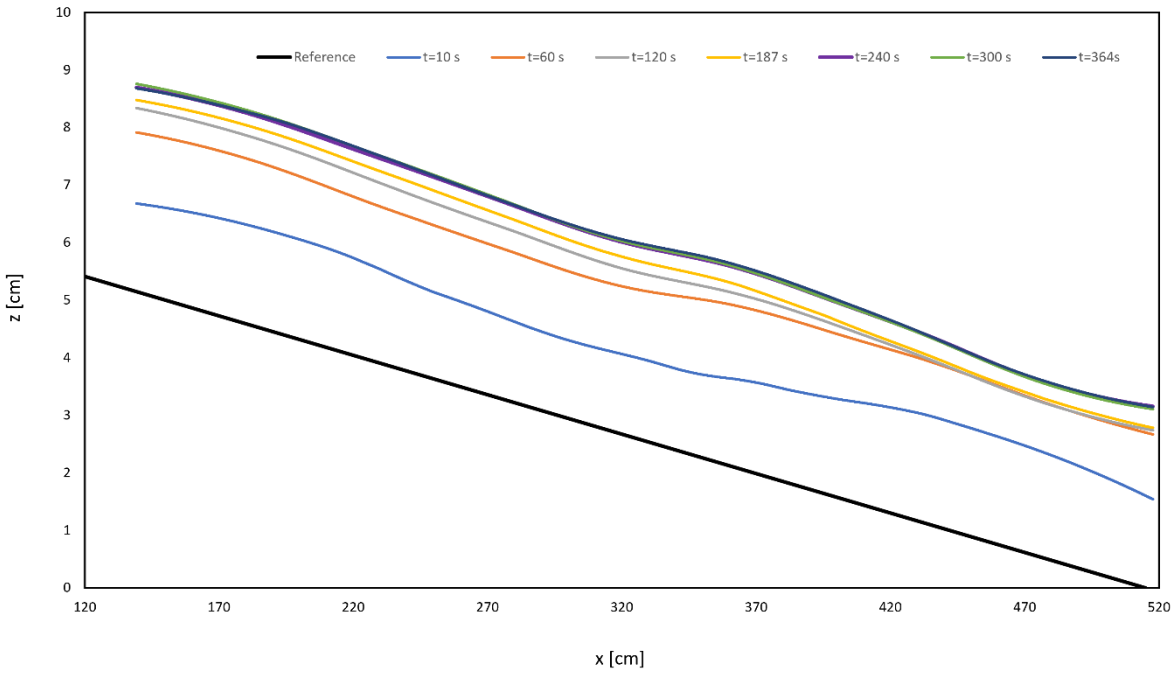
Phase	T (s)	S_0 (%)	Q (l/s)	h_0 (cm)	Fr	Vibration level	*Qsin (m³/s)*	*Qs0 (m³/s)*	Lr
P1	187	1.37	4	2.31	1.21	7.6	1.40E-04	1.08E-04	1.27
P2	177	1.55	5	2.56	1.30	7.8	1.43E-04	1.38E-04	1.04



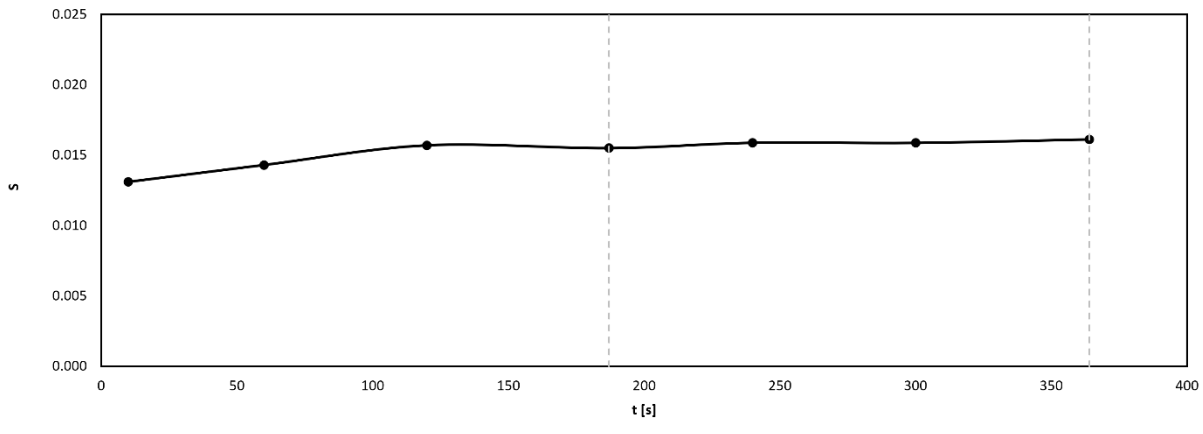
UnAE09 Temporal Evolution of Q_{sin}



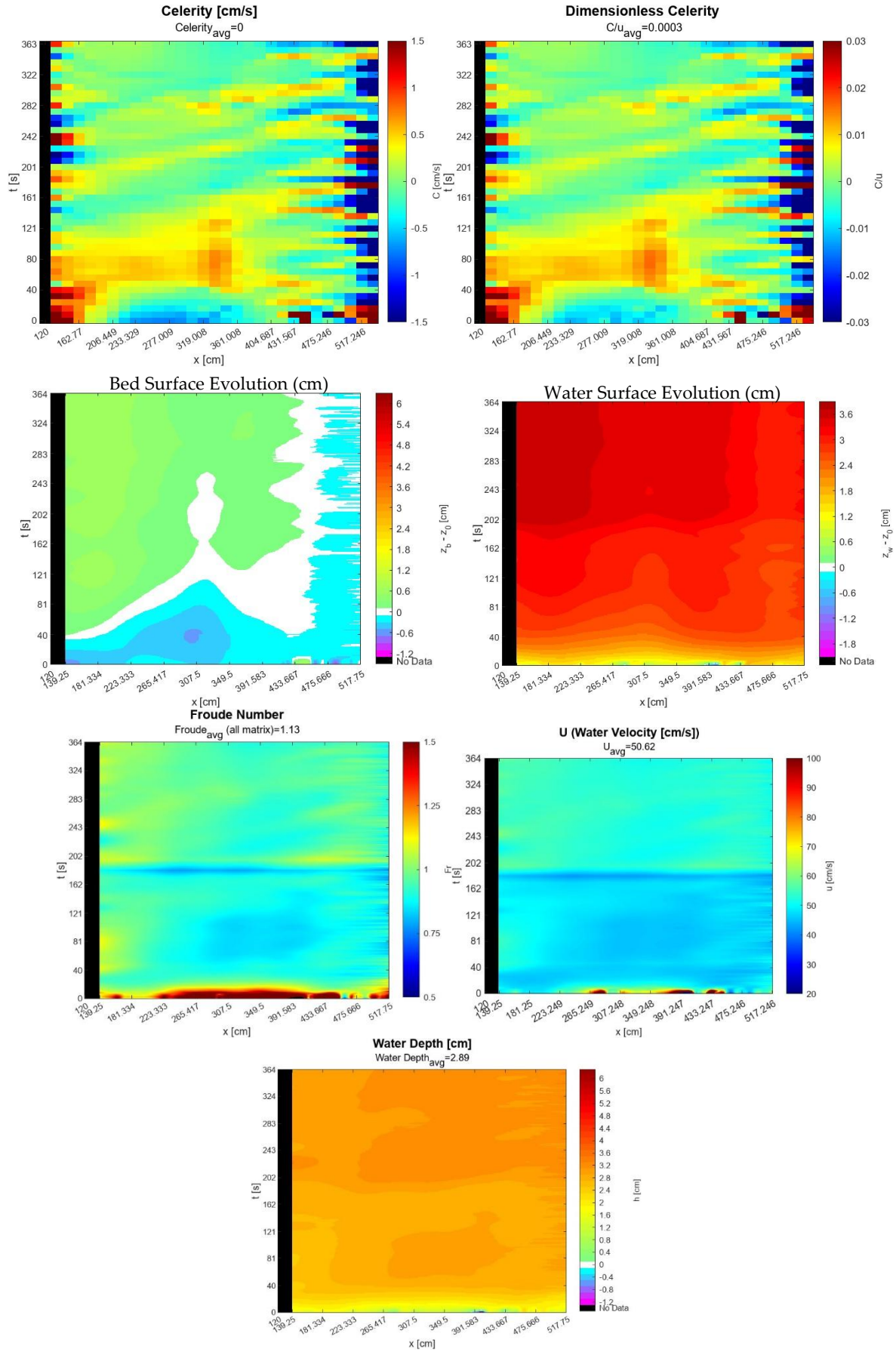
UnAE9 Spatial Bed Surface Elevation Profiles



UnAE09 Spatial Water Surface Elevation Profiles



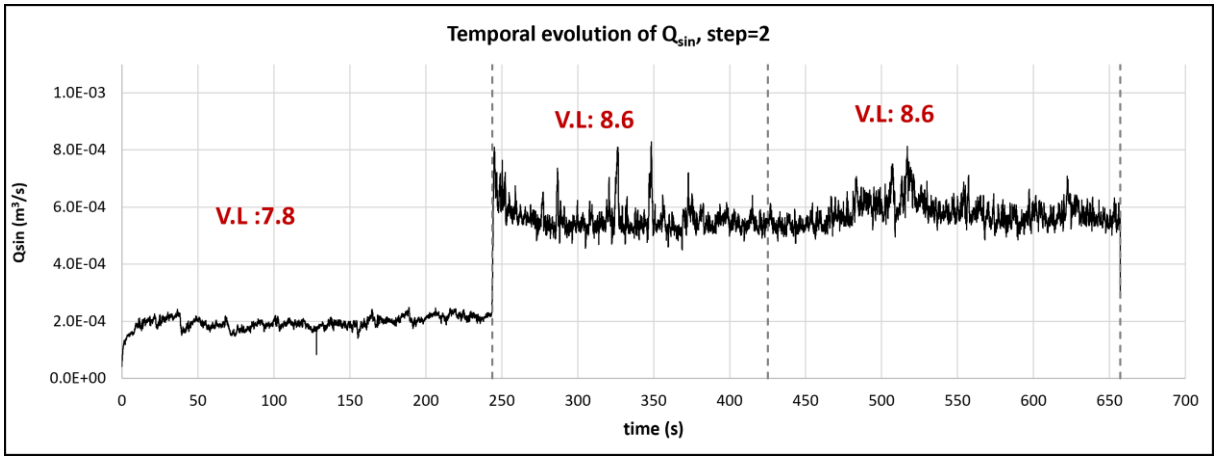
UnAE09 Temporal Evolution of Bed Slope



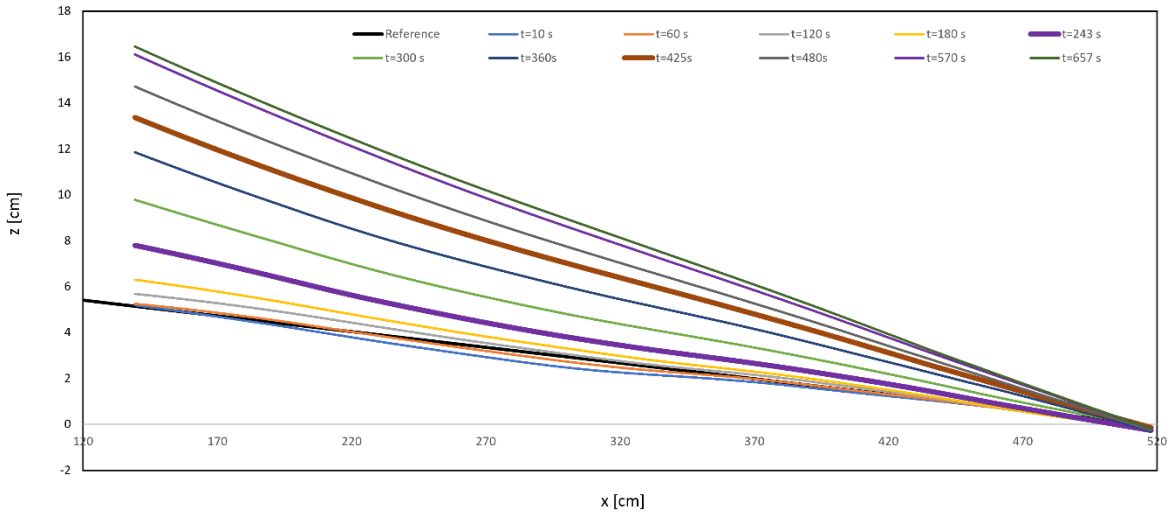
UnAE09 Color Gradient Maps

Experiment UnAE10 Parameters

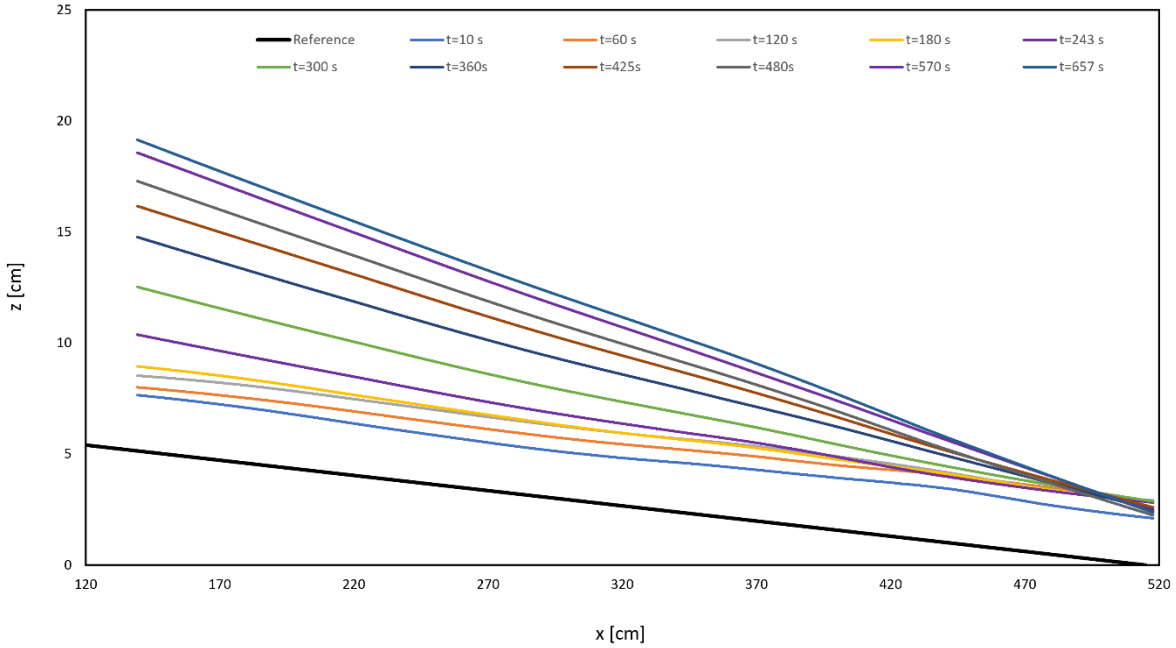
Phase	T (s)	S_0 (%)	Q (l/s)	h_0 (cm)	Fr	Vibration level	*Qsin (m^3/s)*	*Qs0 (m^3/s)*	Lr
P1	265	1.37	5	2.67	1.22	7.8	1.95E-04	1.48E-04	1.29
P2	160	2.04	6	2.57	1.54	8.6	5.57E-04	3.57E-04	1.56
P3	232	3.46	5	1.99	1.90	8.6	5.78E-04	4.01E-04	1.44



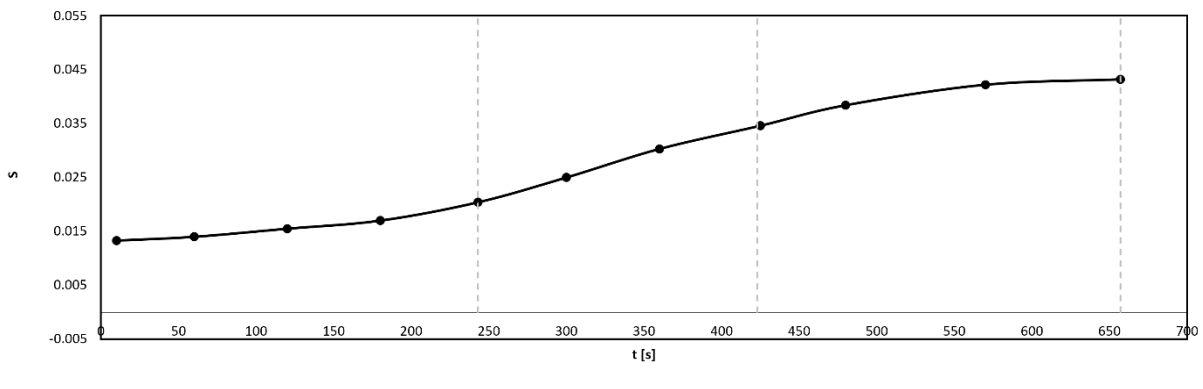
UnAE10 Temporal Evolution of Q_{sin}



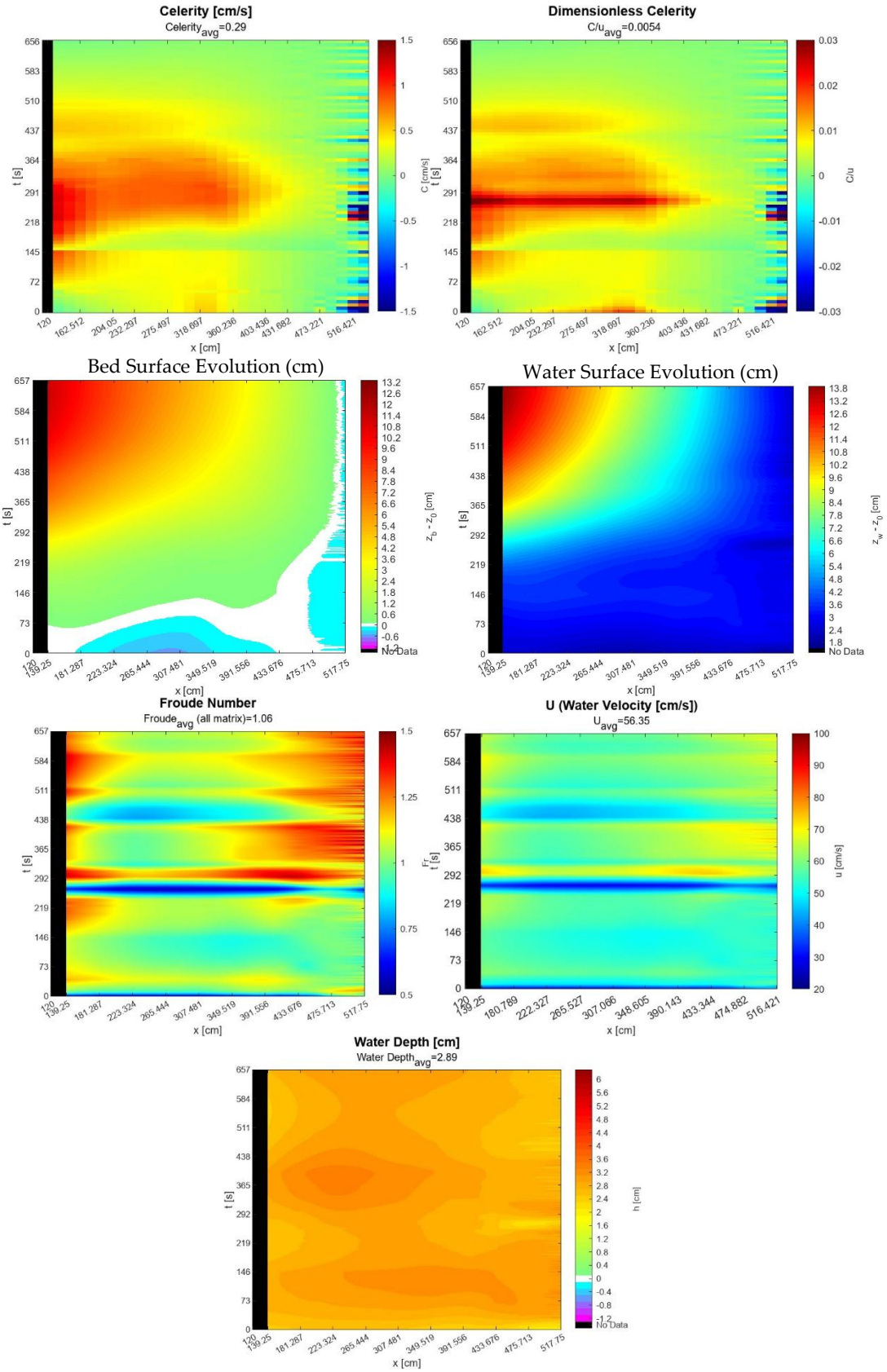
UnAE9 Spatial Bed Surface Elevation Profiles



UnAE9 Spatial Water Surface Elevation Profiles



UnAE010 Temporal Evolution of Bed Slope



UnAE010 Color Gradient Maps

List of Figures

Figure 1.1: Zingg diagram for grain shape classification 10

Figure 1.2 Grain radii (Friedman et al., 1992) 10

Figure 1.3: Grain roundness classes (Powers, 1953) 10

Figure 1.4: Forms of sediment transport (Fryirs & Brierley, 2019) 11

Figure 1.5: Definition sketch of threshold velocity concept 12

Figure 1.6: Threshold velocities vs. median particle size for quartz sediments (Vanoni, 1977) 13

Figure 1.7: Forces acting on a sediment particle (Rowinski, 2014) 14

Figure 1.8: Shields diagram — Θc as a function of $R*$(Shields, 1936) 14

Figure 1.9: Particle equilibrium in transitional and rough flow (Rowinski, 2014) 14

Figure 1.10: Particle equilibrium in smooth flow (Rowinski, 2014) 15

Figure 2.1: Schematic representation of experimental setup and camera positions (Eslami,2025) 21

Figure 2.2: Experimental setup 22

Figure 2.3: (a) Screw jack and (b) Laser distance meter 23

Figure 2.4 Relationship between laser distance reading and channel slope (Fazzini and Mottini, 2015) 23

Figure 2.5: Fixed plastic plates at upstream and downstream ends (Gamal et, al.,2023) 24

Figure 2.6: (a) Upstream water tank and (b) Flow meter 24

Figure 2.7: Two downstream collectors 25

Figure 2.8: Modified underground channel 26

Figure 2.9: Inlet tank water level monitoring system: (a) computer setup; (b) laser sensor installation slot 27

Figure 2.10: PVC sediment particles — (a) new and (b) old material 27

Figure 2.11: CFD plots of new material — (a) height, (b) equivalent mean diameter, (c) volume 29

Figure 2.12: (a) adjustable gate and vibrating channel; (b) vibration intensity indicator; (c) location of the hopper within the experimental channel 32

Figure 2.13: Sediment feeding rates across vibration levels and opening heights 33

Figure 2.14: Transfer functions for all opening heights — current work (red numbers: vibration levels) 34

Figure 2.15: Comparison of transfer functions between current and previous campaign in different vibration levels for opening height = 3 cm 35

Figure 2.16: Temporal evolution of (a) Umean and (b) Qsin for experiment UnAE05 36

Figure 2.17: Sediments spread for drying 39

Figure 2.18: Camera 1 positioned along the channel side 40

Figure 2.19: Camera 2 positioned above the vibrating channel 41

Figure 2.20: Camera 3 recording the flowmeter 41

Figure 2.21: Comparison between flume and flowmeter discharge — UnAE03 43

Figure 2.22: (a) first selected frame F1; (b) second selected frame F2 44

Figure 2.23: graphical explanation of Jump and Step parameters 44

Figure 2.24: working area defined within F1 45

Figure 2.25: Working area and cartesian direction 46

Figure 2.26: Width of vibrating channel — 22 cm 46

Figure 2.27: Cropped grayscale frame of the channel during UnAE05 48

Figure 2.28: Binary image showing detected motion in black 49

Figure 2.29: Schematic of moving window in initial position 49

Figure 2.30: Selected vertical column used to extract the intensity profile. 49

Figure 2.31: Intensity profile used to identify the water surface and stationary bed boundaries. 49

Figure 2.32: Bed elevation profile (Eslami et al.,2022) 50

Figure 2.33: *Three types of errors in the detection process — (a) residual noise; (b) detection gap; (c) external motion (Achkar et al.,2024)* 50

Figure 2.34: Three types of errors in the detection process — (a) residual noise; (b) detection gap; (c) external motion (Achkar et al.,2024) 51

Figure 2.35: (a) Black Curtain Covering Windows (b) Green Paper Covering Noises Behind Channel 51

Figure 2.36: (a) Corrected bed and (b) Water surface profiles (Eslami et al.,2022) 51

Figure 2.37: Bed and water surface profiles in the referenced coordinate system at t = 180 seconds during experiment UnAE06, with the reference initial bed defined by black tapes positioned 15 cm above the channel bottom. 52

Figure 2.38: SC test temporal evolution of Qsin from PIV 55

Figure 2.39: Temporal evolution of bed elevation at different x 56

Figure 2.40: Channel sections location 56

Figure 2.41 (a) CU (b) IU explanatory sketches in UnAE01 58

Figure 2.42: Comparison of V_(measured_bed) between CU and IU scenarios(UnAE03) 59

Figure 2.43: Temporal evolution of V_(measured_bed) for Phase 1 of UnAE08 —IU, CU scenarios — 5%, 10%, and 15% slope evolution thresholds 61

Figure 3.1: Schematic representation of a 5-step hydrograph used in experiments 63

Figure 3.2: Temporal evolution of water discharge and Qs, in *for UnAE05 & UnAE07* 64

Figure 3.3: Spatial profiles of (a) bed elevation and (b) water elevation at selected times during experiment UnAE05. The black line indicates the initial bed profile. Bold lines correspond to the onset times of the second and third phases (t = 238 s and t = 420 s, respectively). 70

Figure 3.4: Temporal profiles of (a) bed elevation (b) water elevation at the selected locations along the channel during experiment UnAE05. The horizontal dash lines, matching the colors of the evolution curves, indicate the initial reference bed position at the corresponding locations. 71

Figure 3.5: Spatial profiles of (a) bed elevation and (b) water elevation at selected times during experiment UnAE07. The black line indicates the reference bed profile. Bold lines correspond to the onset times of the second, third, fourth, and fifth phases (t = 180 s, 359 s, 512 s, and 750 s, respectively). 72

Figure 3.6: Temporal profiles of (a) bed elevation (b) water elevation at the selected locations along the channel during experiment UnAE07. The horizontal dash lines, matching the colors of the evolution curves, indicate the initial reference bed position at the corresponding locations. 73

Figure 3.7: Temporal evolution of bed slope (a) UnAE05 & (b) UnAE07 75

Figure 3.8: Color gradient maps of (a) bed elevation and (b) water elevation for experiment UnAE05 76

Figure 3.9: Color gradient maps of (a) bed elevation and (b) water elevation for experiment UnAE07 77

Figure 3.10: Color gradient maps of (a) Froude number, (b) water velocity and (c) water depth for experiment UnAE05 79

Figure 3.11: Color gradient maps of (a) Froude number, (b) water velocity and (c) water depth for experiment UnAE07 80

Figure 3.12: Comparison of the results from different methods used to estimate $Qs0$. 84

Figure 3.13: Comparison between $Qs0, continuity_average$ *and* $Qs0, continuity_average, CU1, IU1$ 87

Figure 3.14: Comparison between SC test & continuity method. 88

Figure 3.15: $QS0$ as a function of bed slope $S0$ (initial slope of each phase), grouped by water discharge 89

Figure 3.16: Different types of sediment front: (a) Translating; (b) Dispersive (Eslami, 2025) 90

Figure 3.17: Elevation difference at constant location 91

Figure 3.18: Elevation difference at constant time 92

Figure 3.19: Schematic representation of the space–time bed elevation matrix 92

Figure 3.20: Influence of spatial increment on celerity estimation 93

Figure 3.21: Color gradient maps of dimensional celerity C and dimensionless celerity C for experiment UnAE05* 94

Figure 3.22: Color gradient maps of dimensional celerity C and dimensionless celerity C for experiment UnAE07* 94

Figure 3.23: Example of bed and water surface detection uncertainty during the initial stage of UnAE05 95

Figure 3.24: Dimensionless characteristic time τ as a function of $FrS0$ for the steady-flow experimental dataset, together with the corresponding parabolic fit. 97

Figure 3.25: Relationship between Dimensionless Maximum Celerity and Loading Ratio (Steady Campaign) 100

Figure 3.26: Schematic representation of the triangular averaging regions used for the bulk celerity calculation UnAE05 101

Figure 3.27: Dimensionless bulk celerity $Cave/U$ as a function of Lr, with unsteady campaign data grouped by experiment 102

Figure 3.28: Dimensionless bulk celerity $Cave/U$ as a function of Lr, with unsteady campaign data grouped by phase number 103

Figure 3.29: Average Dimensionless Bulk Celerity for the Combined Steady and Unsteady Campaigns 104

Figure 3.30: Dimensionless temporal evolution of bed slope for the complete steady-flow dataset, compared with the fitted curve f(τ) 108

Figure 3.31: Dimensionless bed-slope evolution for all unsteady phases. Grey symbols represent phases with Lr < 1.42, while colored symbols indicate phases with Lr ≥ 1.42. The solid curve corresponds to the steady-flow fitted relationship. 109

Figure 3.32: Comparison between the dimensionless bed-slope evolution observed in the steady-flow and unsteady datasets for phases with Lr ≥ 1.42. 110

List of Tables

Table 1.1 Parameters of AE, steady campaign 18

Table 2.1 Material characteristics comparison 31

Table 2.2: Technical specifications of cameras 39

Table 2.3 SCQ5 Experimental results 54

Table 3.1: Unsteady experiments main parameters 65

Table 3.2: Mass conservation results of unsteady campaign 68

Table 3.3: Initial sediment transport capacity of the channel determined using different methods. 82

Table 3.4: Comparison between $Qs0, continuity_average$ *and* $Qs0, continuity_average, CU1, IU1$ 85

Table 3.5: Characteristic arrival time te *and corresponding averaging region parameters for all experimental phases* 98

Acknowledgments

I would like to express my deepest gratitude to Professor Alessio Radice for his invaluable support, guidance, and encouragement throughout the development and completion of this thesis. His expertise, insightful feedback, and continuous mentorship were instrumental in helping me navigate the challenges and complexities of this research.

I am also sincerely grateful to my co-supervisor, Dr. Hasan Eslami, for his dedicated assistance, valuable advice, and unwavering support during this work. His contributions and guidance played a significant role in shaping the direction and content of this thesis.

Finally, my heartfelt thanks go to my dear friend, Amir A., who was always there for me with his support, encouragement, and friendship. Through difficult moments and better ones alike, his kindness and support helped me move forward. I am deeply grateful for having him beside me throughout this journey.

